

University of São Paulo
Institute of Geosciences

Stefano Crivellari

**Effects of abrupt changes in the Atlantic meridional overturning circulation over the
Amazon Basin: an isotopic and elemental approach**

São Paulo

2018

STEFANO CRIVELLARI

Effects of abrupt changes in the Atlantic meridional overturning circulation over the Amazon Basin: an isotopic and elemental approach

PhD. Thesis presented to the Graduate Program in Geochemistry and Geotectonics at the Institute of Geosciences, University of São Paulo, Brazil to obtain the degree of Doctor of Science.

Supervisor: Prof. Dr. Cristiano Mazur Chiessi

São Paulo, 2018

Autorizo a reprodução e divulgação total ou parcial deste trabalho, por qualquer meio convencional ou eletrônico, para fins de estudo e pesquisa, desde que citada a fonte.

Research is what I'm doing when I don't know what I'm doing.

Wernher von Braun

Acknowledgments

I would like to thank my advisor Cristiano Chiessi for his impeccable mentorship, guidance and for his fresh scientific inspiration that directed my research over the past four years. I would also like to thank Stefan Mulitza, Henning Kuhnert, for their close collaboration to the manuscripts that have been produced over the course of this PhD. I would like to thank Igor Venancio among the rest for his wonderful hospitality by the time of my visit to the University of Bremen. I would like to thank Christoph Häggi, Rodrigo da Costa Portilho-Ramos, Yancheng Zhang, Enno Schefuß, Gesine Mollenhauer, Jens Hefter, Felipe Alexandre, Gilvan Sampaio for their important contribution to this research. Thanks to Francisco Cruz for our long discussions on South American paleoclimatology and for all the friendly conversations.

Thanks to all my collaborators at the Paleoceanography and Paloclimatology Laboratory (P2L) facility at School of Arts, Sciences and Humanities, University of São Paulo, which includes Prof. Dr. Marcio Gurgel, Prof. Dr. Wania Duleba, Prof. Dr. Vinícius Ribau Mendes, post-doctorate researchers Dr. Grasiene Luz Mathias, Dr. Rodrigo da Costa Portilhos-Ramos, doctorate students MSc. Marilia de Carvalho Campos and MSc. Ligia Pereira, masters students Patrícia Júnia Viana and Marina Fagundes Pantoja, and scientific initiation students Tainã Pinho, Beatriz Félix Silva and Natália Maia Marciano.

The execution of this research would have not been possible without the funding from the FAPESP (scholarship 2013/22521-2 part of the umbrella project 2012/17517-3), CAPES (scholarship 88887.123926/2015-00 part of the umbrella project 564/2015), and CNPq (project 422255/2016-5).

Finally thanks to Maria Carolina Catunda and Diego Souza for their friendly welcoming to Brazil and to Luana Mincoff Menegon for her true patience and love.

Table of contents

ACKNOWLEDGMENTS.....	I
LIST OF FIGURES	IV
LIST OF TABLES	VIII
LIST OF ABBREVIATIONS	IX
ABSTRACT	XI
RESUMO	XIV
CHAPTER 1 . INTRODUCTION	17
1.1 FUNDAMENTAL NOTIONS AND RESEARCH MOTIVATION.....	17
1.2 ENVIRONMENTAL SETTING.....	24
1.2.1 Modern Amazonian hydrology	24
1.2.2 Western tropical Atlantic circulation and Amazon River's output.....	25
1.3 PALEOCLIMATOLOGY OF THE WESTERN TROPICAL ATLANTIC AND THE AMAZON BASIN	27
1.4 RESEARCH OBJECTIVES AND THESIS OUTLINE	29
1.5 REFERENCES	33
CHAPTER 2 . INCREASED PRECIPITATION IN THE WESTERN EQUATORIAL ATLANTIC DURING LATE HEINRICH STADIAL 1.....	41
ABSTRACT	41
2.1 INTRODUCTION	42
2.2 REGIONAL SETTING.....	43
2.2.1 Amazon continental margin hydrology	43
2.2.2 Amazon sediments	46
2.3 MATERIAL AND METHODS.....	46
2.3.1 Sediment cores GeoB16224-1 and GeoB16212-2.....	46
2.3.2 Age models.....	47
2.3.3 Stable oxygen isotopes, Mg/Ca measurements and <i>G. ruber</i> abundance	48
2.3.4 Reconstruction of ice volume corrected sea water oxygen isotope values	51
2.3.5 Small-scale estimation of calcification ranges on site GeoB16212-2.....	51
2.3.6 δD of palmitic acid and BIT index.....	52
2.4 RESULTS.....	53
2.4.1 $\delta^{18}O$, Mg/Ca and reconstructed sea surface hydrography.....	54
2.4.2 Continental climate indicators	56
2.5 DISCUSSION	56
2.5.1 Sediment production and terrigenous input	58
2.5.2 Changes in SST and SSS at the core location.....	61
2.5.3 Changes in continental hydroclimate and its effect on Amazon River freshwater discharge.	64
2.6 CONCLUSIONS	66
2.7 REFERENCES	66
CHAPTER 3 . DIFFERENT PRECIPITATION PATTERNS ACROSS TROPICAL SOUTH AMERICA DURING HEINRICH AND DANSGAARD-OESCHGER STADIALS.....	73
DISCLAIMER:.....	73
ABSTRACT:	73
3.1 INTRODUCTION	74
3.2 MATERIAL AND METHODS	75
3.2.1 Sediment core GeoB16224-1	75
3.2.2 Age model	76
3.2.3 Major element composition	77
3.2.4 Endmember unmixing analysis.....	78
3.2.5 Alkenone analysis	79
3.3 RESULTS.....	80
3.4 DISCUSSION	81
3.4.1 Increases in the Fe/Ca ratio during H and DO stadials.....	81
3.4.2 Spatial changes in South American precipitation during H and DO stadials.....	85

3.5	CONCLUSIONS	88
3.6	REFERENCES	89
CHAPTER 4 . THE THERMAL RESPONSE OF THE WESTERN TROPICAL ATLANTIC TO SLOWDOWN EVENTS OF THE ATLANTIC MERIDIONAL OVERTURNING CIRCULATION.....		
	ABSTRACT	94
4.1	INTRODUCTION	95
4.2	CORE LOCATION AND REGIONAL SETTING.....	96
4.3	MATERIAL AND METHODS	97
4.3.1	Chronology.....	97
4.3.2	Mg/Ca-based temperatures.....	99
4.3.3	U ^k ₃₇ and TEX ₈₆ -based temperatures.....	100
4.3.4	Planktonic foraminiferal assemblage and MAT-based temperatures.....	102
4.4	RESULTS.....	102
4.4.1	Mg/Ca temperatures.....	102
4.4.2	TEX ₈₆ L temperatures and crenarchaeol concentrations.....	104
4.4.3	U ^k ₃₇ temperatures.....	104
4.4.4	Planktonic foraminiferal assemblage and MAT-based temperatures.....	105
4.5	DISCUSSION	105
4.5.1	Mg/Ca temperature record from GeoB16224-1 compared to other reconstructions.....	105
4.5.2	U ^k ₃₇ and TEX ₈₆ L temperature records from GeoB16224-1 compared to other reconstructions.....	107
4.5.3	Considerations on the use of Mg/Ca, TEX ₈₆ L and U ^k ₃₇ as temperature proxies.....	107
4.5.4	Possible effects of seasonality on U ^k ₃₇ temperature reconstructions.....	110
4.5.5	Subsurface sensitivity of U ^k ₃₇ temperatures and MAT-based temperatures from GeoB16224-1.....	113
4.6	CONCLUSIONS	114
4.7	REFERENCES	115
CHAPTER 5 . CONCLUDING REMARKS.....		
	5.1 SUMMARY OF THE RESEARCH.....	121
	5.2 GENERAL OVERVIEW	121
CHAPTER 6 . APPENDIX 1 – SUPPLEMENTARY MATERIAL TO CHAPTER 2.....		
	6.1 REFERENCES	125
CHAPTER 7 . APPENDIX 2 – SUPPLEMENTARY MATERIAL TO CHAPTER 3.....		
	7.1 REFERENCES	131

List of figures

- Figure 1-1.** Schematic representation of the main components of the Atlantic Meridional Overturning Circulation (AMOC). The northward flowing upper branch of the AMOC (red arrow) transports warm and saline waters to the North Atlantic. The formation of the North Atlantic Deep Waters (NADW) occurs at high latitudes in the North Atlantic. The southward flowing NADW lies above the abyssal Antarctic Bottom Water (AABW)..... 18
- Figure 1-2.** Schematic representation of the Atlantic Meridional Overturning Circulation (AMOC) under different climatic states. a) A warm mode, analogue to the Holocene, describes a vigorous overturning with strong production of North Atlantic Deep Water (NADW) at northern high latitudes. The northern penetration of the Antarctic Bottom Water (AABW) is reduced. b) A cold mode, analogue to the Last Glacial Maximum (LGM), presents a reduced production of NADW, extensive sea-ice and a further penetration of southern sourced AABW. c) The overturning circulation is greatly or completely reduced. This state is analogue to Heinrich Stadials which are characterized by the absence of NADW formation, release of iceberg armadas and prevailing northward penetration of AABW throughout most of the abyssal Atlantic. Figure adapted from Böhm et al. (2015). 20
- Figure 1-3.** Comparison between corrected $\delta^{18}\text{O}$ ($\delta^{18}\text{O}_{\text{corr}}$) ice core records from the (a) EPICA Dronning Maud Land (EDML) site in Antarctic (Barbante et al., 2006) and (b) North Greenland Ice Core Project (NGRIP) site from Greenland (Andersen et al., 2004). Figure adapted from Barbante et al. (2006). On the EDML curve Marine Isotope Stages (MIS) 5.5 to 1 are labeled. Last Glacial Maximum (LGM) is also highlighted. On the NGRIP curve Dansgaard-Oeschger (DO) events 25 to 1 are reported by the numbers in black. 21
- Figure 1-4.** Monthly precipitation averages over the period 1981-2010 for August and January over South America. White dashed lines highlight the mean position of the Intertropical Convergence Zone (ITCZ) and the South Atlantic Convergence Zone (SACZ). The precipitation data was obtained from GPCC (Schneider et al., 2015)..... 24
- Figure 1-5.** (a) Western tropical Atlantic mean annual salinity map and (b) mean annual salinity profile along the transect highlighted with a black line on panel a. (c) Mean annual temperature and (d) vertical temperature profile along the transect highlighted with a black line on panel c (Locarnini et al., 2013). 26
- Figure 2-1.** Location of the marine sediment cores investigated in this study (black pentagons, gravity core GeoB16224-1 and multicore GeoB16212-2). The main surface currents are schematically represented by the white arrows (Peterson and Stramma, 1991). Both core sites are under the influence of the Amazon low salinity plume and the northwestward-flowing North Brazil Current. The dotted lines display the approximate locations of the Intertropical Convergence Zone (ITCZ) over the Atlantic Ocean during boreal (June-August) and austral (December-February) summers. Annual salinities are displayed in the color shading (Levitus et al., 2013). 44
- Figure 2-2.** a) Annual sea surface salinity (Levitus et al., 2013) and location of areas (white rectangles) used in panels b, c and e. The star on the map represents the location of CTD cast at $3^{\circ} 6' \text{ N}$, $49^{\circ} 12' \text{ W}$ for August, used for the calculation of the predicted calcite $\delta^{18}\text{O}$ in panel d. (b, c) Integrated vertical salinity profiles for the annual sea surface salinity minima (May – July, orange lines) and maxima (November – January, blue lines) (Salisbury et al., 2011), including the respective standard deviations. Data was extracted from unprocessed CTD casts made available from the World Ocean Database 2013 (https://www.nodc.noaa.gov/OC5/WOD/pr_wod.html; Levitus et al., 2013). Area b is centered at 52° W , 17 stations were sampled, the location is under the influence of the Amazon low salinity plume; area c is centered at 46° W , 7 stations were sampled, the area is not under the influence of the Amazon low salinity plume. (d) Vertical profile for the predicted calcite $\delta^{18}\text{O}$ for the site of the CTD cast (proximal to multicore GeoB16212-2). The site is in the Amazon shelf under the direct influence of the Amazon low salinity plume. (e) The black line with the gray shading represent the average salinity profile and the standard deviation for June for area e, which enclose site GeoB16212-2 (area centered at 3° N , 49° W , 24 stations sampled) (Levitus et al., 2013). The orange and dark blue lines represent the salinity and temperature profiles, respectively, from the CTD cast for August, used for the calculation of the predicted calcite $\delta^{18}\text{O}$ (panel d). For details on the calculation of the predicted calcite $\delta^{18}\text{O}$ please see section 2.3.5. The gray vertical bar indicate the main layers of the upper water column..... 45

- Figure 2-3.** Age model of core GeoB16224-1, based on radiocarbon (^{14}C) measurements (red symbols) previously published by Zhang et al. (2015). An additional age control point at 710 cm was assumed with age 46830±470 years, from a well-dated stalagmite from El Condor (Cheng et al., 2013). The age model and associated uncertainties were calculated by using the R script BACON version 2.2 (Blaauw and Christen, 2011) and the IntCal13 calibration curve (Reimer et al., 2013) with a reservoir correction age of 400 ± 100 yr. (1σ error). The construction of the age model follows the methodology applied by Zhang et al. (2017) and Haggi et al. (2017) on the same core. Grey dotted lines indicate the analytical uncertainty of the median age (red dotted line) and the 2σ uncertainty at 5 mm resolution calculated by combining down core Monte Carlo proxy time series realizations. Note that prior to ca 12 ka BP there might be a hiatus. 47
- Figure 2-4.** (a) Distribution of *Globigerinoides ruber* (red bars) and *Globigerinoides sacculifer* (orange bars) $\delta^{18}\text{O}$ from multicore GeoB16212-2. The gray vertical bar indicate the main layers of the upper water column. (b) Downcore *G. ruber* (red circles) and *G. sacculifer* (orange rhomboids) $\delta^{18}\text{O}$ from multicore GeoB16212-2. Note that although *G. ruber* shows a wide range of $\delta^{18}\text{O}$, *G. sacculifer* shows consistently heavier values, preferring deeper calcification depths, below the low salinity plume. 49
- Figure 2-5.** Proxy records from gravity core GeoB16224-1 together with a sea surface temperature (SST) record off northeastern Brazil, northward heat transport from a transient model run and ice core $\delta^{18}\text{O}$. (a) $\delta^{18}\text{O}$ of *Globigerinoides ruber* and *Globigerinoides sacculifer* from core GeoB16224-1 (solid lines are five points moving average) (this study). (b) Insolation curve at 15° S for austral summer months (DJF). (c) Sea water ice volume corrected $\delta^{18}\text{O}$ ($\delta^{18}\text{O}_{\text{sw-ivc}}$) from core GeoB16224-1 (solid line is five points moving average) (this study). (d) δD of palmitic acid from core GeoB16224-1 (solid line is three points moving average) (this study). (e) *G. ruber* Mg/Ca derived SST from core GeoB16224-1 (this study). Note that from ca. 17.5 cal ka BP onwards, temperatures show a slight increase as highlighted by the black dotted line (linear regression from 17.5 cal ka BP onwards) consistent with a deglacial trend (Jaeschke et al., 2007). (f) TraCE-21k model output for the northward heat transport in the Atlantic (Liu et al., 2009), integrated over an area ($5^\circ 42' \text{ N} - 7^\circ 42' \text{ N}$ and $53^\circ \text{ W} - 51^\circ \text{ W}$) that include site GeoB16224-1. (g) Mg/Ca SST off northeastern Brazil (Weldeab et al., 2006). (h) $\delta^{13}\text{C}$ of *Cibicidoides wuellerstorfi* from core GeoB16224-1 (Voigt et al., 2017). (i) North Greenland Ice Core Project (NGRIP) $\delta^{18}\text{O}$ (Andersen et al., 2004). Gray triangles over the horizontal axis show the calibrated radiocarbon ages and respective errors. The two Heinrich Stadial (HS) 1 phases (HS1a and HS1b) are indicated by the gray bars. 54
- Figure 2-6.** Proxy records from gravity core GeoB16224-1 together with speleothems and glacier records from the tropical Andes. (a) Sea water ice volume corrected $\delta^{18}\text{O}$ ($\delta^{18}\text{O}_{\text{sw-ivc}}$) on core GeoB16224-1 (solid line is five point moving average) (this study). (b) $\delta^{18}\text{O}$ record from Huascaran ice core (Thompson et al., 1995). (c) $\delta^{18}\text{O}$ record from Pacupahuain cave speleothem (Kanner et al., 2012), dating error bars are displayed underneath the curve. (d) $\delta^{18}\text{O}$ record from Diamante cave speleothem (Cheng et al., 2013), dating error bars are displayed underneath the curve. (e) *Globigerinoides ruber* abundance from core GeoB16224-1 (this study). (f) $\ln(\text{Fe}/\text{Ca})$. (g) Branched GDGT (brGDGT) concentration normalized for sample weight from core GeoB16224-1 (this study). (h) Branched and isoprenoid tetraether (BIT) index representing terrestrial vs marine contribution of organic matter, constructed using the ration between brGDGT and crenarchaeol organic molecules from core GeoB16224-1 (this study). Note that a marked increase in the terrestrial brGDGT is following the BIT signal suggesting that terrestrial sediment apportionment is increasing predominantly on HS1a whereas crenarchaeol concentration remains mostly stable (see Fig. S6-2). Gray triangles over the horizontal axis show the calibrated radiocarbon ages and respective errors. The two Heinrich Stadial (HS) 1 phases (HS1a and HS1b) are indicated by the gray bars. 59
- Figure 2-7.** Selected atmospheric and continental indicators discussed in the text. (a) Reflectance record from Cariaco Basin (Deplazes et al., 2013). (b) δD on palmitic acid from core GeoB16224-1 (this study). (c) $\delta^{13}\text{C}$ *n*-alkanes from core GeoB16224-1 (Haggi et al., in revision). (d) $\delta^{18}\text{O}$ record from North Greenland Ice Core Project (NGRIP) (Andersen et al., 2004). Gray triangles over the horizontal axis show the calibrated radiocarbon ages and respective errors. The two Heinrich Stadial (HS) 1 phases (HS1a and HS1b) are indicated by the gray bars. 65
- Figure 3-1.** Location of paleorecords and environmental setting over tropical South America and the adjacent oceans. Monthly averaged terrestrial precipitation (1981e2010) from the University of Delaware (<http://climate.geog.udel.edu/~climate/>), wind field from the NOAA/OAR/ESRL PSD (<http://www.esrl.noaa.gov/psd/>) and mean sea surface salinity (SSS) from the World Ocean Atlas 2013 (Zweng et al., 2013) are given for (a) austral summer (December-January-February (DJF) for precipitation, March for SSS) and (b) austral winter (June- July-August (JJA) for precipitation,

September for SSS). The schematic positions of the Intertropical Convergence Zone (ITCZ) over the Atlantic during DJF and JJA (black lines) are also shown. (c) Grey arrows mark surface currents over the western tropical Atlantic (Johns et al., 1998) that are relevant for this study, circles denote the location of sediment core GeoB16224-1 (black, the same as in (a) and (b)) and previously published paleoclimate records (red) discussed in the text (for detailed information about each site see Table 1) as well as the suspended sediment samples (grey circles with black outlines for published results, grey circles without outline for new data) used for the endmember unmixing analysis (see section 3.2.4). (For interpretation of the references to colour in this figure legend, the reader is referred to the web version of this article.)

..... 76

Figure 3-2. Age model of core GeoB16224-1 based on calibrated ^{14}C ages by the IntCal13 curve (black dots) and BACON software (solid lines). Grey lines represent the median age and 2σ uncertainty (dashed grey) derived from the BACON software (section 3.2.2 of the main text). We assume an age control point at 710 cm as 46830 ± 470 years from a well-dated stalagmite from El Condor (Cheng et al., 2013a) to obtain the age model for whole core GeoB16224-1 using the BACON software, based on i) small changes in accumulation rate of sediment core GeoB16224-1, ii) the similarity between variations of both inorganic (Fe/Ca, $\delta^{13}\text{C}$ and $\delta^{18}\text{O}$ of benthic foraminifers (unpublished data)) and organic proxies in this core with stalagmite $\delta^{18}\text{O}$ records from the Andes. The inclusion of this age tie point at 710 cm would not modify the age model of the investigated period between 13 and 41 ka BP (please note that there might also be a hiatus prior to ca. 12 ka BP)..... 77

Figure 3-3. Downcore geochemistry of sediment core GeoB16224-1. (a) NGRIP ice core $\delta^{18}\text{O}$ record to highlight Heinrich (H) stadials 1e4 (pink bars) and Dansgaard-Oeschger (DO) stadials (cyan bars) (Rasmussen et al., 2014), (b) $\ln(\text{Fe}/\text{Ca})$, (c) alkenone $\text{C}_{37}/\text{C}_{38}$ and (d) C_{37} concentration, (e) $\ln(\text{Fe}/\text{K})$, (f) Al/Si as well as (g) the endmember (EM) modeled proportions based on major elements. (For interpretation of the references to colour in this figure legend, the reader is referred to the web version of this article.)..... 81

Figure 3-4. Paleoprecipitation records across Central and tropical South America. (a) NGRIP ice core $\delta^{18}\text{O}$ record and time windows of Heinrich (H) stadials (pink bars) and Dansgaard-Oeschger (DO) stadials (cyan bars) (Rasmussen et al., 2014), (b) magnetic susceptibility from Lake Petén Itzá (Escobar et al., 2012), (c) total reflectance of sediment core MD03-2621 (Deplazes et al., 2013), (d) Pacupahuain Cave $\delta^{18}\text{O}$ record (Kanner et al., 2012), (e) $\ln(\text{Fe}/\text{Ca})$ and (g) proportion of Andean material within the terrigenous fraction of core GeoB16224-1 (this study), (f) $^{231}\text{Pa}/^{230}\text{Th}$ from Bermuda Rise (combination of 15.2-24.8 ka BP from ODP 1063 (Böhm et al., 2015) and 24.8-41 ka BP from CDH19 (Henry et al., 2016)), (h) Ti/Ca record of sediment core CDH86 (Nace et al., 2014), (i) Ti/Ca record of sediment core GeoB3910-2 (Jaeschke et al., 2007). Note that H stadal 2 in core CDH86 (h) is misplaced (it thus requires direct radiocarbon measurement for last 20 ka of this core, Nace et al., 2014)..... 83

Figure 3-5. Detailed comparison of paleoprecipitation records for tropical South America between 40 and 28 ka BP. (a) time windows of Heinrich (H) stadials (pink bars) and Dansgaard-Oeschger (DO) stadials (cyan bars) as outlined from the NGRIP ice core $\delta^{18}\text{O}$ record (Rasmussen et al., 2014), (b) total reflectance of core MD03-2621 (Deplazes et al., 2013), (c) Pacupahuain Cave $\delta^{18}\text{O}$ record (Kanner et al., 2012), (d) $\ln(\text{Fe}/\text{Ca})$ record of core GeoB16224-1, (e) Ti/Ca record of core CDH86 (Nace et al., 2014). 87

Figure 4-1. Location of marine sediment core GeoB16224-1 investigated in this study (black pentagon), as well as the following other sediment cores mentioned in the text (black circles): M35003-4 (Portilho-Ramos et al., 2017), MD03-2616 (Rama-Corredor et al., 2015), GeoB16206-1 (Portilho-Ramos et al., 2017), GeoB3910-2 (Jaeschke et al., 2007). The northwestward-flowing North Brazil Current and the eastward-flowing North Equatorial Counter Current are represented by the white arrows (Peterson and Stramma, 1991). Schematized provenience of prevalent trade winds is illustrated with group of three white arrows. The dotted lines display the approximate locations of the Intertropical Convergence Zone (ITCZ) during austral winter (June-August) and austral summer (December-February). Annual sea surface temperature is displayed in the color shading (Locarnini et al., 2013). 97

Figure 4-2. Age model of core GeoB16224-1, based on radiocarbon (^{14}C) measurements (grey symbols) by Zhang et al. (2015), also used in the present study. An additional age control point (46830 ± 470 years) at 710 cm core depth was assumed by fitting the Heinrich Stadal 5 Fe/Ca peak from GeoB16224-1 to the well-dated stalagmite from El Condor (Cheng et al., 2013). The age model and associated uncertainties were calculated with the R script BACON version 2.2 (Blaauw and Christeny, 2011) and the IntCal13 calibration curve (Reimer et al., 2013) with a reservoir correction age of 400 ± 100 yr. (1σ error). The construction of the age model follows the methods applied by Zhang et al. (2017) and Häggi et al. (2017)

- on the same core. Grey dotted lines indicate the analytical uncertainty of the median age (blue line) and the 2σ uncertainty at 5 mm resolution calculated by combining down core Monte Carlo proxy time series realizations. Note that prior to ca 12 cal ka BP there might be a sedimentary hiatus in core GeoB16224-1. 98
- Figure 4-3.** Temperature proxy records from gravity core GeoB16224-1 together with $U^{k'_{37}}$ temperatures from the Guiana Basin and off NE Brazil, as well as an Antarctic stable oxygen isotope ($\delta^{18}O$) record. (a) $\delta^{18}O$ record from the EPICA Dronning Maud Land (EDML) ice core. Antarctica Isotope Maxima (AIM) are labeled above each event (Barbante et al., 2006). (b) *Globigerinoides ruber* Mg/Ca-based temperatures from core GeoB16224-1 (this study). (c) $TEX_{86}H$ and $TEX_{86}L$ -based temperatures from core GeoB16224-1 (this study). (d) $U^{k'_{37}}$ temperatures from core GeoB16224-1 (this study). (e) $U^{k'_{37}}$ temperatures from core GeoB3910-2 retrieved off NE Brazil (Jaeschke et al., 2007). (f) $U^{k'_{37}}$ temperatures from core MD03-2616 retrieved from the Guiana Basin (Rama-Corredor et al., 2015). Black triangles over the horizontal axis show the calibrated radiocarbon ages of core GeoB16224-1 as well the tie-point used to produce its age model. The Heinrich Stadial (HS) events 5 to 1 are indicated by the blue bars. 103
- Figure 4-4.** Comparison between $TEX_{86}L$ -based temperatures, $\ln(Fe/Ca)$ (indicating terrigenous input), and concentration of crenarchaeol (marine GDGTs) indicating from core GeoB16224-1. (a) $TEX_{86}L$ -based temperatures from core GeoB16224-1 (this study). (b) $\ln(Fe/Ca)$ from core GeoB16224-1 (Zhang et al., 2017). (c) Crenarchaeol concentration normalized for sample weight from core GeoB16224-1 (this study). Black triangles as in Fig. 4-3. The Heinrich Stadial (HS) events 5 to 1 are indicated by the blue bars. 110
- Figure 4-5.** Comparison between the $U^{k'_{37}}$ and modern analog technique (MAT) -based temperature records from gravity core GeoB16224-1 with $U^{k'_{37}}$ and MAT-based temperature reconstructions from other locations in the western tropical Atlantic. (a) Stable oxygen isotope ($\delta^{18}O$) record from the EPICA Dronning Maud Land (EDML) ice core. Antarctica Isotope Maxima (AIM) are labeled above each event (Barbante et al., 2006). (b) $U^{k'_{37}}$ temperatures from core M35003-4 from the Tobago Basin (Rühlemann et al., 1999). (c) MAT temperatures from core M35003-4 (Portilho-Ramos et al., 2017; Hüls and Zahn, 2000). (d) $U^{k'_{37}}$ temperatures from core GeoB16224-1 (this study). (e) MAT temperatures from core GeoB16224-1 (this study). (f) $U^{k'_{37}}$ temperatures from core GeoB3910-2 retrieved off NE Brazil (Jaeschke et al., 2007). (g) MAT temperatures from core GeoB16206-1 (Portilho-Ramos et al., 2017). (h) $U^{k'_{37}}$ temperatures from core MD03-2616 from the Guiana Basin (Rama-Corredor et al., 2015). Black triangles as in Fig. 4-3. The Heinrich Stadial (HS) events 5 to 1 are indicated by the blue bars. 112
- Figure S6-1.** Comparison between (a) the branched and isoprenoid tetraether (BIT) index and its components namely the concentration of (b) brGDGT and (c) crenarchaeols from core GeoB16224-1 investigated in this study. Notice that the BIT index record closely resembles the brGDGT concentration record, suggesting that changes in the terrestrial component of the BIT index largely dominate the BIT index signal. 124
- Figure S6-2.** Comparison between (a) $\ln(Fe/Ca)$ and (b) $\ln(Fe/K)$ from core GeoB16224-1 (Zhang et al., 2017) investigated in this study. 125
- Figure S6-3.** Comparison between (a) Pa/Th record of core OCE326-GGC5 from the Bermuda Rise (McManus et al., 2004) and (b) $\delta^{13}C$ of the benthic species *Cibicidoides wuellerstorfi* from core GeoB16224-1 (Voigt et al., 2017) investigated in this study. 125
- Figure S7-1.** Comparison of elemental ratios in core GeoB16224-1 obtained by energy dispersive polarization X-ray fluorescence (EDP-XRF) spectroscopy and XRF-calibrated data. Down core $\ln(Fe/Ca)$ values are presented versus depth for both the XRF-calibrated data (grey line) and the EDP-XRF measurements (crossed dots). The R_2 ($R_2=0.83$) value is the mean R_2 of all element/Ca log-ratio regressions (Weltje and Tjallingii, 2008). 126
- Figure S7-2.** The C_{37} alkenone flux calculated based on i) C_{37} alkenone concentration and ii) accumulation rate and iii) dry bulk density of sediment in core GeoB16224-1. In general, the C_{37} alkenone flux showed similar pattern as the C_{37} alkenone concentration. For DO stadials 8-7, we note a relatively high C_{37} alkenone flux. Because there are no significant changes in dry bulk density of sediment core GeoB16224-1, the higher C_{37} flux is closely related to the sedimentation rate. We suggest that more radiocarbon dates, in particular for the DO cycles, may allow a clear understanding of sediment deposition and thus the C_{37} alkenone flux calculation. 127

- Figure S7-3.** The fragmentation index by using abundance of planktonic and benthic foraminifera from totally 102 samples in core GeoB16224-1, which indicated the variations of carbonate dissolution over the past 40 ka BP. If compared to the $\ln(\text{Fe}/\text{Ca})$ ratios, we clearly observed reduced dissolution of marine carbonate (as highlighted by decreased values of fragmentation index) during both the H and DO stadials. Thus, this result exclude our assumption that the carbonate dissolution contribute somehow to the changes of $\ln(\text{Fe}/\text{Ca})$ ratios. 128
- Figure S7-4.** Results of the endmember unmixing analyses based on different Si hypotheses for lowland and Andes endmembers. We use a range of the Si proportions from 57.5% to 62.5% for the Andes (see panels in horizontal direction); while for the lowland, we use the range between 40% and 50% (see panels in vertical direction) (note the x-axis is the number of XRF scanning data with a step of 5mm, thus double as core length 750cm). Table S2. Summary of the terrigenous and marine biogenic endmembers (EM) used in the unmixing analysis (section 3.2.4 of the main text) for sediment core GeoB16224-1. Numbers in terrigenous EM columns refer to Table S7-1. 131

List of tables

- Table 2-1.** Summary of proxy response to the two phases of Heinrich Stadial (HS) 1 phases (HS1a and HS1b). The location, proxy type, reconstructed environmental parameter, change in the reconstructed parameter and the reference is provided for each record. The amount of plus (minus) signs indicate the strength of the increase (decrease) in the reconstructed parameter for each HS1 phase in relation to the previous period. Dots represents unappreciable change in the reconstructed parameter. HS1a is placed after to HS1b for visual consistence with Figs. 5-7. BIT: branched and isoprenoid tetraether index; brGDGT: branched and isoprenoid glycerol dialkyl glycerol tetraethers; SSS: sea surface salinity; SST: sea surface temperature. 58
- Table 3-1.** Coordinates and other information for sediment core GeoB16224-1 and previously published paleorecords depicted in Figs.3-1, 3-4 and 3-5. * Represents the measurement step (in mm) and the related temporal resolution (in year). 86
- Table 4-1.** Radiocarbon ages employed in the construction of the age model of gravity core GeoB16224-1. AMS radiocarbon ages are from (Zhang et al., 2015). The age at 710 cm has been calculated by matching of the XRF record of core GeoB16224-1 (Zhang et al., 2015) to the El Condor speleothem chronology (Cheng et al., 2013). The radiocarbon ages at 6 cm and at 50 cm were excluded from the age model. 99
- Table S7-1.** Major element composition of river suspended material used for the endmember unmixing analysis (elemental proportions are given in weight percent and were calculated such as the sum of the six elements considered in this study is 100%). * Because of Si loss during total digestion (section 3.2.3 of the main text), the Si proportion of the 28 new river samples is assigned, i.e., 60% for samples from Andean tributaries Solimões and Madeira Rivers based on previously published data (Bouchez et al., 2011, 2012), and 45% for samples in lowland tributaries Negro (Govin et al., 2014), Tapajós and Xingu Rivers (Sholkovitz et al., 1978). An error of Si proportion (e.g., $\pm 2.5\%$) is also included in the endmember unmixing analysis. We run three sets of 1000 Monte-Carlo iterations with different Si proportions of river suspended samples. 130
- Table S7-2.** Summary of the terrigenous and marine biogenic endmembers (EM) used in the unmixing analysis (section 3.2.4 of the main text) for sediment core GeoB16224-1. Numbers in terrigenous EM columns refer to Table S7-1. a The marine biogenic endmember includes only Ca and Si, which are derived from the carbonate and biogenic opal content of surface sediments in nearby sites (Lochte et al., 2000; <http://doi.pangaea.de/10.1594/PANGAEA.53229>). Values in parentheses are the errors on the composition included in the 95% confidence intervals of endmember unmixing analysis. b Nutrient-rich freshwater from the Amazon River stimulates siliceous productivity in surface waters off the Amazon mouth, as substantiated by high diatom abundance and high biogenic silica (up to 40 %) (DeMaster et al., 1983). However, the low carbonate content (ca. 7.5 %) measured in our study area indicates low biological activity, which was not sufficiently large to raise the carbonate content to 10% (Gibbs, 1973). Thus, the low biogenic silica content (< 1 %) of surface sediments still generates the high Si proportion in the endmember's composition. In addition, the error on respective Ca and Si proportions that we used during the Monte-Carlo analysis accounts for small variations in biogenic opal content. 131

List of abbreviations

- $\delta^{13}\text{C}$ – Stable carbon isotopic composition
 $\delta^{18}\text{O}$ – Stable oxygen isotopic composition
 δD – Stable deuterium isotopic composition
 ^{14}C – Radiocarbon
AABW – Antarctic Bottom Water
AIM – Antarctic Isotope Maxima
AMOC – Atlantic Meridional Overturning Circulation
AMS – Accelerator mass spectrometry
APCI – Atmospheric Pressure Chemical Ionization
BA – Bølling-Allerød (14.5-13 cal ka BP)
BC – Brazil Current
BIT – Branched and Isoprenoid Tetraether
brGDGT – Branched and isoprenoid glycerol dialkyl glycerol tetraethers
CTD – Conductivity temperature density
DCM – Dichloromethane
DO – Dansgaard-Oeschger
DOS – Dansgaard-Oeschger Stadial
DJF – Austral summer months (December-January-February)
EDML – EPICA Dronning Maud Land
ENSO – El Niño-Southern Oscillation
EPICA – European Project for Ice Coring in Antarctica
ESL – Estimated sea level
FAME – Fatty Acid Methyl Esters
GCh – Gas Chromatographer
GC – Guiana Current
GDGT – Isoprenoid glycerol dialkyl glycerol tetraethers
HS – Heinrich Stadial
HS1 – Heinrich Stadial 1 (18-15 cal ka BP)
HS1a – First part of Heinrich Stadial 1 (18-16.9 cal ka BP)
HS1b – Second part of Heinrich Stadial 1 (16.9 to 14.8 ka BP)
IRD – Ice-rafted debris
ITCZ – Intertropical Convergence Zone
Ka BP – Thousand years before present (present day is defined at year 1950)
LC – Liquid chromatography
LGM – Last Glacial Maximum (23-19 cal ka BP)
LLJ – Low level jet
MAT – Modern Analogue Technique

MSM20/3 RV – Maria S. Merian cruise 20/3
NADW – North Atlantic Deep Water
NBC – North Brazil Current
NECC – North Equatorial Counter Current
NGRIP – North Greenland Ice Core Project
POC – Particulate organic carbon
SACZ – South Atlantic convergence zone
SASM – South American summer monsoon
SMOW – Standard Mean Ocean Water
SSS – Sea surface salinity
SST – Sea surface temperature
VPDB – Vienna Pee Dee Belemnite
VSMOW – Vienna Standard Mean Ocean Water
XRF – X-ray fluorescence
YD – Younger Dryas (12.9-11.7 cal ka BP)

Abstract

Crivellari S. **Effects of abrupt changes in the Atlantic meridional overturning circulation over the Amazon Basin: an isotopic and elemental approach.** 2018. 138 pp. Thesis (Doctorate) – Institute of Geosciences, University of São Paulo, São Paulo.

One of the most important findings emerging from paleoclimate research of the last 20 years is the fact that global climate has the potential to abruptly switch between states. Gradual changes in climate during the last 50 ka are punctuated by fast transitions whose onsets occurred within a few decades. These abrupt climatic changes are probably the closest analogues to the pace of modern climate change. It is well established that abrupt climate changes during late Quaternary are associated to severe reorganization of the atmospheric and oceanic circulations. In this thesis we attempt to advance the understanding of the context in which natural forcing lead to abrupt climate change. This is of paramount importance in order to provide a solid framework for understanding modern climate change and actualize effective mitigation policies.

A key component of the global climate system is the Atlantic Meridional Overturning Circulation (AMOC). The AMOC is responsible for the transport of heat and salt to the high latitudes of the North Atlantic. A deviation from the equilibrium state in the rate of the AMOC flow is associated to severe reorganization of atmospheric and oceanic circulation which is undoubtedly a fundamental mechanism used for explaining abrupt climate change. A decrease in the export of heat to the northern hemisphere causes a steeper latitudinal sea surface temperature (SST) gradient in that hemisphere intensifying the northeastern trade winds. This, in turn, has a direct effect on tropical South American precipitation as more moisture from the adjacent ocean is brought into the continent. Sites located at the western tropical Atlantic Ocean are sensitive to both changes in continental hydrology as well as regional oceanography. Therefore, they represent ideal targets for paleo-records and an opportunity for paleoclimate reconstructions.

A well dated sediment core (i.e., GeoB16224-1), collected 400 km to the north of the Amazon River mouth off French Guiana (7° N) was retrieved and analysed at high resolution with a multitude of paleo-proxies. The core site is located under the full influence of the Amazon River discharge, offering for the first time a basin-wide integrated record of past changes in Amazonian hydrology. We targeted the last glacial-interglacial transition as well as abrupt millennial-scale climatic changes of the late Pleistocene (last 45 ka). We were able

to obtain on the one hand relevant information on the hydrological history of the Amazon Basin and the regional changes in marine properties with special emphasis on Heinrich Stadial (HS) 1 (about 18 to 15 cal ka BP, Chapter 2), Dansgaard-Oeschger Stadials (DOS) 8 to 5 (about 37 to 31 cal ka BP, Chapter 3), and on the other hand relevant information on the thermal history of the upper water column in the western tropical Atlantic for the last 45 ka (Chapter 4), resolving important discrepancies in previously published records. Thus, the main objectives of this thesis were: (i) to investigate the internal structure of HS1 and its effect on Amazonian hydrology at high resolution; (ii) to investigate the different impact of HS and DOS on precipitation within the Amazon Basin; and (iii) to understand the thermal evolution of the upper water column in the western tropical Atlantic during the last 45 ka with emphasis on millennial-scale anomalies.

We first explored the relationship between HS 1 and Amazonian hydroclimate. We present a high resolution multiproxy study based on samples from gravity core GeoB16224-1. We reconstructed surface water hydrography using oxygen stable isotopes ($\delta^{18}\text{O}$) and Mg/Ca-derived paleotemperatures from planktonic foraminifera *Globigerinoides ruber*, as well as salinity based on stable hydrogen isotopes (δD) of palmitic acid. We also analysed branched and isoprenoid tetraether (BIT) concentrations and compared them to existing records of bulk sediment $\ln(\text{Fe}/\text{Ca})$ data and vegetation reconstruction based on stable carbon isotopes from *n*-alkanes, in order to understand the relationship between continental precipitation, changes in vegetation and sediment production. Our results indicate a two-phased HS1 (HS1a and HS1b). During HS1a (18-16.9 cal ka BP), a first sudden increase in SST in the western tropical Atlantic correlated with the slowdown of the AMOC and the associated southern hemisphere warming phase of the bipolar seesaw. This phase was also characterized by an increased delivery of terrestrial material. During HS1b (16.9-14.8 cal ka BP), a decrease in terrestrial input was, however, associated with a marked decline of seawater $\delta^{18}\text{O}$ ($\delta^{18}\text{O}_{\text{sw}}$) and palmitic acid δD . Both isotopic proxies independently indicate a drop in sea surface salinity (SSS). Our records thus suggest that the expected increase in SSS due to the AMOC slowdown was overridden by a two-phased positive precipitation anomaly in Amazonian hydroclimate. Moreover, progressively lower values of $\ln(\text{Fe}/\text{Ca})$ and BIT index values coincident with depleted $\delta^{18}\text{O}_{\text{sw}}$ during HS1b might suggest a shift in the main locus of precipitation within tropical South America towards regions less affected by erosion (i.e., Amazonian Plain and Brazilian Shields).

Consequently, we were interested in understanding the different impact of HS-type from DOS-type climatic events in Amazonian hydrology. Older sections of the same marine sediment core were therefore investigated for $\ln(\text{Fe}/\text{Ca})$, alkenone C_{37} and carbonate fragmentation index, and compared with previously published continental paleo-records across different latitudes of the tropical Americas. A discernible difference in the effect of HS is appreciable when compared to DOS-type of millennial-scale climatic events. We find that northeastern Brazilian precipitation experienced significant increases during HS but was characterized by only subtle changes during DOS. This is associated with the degree of the Intertropical Convergent Zone dislocation caused by a reduction in the strength of the AMOC.

Finally, we found the need to better characterize the actual thermal behaviour of the upper water column at the western tropical Atlantic for the last 45 ka. We therefore performed a multiproxy, high resolution temperature reconstruction from marine sediment core GeoB16224-1, which is based on Mg/Ca on *G. ruber*, alkenone unsaturation index $\text{U}^{\text{K}'}_{37}$, TEX_{86} , and the modern analogue technique (MAT) applied to planktonic foraminifera assemblages. We detected positive temperatures anomalies during slowdown events of the AMOC HS4-HS1, as our Mg/Ca -derived SST and TEX_{86} clearly show. Positive SST anomalies in our Mg/Ca record coincide with Antarctic isotope maxima (AIM)12 to AIM1 from the EPICA Dronning Maud Land ice core $\delta^{18}\text{O}$ record. Nevertheless, $\text{U}^{\text{K}'}_{37}$ and MAT (50 m) temperature reconstruction on GeoB16224-1 show negative anomalies during HS3 and HS1. We infer that whereas TEX_{86} and Mg/Ca respond to surface temperatures, $\text{U}^{\text{K}'}_{37}$ and MAT (50 m) are affected by subsurface temperature variations which respond to vertical movement of the thermocline. The presence of ITCZ related precipitation is the most likely responsible for the increased stratification and consequent shoaling of the thermocline. Nevertheless important non-thermal physiological effects on the alkenone export has also to be taken into account. The presence of low SSS and large amount of suspended particulate related to the Amazon River increased discharge might imprint a negative temperature bias on the $\text{U}^{\text{K}'}_{37}$. However, this alone is unlikely to explain the entire variability in the $\text{U}^{\text{K}'}_{37}$ temperature signal.

Key words: paleoclimatology, paleoceanography, late Pleistocene, geochemistry, foraminifera, AMOC, millennial events, precipitation.

Resumo

Uma das mais importantes descobertas das pesquisas paleoclimáticas dos últimos 20 anos é o fato de que o clima global tem o potencial de mudar abruptamente entre diferentes estados. Mudanças graduais no clima durante os últimos 50 ka foram pontuadas por transições rápidas cujo início pôde se estabelecer em poucas décadas. Essas mudanças climáticas abruptas são provavelmente o análogo mais próximo à velocidade das mudanças climáticas modernas. Está bem estabelecido que as mudanças climáticas abruptas do Quaternário tardio estiveram associadas à reorganização severa da circulação atmosférica e oceânica. Nesta tese, tentamos avançar a compreensão do contexto no qual as forças naturais levam às mudanças climáticas abruptas. Isso é de suma importância, a fim de fornecer um quadro sólido para a compreensão das mudanças climáticas atuais e atualizar políticas efetivas de mitigação.

Um dos principais componentes do sistema climático global é a Célula de Revolvimento Meridional do Atlântico (AMOC, na sigla em Inglês). A AMOC é responsável pelo transporte de calor e sal para latitudes altas do Atlântico Norte. Um desvio do estado de equilíbrio da AMOC está associado à reorganização severa da circulação atmosférica e oceânica, que é sem dúvida um mecanismo fundamental usado para explicar as mudanças climáticas abruptas. A diminuição na exportação de calor para o hemisfério norte provoca um gradiente de temperatura da superfície (SST, na sigla em Inglês) latitudinal mais acentuado naquele hemisfério, intensificando os ventos alísios de nordeste. Isso, por sua vez, tem um efeito direto na precipitação sobre a América do Sul tropical à medida que mais umidade do oceano adjacente é trazida para o continente. Testemunhos sedimentares da porção tropical oeste do Oceano Atlântico são sensíveis às mudanças na hidrologia continental, bem como na oceanografia regional. Eles, portanto, representam um alvo ideal para registros paleoclimáticos e uma oportunidade para reconstruções paleoclimáticas.

Um testemunho sedimentar bem datado (i.e., GeoB16224-1), coletado 400 km ao norte da desembocadura do rio Amazonas na margem continental da Guiana Francesa (7° N) foi recuperado e analisado em alta resolução com uma multiplicidade de paleo-proxies. O local de retirada do testemunho está sob a franca influência da descarga do rio Amazonas, oferecendo pela primeira vez uma imagem integrada das mudanças na hidrologia amazônica. Nós almejamos a última transição glacial-interglacial, bem como as mudanças climáticas abruptas no Pleistoceno tardio (últimos 45 ka). Conseguimos obter informações relevantes sobre a história hidrológica da Bacia Amazônica e as mudanças regionais nas propriedades

marinhas, com ênfase especial no *Heinrich Stadal* (HS) 1 (cerca de 18 a 15 cal ka BP, Capítulo 2) e nos *Dansgaard-Oeschger Stadials* (DOS) 8 a 5 (cerca de 37 a 31 cal ka BP, Capítulo 3), além de caracterizar cuidadosamente a história térmica da coluna de água superior no Atlântico tropical oeste para os últimos 45 ka (Capítulo 4), resolvendo importantes discrepâncias em registros previamente publicados. Portanto, os principais objetivos desta tese foram: (i) investigar a estrutura interna do HS1 e seu efeito na hidrologia amazônica em alta resolução; (ii) investigar os diferentes impactos dos HS e DOS sobre a precipitação na Bacia Amazônica; e (iii) compreender a evolução térmica da coluna de água superior no Atlântico equatorial oeste durante os últimos 45 ka com ênfase em anomalias da escala milenar.

Primeiro exploramos a relação entre o HS1 e o hidroclima da Amazônia, em um estudo multiproxy de alta resolução baseado em amostras do testemunho sedimentar marinho GeoB16224-1. Nós reconstruímos as condições hidrográficas das águas superficiais usando a composição dos isótopos estáveis de oxigênio ($\delta^{18}\text{O}$) e as SST derivadas de Mg/Ca da espécie de foraminífero planctônico *Globigerinoides ruber*, bem como a salinidade com base na composição dos isótopos estáveis de hidrogênio (δD) do ácido palmítico. Também analisamos as concentrações de isoprenóides tetraéteres ramificados (BIT, na sigla em Inglês) e as comparamos com registros existentes do aporte de sedimentos terrígenos $\ln(\text{Fe}/\text{Ca})$ e de vegetação com base na composição dos isótopos estáveis de carbono a partir de *n*-alcanos, para entender a relação entre precipitação continental, mudanças de vegetação e produção de sedimentos. Nossos resultados indicam um HS1 de duas fases (HS1a e HS1b). Durante o HS1a (18-16.9 cal ka BP), um primeiro aumento súbito na SST do Atlântico equatorial oeste esteve correlacionado com a desaceleração da AMOC e a fase de aquecimento do hemisfério sul da *gangorra bipolar*. Esta fase também foi caracterizada por um maior descarga de sedimentos continentais. No entanto, durante o HS1b (16.9-14.8 cal ka BP), uma diminuição na descarga de sedimentos continentais foi associada a um declínio acentuado do $\delta^{18}\text{O}$ da água do mar ($\delta^{18}\text{O}_{\text{sw}}$) e do δD do ácido palmítico. Ambos proxies indicam de forma independente uma queda na salinidade da superfície do mar (SSS, na sigla em Inglês). Nossos registros sugerem, assim, que o aumento esperado na SSS devido à desaceleração AMOC foi cancelado por uma anomalia de precipitação positiva em duas fases no hidroclima da Amazônia. Além disso, os valores progressivamente mais baixos dos valores do $\ln(\text{Fe}/\text{Ca})$ e índice BIT coincidentes com o $\delta^{18}\text{O}_{\text{sw}}$ empobrecido durante o HS1b podem sugerir uma

mudança na principal região de precipitação na América do Sul equatorial para regiões menos afetadas pela erosão (i.e., Planície Amazônica e Escudos Brasileiros).

Consequentemente, buscamos entender os diferentes impactos dos eventos climáticos HS e DOS na hidrologia amazônica. As seções mais antigas do mesmo testemunho sedimentar marinho foram, portanto, investigadas para $\ln(\text{Fe}/\text{Ca})$ e C_{37} alkenonas e comparadas com registros paleoclimáticos continentais previamente publicados oriundos de diferentes latitudes da porção tropical das Américas. Os efeitos dos HS são efetivamente distintos daqueles associados aos efeitos dos DOS. A precipitação sobre o Nordeste brasileiro experimentou aumentos significativos durante os HS, mas foi caracterizada por fracas mudanças durante os DOS. Esta resposta distinta está associada à magnitude do deslocamento da Zona de Convergência Intertropical causado pela redução da intensidade da AMOC.

Finalmente, encontramos a necessidade de melhor caracterizar o comportamento térmico da coluna de água superior da porção oeste do Atlântico durante os últimos 45 ka. Realizamos, portanto, uma reconstituição de temperatura multi-indicadores com alta resolução a partir do testemunho sedimentar marinho GeoB16224-1, baseada em Mg/Ca de *G. ruber*, índice de insaturação de alkenona $\text{U}^{\text{K}'}_{37}$, TEX_{86} e a técnica dos análogos modernos (MAT) aplicada às assembleias de foraminíferos planctônicos. Identificamos anomalias positivas de temperaturas durante os eventos de desaceleração da AMOC HS4-HS1, como mostrado pelos dados de Mg/Ca -SST e TEX_{86} . As anomalias de SST positivas em nosso registro de Mg/Ca coincidem com valores máximos de isótopos estáveis de oxigênio da Antártica (AIM, na sigla em Inglês) 12 a AIM1 do registro do EPICA Dronning Maud Land. No entanto, as reconstituições de temperatura por alkenonas e MAT mostram anomalias negativas durante o HS3 e o HS1. Inferimos que, enquanto o TEX_{86} e o Mg/Ca respondem às temperaturas da superfície, o $\text{U}^{\text{K}'}_{37}$ e o MAT (50 m) são afetados pelas variações de temperatura do subsolo que respondem ao movimento vertical da termoclina. A presença de precipitação relacionada à ITCZ é a mais provável responsável pela estratificação aumentada e consequente descida da termoclina. No entanto, importantes efeitos fisiológicos não térmicos na exportação de alquenona também devem ser levados em conta. A presença de baixa SSS e grande quantidade de partículas suspensas relacionadas ao aumento da descarga do Rio Amazonas pode imprimir um sinal de temperatura negativo no $\text{U}^{\text{K}'}_{37}$. No entanto, é pouco provável que isso explique toda a variabilidade do sinal de temperatura do $\text{U}^{\text{K}'}_{37}$.

Chapter 1 . Introduction

1.1 Fundamental notions and research motivation

During the last 20 years paleoclimate records recovered from the oceans, continents and ice caps indicate a dynamical global climate over most of the last glacial cycle. At many locations in the northern hemisphere, the occurrence of abrupt climate changes were often characterized by very fast transitions taking place in a matter of decades or less (Alley & Clark, 1999; Voelker, 2002). The records from Greenland's ice clearly show examples of fast climate variability that are referred to Dansgaard-Oeschger (DO) events (Andersen et al., 2004). An abrupt climate change is defined as a modification of the climate system, forced to cross a certain threshold by a climatic forcing, reaching a new climatic state at a rate that is faster than the change of the forcing (Rahmstorf, 2001; Alley et al., 2003). Several mechanisms have been put forward to explain the abrupt climate variability including sea-ice interaction (Gildor & Tziperman, 2003; Li et al., 2005), ice-shelf or ice-sheet growth and decay (Petersen et al., 2013; Zhang et al., 2014), shifts in preferred northern hemisphere planetary wave patterns (Seager & Battisti, 2007; Wunsch 2006), and changes in the tropics (Clement et al., 2001). Nevertheless, at present, one of the dominant paradigm is that fluctuation in the northward heat transport by the Atlantic Meridional Overturning Circulation (AMOC) plays an important role in the mechanics of abrupt climate change (Broecker et al., 1985; Clark et al., 2002; Rahmstorf 2002).

Broecker (1997) called the AMOC the Achilles' heel of the climate system because of its sensitivity to small changes in freshwater influx and made the analogy to a heat-distributing conveyor belt. The AMOC constitutes a key component in the global climate system insofar the amount of heat is retained or exported from the tropical latitudes towards the poles. Among others, the AMOC, has the unique peculiarity of having a northward heat transport at all latitudes (Trenberth & Caron, 2001). The AMOC has a pivotal role in the distribution of heat between hemispheres. In fact, it is responsible for the net transport of ca. 1.33 ± 0.40 PW (1 PW = 10^{15} Watt) from the southern hemisphere to the northern hemisphere (Trenberth & Caron, 2001). The AMOC involves not only the northward transport of warm waters, but also of salty waters to the North Atlantic, and the formation of deep waters in the Nordic and Labrador Seas, which spills over the Denmark Strait and Iceland-Faroes Rise into the deep North Atlantic and mixes with Labrador Sea Water to form North Atlantic Deep

Water (NADW). Antarctic Bottom Water (AABW) formed around Antarctica is colder and denser than NADW and fills the deepest abyssal plains of the Atlantic below NADW (Fig 1-1).

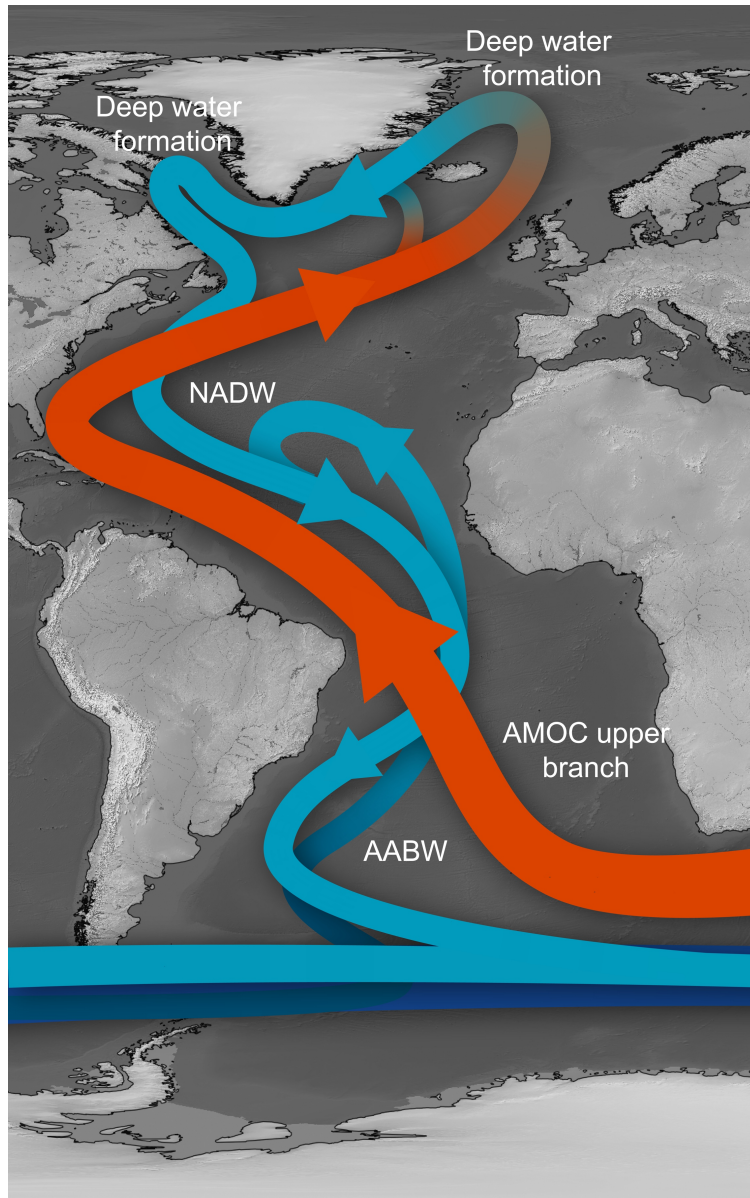


Figure 1-1. Schematic representation of the main components of the Atlantic Meridional Overturning Circulation (AMOC). The northward flowing upper branch of the AMOC (red arrow) transports warm and saline waters to the North Atlantic. The formation of the North Atlantic Deep Waters (NADW) occurs at high latitudes in the North Atlantic. The southward flowing NADW lies above the abyssal Antarctic Bottom Water (AABW).

Evidence from the North Atlantic suggests that the AMOC may operate in three different states (Fig. 1-2) (Böhm et al., 2015; Howe et al. 2016; Lynch-Stieglitz et al., 2007; Rahmstorf, 2002): i) A modern warm interglacial (interstadial) state, with a vigorous overturning circulation and deep water formation at high latitudes forming NADW (Fig. 1-2a); ii) a cold glacial (stadial) state, with a less vigorous and shallower AMOC, as well as a further northward penetration of AABW (Fig. 1-2b); and iii) a Heinrich state, with little or no overturning circulation, ceased production of NADW and extensive northward reach of AABW (Fig. 1-2c). AMOC's flow variability is linked to the amount of fresh water released at the high latitudes of the North Atlantic. When fresh water is released from melting ice sheets, surface waters are no longer capable to increase their densities and to sink forming deep waters. This normally occurs through decreasing temperatures as the AMOC upper branch travels toward higher latitudes, and by brine rejection during sea ice formation (Broecker, 2000; Lynch-Stieglitz et al., 2014; Stanford et al., 2011).

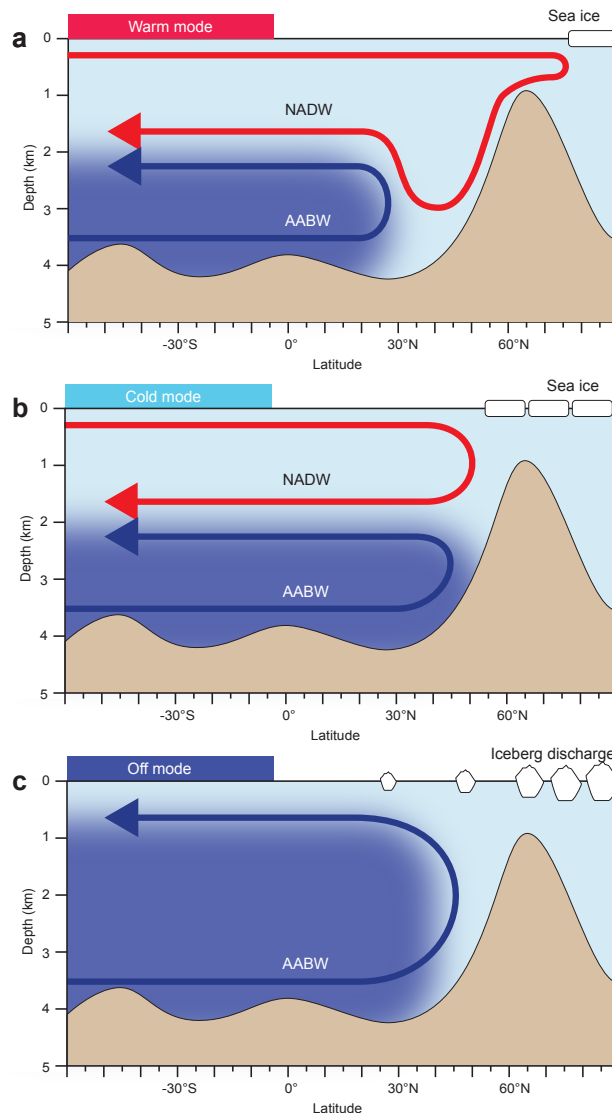


Figure 1-2. Schematic representation of the Atlantic Meridional Overturning Circulation (AMOC) under different climatic states. a) A warm mode, analogue to the Holocene, describes a vigorous overturning with strong production of North Atlantic Deep Water (NADW) at northern high latitudes. The northern penetration of the Antarctic Bottom Water (AABW) is reduced. b) A cold mode, analogue to the Last Glacial Maximum (LGM), presents a reduced production of NADW, extensive sea-ice and a further penetration of southern sourced AABW. c) The overturning circulation is greatly or completely reduced. This state is analogue to Heinrich Stadials which are characterized by the absence of NADW formation, release of iceberg armadas and prevailing northward penetration of AABW throughout most of the abyssal Atlantic. Figure adapted from Böhm et al. (2015).

Periodic purges of the continental ice directly into the North Atlantic are evident throughout the last glacial cycle. These Heinrich events are defined as 10–15 cm thick layers of debris rafted from a large quantity of icebergs and deposited across a wide area in the North Atlantic Ocean (Bond et al., 1992; Andrews & Voelker 2018). Massive iceberg

discharges from North American and European ice sheets could have provided enough fresh water to interrupt the AMOC. During phases of abrupt climate change coinciding with the Heinrich Stadials (HS) reduced AMOC flow substantially decreases its capability to transport heat to the northern hemisphere (Dahl et al., 2005). Heat is accumulated in the South Atlantic (Barker et al. 2009; Chiessi et al. 2015) whereas northern latitudes experiences colder temperatures (Stocker & Johnsen, 2003; Toggweiler & Lea, 2010). In fact, if Greenland abrupt temperature oscillations recorded in ice cores (e.g., Andersen et al., 2004) are compared to Antarctic temperature records (e.g., Barbante et al., 2006) an antiphase relationship between both records emerges (Fig 1-3).

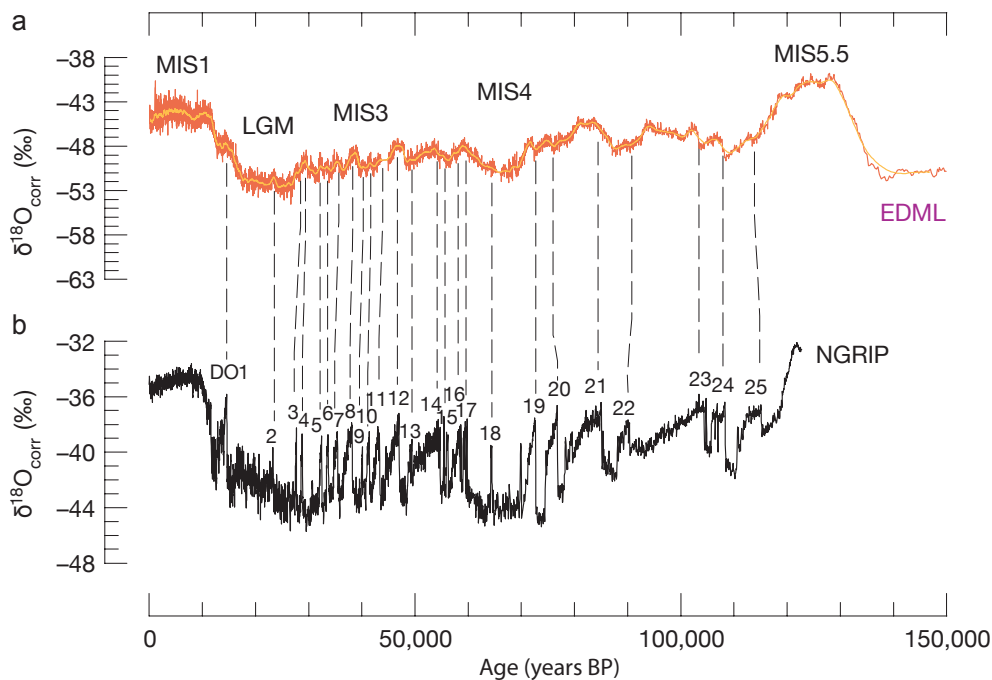


Figure 1-3. Comparison between corrected $\delta^{18}\text{O}$ ($\delta^{18}\text{O}_{\text{corr}}$) ice core records from the (a) EPICA Dronning Maud Land (EDML) site in Antarctic (Barbante et al., 2006) and (b) North Greenland Ice Core Project (NGRIP) site from Greenland (Andersen et al., 2004). On the EDML curve Marine Isotope Stages (MIS) 5.5 to 1 are labeled. Last Glacial Maximum (LGM) is also highlighted. On the NGRIP curve Dansgaard-Oeschger (DO) events 25 to 1 are reported by the numbers in black. Figure adapted from Barbante et al. (2006).

Antarctic warming is contemporaneous with North Atlantic cooling and vice versa. Intervals of heat retention in the southern hemisphere at the expense of heat export to the northern hemisphere were likely caused by slowdown events of the AMOC (Barker et al., 2009; Broecker, 1998; Chiessi et al. 2015; Stocker, 2003). The thermal *bipolar seesaw* (Mix

et al., 1986) is a fundamental mechanism responsible for sea surface temperature (SST) variability in the Atlantic Ocean during millennial-scale climate change events. Most water hosing climate model experiments, forced by transient injections of fresh water in the North Atlantic, coherently represent the *bipolar seesaw* mechanism with the formation of steeper temperature gradients in the North Atlantic as result of decreased AMOC strength (Kageyama et al., 2009; Knutti et al., 2004; Liu et al., 2009; Lohmann, 2003).

A steeper latitudinal temperature gradient is therefore installed in the North Atlantic which has a direct impact on the intensification of northeast (NE) trade winds. The rearranged oceanic heat balance changes the latitudinal position of the thermal equator, affecting the location of the tropical rain belt (Street-Perrott and Perrott, 1990; McGee et al., 2014; Schneider et al., 2014; Mulitza et al. 2017) and of the mean position of the Intertropical Convergence Zone (ITCZ) (Marshall et al., 2014). Evidence from planktonic foraminifera suggest a southward shift of the ITCZ by ca. 5° (Portilho-Ramos et al. 2017). Historical interannual to multidecadal changes in the mean position of the ITCZ is about $\pm 2^{\circ}$ (Chiang et al., 2002). Consequently, equatorial Atlantic moisture is transported further into tropical South America by the NE trade winds. The low level jet (LLJ) feed the South America monsoon system (Cook and Vizy, 2006) and, as a result, anomalously wet conditions during HS1 are found over the western Amazon Basin / equatorial Andes (e.g., Blard et al., 2011; Kanner et al., 2012; Mosblech et al., 2012; Cheng et al., 2013), and northeastern Brazil (e.g., Arz et al. 1998; Wang et al., 2004; Dupont et al., 2010; Strikis et al., 2015; Zhang et al., 2015; Mulitza et al. 2017). Expectedly, decreased precipitation at northern South America has been observed as the tropical rain belt migrated southward (Deplazes et al., 2013; Escobar et al., 2012; Peterson, 2000).

The abrupt nature of climate changes observed in the past are relevant analogues for the understanding of present and future climate change. According to recent climate model simulations the AMOC has a high degree of probability of slowing down by the end of this century as a response of modern climate change (Kirtman et al., 2013; Rahmstorf et al., 2015). In order to understand the natural context of AMOC-related climate change we investigated analogue intervals of the AMOC slowdown in paleoclimatic records, i.e., HS (Bond et al., 1993) and the stadial phases of the Dansgaard-Oeschger (DO) cycles (DOS) (Dansgaard et al., 1993). The potential effects of such AMOC slowdown and its climatic consequence on society and global ecosystem are of primary relevance today. We believe that the political response to such climatic events can be efficiently informed by the

investigation of past abrupt climate change. The research in this thesis aims to contribute to this endeavour and to subsidize the ever growing body of knowledge on the topic of past abrupt climate change.

1.2 Environmental setting

1.2.1 Modern Amazonian hydrology

Modern climate in the Amazon Basin is characterized by the seasonally modulated moisture brought by the NE trade wind system. The meridional position of the NE trade winds band is determined by the position of the ITCZ. The ITCZ is the tropical belt of minimum pressure where NE and SE trade winds converge at low latitudes over the ocean (Fig. 1-4). The ITCZ migrates seasonally in response to the seasonal interhemispheric heat balance. The modern range of the seasonal ITCZ migration is characterized by the northernmost location at 10° N in August and the southernmost position at 1° S in March (Nobre and Shukla 1996). During austral winter months (June to August), continental rainfall maxima is located north of the equator. Central and southern Amazonia experience low precipitation.

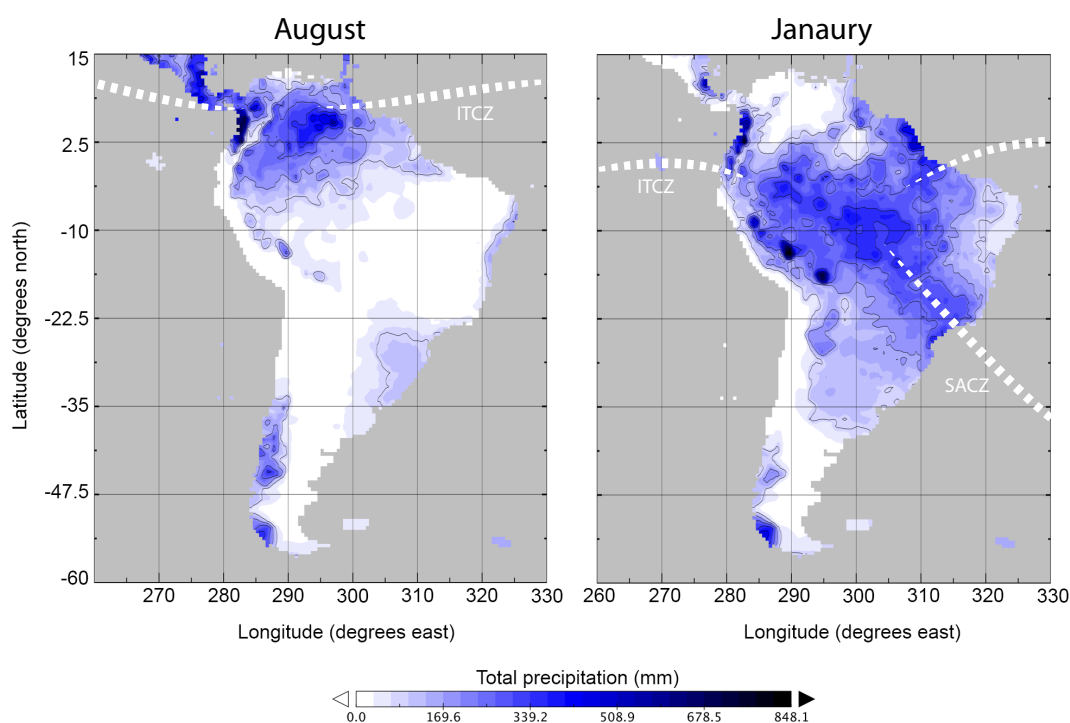


Figure 1-4. Monthly precipitation averages over the period 1981-2010 for August and January over South America. White dashed lines highlight the mean position of the Intertropical Convergence Zone (ITCZ) and the South Atlantic Convergence Zone (SACZ). The precipitation data was obtained from GPCP (Schneider et al., 2015).

During austral summer an intensification of NE trade winds follows the seasonal southward migration of the ITCZ and is responsible for the formation of the South American Summer Monsoon (SAMS) (Vera et al., 2006). During its onset in October an efficient transport of moisture into the Amazon Basin from the adjacent ocean takes place feeding intense convective storms as far as 35° S (Garreaud et al., 2009). The moisture influx is facilitated by the increased sea-land thermal gradient and stronger NE trade winds. As convection over the Amazon Basin takes place, higher summer insolation intensifies the LLJ drawing more moisture from the western Amazon and eastern tropical Andes towards subtropical South American latitudes (Garreaud et al., 2009). Over the western Amazon Basin and tropical Andes latent heat is released creating a zone of upper-level high pressure over the Bolivian Andes (Bolivian High) that increases the transport of moisture onto the Bolivian Altiplano (Lenters and Cook, 1997; Vizzy and Cook, 2007). Concomitantly, precipitation over Northeastern Brazil are strongly reduced by the installation of a Walker circulation cell determining tropical dry conditions with recurrent droughts (Moura and Shukla, 1981).

The convection system rapidly shifts southward, and the different thermal inertia between continent and the ocean deflects the ITCZ down to 15° S, extending heavy precipitation from the southern part of the Amazon to northern Argentina (Garreaud et al., 2009). The southward extension of the mean low level convergence from the southeastern Amazon Basin, collides with the southern hemisphere cold frontal system and results in a diagonal band of precipitation maxima over southeastern Brazil known as the South Atlantic Convergence Zone (SACZ) (Carvalho et al., 2004; Kodama, 1992; Vera et al., 2006).

During austral winter, strongest precipitations are located over the northern South America aligned with the oceanic ITCZ. During this time, the central South America and southern Amazonia experience its dry season.

1.2.2 Western tropical Atlantic circulation and Amazon River's output

The surface circulation in the western tropical Atlantic Ocean is dominated by the North Brazil Current (NBC) which originates from the South Equatorial Current after it splits at ca. 10° S in the western Atlantic into Brazil Current (BC) and NBC (Stramma et al., 2005). SST is on average 27.7°C and varies between about 27 °C in January - March and 28 °C in

July - September (Locarnini et al., 2013). Modern sea surface salinity (SSS) at our core location is directly influenced by the Amazon River freshwater discharge (Lentz, 1995; Müller-Karger et al., 1988). The annual cycle of SSS ranges from ca. 32 in November – January to ca. 25 in May – July (Salisbury et al., 2011) coinciding with minimum Amazon River discharge in November (ca. $0.8 \times 10^5 \text{ m}^3 \text{ sec}^{-1}$) and maximum discharge in May (ca. $2.4 \times 10^5 \text{ m}^3 \text{ sec}^{-1}$), respectively (Lentz, 1995). Most eminent among rivers, the Amazon accounts for nearly 20 % of total global river discharges into the Atlantic Ocean with an average output of $1.55 \times 10^5 \pm 0.13 \text{ m}^3 \text{ s}^{-1}$ (Wisser et al., 2010; Salisbury et al., 2011) and with bursts of up to $4 \times 10^5 \text{ m}^3 \text{ s}^{-1}$. For comparison, the average flow of all European rivers is around $0.4 \times 10^5 \text{ m}^3 \text{ s}^{-1}$.

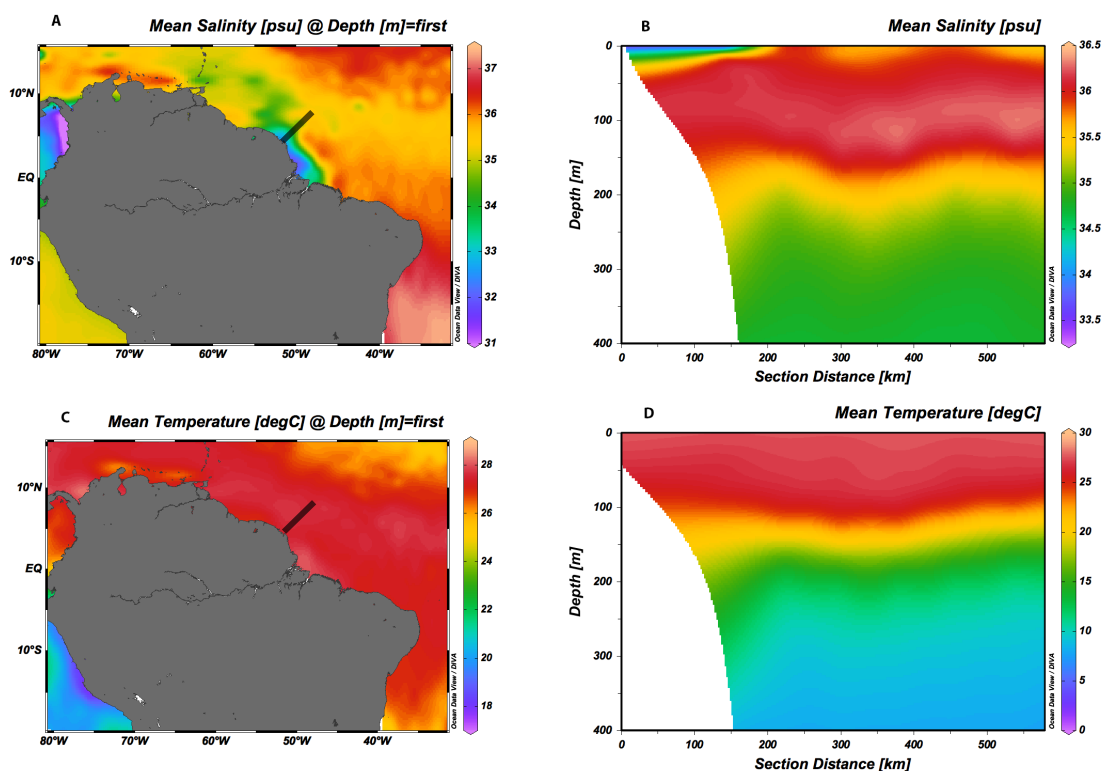


Figure 1-5. (a) Western tropical Atlantic mean annual salinity map and (b) mean annual salinity profile along the transect highlighted with a black line on panel a. (c) Mean annual temperature and (d) vertical temperature profile along the transect highlighted with a black line on panel c (Locarnini et al., 2013).

The thickness of the Amazon freshwater plume is typically 3 to 20 m (Lentz and Limeburner, 1995) and its width range from 80 to over 200 km (Fig. 1-5). The Amazon fresh

water plumes enters the western tropical Atlantic near the equator and is deflected north-westwards along the Brazilian continental margin by the North Brazil Current (NBC) flowing north-westwards (Johns et al., 1998). A tongue of low salinity waters flows over the continental shelf with a strong seasonal behaviour. At 10° N the plume often bifurcates. During austral winter and spring (low flow) the bulk of the plume flows north-westwards and feeds into the Caribbean. Through austral summer and fall (high flow) much of the plume is carried eastwards as the seasonal North Equatorial Counter Current (NECC) strengthens (Del Vecchio and Subramaniam, 2004).

A large amount of fluvial sediments (ca. $1.2 \times 10^9 \text{ t yr}^{-1}$) is discharged by the Amazon River into the western equatorial Atlantic to then be spread over the NBC path towards the continental margin off French Guiana and beyond (Allison et al., 2000). The seasonal pattern of sediment discharge is controlled by sediment erosion coming from the Andes (Gibbs, 1967), but also by sediment storage and resuspension within the basin (Meade et al., 1985) and by seasonal changes in the Amazon River's waterbed level (Zell et al., 2013). Maximum sediment discharge (up to $1.3 \times 10^9 \text{ t yr}^{-1}$) precedes peak water discharge by 2 - 3 months and is about 6 times the load of low sediment discharge months (Meade et al., 1985). The terrigenous fraction deposited on the continental margin is continuously provided by the Amazon Basin during the last 30 ka (Zhang et al. 2015). Evidence from sedimentary neodymium composition and endmember unmixing models (Mulitza et al., 2010; Collins et al., 2013) indicate that up to ca. 90% of the terrigenous fraction is sourced from intense Andean chemical weathering (Zhang et al., 2015). Inorganic particulate joins white water tributaries which drains the Andean highlands therefore characterized by higher amounts of inorganic material. In contrast, particulate organic carbon (POC) are mainly sourced from black water tributaries of the Amazon River which drain large floodplain areas. Lowland soils have the highest concentrations of dissolved humic substances (Mounier et al., 1999) and POC (Quay et al., 1992; Mayorga et al., 2005).

1.3 Paleoclimatology of the western tropical Atlantic and the Amazon Basin

Over the last glacial cycle, Amazonian hydrology and the SAMS variability have been associated to forcings operating at regional up to global scale (Baker et al., 2001; Cheng et al., 2013; Häggi et al. 2017; Kanner et al., 2012; Mosblech et al., 2012; Wang et al., 2001). Regional forcings often include summer insolation variability dominated by precessional

cycles of about 21 ka. Strong covariance between $\delta^{18}\text{O}$ variations on speleothem carbonate from Botuverá cave and the February insolation curve at 30°S strongly suggests that summer insolation maxima are generally in phase with monsoon-derived positive precipitation anomalies in the Amazon Basin and southern subtropics (Cruz et al., 2006, 2005). Yet regional heterogeneities are observed. For instance, an east-west precipitation dipole has been identified at orbital timescales whereby positive precipitation anomalies in the western Amazon Basin are contrasted by increased aridity over the eastern tropical South America. (Cheng et al., 2013; Cruz et al. 2009; Sylvestre, 2009). Moreover, speleothem records from the Andes and western Amazonia, as well as from southern Brazil show weak or absent precessional influence during the last glacial period (Cheng et al., 2013; Kanner et al., 2012; Mosblech et al., 2012).

Although the glacial Amazon lowland paleohydrology is still controversially debated largely because most of the records are located on the fringe of the basin, there is increasing evidence that a generally drier background climate took place over the Amazon Basin during glacial times relative to the late Holocene (e.g., Häggi et al. 2017; Wainer et al., 2005, Wang et al. 2017). Generally, the extent of the aridity has been linked to the degree of cooling in the tropical Atlantic and surrounding oceans (Vizy and Cook, 2005).

Millennial-scale climate variability (e.g., DOS and HS) has an important effect at low latitudes (Kanner et al., 2012). Northern hemisphere ice sheet instability (during HS) and rapid temperature shifts (during DOS) over the last glacial period and deglaciation are found to be linked to abrupt changes in precipitation over tropical South America (e.g., Cheng et al., 2013; Kanner et al., 2012). Evidence from the ratio between ^{231}Pa and ^{230}Th from sediment cores in the western Atlantic suggests that AMOC flow was significantly reduced during HS1 (ca. 18-15 cal ka BP) and the YD (12.9 – 11.7 cal ka BP) (McManus et al., 2004; Mulitza et al., 2017). The diminished northward oceanic heat transport across the equator caused cooler SST in the high latitudes of the North Atlantic and warmer SST in the tropical and South Atlantic in a *bipolar seesaw* (Barker et al., 2009; Chiessi et al. 2015; Marino et al., 2015; Mix et al., 1986; Shakun et al., 2012). Tropical Atlantic SST anomalies and cross-equatorial temperature gradient have a strong influence on precipitation in tropical South America through shifts in the latitudinal position of the ITCZ (e.g., Mechoso et al. 1990; Giannini et al. 2001, and references therein). A southward ITCZ displacement during millennial-scale AMOC reduction determined a marked decrease in precipitation over northern South America (Deplazes et al., 2013; Peterson, 2000) and a significant increase in

precipitation over Northeastern Brazil (Arz et al. 1998; Wang et al., 2004; Mulitza et al. 2017). In the tropical and subtropical Andes, evidence from stalagmite $\delta^{18}\text{O}$ show increased precipitation related to strengthening of the SASM during HS (Cheng et al., 2013; Kanner et al., 2012; Mosblech et al., 2012). DO variability is, however, poorly represented in South America continental and marine records. This is likely because DOS involves only moderate AMOC reductions (Böhm et al., 2015; Yu et al., 2014; Zhang et al., 2014).

HS1 and LGM boundary conditions have been extensively investigated with climate models of different complexity. When freshwater-hosing forcing was applied to the North Atlantic, models successfully registered a marked southward shift of the Atlantic ITCZ under LGM (e.g., Kageyama et al., 2013) and modern boundary conditions (e.g., Stouffer et al., 2006). Yet, simulated rainfall patterns show large variability across central and western Amazon among different models, even though these regions are mainly dominated by the SASM at present. Nevertheless, there is general agreement between model output and paleoclimate records insofar wet conditions are observed over the tropical Andes and dry conditions over northernmost South America (Kageyama et al., 2013 and references therein; Zhang et al., 2016).

1.4 Research objectives and thesis outline

The primary objective of this thesis is at first to characterize the climatic impact of millennial events (HS and DOS) on the Amazon Basin and the adjacent ocean. Special emphasis was given to HS1 as it is represented in high resolution in our record (ca. 150 years between data points). Secondly, an accurate temperature reconstruction of the upper water column in the western tropical Atlantic became our goal. The achievement of these objectives was made possible by the study of marine sediment core GeoB16224-1, retrieved off French Guiana ($6^{\circ}39.38'$ N, $52^{\circ}04.99'$ W, 2510 m water depth) (Fig. 2-1). Core GeoB16224-1 has remarkable stratigraphical continuity (Zhang et al., 2015; Häggi et al., 2017; Zhang et al., 2017; Crivellari et al., 2018). The age model of sediment core GeoB16224-1 is based on 13 calibrated radiocarbon (^{14}C) ages as well as one tie point beyond the radiocarbon range to the well dated stalagmite from El Condor Cave (Cheng et al., 2013) as previously published by Zhang et al. (2015) and Häggi et al. (2017). The age model of core GeoB16224-1 used in this thesis is the same being utilized in Häggi et al. (2017) and Zhang et al. (2017). Paleoceanographic and paleoclimatic records from the region of core GeoB16224-1 are ideal

for reconstructions of the western tropical Atlantic and the Amazon Basin. The main reasons therefore are: (i) the site is under the influence of the Amazon River's freshwater and terrigenous discharge, being sensitive to changes in continental hydrology and climate; (ii) the site has sedimentation rates of ca. 20 cm/kyr, appropriate for high resolution studies of millennial-scale climate events, still allowing the recovery of ca. 49 ka record in a typical 7 m-long gravity core; and (iii) the fully marine setting in which GeoB16224-1 record is located allows for purely oceanographic signals to be registered in the sedimentary archive which is critical for parsing changes in the oceanic realm with changes in continental climate. Thus, marine sediment core GeoB16224-1 holds extremely important information about the late Pleistocene paleoclimatological and paleoceanographic setting in the western tropical Atlantic that was partially unravelled in the three manuscripts that compose this thesis.

In the first manuscript – *Increased precipitation in the western equatorial Atlantic during late Heinrich Stadial 1* – (Chapter 2), we present a high temporal resolution multiproxy study based on marine sediment core GeoB16224-1 retrieved off French Guiana. The core location is under the influence of the Amazon freshwater and terrigenous discharge (Lentz and Limeburner, 1995; Muller-Karger et al., 1988). On *Globigerinoides ruber* tests we measured $\delta^{18}\text{O}$, Mg/Ca-SST and relative abundance, to reconstruct the surface water response to changes in Amazon River outflow as a function of terrestrial precipitation. We also analysed the branched and isoprenoid tetraether (BIT) index, and compared it to existing data from bulk sediment $\ln(\text{Fe}/\text{Ca})$ (Zhang et al., 2017) and carbon stable isotopes ($\delta^{13}\text{C}$) of *n*-alkanes (Häggi et al., 2017) obtained from the same core, to decipher the interaction among soil discharge, riverine sediment transport and continental vegetation. We focus on the Last Glacial Maximum (LGM)-HS1 interval (22-14 cal ka BP). We find two distinct phases of increased precipitation within HS1. The first phase (18-16.9 cal ka BP) is characterized by an increase in terrigenous input and SST increase. In the second phase (16.9-14.8 cal ka BP) we register a drop in SSS related to increased Amazon River fresh water discharge but decreased terrigenous sediment input to the western equatorial Atlantic. We formulated the hypotheses that sediment production within the Amazon Basin evolves geographically and it is related to the migration and strengthening of the main locus of precipitation from the western Amazon/tropical Andes to the central Amazonian plains/cratonic Brazilian shield. This is the first marine core capable to register increased precipitation at sub-millennial-scale in the western equatorial Atlantic, offering a high-resolution integrated picture of Amazonian hydrology.

Additionally, we present *G. ruber* and *Globigerinoides sacculifer* $\delta^{18}\text{O}$ data from multicore GeoB16212-2 retrieved from the Amazon submarine delta on the Brazilian continental shelf directly off the Amazon River mouth, in order to identify whether *G. ruber* and *G. sacculifer* are capable to recording the hydrography of the Amazon-influenced low-salinity surface layer. We show that the specific use *G. sacculifer* as proxy for sea surface salinities is unreliable for the reason that this species have shown muted response in nutrient rich, low salinity surface water lenses (Hemleben et al., 1987; Schmuker and Schiebel, 2002), suggesting that it preferentially calcifies at depths that are outside the reach of the Amazon freshwater plume (Dekens et al., 2002; Farmer et al., 2007).

In the second manuscript – *Different precipitation patterns across tropical South America during Heinrich and Dansgaard-Oeschger stadials* – (Chapter 3), we differentiate the regional characteristics of the SASM and the ITCZ in response to HS and DOS over the Amazon Basin by comparing well-dated records along a north-south transect between ca. 17° N and 4° S across Central and South America. Firstly, by using sediment core GeoB16224-1 we identify an inverse covariance between $\ln(\text{Fe}/\text{Ca})$ X-ray fluorescence record and alkenone C_{37} concentration together with $\text{C}_{37}/\text{C}_{38}$ ratio over HS and DOS between 41 and 13 cal ka BP. This indicates enhanced precipitation as result of southward migration of the ITCZ, associated with decrease in primary productivity at our core site as supported by decreased C_{37} concentration. Secondly, we compared our results to six high temporal resolution paleohydrological records from Central and South America to investigate the spatial characteristics of terrestrial precipitation during HS and DOS. Our results highlight different magnitudes of increased precipitation over NE Brazil between HS and DOS, which were probably related to the different magnitudes of the corresponding AMOC slowdowns (Henry et al., 2016). During HS, the compiled records indicate decreased rainfall to the north of our core site (Deplazes et al., 2013; Escobar et al., 2012), but increased rainfall to the south of our core site (Jaeschke et al., 2007; Kanner et al., 2012; Nace et al., 2014). During DOS, and in particular for DOS 8-5, we suggest the same antiphased relationship of terrestrial precipitation between Pacupahuain cave (Kanner et al., 2012) and two cores (Escobar et al., 2012; Rasmussen et al., 2014) to the north of our core site.

Both HS and DOS triggered a strengthening of the SASM and a southward migration of the ITCZ (Kanner et al., 2012). However, NE Brazilian precipitation, which is today primarily under the control of the ITCZ, experienced significant precipitation increases during HS but no evident changes during DOS. We suggest that the moderate reduction of

the AMOC during DOS, if compared to the nearly shutdown during HS, was likely unable to shift the ITCZ mean position far enough to the south in order to substantially increase precipitation over NE Brazil.

The third manuscript – *The thermal response of the western tropical Atlantic to slowdown events of the Atlantic Meridional Overturning Circulation* – (Chapter 4), aims to systematically investigate several temperature proxies on the same core (GeoB16224-1). Our goal is to identify the thermal response of the upper water column to slowdown events of the AMOC during the last ca. 49 ka and to contextualize our findings with published temperature records in the region. SST reconstructions at various latitudes within the western tropical Atlantic are of critical importance in order to map the temperature gradient that installs during variations of the AMOC strength. However, previously available SST reconstructions in the western margin of the tropical Atlantic show a degree of equivocality. For instance, positive SST anomalies during AMOC slowdown events have been described for the continental margin off NE Brazil (Arz et al., 1999; Nace et al., 2014; Weldeab et al., 2006) during northern hemisphere millennial cold events. Similar positive SST anomalies have been observed in the Guiana Basin (Crivellari et al., 2018), the western Caribbean Sea (Schmidt et al., 2004), Tobago Basin (Hüls and Zahn, 2000; Rühlemann et al., 1999) and Gulf of Mexico (Flower et al., 2004). Oppositely, Jaeschke et al. (2007) $U^{k'}_{37}$ temperature reconstructions found consistently colder temperature during HS 4, 3 and 2. Similarly, a paleotemperature reconstruction from Guiana Basin also show negative $U^{k'}_{37}$ -based temperature anomalies during these periods (Rama-Corredor et al., 2015). While Mg/Ca-derived SST records show positive anomalies during slowdown events of the AMOC, nearby $U^{k'}_{37}$ temperature records show negative anomalies during the same millennial-scale events. Moreover, the available Mg/Ca-derived SST reconstructions from the western tropical Atlantic either show low resolution (i.e., Nace et al., 2014) or encompass only HS 1 (i.e., Weldeab et al., 2006). Thus, the sea surface thermal response of the western tropical Atlantic to AMOC slowdown events remains equivocal. Here we present a multiproxy, high resolution SST reconstruction based on Mg/Ca from *G. ruber*, alkenone unsaturation index $U^{k'}_{37}$, TEX_{86} , and modern analogue technique (MAT) applied to planktonic foraminifera assemblage calibrated for 50 m water depth. All methods were applied to core GeoB16224-1. We detect positive temperature anomalies during slowdown events of the AMOC HS4-HS1, as our Mg/Ca-derived SST and TEX_{86} indicate. Positive SST anomalies in our Mg/Ca record coincide with Antarctic Isotope Maxima (AIM)5 to AIM1 originally identified from

the EDML ice core $\delta^{18}\text{O}$ record (Barbante et al., 2006). Nevertheless, U^{k}_{37} and MAT (50 m) temperature reconstruction on GeoB16224-1 tend to show negative anomalies during HS3 and HS1. Our multiproxy high-resolution temperature reconstruction provide critical information on: (i) the actual thermal behaviour of upper water column during millennial events; (ii) the transmission of fast climate variability from high latitudes to the tropics; and (iii) the usability of the alkenone temperature proxy in the context of environments under the influence of large rivers. These issues are of fundamental importance given the essential role of these regions in regulating the transport of heat across hemispheres (Macdonald and Wunsch, 1996).

1.5 References

- Alley, R.B., 2003. Abrupt Climate Change. *Science* (80-.). 299, 2005–2010. doi:10.1126/science.1081056
- Allison, M.A., Lee, M.T., Ogston, A.S., Aller, R.C., 2000. Origin of Amazon mudbanks along the northeastern coast of South America. *Mar. Geol.* 163, 241–256. doi:10.1016/S0025-3227(99)00120-6
- Andersen, K.K., Azuma, N., Barnola, J.-M., Bigler, M., Biscaye, P., Caillon, N., Chappellaz, J., Clausen, H.B., Dahl-Jensen, D., Fischer, H., Flückiger, J., Fritzsche, D., Fujii, Y., Goto-Azuma, K., Grønvold, K., Gundestrup, N.S., Hansson, M., Huber, C., Hvidberg, C.S., Johnsen, S.J., Jonsell, U., Jouzel, J., Kipfstuhl, S., Landais, A., Leuenberger, M., Lorrain, R., Masson-Delmotte, V., Miller, H., Motoyama, H., Narita, H., Popp, T., Rasmussen, S.O., Raynaud, D., Rothlisberger, R., Ruth, U., Samyn, D., Schwander, J., Shoji, H., Siggard-Andersen, M.-L., Steffensen, J.P., Stocker, T., Sveinbjörnsdóttir, A.E., Svensson, A., Takata, M., Tison, J.-L., Thorsteinsson, T., Watanabe, O., Wilhelms, F., White, J.W.C., 2004. High-resolution record of Northern Hemisphere climate extending into the last interglacial period. *Nature* 431, 147–151. doi:10.1038/nature02805
- Andrews, J.T., Voelker, A.H.L., 2018. “Heinrich events” (& sediments): A history of terminology and recommendations for future usage. *Quat. Sci. Rev.* 187, 31–40. doi:10.1016/j.quascirev.2018.03.017
- Arz, H.W., Pätzold, J., Wefer, G., 1999. The deglacial history of the western tropical Atlantic as inferred from high resolution stable isotope records off northeastern Brazil. *Earth Planet. Sci. Lett.* 167, 105–117. doi:10.1016/S0012-821X(99)00025-4
- Baker, P.A., Rigsby, C.A., Seltzer, G.O., Fritz, S.C., Lowenstein, T.K., Bacher, N.P., Veliz, C., 2001. Tropical climate changes at millennial and orbital timescales on the Bolivian Altiplano. *Nature* 409, 698–701. doi:10.1038/35055524
- Barbante, C., Barnola, J.-M., Becagli, S., Beer, J., Bigler, M., Boutron, C., Blunier, T., Castellano, E., Cattani, O., Chappellaz, J., Dahl-Jensen, D., Debret, M., Delmonte, B., Dick, D., Falourd, S., Faria, S., Federer, U., Fischer, H., Freitag, J., Frenzel, A., Fritzsche, D., Fundel, F., Gabrielli, P., Gaspari, V., Gersonde, R., Graf, W., Grigoriev, D., Hamann, I., Hansson, M., Hoffmann, G., Hutterli, M.A., Huybrechts, P., Isaksson, E., Johnsen, S., Jouzel, J., Kaczmarek, M., Karlin, T., Kaufmann, P., Kipfstuhl, S., Kohno, M., Lambert, F., Lambrecht, A., Landais, A., Lawer, G., Leuenberger, M., Littot, G., Loulergue, L., Lüthi, D., Maggi, V., Marino, F., Masson-Delmotte, V., Meyer, H., Miller, H., Mulvaney, R., Narcisi, B., Oerlemans, J., Oerter, H., Parrenin, F., Petit, J.-R., Raisbeck, G., Raynaud, D., Röthlisberger, R., Ruth, U., Rybak, O., Severi, M., Schmitt, J., Schwander, J., Siegenthaler, U., Siggard-Andersen, M.-L., Spahni, R., Steffensen, J.P., Stenni, B., Stocker, T.F., Tison, J.-L., Traversi, R., Udisti, R., Valero-Delgado, F., van den Broeke, M.R., van de Wal, R.S.W., Wagenbach, D., Wegner, A., Weiler, K., Wilhelms, F., Winther, J.-G., Wolff, E., 2006. One-to-one coupling of glacial climate variability in Greenland and Antarctica. *Nature* 444, 195–198. doi:10.1038/nature05301
- Barker, S., Diz, P., Vautravers, M.J., Pike, J., Knorr, G., Hall, I.R., Broecker, W.S., 2009. Interhemispheric Atlantic seesaw response during the last deglaciation. *Nature* 457, 1097–1102. doi:10.1038/nature07770

- Blard, P.H., Sylvestre, F., Tripathi, A.K., Claude, C., Causse, C., Coudrain, A., Condom, T., Seidel, J.L., Vimeux, F., Moreau, C., Dumoulin, J.P., Lavé, J., 2011. Lake highstands on the Altiplano (Tropical Andes) contemporaneous with Heinrich 1 and the Younger Dryas: New insights from ^{14}C , U-Th dating and $\delta^{18}\text{O}$ of carbonates. *Quat. Sci. Rev.* 30, 3973–3989. doi:10.1016/j.quascirev.2011.11.001
- Böhm, E., Lippold, J., Gutjahr, M., Frank, M., Blaser, P., Antz, B., Fohlmeister, J., Frank, N., Andersen, M.B., Deininger, M., 2015. Strong and deep Atlantic meridional overturning circulation during the last glacial cycle. *Nature* 517, 73–76. doi:10.1038/nature14059
- Böhm, E., Lippold, J., Gutjahr, M., Frank, M., Blaser, P., Antz, B., Fohlmeister, J., Frank, N., Andersen, M.B., Deininger, M., 2014. Strong and deep Atlantic meridional overturning circulation during the last glacial cycle. *Nature* 517, 73–76. doi:10.1038/nature14059
- Bond, G., Broecker, W., Johnsen, S., McManus, J., Labeyrie, L., Jouzel, J., Bonani, G., 1993. Correlations between climate records from North Atlantic sediments and Greenland ice. *Nature* 365, 143–147. doi:10.1038/365143a0
- Bond, G., Heinrich, H., Broecker, W., Labeyrie, L., McManus, J., Andrews, J., Huon, S., Jantschik, R., Clasen, S., Simet, C., Tedesco, K., Klas, M., Bonani, G., Ivy, S., 1992. Evidence for massive discharges of icebergs into the North Atlantic ocean during the last glacial period. *Nature* 360, 245–249. doi:10.1038/360245a0
- Broecker, W.S., 2000. Was a change in thermohaline circulation responsible for the Little Ice Age? *Proc. Natl. Acad. Sci. U. S. A.* 97, 1339–1342. doi:10.1073/pnas.97.4.1339
- Broecker, W.S., 1998. Paleoocean circulation during the 1st deglaciation: A bipolar seasaw? *Paleoceanography* 13, 119–121.
- Broecker, W.S., 1997. Thermohaline circulation, the achilles heel of our climate system: Will man-made CO_2 upset the current balance? *Science* (80-). 278, 1582–1588. doi:10.1126/science.278.5343.1582
- Broecker, W.S., Peteet, D.M., Rind, D., 1985. Does the ocean-atmosphere system have more than one stable mode of operation? *Nature* 315, 21–26. doi:10.1038/315021a0
- Carvalho, L.M.V., Jones, C., Liebmann, B., 2004. The South Atlantic convergence zone: Intensity, form, persistence, and relationships with intraseasonal to interannual activity and extreme rainfall. *J. Clim.* 17, 88–108. doi:10.1175/1520-0442(2004)017<0088:TSACZI>2.0.CO;2
- Cheng, H., Sinha, A., Cruz, F.W., Wang, X., Edwards, R.L., d’Horta, F.M., Ribas, C.C., Vuille, M., Stott, L.D., Auler, A.S., 2013. Climate change patterns in Amazonia and biodiversity. *Nat. Commun.* 4, 1411. doi:10.1038/ncomms2415
- Chiang, J.C.H., Kushnir, Y., Giannini, A., 2002. Deconstructing Atlantic ITCZ variability: Influence of the local cross-equatorial SST gradient, and remote forcing from the eastern equatorial Pacific 3. *Atlantic* 107, 1–63.
- Clark, P.U., Alley, R.B., Pollard, D., 1999. Northern hemisphere ice-sheet influences on global climate change. *Science* (80-). doi:10.1126/science.286.5442.1104
- Clark, P.U., Pisias, N.G., Stocker, T.F., Weaver, A.J., 2002. The role of the thermohaline circulation in abrupt climate change. *Nature*. doi:10.1038/415863a
- Clement, A.C., Cane, M.A., Seager, R., 2001. An Orbitaly Driven Tropical Source for Abrupt Climate Change*. *J. Clim.* 14, 2369–2375. doi:10.1175/1520-0442(2001)014<2369:AODTSF>2.0.CO;2
- Collins, J.A., Govin, A., Mulitza, S., Heslop, D., Zabel, M., Hartmann, J., Röhl, U., Wefer, G., 2013. Abrupt shifts of the Sahara-Sahel boundary during Heinrich stadials. *Clim. Past* 9, 1181–1191. doi:10.5194/cp-9-1181-2013
- Cook, K.H., Vizy, E.K., 2006. South American climate during the Last Glacial Maximum: Delayed onset of the South American monsoon. *J. Geophys. Res. Atmos.* 111, 1–21. doi:10.1029/2005JD005980
- Crivellari, S., Chiessi, C.M., Kuhnert, H., Häggi, C., da Costa Portilho-Ramos, R., Zeng, J.-Y., Zhang, Y., Schefuß, E., Mollenhauer, G., Hefter, J., Alexandre, F., Sampaio, G., Mulitza, S., 2018. Increased Amazon freshwater discharge during late Heinrich Stadial 1. *Quat. Sci. Rev.* 181, 144–155. doi:10.1016/j.quascirev.2017.12.005

- Cruz, F.W., Burns, S.J., Karmann, I., Sharp, W.D., Vuille, M., 2006. Reconstruction of regional atmospheric circulation features during the late Pleistocene in subtropical Brazil from oxygen isotope composition of speleothems. *Earth Planet. Sci. Lett.* 248, 494–506. doi:10.1016/j.epsl.2006.06.019
- Cruz, F.W., Karmann, I., Viana, O., Burns, S.J., Ferrari, J.A., Vuille, M., Sial, A.N., Moreira, M.Z., 2005. Stable isotope study of cave percolation waters in subtropical Brazil: Implications for paleoclimate inferences from speleothems. *Chem. Geol.* 220, 245–262. doi:10.1016/j.chemgeo.2005.04.001
- Dahl, K.A., Broccoli, A.J., Stouffer, R.J., 2005. Assessing the role of North Atlantic freshwater forcing in millennial scale climate variability: A tropical Atlantic perspective. *Clim. Dyn.* 24, 325–346. doi:10.1007/s00382-004-0499-5
- Dansgaard, W., Johnsen, S.J., Clausen, H.B., Dahl-Jensen, D., Gundestrup, N.S., Hammer, C.U., Hvidberg, C.S., Steffensen, J.P., Sveinbjörnsdóttir, A.E., Jouzel, J., Bond, G., 1993. Evidence for general instability of past climate from a 250-kyr ice-core record. *Nature* 364, 218–220. doi:10.1038/364218a0
- Dekens, P.S., Lea, D.W., Pak, D.K., Spero, H.J., 2002. Core top calibration of Mg/Ca in tropical foraminifera: Refining paleotemperature estimation. *Geochemistry, Geophys. Geosystems* 3, 1–29. doi:10.1029/2001GC000200
- Del Vecchio, R., Subramaniam, A., 2004. Influence of the Amazon River on the surface optical properties of the western tropical North Atlantic Ocean. *J. Geophys. Res. Ocean.* 109, 1–13. doi:10.1029/2004JC002503
- Deplazes, G., Lückge, A., Peterson, L.C., Timmermann, A., Hamann, Y., Hughen, K.A., Röhl, U., Laj, C., Cane, M.A., Sigman, D.M., Haug, G.H., 2013. Links between tropical rainfall and North Atlantic climate during the last glacial period. *Nat. Geosci.* 6, 213–217. doi:10.1038/ngeo1712
- Dupont, L.M., Schlütz, F., Ewah, C.T., Jennerjahn, T.C., Paul, A., Behling, H., 2010. Two-step vegetation response to enhanced precipitation in Northeast Brazil during Heinrich event 1. *Glob. Chang. Biol.* 16, 1647–1660. doi:10.1111/j.1365-2486.2009.02023.x
- Escobar, J., Hodell, D.A., Brenner, M., Curtis, J.H., Gilli, A., Mueller, A.D., Anselmetti, F.S., Ariztegui, D., Grzesik, D.A., Pérez, L., Schwab, A., Guilderson, T.P., 2012. A ~43-ka record of paleoenvironmental change in the Central American lowlands inferred from stable isotopes of lacustrine ostracods. *Quat. Sci. Rev.* 37, 92–104. doi:10.1016/j.quascirev.2012.01.020
- Farmer, E.C., Kaplan, A., de Menocal, P.B., Lynch-Stieglitz, J., 2007. Corroborating ecological depth preferences of planktonic foraminifera in the tropical Atlantic with the stable oxygen isotope ratios of core top specimens. *Paleoceanography* 22, 1–14. doi:10.1029/2006PA001361
- Flower, B.P., Hastings, D.W., Hill, H.W., Quinn, T.M., 2004. Phasing of deglacial warming and Laurentide Ice Sheet meltwater in the Gulf of Mexico. *Geology* 32, 597–600. doi:10.1130/G20604.1
- Garreaud, R.D., Vuille, M., Compagnucci, R., Marengo, J., 2009. Present-day South American climate. *Palaeogeogr. Palaeoclimatol. Palaeoecol.* 281, 180–195. doi:10.1016/j.palaeo.2007.10.032
- Giannini, A., Chiang, J.C.H., Cane, M.A., Kushnir, Y., Seager, R., 2001. The ENSO teleconnection to the Tropical Atlantic Ocean: Contributions of the remote and local SSTs to rainfall variability in the Tropical Americas. *J. Clim.* 14, 4530–4544. doi:10.1175/1520-0442(2001)014<4530:TETTTT>2.0.CO;2
- Gibbs, R.J., 1967. Amazon River: Environmental Factors That Control Its Dissolved and Suspended Load 4.
- Gildor, H., Tziperman, E., 2003. Sea-ice switches and abrupt climate change. *Philos. Trans. R. Soc. A Math. Phys. Eng. Sci.* 361, 1935–1944. doi:10.1098/rsta.2003.1244
- Häggi, C., Chiessi, C.M., Merkel, U., Mulitza, S., Prange, M., Schulz, M., Schefuß, E., 2017. Response of the Amazon rainforest to late Pleistocene climate variability. *Earth Planet. Sci. Lett.* 479, 50–59. doi:10.1016/j.epsl.2017.09.013
- Hemleben, C., Spindler, M., Breiting, I., Ott, R., 1987. Morphological and physiological responses of *Globigerinoides sacculifer* (Brady) under varying laboratory conditions. *Mar. Micropaleontol.* 12, 305–324. doi:10.1016/0377-8398(87)90025-9
- Henry, L.G., McManus, J.F., Curry, W.B., Roberts, N.L., Piotrowski, A.M., Keigwin, L.D., 2016. North Atlantic ocean circulation and abrupt climate change during the last glaciation 5529. doi:10.1126/science.aaf5529

- Howe, J.N.W., Piotrowski, A.M., Noble, T.L., Mulitza, S., Chiessi, C.M., Bayon, G., 2016. North Atlantic Deep Water Production during the Last Glacial Maximum. *Nat. Commun.* 7, 11765. doi:10.1038/ncomms11765
- Hüls, M., Zahn, R., 2000. Millennial-scale sea surface temperature variability in the western tropical North Atlantic from planktonic foraminiferal census counts. *Paleoceanography* 15, 659–678. doi:10.1029/1999PA000462
- Jaeschke, A., Rühlemann, C., Arz, H., Heil, G., Lohmann, G., 2007. Coupling of millennial-scale changes in sea surface temperature and precipitation off northeastern Brazil with high-latitude climate shifts during the last glacial period. *Paleoceanography* 22, 1–10. doi:10.1029/2006PA001391
- Johns, W.E., Lee, T.N., Beardsley, R., Candela, J., Limeburner, R., Castro, B.M., 1998. Annual Cycle and Variability of the North Brazil Current. *J. Phys. Oceanogr.* 28, 103–128.
- Kageyama, M., Merkel, U., Otto-Bliesner, B., Prange, M., Abe-Ouchi, A., Lohmann, G., Ohgaito, R., Roche, D.M., Singarayer, J., Swingedouw, D., Zhang, X., 2013. Climatic impacts of fresh water hosing under last glacial Maximum conditions: A multi-model study. *Clim. Past* 9, 935–953. doi:10.5194/cp-9-935-2013
- Kageyama, M., Mignot, J., Swingedouw, D., Marzin, C., Alkama, R., Marti, O., 2009. Glacial climate sensitivity to different states of the Atlantic Meridional Overturning Circulation: results from the IPSL model. *Clim. Past* 5, 551–570. doi:10.5194/cp-5-551-2009
- Kanner, L.C., Burns, S.J., Cheng, H., Edwards, R.L., 2012. High-Latitude Forcing of the South American Summer Monsoon During the Last Glacial. *Science* (80-.). 335, 570–573. doi:10.1126/science.1213397
- Kirtman, B.P., Stockdale, T., Burgman, R., 2013. Chapter 24 - The Ocean's Role in Modeling and Predicting Seasonal-to-Interannual Climate Variations, in: *Ocean Circulation and Climate: A 21st Century Perspective*. pp. 625–643. doi:http://dx.doi.org/10.1016/B978-0-12-391851-2.00024-6
- Knutti, R., Flückiger, J., Stocker, T.F., Timmermann, A., 2004. Strong hemispheric coupling of glacial climate through freshwater discharge and ocean circulation. *Nature* 430, 851–856. doi:10.1038/nature02786
- Kodama, Y., 1992. Large-scale common features of subtropical precipitation zones (the Baiu Frontal Zone , the SPCZ , and the SACZ) Part I: Characteristics of subtropical frontal zones. *J. Meteorol. Soc. Japan* 70, 813–836. doi:10.1248/cpb.37.3229
- Lenters, J.D., Cook, K.H., 1997. On the Origin of the Bolivian High and Related Circulation Features of the South American Climate. *J. Atmos. Sci.* 54, 656–678. doi:10.1175/1520-0469(1997)054<0656:OTOOTB>2.0.CO;2
- Lentz, S.J., 1995. Seasonal variations in the horizontal structure of the Amazon Plume inferred from historical hydrographic data. *J. Geophys. Res.* 100, 2391. doi:10.1029/94JC01847
- Lentz, S.J., Limeburner, R., 1995. The Amazon River Plume during AMASSEDS: Spatial characteristics and salinity variability. *J. Geophys. Res.* 100, 2355. doi:10.1029/94JC01411
- Li, C., Battisti, D.S., Schrag, D.P., Tziperman, E., 2005. Abrupt climate shifts in Greenland due to displacements of the sea ice edge. *Geophys. Res. Lett.* 32, 1–4. doi:10.1029/2005GL023492
- Liu, Z., Otto-Bliesner, B.L., He, F., Brady, E.C., Tomas, R., Clark, P.U., Carlson, A.E., Lynch-Stieglitz, J., Curry, W., Brook, E., Erickson, D., Jacob, R., Kutzbach, J., Cheng, J., 2009. Transient Simulation of Last Deglaciation with a New Mechanism for Bolling-Allerod Warming. *Science* (80-.). 325, 310–314. doi:10.1126/science.1171041
- Locarnini, R.A., Mishonov, A. V., Antonov, J.I., Boyer, T.P., Garcia, H.E., Baranova, O.K., Zweng, M.M., Paver, C.R., Reagan, J.R., Johnson, D.R., Hamilton, M., Seidov, D., 2013. *World Ocean Atlas 2013. Vol. 1: Temperature.*, S. Levitus, Ed.; A. Mishonov, Technical Ed.; NOAA Atlas NESDIS. doi:10.1182/blood-2011-06-357442
- Lohmann, G., 2003. Atmospheric and oceanic freshwater transport during weak Atlantic overturning circulation. *Tellus, Ser. A Dyn. Meteorol. Oceanogr.* 55, 438–449. doi:10.1034/j.1600-0870.2003.00028.x
- Lynch-Stieglitz, J., Adkins, J.F., Curry, W.B., Dokken, T., Hall, I.R., Herguera, J.C., Hirschi, J.J.-M., Ivanova, E. V., Kissel, C., Marchal, O., Marchitto, T.M., McCave, I.N., McManus, J.F., Mulitza, S., Ninnemann, U., Peeters, F., Yu, E.-F., Zahn, R., 2007. Atlantic Meridional Overturning Circulation During the Last Glacial Maximum. *Science* (80-.). 316, 66–69. doi:10.1126/science.1137127

- Lynch-Stieglitz, J., Schmidt, M.W., Gene Henry, L., Curry, W.B., Skinner, L.C., Mulitza, S., Zhang, R., Chang, P., 2014. Muted change in Atlantic overturning circulation over some glacial-aged Heinrich events. *Nat. Geosci.* 7, 144–150. doi:10.1038/ngeo2045
- Macdonald, A.M., Wunsch, C., 1996. An estimate of global ocean circulation and heat fluxes. *Nature* 382, 436–439. doi:10.1038/382436a0
- Marino, G., Rohling, E.J., Rodriguez-Sanz, L., Grant, K.M., Heslop, D., Roberts, A.P., Stanford, J.D., Yu, J., 2015. Bipolar seesaw control on last interglacial sea level. *Nature* 522, 197–201. doi:10.1038/nature14499
- Marshall, J., Donohoe, A., Ferreira, D., McGee, D., 2014. The ocean's role in setting the mean position of the Inter-Tropical Convergence Zone. *Clim. Dyn.* 42, 1967–1979. doi:10.1007/s00382-013-1767-z
- Mayorga, E., Aufdenkampe, A.K., Masiello, C.A., Krusche, A. V., Hedges, J.I., Quay, P.D., Richey, J.E., Brown, T.A., 2005. Young organic matter as a source of carbon dioxide outgassing from Amazonian rivers. *Nature* 436, 538–541. doi:10.1038/nature03880
- McGee, D., Donohoe, A., Marshall, J., Ferreira, D., 2014. Changes in ITCZ location and cross-equatorial heat transport at the Last Glacial Maximum, Heinrich Stadial 1, and the mid-Holocene. *Earth Planet. Sci. Lett.* 390, 69–79. doi:10.1016/j.epsl.2013.12.043
- McManus, J.F., Francois, R., Gherardi, J.-M., Keigwin, L.D., Brown-Leger, S., 2004. Collapse and rapid resumption of Atlantic meridional circulation linked to deglacial climate changes. *Nature* 428, 834–837. doi:10.1038/nature02494
- Meade, R.H., Dunne, T., Richey, J.E., De M. Santos, U., Salati, E., 1985. Storage and Remobilization of Suspended Sediment in the Lower Amazon River of Brazil. *Science* (80-.). 228, 488–490. doi:10.1126/science.228.4698.488
- Mechoso, C.R., Lyons, S.W., Spahr, J.A., 1990. The Impact of Sea Surface Temperature Anomalies on the Rainfall over Northeast Brazil. *J. Clim.*
- Mix, A.C., Ruddiman, W.F., McIntyre, A., 1986. Late Quaternary paleoceanography of the Tropical Atlantic, 1: Spatial variability of annual mean sea-surface temperatures, 0-20,000 years B.P. *Paleoceanography* 1, 43–66. doi:10.1029/PA001i001p00043
- Mosblech, N.A.S., Bush, M.B., Gosling, W.D., Hodell, D., Thomas, L., van Calsteren, P., Correa-Metrio, A., Valencia, B.G., Curtis, J., van Woesik, R., 2012. North Atlantic forcing of Amazonian precipitation during the last ice age. *Nat. Geosci.* 5, 817–820. doi:10.1038/ngeo1588
- Mounier, S., Braucher, R., Benaïm, J.Y., 1999. Differentiation of organic matter's properties of the Rio Negro basin by crossflow ultra-filtration and UV-spectrofluorescence. *Water Res.* 33, 2363–2373. doi:10.1016/S0043-1354(98)00456-4
- Mulitza, S., Chiessi, C.M., Schefuß, E., Lippold, J., Wichmann, D., Antz, B., Mackensen, A., Paul, A., Prange, M., Rehfeld, K., Werner, M., Bickert, T., Frank, N., Kuhnert, H., Lynch-Stieglitz, J., Portillo-Ramos, R.C., Sawakuchi, A.O., Schulz, M., Schwenk, T., Tiedemann, R., Vahlenkamp, M., Zhang, Y., 2017. Synchronous and proportional deglacial changes in Atlantic meridional overturning and northeast Brazilian precipitation. *Paleoceanography* 32, 622–633. doi:10.1002/2017PA003084
- Mulitza, S., Heslop, D., Pittauerova, D., Fischer, H.W., Meyer, I., Stuut, J.-B., Zabel, M., Mollenhauer, G., Collins, J.A., Kuhnert, H., Schulz, M., 2010. Increase in African dust flux at the onset of commercial agriculture in the Sahel region. *Nature* 466, 226–228. doi:10.1038/nature09213
- Muller-Karger, F.E., McClain, C.R., Richardson, P.L., 1988. The dispersal of the Amazon's water. *Nature* 333, 56–59. doi:10.1038/333056a0
- Nace, T.E., Baker, P.A., Dwyer, G.S., Silva, C.G., Rigsby, C.A., Burns, S.J., Giosan, L., Otto-Bliesner, B., Liu, Z., Zhu, J., 2014. The role of North Brazil Current transport in the paleoclimate of the Brazilian Nordeste margin and paleoceanography of the western tropical Atlantic during the late Quaternary. *Palaeogeogr. Palaeoclimatol. Palaeoecol.* 415, 3–13. doi:10.1016/j.palaeo.2014.05.030
- Nobre, P., Shukla, J., 1996. Variations of sea surface temperature, wind stress, and rainfall over the tropical Atlantic and South America. *J. Clim.* 9, 2464–2479. doi:10.1175/1520-0442(1996)009<2464:VOSSTW>2.0.CO;2
- Petersen, S. V., Schrag, D.P., Clark, P.U., 2013. A new mechanism for Dansgaard-Oeschger cycles. *Paleoceanography* 28, 24–30. doi:10.1029/2012PA002364

- Peterson, L.C., 2000. Rapid Changes in the Hydrologic Cycle of the Tropical Atlantic During the Last Glacial. *Science* (80-.). 290, 1947–1951. doi:10.1126/science.290.5498.1947
- Quay, P.D., Wilbur, D. O., Richey, J.E., Hedges, J.I., Devol, A.H., Victoria, R., 1992. Carbon cycling in the Amazon River: Implications from the ¹³C compositions of particles and solutes. *Limnol. Oceanogr.* doi:10.4319/lo.1992.37.4.0857
- Rahmstorf, S., 2002. Ocean circulation and climate during the past 120,000 years. *Nature* 419, 207–214. doi:10.1038/nature01090
- Rahmstorf, S., 2001. Abrupt Climate Change, in: *Encyclopedia of Ocean Sciences*. pp. 1–6. doi:10.1006/rwos.2001.0269
- Rahmstorf, S., Box, J.E., Feulner, G., Mann, M.E., Robinson, A., Rutherford, S., Schaffernicht, E.J., 2015. Exceptional twentieth-century slowdown in Atlantic Ocean overturning circulation. *Nat. Clim. Chang.* 5, 475–480. doi:10.1038/nclimate2554
- Rama-Corredor, O., Martrat, B., Grimalt, J.O., López-Otalvaro, G.E., Flores, J.A., Sierro, F., 2015. Parallelisms between sea surface temperature changes in the western tropical Atlantic (Guiana Basin) and high latitude climate signals over the last 140 000 years. *Clim. Past* 11, 1297–1311. doi:10.5194/cp-11-1297-2015
- Rasmussen, S.O., Bigler, M., Blockley, S.P., Blunier, T., Buchardt, S.L., Clausen, H.B., Cvijanovic, I., Dahl-Jensen, D., Johnsen, S.J., Fischer, H., Gkinis, V., Guillevic, M., Hoek, W.Z., Lowe, J.J., Pedro, J.B., Popp, T., Seierstad, I.K., Steffensen, J.P., Svensson, A.M., Vallelonga, P., Vinther, B.M., Walker, M.J.C., Wheatley, J.J., Winstrup, M. 2014. A stratigraphic framework for abrupt climatic changes during the Last Glacial period based on three synchronized Greenland ice-core records: refining and extending the INTIMATE event stratigraphy. *Quat. Sci. Rev.* 106, 14–28.
- Rühlemann, C., Mulitza, S., Muller, P.J., Wefer, G., Zahn, R., 1999. Warming of the tropical Atlantic Ocean and slowdown of thermohaline circulation during the last deglaciation. *Nature* 402, 511–514. doi:10.1038/990069
- Salisbury, J., Vandemark, D., Campbell, J., Hunt, C., Wisser, D., Reul, N., Chapron, B., 2011. Spatial and temporal coherence between Amazon River discharge, salinity, and light absorption by colored organic carbon in western tropical Atlantic surface waters. *J. Geophys. Res. Ocean.* 116, 1–14. doi:10.1029/2011JC006989
- Schmidt, M.W., Spero, H.J., Lea, D.W., 2004. Links between salinity variation in the Caribbean and North Atlantic thermohaline circulation. *Nature* 428, 160–163. doi:10.1038/nature02346
- Schmuker, B., Schiebel, R., 2002. Planktic foraminifers and hydrography of the eastern and northern Caribbean Sea. *Mar. Micropaleontol.* 46, 387–403. doi:10.1016/S0377-8398(02)00082-8
- Schneider, T., Bischoff, T., Haug, G.H., 2014. Migrations and dynamics of the intertropical convergence zone. *Nature*. doi:10.1038/nature13636
- Schneider, U., Becker, A., Finger, P., Meyer-Christoffer, A., Rudolf, B., Ziese, M., 2015. GPCC Full Data Reanalysis Version 7.0 at 0.5°: Monthly Land-Surface Precipitation from Rain-Gauges built on GTS-based and Historic Data, Global Precipitation Climatology Centre. doi:10.5676/DWD_GPCC/FD_M_V6_050
- Seager, R., Battisti, D.S., 2007. Challenges to our understanding of the general circulation: abrupt climate change. *Glob. Circ. Atmos.* 331–371.
- Shakun, J.D., Clark, P.U., He, F., Marcott, S.A., Mix, A.C., Liu, Z., Otto-Bliesner, B., Schmittner, A., Bard, E., 2012. Global warming preceded by increasing carbon dioxide concentrations during the last deglaciation. *Nature* 484, 49–54. doi:10.1038/nature10915
- Stanford, J.D., Rohling, E.J., Bacon, S., Roberts, A.P., Grousset, F.E., Bolshaw, M., 2011. A new concept for the paleoceanographic evolution of Heinrich event 1 in the North Atlantic. *Quat. Sci. Rev.* 30, 1047–1066. doi:10.1016/j.quascirev.2011.02.003
- Stocker, T.F., 2003. Global change: south dials north. *Nature* 424, 496–499. doi:10.1038/424496a
- Stocker, T.F., Johnsen, S.J., 2003. A minimum thermodynamic model for the bipolar seesaw. *Paleoceanography* 18, 1–9. doi:10.1029/2003PA000920

- Stouffer, R.J., Yin, J., Gregory, J.M.J.M., Dixon, K.W., Spelman, M.J., Hurlin, W., Weaver, a. J., Eby, M., Flato, G.M., Hasumi, H., Hu, A., Jungclaus, J.H., Kamenkovich, I. V., Levermann, A., Montoya, M., Murakami, S., Nawrath, S., Oka, A., Peltier, W.R., Robitaille, D.Y., Sokolov, A.P., Vettoretti, G., Weber, S.L., Weber, N., 2006. Investigating the causes of the response of the thermohaline circulation to past and future climate changes. *J. Clim.* 19, 1365–1387. doi:10.1175/JCLI3689.1
- Stramma, L., Rhein, M., Brandt, P., Dengler, M., Böning, C., Walter, M., 2005. Upper ocean circulation in the western tropical Atlantic in boreal fall 2000. *Deep. Res. Part I Oceanogr. Res. Pap.* 52, 221–240. doi:10.1016/j.dsr.2004.07.021
- Street-Perrott, F.A., Perrott, R.A., 1990. Abrupt climate fluctuations in the tropics: the influence of Atlantic Ocean circulation. *Nature* 343, 607–612. doi:10.1038/343607a0
- Strikis, N.M., Chiessi, C.M., Cruz, F.W., Vuille, M., Cheng, H., De Souza Barreto, E.A., Mollenhauer, G., Kasten, S., Karmann, I., Edwards, R.L., Bernal, J.P., Sales, H.D.R., 2015. Timing and structure of Mega-SACZ events during Heinrich Stadial 1. *Geophys. Res. Lett.* 42, 5477–5484. doi:10.1002/2015GL064048
- Sylvestre, F., 2009. Moisture Pattern During the Last Glacial Maximum in South America, in: *Past Climate Variability in South America and Surrounding Regions*. pp. 3–27. doi:10.1007/978-90-481-2672-9_1
- Toggweiler, J.R., Lea, D.W., 2010. Temperature differences between the hemispheres and ice age climate variability. *Paleoceanography* 25. doi:10.1029/2009PA001758
- Trenberth, K.E., Caron, J.M., 2001. Estimates of Meridional Atmosphere and Ocean Heat Transports. *J. Clim.* 14, 3433–3443. doi:10.1175/1520-0442(2001)014<3433:EOMAAO>2.0.CO;2
- Vera, C., Higgins, W., Amador, J., Ambrizzi, T., Garreaud, R., Gochis, D., Gutzler, D., Lettenmaier, D., Marengo, J., Mechoso, C.R., Nogues-Paegle, J., Silva Dias, P.L., Zhang, C., 2006. Toward a unified view of the American monsoon systems. *J. Clim.* 19, 4977–5000. doi:10.1175/JCLI3896.1
- Vizy, E.K., Cook, K.H., 2007. Relationship between Amazon and high Andes rainfall. *J. Geophys. Res. Atmos.* 112, 1–14. doi:10.1029/2006JD007980
- Vizy, E.K., Cook, K.H., 2005. Evaluation of last glacial maximum sea surface temperature reconstructions through their influence on South American climate. *J. Geophys. Res. D Atmos.* doi:10.1029/2004JD005415
- Voelker, A.H.L., 2002. Global distribution of centennial-scale records for Marine Isotope Stage (MIS) 3: A database. *Quat. Sci. Rev.* 21, 1185–1212. doi:10.1016/S0277-3791(01)00139-1
- Wainer, I., Clauzet, G., Ledru, M.P., Brady, E., Otto-Bliesner, B., 2005. Last Glacial Maximum in South America: Paleoclimate proxies and model results. *Geophys. Res. Lett.* 32, 1–4. doi:10.1029/2004GL021244
- Wang, X., Auler, A.S., Edwards, R.L., Cheng, H., Cristalli, P.S., Smart, P.L., Richards, D.A., Shen, C.-C., 2004. Wet periods in northeastern Brazil over the past 210 kyr linked to distant climate anomalies. *Nature* 432, 740–743. doi:10.1038/nature03067
- Wang, X., Edwards, R.L., Auler, A.S., Cheng, H., Kong, X., Wang, Y., Cruz, F.W., Dorale, J.A., Chiang, H.-W., 2017. Hydroclimate changes across the Amazon lowlands over the past 45,000 years. *Nature* 541, 204–207. doi:10.1038/nature20787
- Wang, Y.J., Cheng, H., Edwards, R.L., An, Z.S., Wu, J.Y., Shen, C.C., Dorale, J.A., 2001. A high-resolution absolute-dated late Pleistocene Monsoon record from Hulu Cave, China. *Science* 294, 2345–8. doi:10.1126/science.1064618
- Weldeab, S., Schneider, R.R., Kölling, M., 2006. Deglacial sea surface temperature and salinity increase in the western tropical Atlantic in synchrony with high latitude climate instabilities. *Earth Planet. Sci. Lett.* 241, 699–706. doi:10.1016/j.epsl.2005.11.012
- Wisser, D., Fekete, B.M., Vörösmarty, C.J., Schumann, A.H., 2010. Reconstructing 20th century global hydrography: a contribution to the Global Terrestrial Network- Hydrology (GTN-H). *Hydrol. Earth Syst. Sci.* 14, 1–24. doi:10.5194/hessd-6-2679-2009
- Wunsch, C., 2006. Abrupt climate change: An alternative view. *Quat. Res.* 65, 191–203. doi:10.1016/j.yqres.2005.10.006

- Yu, J., Anderson, R.F., Jin, Z., Menviel, L., Zhang, F., Ryerson, F.J., Rohling, E.J., 2014. Deep South Atlantic carbonate chemistry and increased interocean deep water exchange during last deglaciation. *Quat. Sci. Rev.* 90, 80–89. doi:10.1016/j.quascirev.2014.02.018
- Zell, C., Kim, J.H., Abril, G., Sobrinho, R.L., Dorhout, D., Moreira-Turcq, P., Sinninghe Damsté, J.S., 2013. Impact of seasonal hydrological variation on the distributions of tetraether lipids along the Amazon River in the central Amazon basin: Implications for the MBT/CBT paleothermometer and the BIT index. *Front. Microbiol.* 4, 1–14. doi:10.3389/fmicb.2013.00228
- Zhang, X., Lohmann, G., Knorr, G., Purcell, C., 2014. Abrupt glacial climate shifts controlled by ice sheet changes. *Nature* 512, 290–294. doi:10.1038/nature13592
- Zhang, Y., Chiessi, C.M., Mulitza, S., Zabel, M., Trindade, R.I.F., Hollanda, M.H.B.M., Dantas, E.L., Govin, A., Tiedemann, R., Wefer, G., 2015. Origin of increased terrigenous supply to the NE South American continental margin during Heinrich Stadial 1 and the Younger Dryas. *Earth Planet. Sci. Lett.* 432, 493–500. doi:10.1016/j.epsl.2015.09.054
- Zhang, Y., Zhang, X., Chiessi, C.M., Mulitza, S., Zhang, X., Lohmann, G., Prange, M., Behling, H., Zabel, M., Govin, A., Sawakuchi, A.O., Cruz, F.W., Wefer, G., 2016. Equatorial Pacific forcing of western Amazonian precipitation during Heinrich Stadial 1. *Nat. Publ. Gr.* 1–7. doi:10.1038/srep35866
- Zhang, Y., Chiessi, C.M., Mulitza, S., Sawakuchi, A.O., Häggi, C., Zabel, M., Portilho-Ramos, R.C., Schefuß, E., Crivellari, S., Wefer, G., 2017. Different precipitation patterns across tropical South America during Heinrich and Dansgaard-Oeschger stadials. *Quat. Sci. Rev.* 177, 1–9. doi:10.1016/j.quascirev.2017.10.012

Chapter 2 . Increased precipitation in the western equatorial Atlantic during late Heinrich Stadial 1

Stefano Crivellari^{1,*}, Cristiano Mazur Chiessi², Henning Kuhnert³, Christoph Häggi³, Rodrigo da Costa Portilho-Ramos^{1,3}, Jing-Ying Zeng³, Yancheng Zhang³, Enno Schefuß³, Gesine Mollenhauer⁴, Jens Hefter⁴, Felipe Alexandre⁵, Gilvan Sampaio⁵, Stefan Mulitza³

¹Institute of Geosciences – University of São Paulo – São Paulo – Brazil.

²School of Arts, Sciences and Humanities – University of São Paulo – São Paulo – Brazil.

³MARUM – Centre for Marine Environmental Sciences – University of Bremen – Bremen – Germany.

⁴Alfred Wegener Institute for Polar and Marine Research – Bremerhaven – Germany.

⁵INPE – National Institute for Space Research – Cachoeira Paulista – Brazil.

Published in *Quaternary Science Reviews* (2018) 181, 144-155

Abstract

The temporal succession of changes in Amazonian hydroclimate during Heinrich Stadial 1 (HS1) (ca. 18-14.7 cal ka BP) is currently poorly resolved. Here we present HS1 records based on isotope, inorganic and organic geochemistry from a marine sediment core influenced by the Amazon River discharge. Our records offer a detailed reconstruction of the changes in Amazonian hydroclimate during HS1, integrated over the basin. We reconstructed surface water hydrography using stable oxygen isotopes ($\delta^{18}\text{O}$) and Mg/Ca-derived paleotemperatures from the planktonic foraminifera *Globigerinoides ruber*, as well as salinity changes based on stable hydrogen isotope changes (δD) of palmitic acid. We also analysed branched and isoprenoid tetraether concentrations and compared them to existing bulk sediment $\ln(\text{Fe}/\text{Ca})$ data and vegetation reconstruction based on stable carbon isotopes from *n*-alkanes, in order to understand the relationship between continental precipitation, change in vegetation and sediment production. Our results indicate a two-phased HS1 (HS1a and HS1b). During HS1a (18-16.9 cal ka BP), a first sudden increase of sea surface temperatures (SST) in the western equatorial Atlantic correlated with the slowdown of the Atlantic Meridional Overturning Circulation (AMOC) and the associated southern hemisphere warming phase of the bipolar seesaw. This phase was also characterized by an increased delivery of terrestrial material. During HS1b (16.9 – 14.8 cal ka BP), a decrease in terrestrial input was, however, associated with a marked decline of seawater $\delta^{18}\text{O}$ and palmitic acid δD . Both isotopic proxies independently indicate a drop in sea surface salinity (SSS). A number of records under the influence of the North Brazil Current, in contrast, indicate increases in SST and SSS resulting from a weakened AMOC during HS1. Our

records thus suggest that the expected increase in SSS due to the AMOC slowdown was overridden by a two-phased positive precipitation anomaly in Amazonian hydroclimate.

2.1 Introduction

Heinrich Stadial 1 (HS1; 18-14.7 cal ka BP) is associated with a marked slowdown in the Atlantic Meridional Overturning Circulation (AMOC) together with a rearrangement in the poleward heat transport (Dahl et al., 2005). This millennial-scale event changed the latitudinal position of the thermal equator, affecting the location of the tropical rain belt (Street-Perrott and Perrott, 1990; McGee et al., 2014; Schneider et al., 2014) and of the mean position of the Intertropical Convergence Zone (ITCZ) (Marshall et al., 2013). HS1 is known to have triggered an increase in precipitation over the Amazon Basin through an enhanced penetration of moist easterly trade winds into the basin. The extensive compilation of tropical South American hydroclimate records presented by Zhang et al. (2016) clearly shows wet conditions during HS1 especially over the western Amazon Basin and the tropical Andes (Blard et al., 2011; Kanner et al., 2012; Mosblech et al., 2012; Cheng et al., 2013), and Northeastern Brasil (Wang et al., 2004; Dupont et al., 2010; Strikis et al., 2015; Zhang et al., 2015).

However, the Amazon Basin-wide integrated signals reflected in marine sediment cores collected under the influence of the Amazon River discharge (Maslin and Burns, 2000; Maslin et al., 2011) partially showed conflicting results with continental records (Kanner et al., 2012; Mosblech et al., 2012). Temperature and glacio-eustatic corrected oxygen stable isotopes ($\delta^{18}\text{O}$) from the planktonic foraminifera *Globigerinoides sacculifer* suggest a negative anomaly in precipitation between 20.5 and 17 cal ka BP, and during the Antarctic cold reversal (ca. 14.5 – 12.9 cal ka BP) continuing into the Younger Dryas (ca. 12.8 – 11.5 cal ka BP) (Maslin et al., 2011). With the cautious assumption that *G. sacculifer* $\delta^{18}\text{O}$ signal can be used as a precipitation indicator, the results presented in Maslin et al. (2011) are partially inconsistent with stalagmite records from the western Amazon Basin (Kanner et al., 2012; Mosblech et al., 2012) where evidence of wetter conditions existed during HS1 (starting around 18 cal ka BP) and again during the Younger Dryas.

Here we present a high temporal resolution multiproxy study based on marine sediment core GeoB16224-1 retrieved off French Guiana. The site is influenced by the Amazon River freshwater and terrigenous matter discharge (Fig. 2-1). We use planktonic

foraminiferal (*Globigerinoides ruber* and *G. sacculifer*) $\delta^{18}\text{O}$ and Mg/Ca together with hydrogen stable isotopes (δD) from palmitic acid to reconstruct the uppermost water column hydrography in response to changes in Amazon River outflow. We also analysed the branched and isoprenoid tetraether (BIT) index and compared it to with existing data from bulk sediment $\ln(\text{Fe}/\text{Ca})$ and carbon stable isotopes ($\delta^{13}\text{C}$) of *n*-alkanes from the same core, to decipher the interaction among soil discharge, riverine sediment transport, and continental vegetation, from the Amazon Basin. Additionally, we present *G. ruber* and *G. sacculifer* $\delta^{18}\text{O}$ data from multicore GeoB16212-2 retrieved in the Amazon submarine delta on the Brazilian continental shelf directly off the Amazon River mouth (Fig. 2-1), in order to identify whether *G. ruber* records the hydrography of the Amazon-influenced low-salinity surface layer or the normal saline subsurface. Our data from GeoB16224-1 focus on the Last Glacial Maximum (LGM)-HS1 interval (22-14 cal ka BP) and provide an integrated picture of the response of Amazonian hydrology covering HS1. The amount and diversity of the proxies used identify regional changes in precipitation, overcoming the limitation of previous studies.

2.2 Regional setting

2.2.1 Amazon continental margin hydrology

Core GeoB16224-1 was retrieved from the continental margin of French Guiana. The core site is influenced by the Amazon freshwater discharge (Muller-Karger et al., 1988; Lentz, 1995), and the North Brazil Current (NBC) (Johns et al., 1998) (Figs. 1, 2b).

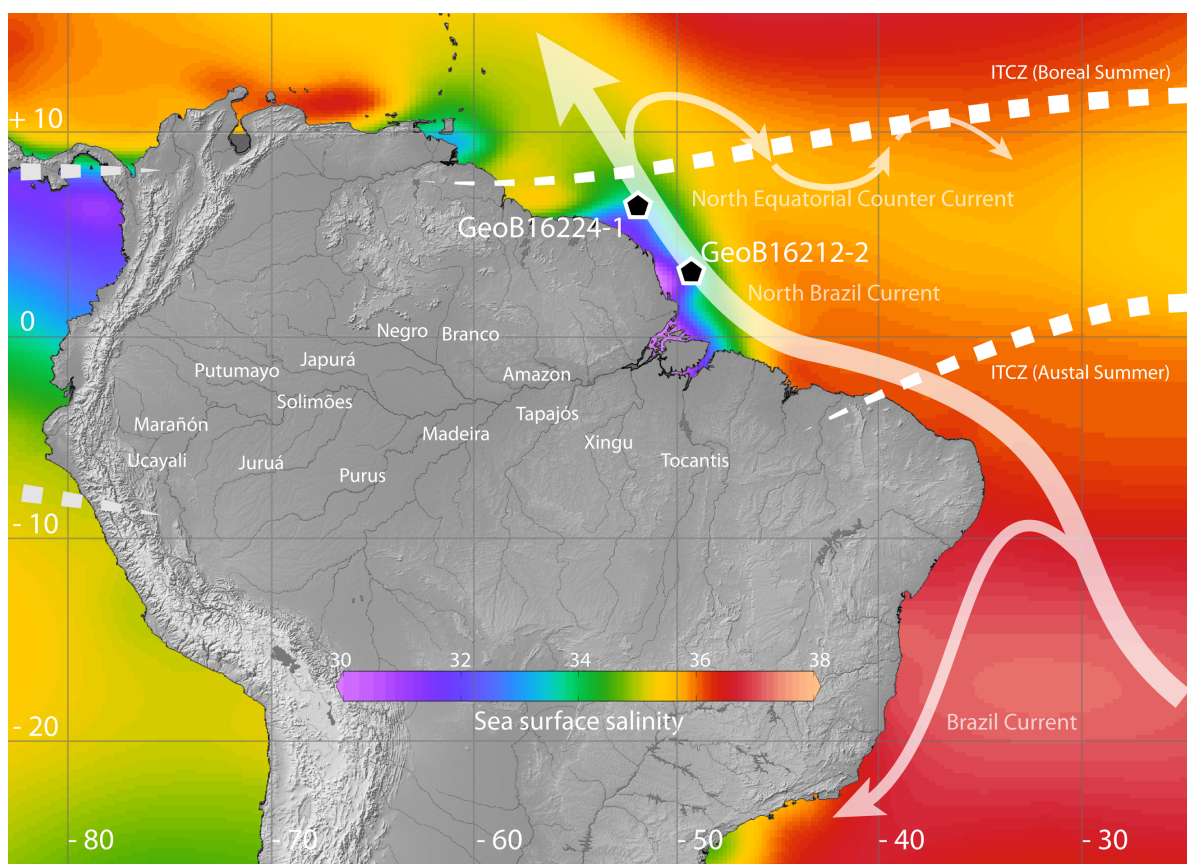


Figure 2-1. Location of the marine sediment cores investigated in this study (black pentagons, gravity core GeoB16224-1 and multicore GeoB16212-2). The main surface currents are schematically represented by the white arrows (Peterson and Stramma, 1991). Both core sites are under the influence of the Amazon low salinity plume and the northwestward-flowing North Brazil Current. The dotted lines display the approximate locations of the Intertropical Convergence Zone (ITCZ) over the Atlantic Ocean during boreal (June-August) and austral (December-February) summers. Annual salinities are displayed in the color shading (Levitus et al., 2013).

Minimum Amazon River discharge occurs in November (ca. $0.8 \times 10^5 \text{ m}^3 \text{ sec}^{-1}$) and maximum discharge in May (ca. $2.4 \times 10^5 \text{ m}^3 \text{ sec}^{-1}$) (Lentz, 1995). Modern SSS at the core location follow a distinct annual cycle and ranges from ca. 32 in November – January to ca. 25 in May – July (Salisbury et al., 2011) (Fig. 2-2b). Modern SST is on average $27.7 \text{ }^\circ\text{C}$ and varies between about $27 \text{ }^\circ\text{C}$ in January - March and $28 \text{ }^\circ\text{C}$ in July - September (Levitus et al., 2013). In the region of core GeoB16224-1, the yearly depth penetration of the low salinity plume is restricted to the uppermost 15 m of the water column (Fig. 2-2b).

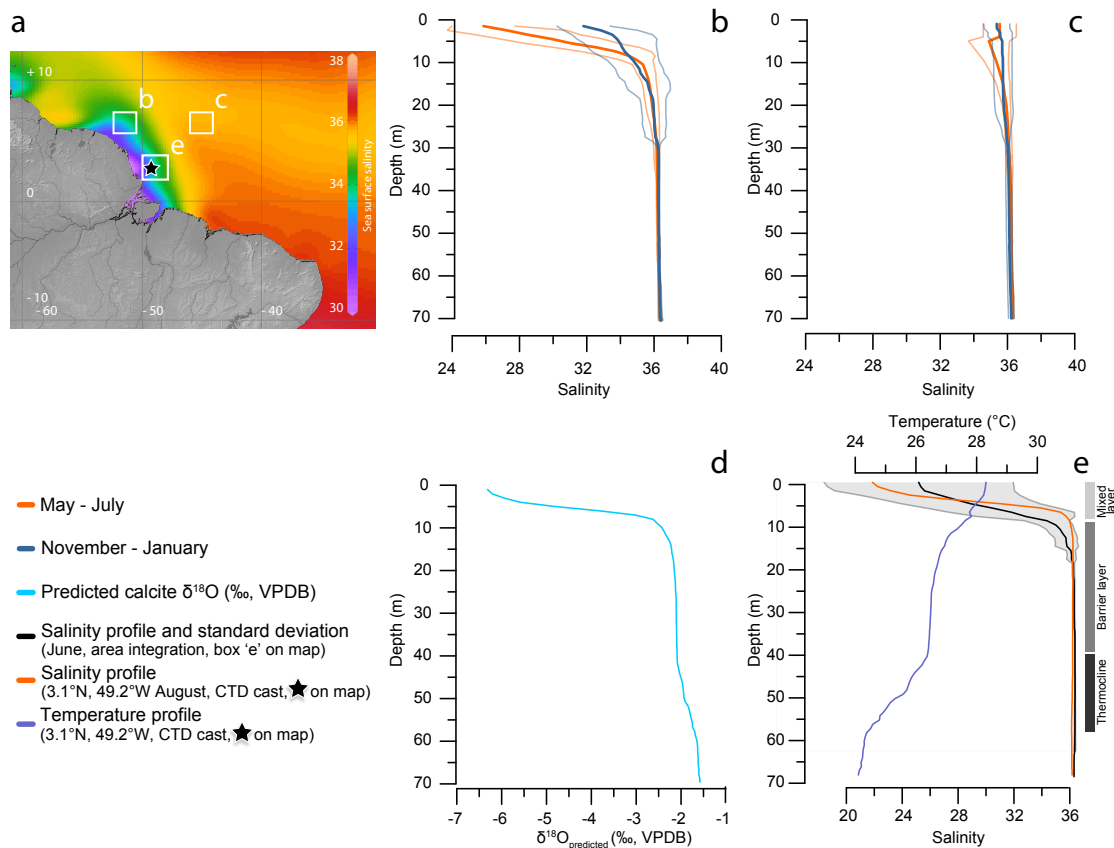


Figure 2-2. a) Annual sea surface salinity (Levitus et al., 2013) and location of areas (white rectangles) used in panels b, c and e. The star on the map represents the location of CTD cast at 3° 6' N, 49° 12' W for August, used for the calculation of the predicted calcite $\delta^{18}\text{O}$ in panel d. (b, c) Integrated vertical salinity profiles for the annual sea surface salinity minima (May – July, orange lines) and maxima (November – January, blue lines) (Salisbury et al., 2011), including the respective standard deviations. Data was extracted from unprocessed CTD casts made available from the World Ocean Database 2013 (https://www.nodc.noaa.gov/OC5/WOD/pr_wod.html; Levitus et al., 2013). Area b is centered at 52° W, 17 stations were sampled, the location is under the influence of the Amazon low salinity plume; area c is centered at 46° W, 7 stations were sampled, the area is not under the influence of the Amazon low salinity plume. (d) Vertical profile for the predicted calcite $\delta^{18}\text{O}$ for the site of the CTD cast (proximal to multicore GeoB16212-2). The site is in the Amazon shelf under the direct influence of the Amazon low salinity plume. (e) The black line with the gray shading represent the average salinity profile and the standard deviation for June for area e, which enclose site GeoB16212-2 (area centered at 3° N, -49° W, 24 stations sampled) (Levitus et al., 2013). The orange and dark blue lines represent the salinity and temperature profiles, respectively, from the CTD cast for August, used for the calculation of the predicted calcite $\delta^{18}\text{O}$ (panel d). For details on the calculation of the predicted calcite $\delta^{18}\text{O}$ please see section 2.3.5. The gray vertical bar indicate the main layers of the upper water column.

Core GeoB16212-2 was retrieved from the Amazon submarine delta at the Brazilian continental shelf (Fig. 2-1). Modern SSS at the core location varies between 24 and 30 (Levitus et al., 2013). At the core site, the presence of a quasi-perennial low density surface water layer (3 - 30 m deep) associated with a deeper thermocline (40 – 50 m deep), induces

the formation of a barrier layer (Fig. 2-2e), enhancing the separation between surface and subsurface waters (Lukas and Lindstrom, 1991).

2.2.2 Amazon sediments

Large amounts (ca. 1.2×10^9 t yr⁻¹) of sediment are presently delivered by the Amazon River to the western equatorial Atlantic Ocean, peaking during February - April (Meade et al., 1985). A large fraction of these sediments is transported north-westward by the NBC to the continental margin of French Guiana and to the Caribbean (Allison et al., 2000). Organic and inorganic sedimentary components have different sources within the Amazon Basin. Black water tributaries of the Amazon River draining large floodplain areas have the highest concentrations of dissolved humic substances (Mounier et al., 1999) and particulate organic carbon (Quay et al., 1992; Mayorga et al., 2005). Organic-rich sediments are predominantly sourced from lowland soils or represent material that is reworked in the floodplains where modern organic matter accumulates, e.g., in the form of plant wax *n*-alkanes (Häggi et al., 2016). Conversely, white water tributaries draining the Andean highlands are characterized by higher amounts of inorganic material. The seasonal pattern of sediment production is controlled by sediment erosion coming from the Andes (Gibbs, 1967), but also by sediment storage and resuspension (Meade et al., 1985) and by seasonal changes in waterbed level (Zell et al., 2013). Maximum sediment discharge (up to 1.3×10^9 t yr⁻¹) precedes peak water discharge by 2 - 3 months and is about 6 times the load of low sediment discharge months (Meade et al., 1985).

2.3 Material and methods

2.3.1 Sediment cores GeoB16224-1 and GeoB16212-2

The 760 cm-long gravity core GeoB16224-1 (6°39.38' N, 52°04.99' W, 2510 m water depth) (Fig. 2-1) was retrieved from the continental slope off French Guiana during RV MS Merian cruise MSM20/3 (Mulitza et al., 2013). During the same cruise, the 53 cm-long multicore GeoB16212-2 (3°06.22' N, 49°23.29' W, 77 m water depth) was collected in the Amazon submarine delta (Fig. 2-1).

2.3.2 Age models

We focus on the depth interval from 272 cm (22.1 cal ka BP) to 92.5 cm (14.1 cal ka BP) of core GeoB16224-1. The entire sediment core (760 cm) extends beyond 41 cal ka BP (oldest calibrated radiocarbon age at 600 cm core depth) (Fig. 2-3). The age model of the core is based on fifteen radiocarbon (^{14}C) measurements previously published by Zhang et al. (2015), where only well-preserved specimens of *G. ruber* (at least 7 mg) were analysed via AMS. The age model and associated uncertainties were calculated by using the R script BACON version 2.2 (Blaauw and Christen, 2011) and the IntCal13 calibration curve (Reimer et al., 2013) with a reservoir correction age of 400 ± 100 yr. (1σ error). A total of 10,000 age-depth realizations have been used to calculate the median age and relative 1σ analytical uncertainty at 5 mm resolution (Fig. 2-3).

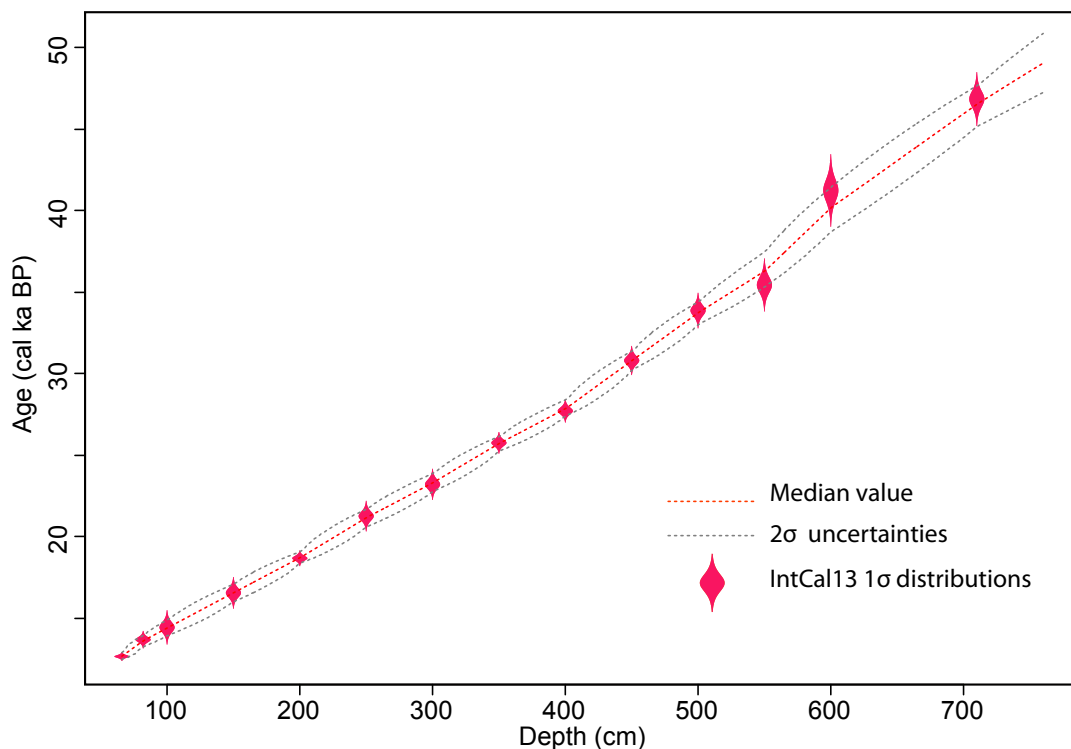


Figure 2-3. Age model of core GeoB16224-1, based on radiocarbon (^{14}C) measurements (red symbols) previously published by Zhang et al. (2015). An additional age control point at 710 cm was assumed with age 46830+470 years, from a well-dated stalagmite from El Condor (Cheng et al., 2013). The age model and associated uncertainties were calculated by using the R script BACON version 2.2 (Blaauw and Christen, 2011) and the IntCal13 calibration curve (Reimer et al., 2013) with a reservoir correction age of 400 ± 100 yr. (1σ error). The construction of the age model follows the methodology applied by Zhang et al. (2017) and Haggi et al. (2017) on the same core. Grey dotted lines indicate the analytical uncertainty of the median age (red dotted line) and the 2σ uncertainty at 5 mm resolution calculated by combining down core Monte Carlo proxy time series realizations. Note that prior to ca 12 ka BP there might be a hiatus.

Typical sedimentation rates for the Amazon submarine delta in the region of core GeoB16212-2 are higher than 1 cm yr^{-1} (Kuehl et al., 1986). These values suggest that all samples from the 53 cm-long multicore GeoB16212-2 were deposited within the last ca. 50 yr.

2.3.3 Stable oxygen isotopes, Mg/Ca measurements and *G. ruber* abundance

We sampled the section of interest of GeoB16224-1 every 2 cm with 10 cm^3 syringes. The entire tube of multicore GeoB16212-2 was sampled in 1-cm slices of 12 cm in diameter. Samples for $\delta^{18}\text{O}$, Mg/Ca, and *G. ruber* abundance were wet-sieved, oven-dried at $50 \text{ }^\circ\text{C}$ overnight, and the residue from the $150 \text{ }\mu\text{m}$ mesh size sieve stored in glass vials. Hand-picking of foraminiferal tests was performed under a binocular microscope. Foraminifera tests were selected to fit sizes between 250 and $350 \text{ }\mu\text{m}$ along the longest axis, free of adherent particles or chamber filling. For core GeoB16224-1 each sample was picked for *G. ruber* and *G. sacculifer* for a total of 80 samples. For multicore GeoB16212-2 *G. ruber* and *G. sacculifer* were picked each 1 cm for the uppermost 12 cm, and every 3 cm from 12 cm to 22 cm core depth. From 22 to 46 cm the core contained insufficient amount of foraminiferal tests for analyses. From 46 to 48 cm the multicore was picked every 1 cm. In total, 17 samples were picked.

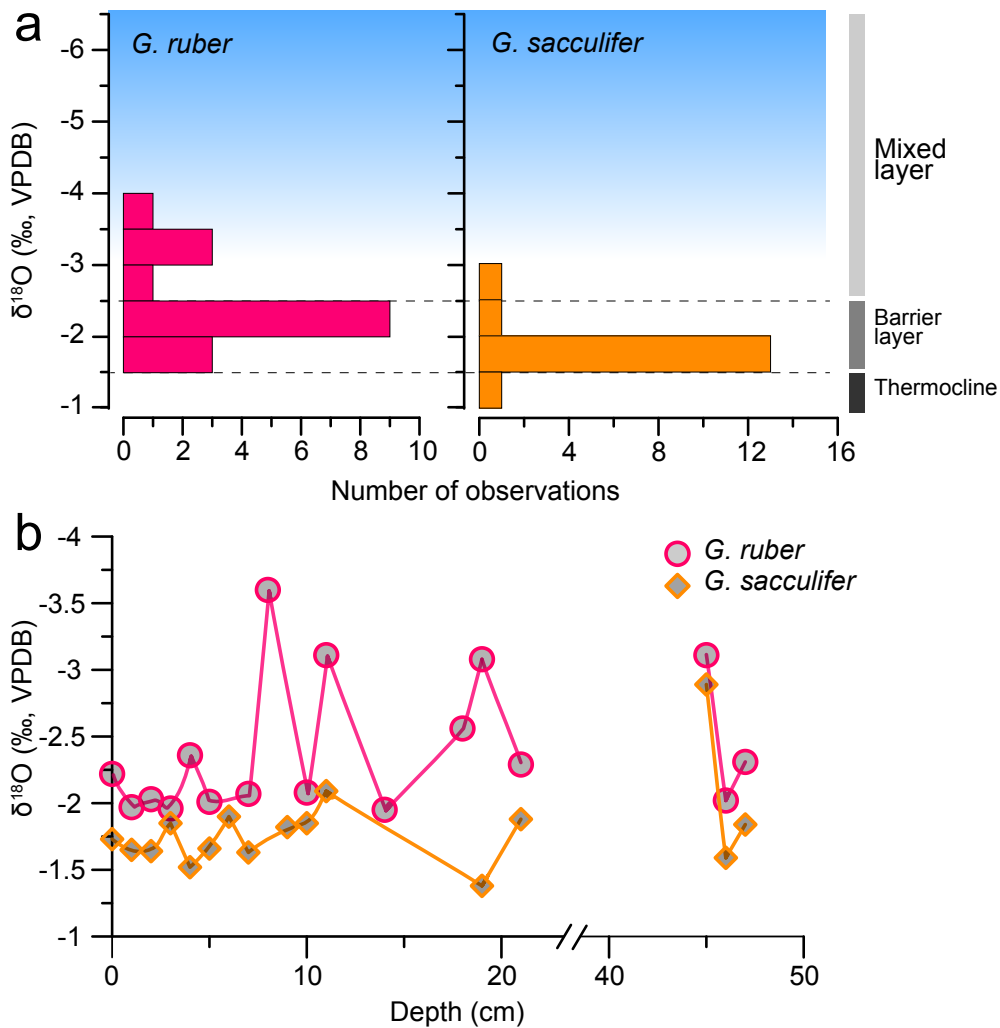


Figure 2-4. (a) Distribution of *Globigerinoides ruber* (red bars) and *Globigerinoides sacculifer* (orange bars) $\delta^{18}\text{O}$ from multicore GeoB16212-2. The gray vertical bar indicate the main layers of the upper water column. (b) Downcore *G. ruber* (red circles) and *G. sacculifer* (orange rhomboids) $\delta^{18}\text{O}$ from multicore GeoB16212-2. Note that although *G. ruber* shows a wide range of $\delta^{18}\text{O}$, *G. sacculifer* shows consistently heavier values, preferring deeper calcification depths, below the low salinity plume.

Stable oxygen isotopes were measured on the shells of planktonic foraminifera *G. ruber* (white, sensu stricto) (Wang, 2000) and *G. sacculifer* (without final chamber) for core GeoB16224-1 and multicore GeoB16212-2. Foraminiferal $\delta^{18}\text{O}$ was measured using a Finnigan-MAT 251 mass spectrometer coupled to a Kiel automated carbonate preparation device. The isotopic composition of foraminiferal calcium carbonate was analysed on the CO_2 retrieved by reaction of the carbonate with phosphoric acid. Solnhofen limestone was used as internal working standard, which has been calibrated against Vienna Pee Dee

Belemnite (VPDB) using the NBS 19 standard. Analytical precision was better than ± 0.07 ‰ for $\delta^{18}\text{O}$ ($\pm 1 \sigma$, $n = 130$).

For Mg/Ca analyses, about 20 - 30 specimens of *G. ruber* (white, sensu stricto) (Wang, 2000) were crushed and cleaned following the protocol described by Barker et al. (2003). Analyses were performed with the same resolution as for stable isotopes. The analytical procedure is essentially identical with that described by Kuhnert et al. (2011). Measurements were carried out on a ThermoQuest Element2 sector field inductively coupled plasma–mass spectrometer. Elemental concentrations were inferred from analysing the isotopes ^{25}Mg and ^{43}Ca in low instrument resolution and ^{27}Al and ^{55}Mn in medium resolution. For Mg and Ca concentrations, the analytical error (± 1 standard error of the mean, based on 10 runs) was always better than 0.2 %. The reproducibility of replicates from the same solutions measured on different days was 0.9 % on average.

The effectiveness of the cleaning procedure was monitored based on the Mn/Ca and Al/Ca ratios. Al/Ca (indicative of clay minerals) was usually below 0.1 mmol/mol, and samples with > 0.3 mmol/mol were discarded. Mn/Ca was 260 $\mu\text{mol/mol}$ on average. Mn/Ca and Mg/Ca showed inverse trends during the deglacial and were otherwise uncorrelated, indicating that Mn-bearing phases did not influence Mg/Ca through addition of Mg. We used the calibration equation from Regenberg et al. (2009) to calculate SST:

1. $\text{Mg/Ca} = 0.4^{(0.094 * \text{SST})}$

We have chosen this species-specific calibration as it has been constructed with a comprehensive set of equatorial Atlantic core top samples. Other equatorial Atlantic calibrations for *G. ruber* are similar (i.e., Dekens et al., 2002; Kisakürek et al., 2008).

Both core sites lie well above the modern and glacial lysocline (Volbers and Henrich, 2004), and hence we assume planktonic foraminiferal faunal composition, shell chemistry, and Mg/Ca paleo-temperatures to be unaffected by dissolution.

For the gravity core GeoB16224-1 samples were analysed for *G. ruber* (white) abundance. Specimens were dry picked from the size fraction above 150 μm and quantified as weight normalized, absolute abundances from splits containing more than 300 specimens per sample. The taxonomical identification was based on Stainforth et al. (1975).

2.3.4 Reconstruction of ice volume corrected sea water oxygen isotope values

In order to determine the Amazon freshwater impact on SSS, we calculated Mg/Ca SST on the same samples analysed for $\delta^{18}\text{O}$ ($\delta^{18}\text{O}_{\text{ca}}$). The SST and $\delta^{18}\text{O}_{\text{ca}}$ records were then used to solve the *G. ruber* paleotemperature equation from Mulitza et al. (2003) for sea water $\delta^{18}\text{O}$ ($\delta^{18}\text{O}_{\text{sw}}$), from the western Atlantic that includes samples from the equatorial region:

$$2. \quad \text{SST} = -4.44(\delta^{18}\text{O}_{\text{ca}} - \delta^{18}\text{O}_{\text{sw}}) + 14.20$$

Vienna Pee Dee Belemnite (VPDB) values of $\delta^{18}\text{O}_{\text{sw}}$ were converted to Vienna Standard Mean Ocean Water (SMOW) by adding 0.27‰ (Hut, 1987), and corrected for ice volume changes using the sea level estimates from Lambeck et al. (2014):

$$3. \quad \delta^{18}\text{O}_{\text{sw-ivc}} = \delta^{18}\text{O}_{\text{sw}} - (\text{ESL} * 1/134)$$

Where $\delta^{18}\text{O}_{\text{sw-ivc}}$ is the sea water oxygen isotopic values corrected for ice volume changes and ESL is the estimated sea level difference to preindustrial sea level in meters (Lambeck et al., 2014). The average global change in $\delta^{18}\text{O}_{\text{sw}}$ since the LGM is assumed to be 1 ‰ (Adkins and Schrag, 2001; Schrag et al., 2002). The $\delta^{18}\text{O}_{\text{sw-ivc}}$ is a first order approximation of SSS. The propagation of uncertainties typically results in a 1σ error of about 0.3 - 0.4 ‰ for $\delta^{18}\text{O}_{\text{sw-ivc}}$ (Schmidt, 1999; Mohtadi et al., 2014).

2.3.5 Small-scale estimation of calcification ranges on site GeoB16212-2

In order to constrain the ability of *G. ruber* and *G. sacculifer* to register the Amazon low salinity plume, $\delta^{18}\text{O}$ measurements of these two species were carried out on multicore GeoB16212-2; the site is influenced by the low salinity plume (Figs. 1, 2e). We estimated $\delta^{18}\text{O}$ calcification ranges by comparing measured $\delta^{18}\text{O}$ of *G. ruber* and *G. sacculifer* to the theoretical calcite $\delta^{18}\text{O}$ predicted from instrumental temperature and salinity (Fig. 2-4a). We used a nearby high resolution CTD dataset from 3°9.11' N, 49°17.35' W (Fig. 2-2a,e) obtained in August which corresponds to the period of increasing salinity following the annual minimum (Levitus et al., 2013). We first calculated $\delta^{18}\text{O}_{\text{sw}}$ by applying the salinity- $\delta^{18}\text{O}_{\text{sw}}$ relationship suggested by Regenberg et al. (2009) for the upper 100 m of the water column. Values were converted to VPDB by subtracting 0.27 ‰ (Hut, 1987). We then constructed a vertical profile of $\delta^{18}\text{O}_{\text{predicted}}$ (Fig. 2-2d) applying the *G. ruber* paleotemperature equation (2) from Mulitza et al. (2003) using same CTD temperatures and

the calculated $\delta^{18}\text{O}_{\text{sw}}$. We applied the same paleotemperature equation for *G. ruber* and *G. sacculifer* as there is no statistically significant difference (Mulitza et al., 2003).

2.3.6 δD of palmitic acid and BIT index

Samples were freeze-dried and ground with an agate mortar and pestle. Lipid extraction was conducted on an ASE200 accelerated solvent extractor using a dichloromethane (DCM): methanol (MeOH) 9:1 solution at 1000 psi and 100 °C for three cycles lasting 5 min each. A standard mixture containing squalene, C₄₆ GDGT standard and erucic acid was added prior to extraction. After lipid extraction, solvents were removed in a Heidolph ROTOVAP system. Asphaltenes were separated over pipette columns consisting of 4 cm of Na₂SO₄ using hexane and DCM as subsequent solvents. The lipid extracts were subsequently saponified using 0.1M KOH in MeOH solution, yielding neutral and acid fractions. Compounds of the neutral fraction were separated using columns with deactivated silica gel 60 (1 % H₂O). Subsequent elution with hexane, DCM and DCM: MeOH 1:1 yielded the hydrocarbon, ketone and polar fractions. The polar fraction was filtered through Restek PTFE syringe filters (4 mm, 0.45 μm) using hexane as solvent. The acid fraction was methylated in methanol of known isotopic composition ($-156 \pm 2 \text{‰}$ vs. VSMOW) yielding the corresponding fatty acid methyl esters (FAMES). The FAMES were subsequently cleaned over pipette columns containing 2 cm silica gel by elution with DCM. FAMES were analysed using a Thermo Fisher Scientific Focus gas chromatograph equipped with a 30 m Rxi™-5ms column (30 m, 0.25 mm, 0.25 μm) and a flame ionization detector. Compounds were quantified by comparing the integrated peak areas of the compounds to peak areas obtained from analyses of external standard solutions.

Compound-specific hydrogen isotope analyses of palmitic acid were carried out on a Thermo Fisher Scientific MAT 253™ Isotope Ratio Mass Spectrometer coupled via a gas chromatographer (GCh) IsoLink operated at 1420 °C to a Thermo Fisher Scientific TRACE™ GCh equipped with a HP-5ms column (30 m, 0.25 mm, 1 μm). For each sample, duplicate injections were conducted. Measurement accuracy was controlled by *n*-alkane standards of known isotopic composition every six measurements and by the daily determination of the H⁺³ factor using H₂ as reference gas. H⁺³ factors varied between 5.3 and 5.9, while the mean absolute deviation of external standards was 2.8 ‰. The results of the stable hydrogen isotope measurements for palmitic acid were corrected for the methyl group

added during methylation. Values of δD of palmitic acid were corrected for ice volume fluctuations based on sea levels estimates by Lambeck et al. (2014).

Branched and isoprenoid glycerol dialkyl glycerol tetraethers (GDGT) were analysed by liquid chromatography (LC) coupled via an atmospheric pressure chemical ionization (APCI) interface to a single quadrupole mass spectrometer (MS), with a method slightly modified from Hopmans et al. (2000). Analyses were performed on an Agilent 1200 series HPLC system and an Agilent 6120 MSD. Separation of the individual GDGT's was achieved on a Prevail Cyano column (Grace, 3 μ m, 150 mm x 2.1 mm) maintained at 30 °C. After sample injection (20 μ L) and 5 min isocratic elution with mobile phase A (hexane/2-propanol/chloroform; 98:1:1) at a flow rate of 0.2 ml/min, the proportion of mobile phase B (hexane/2-propanol/chloroform; 89:10:1) was linearly increased to 10 % within 20 min, and thereafter to 100 % for the next 10 min. After another 7 min and prior to the analysis of the next sample, the column was cleaned in backflush mode for 5 min at a flow of 0.6 ml/min and re-equilibrated with solvent A (10 min, flow 0.2 ml/min). GDGT's were detected using positive-ion APCI-MS and selective ion monitoring (SIM) of their (M+H)⁺ ions (Schouten et al., 2007) with APCI spray-chamber conditions as follows: nebulizer pressure 50 psi, vaporizer temperature 350 °C, N₂ drying gas flow 5 l/min and 350 °C, capillary voltage (ion transfer tube) -4 kV and corona current +5 μ A.

For BIT index analysis, the MS-detector was set for SIM of the following (M+H)⁺ ions: *m/z* 1302.3 (GDGT 0), 1300.3 (GDGT 1), 1298.3 (GDGT 2), 1296.3 (GDGT 3), 1292.3 (GDGT 4 + 4' / crenarchaeol + regio-isomer), 1050 (GDGT III), 1036 (GDGT II), 1022 (GDGT I) and 744 (C₄₆ standard), with a dwell time of 67 ms per ion. Quantification of the individual GDGT's was achieved by integrating the respective peak areas. Compound concentrations were calculated using the response factor obtained from the C₄₆ standard and by normalizing to the amount of extracted sediment. Due to the lack of appropriate standards, individual relative response factors between the C₄₆ standard and the different GDGT's could not be considered; the obtained concentrations should therefore be regarded as being only semi-quantitative.

2.4 Results

2.4.1 $\delta^{18}\text{O}$, Mg/Ca and reconstructed sea surface hydrography

From ca. 22 to 17.1 cal ka BP *G. ruber* $\delta^{18}\text{O}$ values on core GeoB16224-1 are relatively stable around -0.2‰ (Fig. 2-5a). This time period is followed by a rapid decrease by about 0.8‰ within few centuries. Relatively stable values occur again after 16.9 cal ka BP, (Fig. 2-5a). *Globigerinoides sacculifer* $\delta^{18}\text{O}$ is stable at 0‰ from ca. 22 to 17.1 cal ka BP (Fig. 2-5a). Values for *G. sacculifer* are consistently higher by 0.2‰ compared with *G. ruber*. From 17.1 cal ka BP onwards *G. sacculifer* $\delta^{18}\text{O}$ values decrease steadily at ca. 0.2‰ per thousand yr. The offset between $\delta^{18}\text{O}$ values of the two planktonic species increases up to 1‰ at ca. 16 cal ka BP and resumes to pre-HS1 values at ca. 14.6 cal ka BP (Fig. 2-5a).

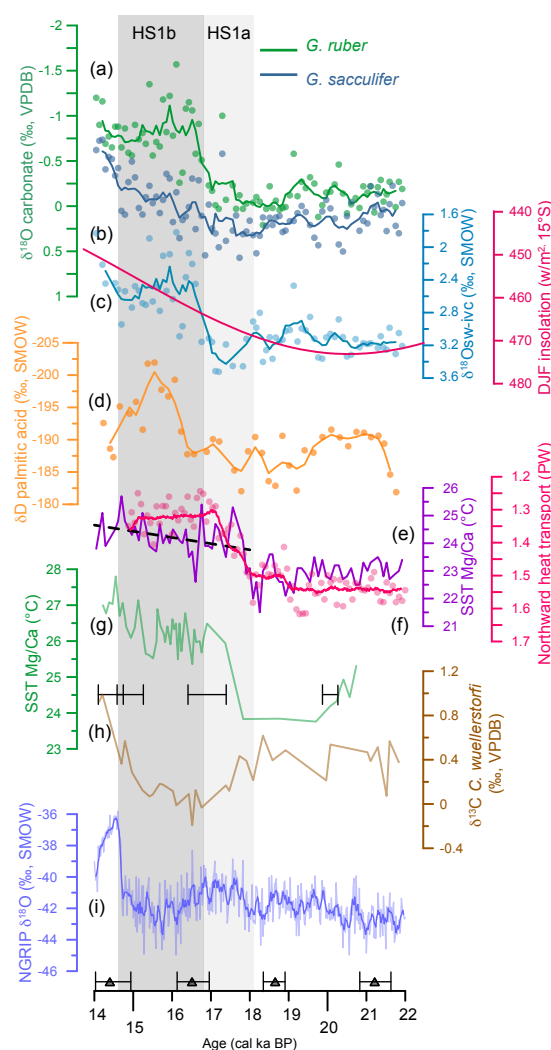


Figure 2-5. Proxy records from gravity core GeoB16224-1 together with a sea surface temperature (SST) record off northeastern Brazil, northward heat transport from a transient model run and ice core $\delta^{18}\text{O}$. (a) $\delta^{18}\text{O}$ of *Globigerinoides ruber* and *Globigerinoides sacculifer* from core GeoB16224-1 (solid lines are five points

moving average) (this study). (b) Insolation curve at 15° S for austral summer months (DJF). (c) Sea water ice volume corrected $\delta^{18}\text{O}$ ($\delta^{18}\text{O}_{\text{sw-ivc}}$) from core GeoB16224-1 (solid line is five points moving average) (this study). (d) δD of palmitic acid from core GeoB16224-1 (solid line is three points moving average) (this study). (e) *G. ruber* Mg/Ca derived SST from core GeoB16224-1 (this study). Note that from ca. 17.5 cal ka BP onwards, temperatures show a slight increase as highlighted by the black dotted line (linear regression from 17.5 cal ka BP onwards) consistent with a deglacial trend (Jaeschke et al., 2007). (f) TraCE-21k model output for the northward heat transport in the Atlantic (Liu et al., 2009), integrated over an area (5°42' N–7°42' N and 53°W–51°W) that include site GeoB16224-1. (g) Mg/Ca SST off northeastern Brazil (Weldeab et al., 2006). (h) $\delta^{13}\text{C}$ of *Cibicidoides wuellerstorfi* from core GeoB16224-1 (Voigt et al., 2017). (i) North Greenland Ice Core Project (NGRIP) $\delta^{18}\text{O}$ (Andersen et al., 2004). Gray triangles over the horizontal axis show the calibrated radiocarbon ages and respective errors. The two Heinrich Stadial (HS) 1 phases (HS1a and HS1b) are indicated by the gray bars.

Mg/Ca values from *G. ruber* range from 3.02 to 4.35 mmol/mol corresponding to 21.5 and 25.4 °C, respectively (Fig. 2-5f). Average pre-HS1 values are 3.43 mmol/mol (22.8 °C), whereas average HS1 values are 3.9 mmol/mol (24.1 °C). When compared to modern values (annual average of 27.5 °C, Levitus et al., 2013), average pre-HS1 SST are 4.7 °C colder and average HS1 SST are 3.4 °C colder. Our temperatures are consistent with other reconstructed LGM temperatures anomalies that register cooling ranging from 1.5 - 3 °C (i.e., Trend-Staid and Prell, 2002; Niebler et al., 2003) to 5 - 6 °C (i.e., Mix et al., 1999). An abrupt increase by ca 1.3 °C occurs between 18.1 and 17.8 cal ka BP. The magnitude of the warming is consistent with other temperature reconstructions from the equatorial Atlantic (Rühlemann et al., 1999; Weldeab et al., 2006; Nace et al., 2014). From 17.8 cal ka BP onwards, SST continues to increase, but more gradually, reaching about 25 °C at 14.8 cal ka BP.

The $\delta^{18}\text{O}_{\text{sw-ivc}}$ record shows relatively stable values (around 3.0 ‰) until ca. 18 cal ka BP when an 0.4 ‰ increase aligns with the sudden 1.3 °C increase in SST (Fig. 2-5c,e). A marked departure of $\delta^{18}\text{O}_{\text{sw-ivc}}$ values from the SST signal occurs between 16.9 and 14.8 cal ka BP; at about 16.9 cal ka BP $\delta^{18}\text{O}_{\text{sw-ivc}}$ decreases abruptly by about 0.75 ‰ within a few centuries. Persisting low $\delta^{18}\text{O}_{\text{sw-ivc}}$ values (2.4 ‰) are sustained until 14.8 cal ka BP.

Values of δD palmitic acid are relatively stable around -187 ‰ from ca 21.5 until ca. 16.9 cal ka BP, with increased scattering after 20 cal ka BP (Fig. 2-5d). A marked negative excursion to -200 ‰ occurs between 16.5 and 14.8 cal ka BP.

Globigerinoides ruber $\delta^{18}\text{O}$ values from multicore GeoB16212-2 consistently display lower values than *G. sacculifer* (Fig. 2-4a,b). *Globigerinoides ruber* values range from -3.6 to -1.95 ‰ with most of them between -2.5 and -2‰, and three values lower than -3‰. The average is -2.39 ‰. *Globigerinoides sacculifer* values range from -2.89 to -1.3 ‰ with an average of -1.8 ‰, whereas most of the values are distributed between -2 and -1.5 ‰.

2.4.2 Continental climate indicators

BIT index values remain relatively stable around 0.6 until ca. 19 cal ka BP when a progressive increase occurs reaching maximum values of 0.75 until at ca. 17.5 cal ka BP (Fig. 2-6h). Values then return to pre-HS1 level between 16.9 to 14.8 cal ka BP. The concentrations of branched GDGT and crenarchaeols were calculated against total dry sample weight (Figs. 6h, S1c), in order to determine if the BIT index signal is mainly driven by the terrestrial or marine component. Land produced branched GDGT clearly show a close correlation to the BIT index record (Fig. 2-6g-h) indicating a control of BIT by soil discharge. From ca. 16.5 to 14.8 cal ka BP both records show a clear decreasing trend, however their correlation tends to degrade. Average concentration values of ca. 300 ng/g are maintained from ca 20 to 18.5 cal ka BP. Concentrations reach their maxima of 600 ng/g in the period from 18.5 to 17.4 cal ka BP and resume background values from 16.7 to 15.7 cal ka BP. Marine produced crenarchaeols (Fig. 2-S1c) show lower average concentrations of ca. 200 ng/g with localized increases at 16.2, 15.1 and 14.2 cal ka BP.

The relative abundance of *G. ruber* displays near-constant values of ca. 22 % until 19 cal ka BP to then increase by almost 10 % prior to 18 cal ka BP (Fig. 2-6e). An abrupt decrease by ca. 15 % characterizes the interval between 18.5 to 17.9 cal ka BP. Between 17.5 to 15 cal ka BP the abundance then gradually recovers to values similar to those before 18 cal ka BP. The *G. ruber* abundance curve has inverse geometry as the $\ln(\text{Fe}/\text{Ca})$ and BIT index records (Figs 6e,f,h).

2.5 Discussion

Our records from core GeoB16224-1 suggest two distinct phases forming an internal structure of HS1, namely from 18 to 16.9 cal ka BP (hereafter HS1a), and from 16.9 to 14.8 cal ka BP (hereafter HS1b) (Figs. 5-7, Table 2-1). We consider the time interval investigated in this work to be well constrained by the age model. Apart for the radiocarbon date at 18.6 cal ka BP the ages at 16.5 and 14.4 cal ka BP include in their error margin, the transition between HS1a and HS1b and the termination of HS1b, respectively. While the onset of HS1a is characterized by an increase in terrigenous input and SST, the onset of HS1b is marked by

. Increased precipitation in the western equatorial Atlantic during late Heinrich Stadial 1

a major drop in SSS. The duration of HS1 documented by our record agrees with the temporal boundaries of Heinrich event *sensu lato* recognised by Stanford et al. (2011).

Region	Location	Proxy	Parameter	HS1b	HS1a	Reference
				16.9 - 14.9 ka BP	18 - 16.9 ka BP	
Tropical Andes	Santiago Cave	$\delta^{18}\text{O}$ Speleothem carbonate	Precipitation	+	++	Mosblech et al. (2009)
	Pacupahuain Cave	$\delta^{18}\text{O}$ Speleothem carbonate	Precipitation	--	+	Kanner et al. (2012)
	El Condor Cave	$\delta^{18}\text{O}$ Speleothem carbonate	Precipitation	-	+	Cheng et al. (2013)
	Diamante Cave	$\delta^{18}\text{O}$ Speleothem carbonate	Precipitation	--	+	Cheng et al. (2013)
	Huascarán	$\delta^{18}\text{O}$ Ice core	Precipitation	--	+++	Thompson et al. (1995)
Northern South America	Cariaco Basin	Sediment lightness	Discharge/runoff	---	-	Deplazes et al. (2013)
Western equatorial Atlantic	GeoB16224-1	$\delta^{13}\text{C}$ n-alkanes	C4 relative to C3	++	.	This study
	GeoB16224-1	Mg/Ca	SST	.	++	This study
	GeoB16224-1	ln(Fe/Ca)	Terrigenous vs marine sediment	--	++	This study
	GeoB16224-1	BIT index	Terrigenous vs marine organic matter	--	++	This study
	GeoB16224-1	brGDGT concentration	Terrigenous	--	++	This study
	GeoB16224-1	G. ruber abundance	Water turbidity	---	+++	This study
	ODP 942 Site	$\delta^{18}\text{O}_{\text{sw}}$	SSS	--	.	Maslin et al. (2011)
	GeoB16224-1	$\delta^{18}\text{O}_{\text{sw}}$	SSS	---	.	This study
GeoB16224-1	δD palmitic acid	SSS	--	.	This study	

Table 2-1. Summary of proxy response to the two phases of Heinrich Stadial (HS) 1 phases (HS1a and HS1b). The location, proxy type, reconstructed environmental parameter, change in the reconstructed parameter and the reference is provided for each record. The amount of plus (minus) signs indicate the strength of the increase (decrease) in the reconstructed parameter for each HS1 phase in relation to the previous period. Dots represents unappreciable change in the reconstructed parameter. HS1a is placed after to HS1b for visual consistence with Figs. 2-5 to 2-7. BIT: branched and isoprenoid tetraether index; brGDGT: branched and isoprenoid glycerol dialkyl glycerol tetraethers; SSS: sea surface salinity; SST: sea surface temperature.

2.5.1 Sediment production and terrigenous input

Existing ln(Fe/Ca) and ln(Fe/K) XRF records for GeoB16224-1 (Zhang et al., 2017) show that a substantial increase in ln(Fe/Ca) and BIT index values characterizes HS1a (Figs. 2-6f,h, S6-2). A similar covariance between ln(Fe/Ca) and BIT index values was described in marine sediment core GeoB3910-2 collected off northeastern Brazil where the onset of HS1 occurs at 18.2 cal ka BP (Stríkis et al., 2015). As discussed in section 2.5.3, the increase in terrigenous input during HS1a is associated with an increase in $\delta^{18}\text{O}_{\text{sw-ivc}}$ (Fig. 2-6a,f,h). A decrease in $\delta^{18}\text{O}_{\text{sw-ivc}}$ occurs at the onset of HS1b lagging the terrigenous signal by ca. 900 yr., during a phase of declining terrigenous input at our core site.

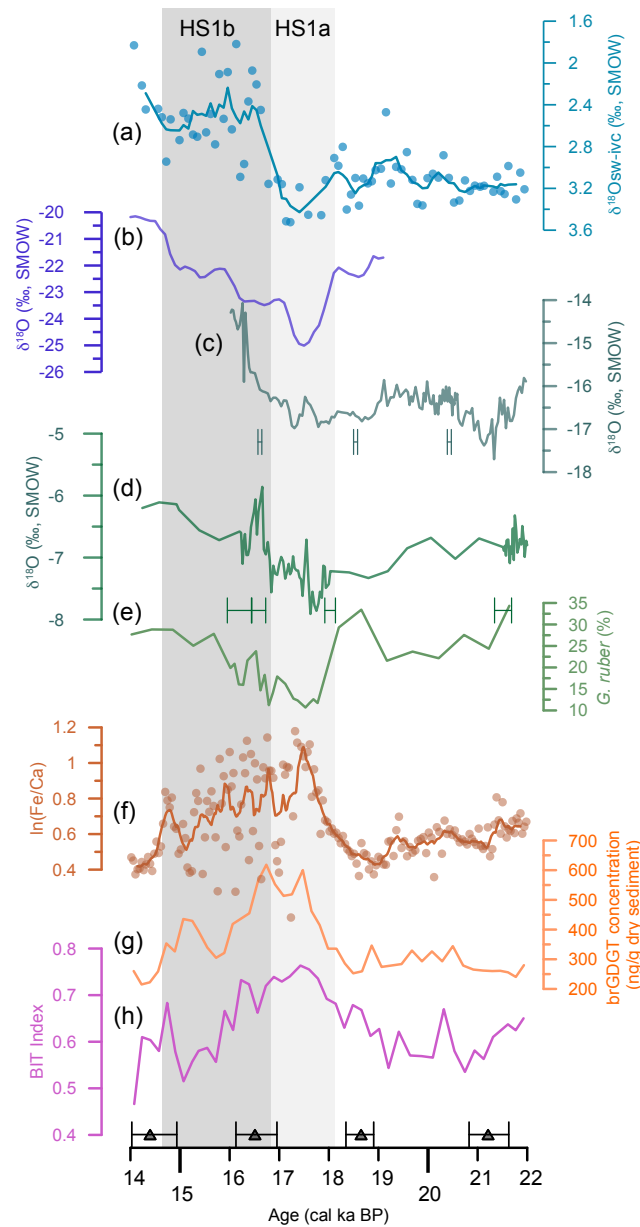


Figure 2-6. Proxy records from gravity core GeoB16224-1 together with speleothems and glacier records from the tropical Andes. (a) Sea water ice volume corrected $\delta^{18}\text{O}$ ($\delta^{18}\text{O}_{\text{sw-ivc}}$) on core GeoB16224-1 (solid line is five point moving average) (this study). (b) $\delta^{18}\text{O}$ record from Huascarán ice core (Thompson et al., 1995). (c) $\delta^{18}\text{O}$ record from Pacupahuain cave speleothem (Kanner et al., 2012), dating error bars are displayed underneath the curve. (d) $\delta^{18}\text{O}$ record from Diamante cave speleothem (Cheng et al., 2013), dating error bars are displayed underneath the curve. (e) *Globigerinoides ruber* abundance from core GeoB16224-1 (this study). (f) $\ln(\text{Fe}/\text{Ca})$. (g) Branched GDGT (brGDGT) concentration normalized for sample weight from core GeoB16224-1 (this study). (h) Branched and isoprenoid tetraether (BIT) index representing terrestrial vs marine contribution of organic matter, constructed using the ratio between brGDGT and crenarchaeol organic molecules from core GeoB16224-1 (this study). Note that a marked increase in the terrestrial brGDGT is following the BIT signal suggesting that terrestrial sediment apportionment is increasing predominantly on HS1a whereas crenarchaeol concentration remains mostly stable (see Fig. S6-2). Gray triangles over the horizontal axis show the calibrated radiocarbon ages and respective errors. The two Heinrich Stadial (HS) 1 phases (HS1a and HS1b) are indicated by the gray bars.

Both, the $\ln(\text{Fe}/\text{Ca})$ and the BIT index are ratios between the relative concentration of an element or molecules produced on land vs. their marine counterparts. Thus, changes in $\ln(\text{Fe}/\text{Ca})$ and BIT index could theoretically also reflect changes in the marine components (Fietz et al., 2011; Govin et al., 2012). However, we find that $\ln(\text{Fe}/\text{Ca})$ correlates well with $\ln(\text{Fe}/\text{K})$ from the same core (Fig S6-2). Therefore, we argue that Fe of terrestrial origin is controlling the signal on the $\ln(\text{Fe}/\text{Ca})$ and $\ln(\text{Fe}/\text{K})$ records, as it is unlikely that K and Ca have similar chemical and sedimentological behaviours (Govin et al., 2012). Moreover, by looking at the concentrations of branched GDGT, that represent the terrestrial component of the BIT index, it is clear that the BIT index is dominated by the terrigenous branched GDGT signal (Figs. 6g,h, S6-1c). Our $\ln(\text{Fe}/\text{Ca})$ and BIT index records thus primarily reflect changes in the flux of terrestrial inorganic and organic materials, respectively, rather than changes in marine productivity (Fietz et al., 2011; Govin et al., 2012).

The increase in terrestrial discharge during HS1a (Fig. 2-6f,h) is associated with a 15% decrease in the abundance of *G. ruber* (Fig. 2-6e). *Globigerinoides ruber* is a surface dwelling, symbiont-bearing species. The decrease in its abundance is likely related to an increase in water turbidity caused by the high concentration of suspended terrigenous material (i.e., Schmuker and Schiebel, 2002; Goes et al., 2014). This limits light penetration and impairs *G. ruber* symbionts' photosynthetic activity. Indeed, the high concentration of suspended material has a profound impact on the composition of the phytoplankton community by restricting the amount of light available for photosynthesis in the modern Amazon River low salinity plume (Goes et al., 2014).

In the modern Amazon Basin, the primary source of inorganic sediments are the sloped highlands of the tropical Andes (Meade et al., 1985; Zhang et al., 2015). Highlands represent ca. 12 % of the total Amazonian catchment, yet more than 80 % of the riverine sediment load is of Andean origin (Gibbs, 1967). We assume that even a marginal increase in precipitation over the tropical Andes would have substantially contributed to the rise in terrigenous input to the western equatorial Atlantic. Indeed, two high resolution and well dated speleothems from Peru suggest higher precipitation over the tropical Andes during HS1 (Kanner et al., 2012; Cheng et al., 2013) (Fig. 2-6c,d). A decrease of about 0.5 ‰ in $\delta^{18}\text{O}$ of the Pacupahuain cave speleothem occurred as early as 19 cal ka BP, reflecting a slightly wetter climate (Kanner et al., 2012). Subsequently, a ca. 2 ‰ increase in stalagmite $\delta^{18}\text{O}$ corresponds to the onset of decrease in $\ln(\text{Fe}/\text{Ca})$ at ca. 17 cal ka BP, denoting drier conditions in the tropical Andes at the onset of HS1b (Fig. 2-6c,f). Analogously, speleothem $\delta^{18}\text{O}$ from

Diamante cave registers a short-lived 0.5 ‰ depletion at ca. 18 cal ka BP, and then rises by 1 ‰ at the onset of HS1b (Fig. 2-6d) (Cheng et al., 2013). The Huascarán ice core $\delta^{18}\text{O}$ record (Thompson et al., 1995) also suggests increased precipitation over the Andes of Peru during HS1a and a gradual shift towards a lower precipitation regime throughout the subsequent HS1 phase (Fig. 2-6b).

In general, at millennial-scale, it is likely that changes in tropical South American sediment transport is tightly coupled with changes in precipitation rather than neo-tectonic activity or basin-wide changes in drainage configuration (e.g., Costa et al., 2001; Zhang et al., 2017). During HS1b, our $\ln(\text{Fe}/\text{Ca})$, BIT index and brGDGT records clearly indicate reduced terrigenous input at site GeoB16224-1 (Fig. 2-6f-h). Moreover, the gradual return of *G. ruber* abundance to pre-HS1 levels (Fig. 2-6e), also suggests less turbid waters most probably related to a decreased sediment load, and more favourable conditions for symbiont photosynthesis. This is consistent with the decrease in precipitation over the tropical Andes as suggested by speleothem and ice core records (Fig. 2-6b-d, Table 2-1). Taken together, these records suggest that the main locus of precipitation migrated away from regions prone to erosion (i.e., tropical Andes), moving for instance towards the central Amazonian plains and the cratonic Brazilian shield. Supporting evidence for a lowland increase in precipitation are found on a speleothem record from Paraíso cave (cratonic Brazilian shield) which shows relatively dry conditions during the LGM and wet conditions during HS1b (Wang et al., 2017). Similarly, the speleothem record from Rio Grande do Norte shows more depleted $\delta^{18}\text{O}$ values during HS1b in relation to HS1a indicating an increase in precipitation during HS1b over northeastern Brazil (Cruz et al., 2009). The dense vegetation and flat topography of the central Amazonian plains and the cratonic Brazilian shield likely limited erosion and sediment mobilization during HS1b compared to HS1a (Gaillardet et al., 1997; Wittmann et al., 2011).

2.5.2 Changes in SST and SSS at the core location

At the onset of HS1a SST warmed abruptly by about 2 °C near site GeoB16224-1 (Fig. 2-5e). This warming was most probably driven by a decrease in AMOC strength and a less efficient heat export to northern high latitudes, commonly referred to as “bipolar seesaw” (Broecker, 1998; Rühlemann et al., 1999; Barker et al., 2009). This caused a steeper meridional SST gradient in the North Atlantic that produced stronger NE trade winds.

Measurements of palmitic acid on GeoB16224-1, a proxy for salinity (Häggi et al., 2015), show no appreciable change in SSS during HS1a. However, we notice a 0.2 ‰ enrichment in $\delta^{18}\text{O}_{\text{sw}}$, which is within the margin of error nonetheless, that could represent an increase in SSS caused by reduced northward salt export (Fig. 2-5e). In any case, increase in SSS due to reduced Amazon freshwater discharge, is incompatible with the increased terrigenous output during HS1a as recorded in our core (Fig. 2-6f,h).

Stronger NE trade winds and regional heat build-up may have contributed to the SSS rise. Indeed, *Globigerinoides ruber* Mg/Ca and $\delta^{18}\text{O}$ from a marine sediments core collected off northeastern Brazil show significantly elevated SST and SSS during HS1 (Weldeab et al., 2006). Further constraints on the increase in SSS and SST resulting from a sluggish AMOC have been suggested by many coupled ocean-atmosphere climate model simulations (e.g., Broccoli et al., 2006; Timm and Timmermann, 2007; Liu et al., 2009).

The GeoB16224-1 SST warming at the onset of HS1 coincides with a decrease in $\delta^{13}\text{C}$ of the benthic foraminifera *Cibicides wuellerstorfi* measured on the same core (Voigt et al., 2017) (Fig. 2-5e,h). $\delta^{13}\text{C}$ of *C. wuellerstorfi* is a tracer of changes in deep water ventilation and hence provides an independent anchor for the onset of AMOC slowdown. The contemporaneous increase in $^{231}\text{Pa}/^{230}\text{Th}$ from the Bermuda Rise at 18 cal ka BP also points to AMOC reduction (McManus et al., 2004) (Fig. S6-3). We also find agreement between SST warming at GeoB16224-1 at the onset of HS1a, and the simulated northward heat transport in the Atlantic from the TraCE-21k transient model run (Liu et al., 2009), and $\delta^{18}\text{O}_{\text{sw-ivc}}$ (Fig. 2-5c,e,f) suggesting that the core location is sensitive to changes in SST induced by the bipolar seesaw.

Our results, however, document a sudden decrease in $\delta^{18}\text{O}_{\text{sw-ivc}}$ (Fig. 2-5c) at the onset of HS1b. Measurements of palmitic acid δD on GeoB16224-1 (Fig. 2-5d) independently confirm the decrease in SSS during HS1b. We argue that this freshening is primarily driven by a marked increase in total Amazon freshwater discharge. Evidence of a very weak AMOC during HS1b by both $^{231}\text{Pa}/^{230}\text{Th}$ from the Bermuda Rise (McManus et al., 2004) and $\delta^{13}\text{C}$ of *C. wuellerstorfi* from core GeoB16224-1 (Voigt et al., 2017) (Figs. 2-5g, S6-3), would suggest more heat and salt to be accumulated in the equatorial Atlantic, in contrast with the recorded reduced SSS (Fig. 2-5c,d).

Another suite of possible mechanisms that might have influenced the surface freshening during HS1b are based on reduced advection of low salinity waters to the

northwest caused by: (i) stronger wind stress resulting from enhanced NE trade winds and/or from an increase in the temperature gradient between ocean and land; and (ii) an intensified seasonal NBC retroflection (Wilson et al., 2011; Govin et al., 2014). Stronger water advection, caused by wind stress or current geometry, would likely increase vertical mixing between freshwater plume and the background water (Curtin, 1986; Hetland, 2005). However, the $\delta^{18}\text{O}$ of *G. sacculifer* in GeoB16224-1 do not record the abrupt freshening during HS1b (Fig. 2-5a). This suggests that the negative SSS anomaly was restricted to the surface layer, and that a strong stratification was maintained. We consider therefore unlikely that the abrupt freshening during HS1b is driven by changes in winds and current geometry.

This requires that *G. sacculifer* produces its calcite tests outside the low salinity plume. To test this assumption, we measured $\delta^{18}\text{O}_{\text{calcite}}$ of *G. sacculifer* and *G. ruber* from multicore GeoB16212-2 and compared it to the theoretical calcite $\delta^{18}\text{O}$ for a first order approximation of their calcification ranges. Generally, we find *G. sacculifer* to calcify deeper than *G. ruber* in the water column (Fig. 2-4). Whilst in some instances *G. sacculifer* and *G. ruber* calcify at comparable depths, *G. sacculifer* rarely calcifies within the low salinity plume, preferring normal saline conditions deeper in the water column. This is consistent with the findings of Farmer et al. (2007) who suggested that *G. ruber* has a calcification range encompassing the uppermost 30 m of the water column, whereas *G. sacculifer* has a calcification range near 30 m with a rather narrow 95 % confidence interval between 18 and 40 m. Similarly, Dekens et al. (2002) found that the best Mg/Ca calibration equation for *G. sacculifer* arises from using temperatures at 20 - 30 m water depth, confirming that the Mg/Ca of *G. sacculifer* records sub-surface temperatures. These findings indicate that *G. sacculifer* tends to inhabit the shallow subsurface below the low salinity surface water lens.

The $\delta^{18}\text{O}$ records of *G. ruber* and *G. sacculifer* from GeoB16224-1 (Fig. 2-5a), indicate that the freshwater signal during HS1b is only registered by *G. ruber* and not by *G. sacculifer*, that calcifies slightly deeper in the water column (Fig. 2-5a) (Chiessi et al., 2007; Steph et al., 2009). The fact that *G. sacculifer* does not register the negative SSS anomaly of HS1b indicates that a freshening process was confined to the surface (e.g., river runoff), with minimal vertical mixing, in a well stratified water column and a shallow low salinity plume. It is also likely that the freshwater signal recorded by *G. ruber* represents an underestimation, since calcification of *G. ruber* can take place below the plume as we observe in core GeoB16212-1 (Fig. 2-4).

2.5.3 Changes in continental hydroclimate and its effect on Amazon River freshwater discharge

The sediment reflectance record from Cariaco Basin indicates decreased terrigenous input during HS1b, due to reduced precipitation (Fig 7a) (Deplazes et al., 2013). The existing *n*-alkane $\delta^{13}\text{C}$ record of GeoB16224-1 (Häggi et al., 2017) indicates a slight increase in grass-savanna (C4) vegetation which likely occurred in the northernmost Amazon Basin during HS1b (Fig. 2-7c). More enriched *n*-alkanes $\delta^{13}\text{C}$ values from GeoB16224-1 correlate well with decreased rainfall over northern South America, as well as with the peak in Amazon freshwater discharge during HS1b (Fig. 2-7a-c). This provides a constraint on the maximum southward shift of the tropical rain belt, and suggests a rapid decrease in precipitation over northern South America due to shorter tropical rain belt residency (Peterson et al., 2000; Escobar et al., 2012; Deplazes et al., 2013). Since *n*-alkanes $\delta^{13}\text{C}$ indicate extensive forest coverage (C3 vegetation) for the Amazon Basin before HS1b, it is likely that the increase in Amazon lowland precipitation during HS1b could not lead to any significant increase in forest cover within the basin. However, an expansion of tropical forest indeed occurred to the southeast of the basin (i.e., northeastern Brazil; Dupont et al., 2010), but could not influence our record, since this region is situated outside of the Amazon Basin. The *n*-alkanes $\delta^{13}\text{C}$ signal primarily reflects an expansion of grass-savanna vegetation in the drier northernmost Amazon Basin during HS1b (Häggi et al. 2017; Hughen et al., 2004).

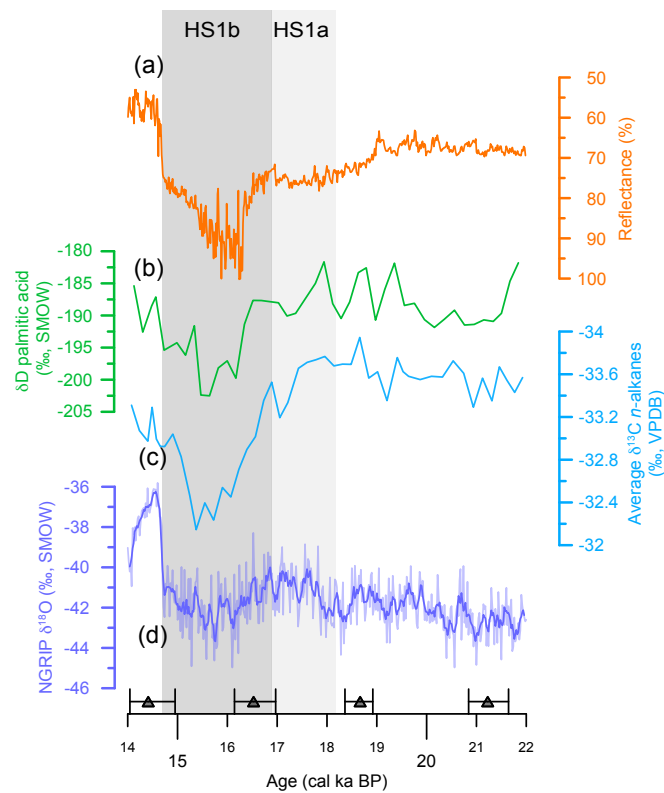


Figure 2-7. Selected atmospheric and continental indicators discussed in the text. (a) Reflectance record from Cariaco Basin (Deplazes et al., 2013). (b) δD on palmitic acid from core GeoB16224-1 (this study). (c) $\delta^{13}C$ *n*-alkanes from core GeoB16224-1 (Häggi et al., in revision). (d) $\delta^{18}O$ record from North Greenland Ice Core Project (NGRIP) (Andersen et al., 2004). Gray triangles over the horizontal axis show the calibrated radiocarbon ages and respective errors. The two Heinrich Stadial (HS) 1 phases (HS1a and HS1b) are indicated by the gray bars.

Over the tropical Andes, precipitation increased during HS1a, ca. 900 yr. before the negative SSS anomaly (Fig. 2-6b-d). This was sufficient to substantially increase erosion and cause the terrigenous input signal recorded at site GeoB16224-1 during HS1a (Fig. 2-6f-h), but insufficient to affect SSS. In contrast to the basin-internal shift of precipitation during HS1a, our $\delta^{18}O_{sw-ivc}$ record suggests higher total precipitation in the integrated Amazon catchment during HS1b. At the same time, erosion rates decreased, as the regions more susceptible to erosion (i.e., tropical Andes) (Gaillardet et al., 1997; Wittman et al., 2011) were now (i.e., HS1b) actually dryer than before (i.e., HS1a) (Fig. 2-6b-d). Moreover, the dense vegetation and flat topography of the humid lowlands did not allow for a comparable production of sediment relative to the Andean highlands.

The slowdown phase of the AMOC and concomitant increase in SST in the western equatorial Atlantic during HS1a was associated with a synchronous and proportional southward shift of the ITCZ and the tropical rain belt (Mulitza et al., 2017). The western

portion of the Amazon Basin also experienced a moderate increase in precipitation synchronous to the AMOC slowdown phase (HS1a) (McManus et al., 2004). Later on, when the AMOC reached minimum strength (HS1b) (McManus et al., 2004), our SSS records indicate enhanced freshwater discharge by the Amazon River (Fig. 2-5c,d), corroborating the suggestion of Mulitza et al. (2017). At this stage, the ITCZ and tropical rain belt were displaced to their southernmost positions, and the associated precipitation maximum over the Amazon Basin migrated from the tropical Andes towards central and eastern Amazonia.

The abrupt nature of the SSS change at the beginning HS1b (Fig. 2-5c,d) might also indicate the presence of positive feedback mechanisms by which an initial decrease in surface water density results in an increase in water stratification that prevents vertical mixing and enhances the retention of low density waters (i.e., Bowden and Din, 1966).

2.6 Conclusions

Isotope, inorganic and organic geochemical records from gravity core GeoB16224-1 resolve the internal structure of HS1 by integrating continental Amazonian hydrology and the hydrography of the adjacent ocean. During the first phase of HS1 from 18 to 16.9 cal ka BP, our records show an abrupt increase in SST concurrent with a prompt increase in the delivery of terrigenous sediments and organic matter to the western equatorial Atlantic. From 16.9 to 14 ka, the second phase of HS1, our records show a decrease in the discharge of sediments associated with decreased SSS in the western equatorial Atlantic. We suggest that the transition from the first to the second phase of HS1 was characterized by: (i) a migration of the main locus of precipitation from the tropical Andes to the central Amazonian plains and the cratonic Brazilian shield, greatly reducing the clastic sediment delivery by the Amazon River; (ii) a southward shift of the tropical rain belt and marked decrease of precipitation over northernmost South America including the northernmost sector of the Amazon Basin; and (iii) a strong reduction in of SSS on the western equatorial Atlantic despite the inefficiency of a sluggish AMOC to export salty waters to the northern hemisphere.

2.7 References

- Adkins, J.F., and Schrag, D.P., 2001, Pore fluid constraints on deep ocean temperature and salinity during the Last Glacial Maximum: *Geophysical Research Letters*, v. 28, no. 5, p. 771–774, doi: 10.1029/2000GL011597.
- Allison, M.A., Lee, M.T., Ogston, A.S., and Aller, R.C., 2000, Origin of Amazon mudbanks along the northeastern coast of South America: *Marine Geology*, v. 163, no. 1-4, p. 241–256, doi: 10.1016/S0025-3227(99)00120-6.
- Barker, S., Greaves, M., and Elderfield, H., 2003, A study of cleaning procedures used for foraminiferal Mg/Ca paleothermometry: *Geochemistry Geophysics Geosystems*, v. 4, no. 9, doi: 10.1029/2003GC000559.
- Barker, S., Diz, P., Vautravers, M.J., Pike, J., Knorr, G., Hall, I.R., and Broecker, W.S., 2009, Interhemispheric Atlantic seesaw response during the last deglaciation: *Nature*, v. 457, no. 7, p. 1097–1102, doi: 10.1038/nature07770.
- Blaauw, M., and Christen, J., 2011, Flexible Paleoclimate Age-Depth Models Using an Autoregressive Gamma Process: *Bayesian Analysis*, v. 6, no. 3, p. 457–474, doi: 10.1214/11-BA618.
- Blard, P.H., Sylvestre, F., Tripathi, A.K., Claude, C., Causse, C., Coudrain, A., Condom, T., Seidel, J.L., Vimeux, F., Moreau, C., Dumoulin, J.P., and Lavé, J., 2011, Lake highstands on the Altiplano (Tropical Andes) contemporaneous with Heinrich 1 and the Younger Dryas: new insights from ^{14}C , U-Th dating and $\delta^{18}\text{O}$ of carbonates: *Quaternary Science Reviews*, v. 30, no. 2, p. 3973–3989, doi: 10.1016/j.quascirev.2011.11.001.
- Bowden, K.F., and Din, S.H.S.E., 1966, Circulation, Salinity and River Discharge in the Mersey Estuary: *Geophysical Journal of the Royal Astronomical Society*, v. 10, no. 4, p. 383–399, doi: 10.1111/j.1365-246X.1966.tb03066.x.
- Broccoli, A.J., Dahl, K.A., and Stouffer, R.J., 2006, Response of the ITCZ to Northern Hemisphere cooling: *Geophysical Research Letters*, v. 33, no. 1, doi: 10.1029/2005GL024546.
- Broecker, W.S., 1998, Paleoocean circulation during the Last Deglaciation: A bipolar seesaw?: *Paleoceanography*, v. 13, no. 2, p. 119–121, doi: 10.1029/97PA03707.
- Cheng, H., Sinha, A., Cruz, F.W., Wang, X., Edwards, R.L., D'Horta, F.M., Ribas, C.C., Vuille, M., Stott, L.D., and Auler, A.S., 2013, Climate change patterns in Amazonia and biodiversity: *Nature Communications*, v. 4, p. 1411, doi: 10.1038/ncomms2415.
- Chiessi, C.M., Ulrich, S., Mulitza, S., Pätzold, J., and Wefer, G., 2007, Signature of the Brazil-Malvinas Confluence (Argentine Basin) in the isotopic composition of planktonic foraminifera from surface sediments: *Marine Micropaleontology*, v. 64, no. 1-2, p. 52–66, doi: 10.1016/j.marmicro.2007.02.002.
- Costa, J.B.C., Bemerguy, R.L., Hasui, Y., Borges, M. da S., 2001. Tectonics and palaeogeography along the Amazon river: *Journal South American Earth Science*, v. 14, p. 335–347.
- Cruz, F.W., Vuille, M., Burns, S.J., Wang, X., Cheng, H., Werner, M., Lawrence Edwards, R., Karmann, I., Auler, A.S., Nguyen, H., 2009. Orbitally driven east–west antiphasing of South American precipitation. *Nature Geoscience* 2, 210–214. doi:10.1038/ngeo444
- Curtin, T.B., 1986, Physical observation in the plume region of the Amazon River during peak discharge - II. Water masses: *Continental Shelf Research*, v. 6, p. 53–72, doi:10.1016/0278-4343(86)90053-1
- Dahl, K.A., Broccoli, A.J., and Stouffer, R.J., 2005, Assessing the role of North Atlantic freshwater forcing in millennial scale climate variability: a tropical Atlantic perspective: *Climate Dynamics*, v. 24, no. 4, p. 325–346, doi: 10.1007/s00382-004-0499-5.
- Dekens, P.S., Lea, D.W., Pak, D.K., and Spero, H.J., 2002, Core top calibration of Mg/Ca in tropical foraminifera: Refining paleotemperature estimation: *Geochemistry Geophysics Geosystems*, v. 3, no. 4, p. 1–29, doi: 10.1029/2001GC000200.
- Deplazes, G., Lückge, A., Peterson, L.C., Timmermann, A., Hamann, Y., Hughen, K.A., Röhl, U., Laj, C., Cane, M.A., Sigman, D.M., and Haug, G.H., 2013, Links between tropical rainfall and North Atlantic climate during the last glacial period: *Nature Geoscience*, v. 6, no. 3, p. 213–217, doi: 10.1038/ngeo1712.
- Dupont, L.M., Schlütz, F., and Ewah, C.T., 2010, Two-step vegetation response to enhanced precipitation in Northeast Brazil during Heinrich event 1: *Global Change Biology*, v. 16, no. 6, p. 1647–1660, doi: 10.1111/j.1365-2486.2009.02023.x.

- Escobar, J., Hodell, D.A., Brenner, M., Curtis, J.H., Gilli, A., Mueller, A.D., Anselmetti, F.S., Ariztegui, D., Grzesik, D.A., Pérez, L., Schwalb, A., and Guilderson, T.P., 2012, A ~43-ka record of paleoenvironmental change in the Central American lowlands inferred from stable isotopes of lacustrine ostracods: *Quaternary Science Reviews*, v. 37, p. 92–104, doi: 10.1016/j.quascirev.2012.01.020.
- Farmer, E.C., Kaplan, A., de Menocal, P.B., and Lynch-Stieglitz, J., 2007, Corroborating ecological depth preferences of planktonic foraminifera in the tropical Atlantic with the stable oxygen isotope ratios of core top specimens: *Paleoceanography*, v. 22, no. 3, doi: 10.1029/2006PA001361.
- Fietz, S., Martínez-García, A., Hugué, C., Rueda, G., and Rosell-Melé, A., 2011, Constraints in the application of the Branched and Isoprenoid Tetraether index as a terrestrial input proxy: *Journal of Geophysical Research - Oceans*, v. 116, no. C10, p. C10032–9, doi: 10.1029/2011JC007062.
- Gaillardet, J., Dupre, B., Allegre, C.J., and Negrel, P., 1997, Chemical and physical denudation in the Amazon River basin: *Chemical Geology*, v. 142, no. 3–4, p. 141–173, doi: 10.1016/S0009-2541(97)00074-0.
- Gibbs, R.J., 1967, Amazon River: Environmental Factors That Control Its Dissolved and Suspended Load: *Science*, v. 156, no. 3, p. 1734–1737, doi: 10.1126/science.156.3783.1734.
- Goes, J.I., Gomes, H.D.R., Chekalyuk, A.M., Carpenter, E.J., Montoya, J.P., Coles, V.J., Yager, P.L., Berelson, W.M., Capone, D.G., Foster, R.A., Steinberg, D.K., Subramaniam, A., and Hafez, M.A., 2014, Influence of the Amazon River discharge on the biogeography of phytoplankton communities in the western tropical north Atlantic: *Progress in Oceanography*, v. 120, no. C, p. 29–40, doi: 10.1016/j.pocean.2013.07.010.
- Govin, A., Holzwarth, U., Heslop, D., Keeling, L.F., Zabel, M., Mulitza, S., Collins, J.A., and Chiessi, C.M., 2012, Distribution of major elements in Atlantic surface sediments (36 degrees N–49 degrees S): Imprint of terrigenous input and continental weathering: *Geochemistry Geophysics Geosystems*, v. 13, no. 1, doi: 10.1029/2011GC003785.
- Govin, A., Chiessi, C.M., Zabel, M., Sawakuchi, A.O., Heslop, D., Hörner, T., Zhang, Y., and Mulitza, S., 2014, Terrigenous input off northern South America driven by changes in Amazonian climate and the North Brazil Current retroflexion during the last 250 ka: *Climate of the Past*, v. 10, no. 2, p. 843–862, doi: 10.5194/cp-10-843-2014.
- Häggi, C., Chiessi, C., and Schefuß, E., 2015, Testing the D/H ratio of alkenones and palmitic acid as salinity proxies in the Amazon Plume: *Biogeosciences Discussions*, v. 12, no. 16, p. 13859–13885, doi: 10.5194/bgd-12-13859-2015.
- Häggi, C., Sawakuchi, A.O., Chiessi, C.M., Mulitza, S., Mollenhauer, G., Sawakuchi, H.O., Baker, P.A., Zabel, M., and Schefuß, E., 2016, Origin, transport and deposition of leaf-wax biomarkers in the Amazon Basin and the adjacent Atlantic: *Geochimica et Cosmochimica Acta*, v. 192, p. 149–165, doi: 10.1016/j.gca.2016.07.002.
- Häggi, C., Chiessi, C. M., Merkel, U., Mulitza, S., Prange, M., Schulz, M., Schefuß, E., 2017, Response of the Amazon rainforest to late Pleistocene climate variability: *Earth and Planetary Science Letters*, v. 479, p. 50–59, doi: 10.1016/j.epsl.2017.09.013
- Hetland, R.D., 2005, Relating River Plume Structure to Vertical Mixing. *Journal of Physical Oceanography*, v. 35, p. 1667–1688, doi:10.1175/JPO2774.1
- Hopmans, E.C., Schouten, S., Pancost, R.D., van der Meer, M., and Damste, J., 2000, Analysis of intact tetraether lipids in archaeal cell material and sediments by high performance liquid chromatography/atmospheric pressure chemical ionization mass spectrometry: *Rapid Communications in Mass Spectrometry*, v. 14, no. 7, p. 585–589, doi: 10.1002/(SICI)1097-0231(20000415).
- Hughen, K.A., Eglinton, T.I., Xu, L., and Makou, M., 2004, Abrupt tropical vegetation response to rapid climate changes: *Science*, v. 304, no. 5679, p. 1955–1959, doi: 10.1126/science.1092995.
- Hut, G., 1987, Stable isotope reference samples for geochemical and hydrological investigations: *Consultants Group Meeting IAEA*, p. 42.
- Jaeschke, A., Rühlemann, C., Arz, H., Heil, G., and Lohmann, G., 2007, Coupling of millennial-scale changes in sea surface temperature and precipitation off northeastern Brazil with high-latitude climate shifts during the last glacial period: *Paleoceanography*, v. 22, no. 4, doi: 10.1029/2006PA001391.

- Kanner, L.C., Burns, S.J., Cheng, H., and Edwards, R.L., 2012, High-latitude forcing of the South American summer monsoon during the Last Glacial: *Science*, v. 335, no. 6068, p. 570–573, doi: 10.1126/science.1213397.
- Kisakürek, B., A. Eisenhauer, F. Böhm, D. Garbe-Schönberg, and J. Erez, 2008, Controls on shell Mg/Ca and Sr/Ca in cultured planktonic foraminifera, *Globigerinoides ruber* (white): *Earth Planetary Science Letters*, v. 273, no. 3–4, p. 260–269, doi:10.1016/j.epsl.2008.06.026.
- Kuehl, S.A., Demaster, D.J., and Nittrouer, C.A., 1986, Nature of sediment accumulation on the Amazon continental shelf: *Continental Shelf Research*, v. 6, no. 1-2, p. 209–225, doi: 10.1016/0278-4343(86)90061-0.
- Kuhnert, H., and Mulitza, S., 2011, Multidecadal variability and late medieval cooling of near-coastal sea surface temperatures in the eastern tropical North Atlantic: *Paleoceanography*, v. 26, no. 4, doi: 10.1029/2011PA002130.
- Lambeck, K., Rouby, H., Purcell, A., Sun, Y., and Sambridge, M., 2014, Sea level and global ice volumes from the Last Glacial Maximum to the Holocene: *Proceedings of the National Academy of Sciences*, v. 111, no. 43, p. 15296–15303, doi: 10.1073/pnas.1411762111.
- Lentz, S.J., 1995, Seasonal variations in the horizontal structure of the Amazon Plume inferred from historical hydrographic data: *Journal of Geophysical Research: Oceans* (1978–2012), v. 100, no. C2, p. 2391–2400, doi: 10.1029/94JC01847.
- Levitus, S., Antonov, J.I., Baranova, O.K., Boyer, T.P., Coleman, C.L., Garcia, H.E., Grodsky, A.I., Johnson, D.R., Locarnini, R.A., Mishonov, A.V., Reagan, J.R., Sazama, C.L., Seidov, D., Smolyar, I., et al., 2013, The World Ocean Database: *Data Science Journal*, v. 12, no. 0, p. WDS229–WDS234, doi: 10.2481/dsj.wds-041.
- Liu, Z., Otto-Bliesner, B.L., He, F., Brady, E.C., Tomas, R., Clark, P.U., Carlson, A.E., Lynch-Stieglitz, J., Curry, W., Brook, E., Erickson, D., Jacob, R., Kutzbach, J., and Cheng, J., 2009, Transient Simulation of Last Deglaciation with a New Mechanism for Bolling-Allerod Warming: *Science*, v. 325, no. 5938, p. 310–314, doi: 10.1126/science.1171041.
- Lukas, R., and Lindstrom, E., 1991, The Mixed Layer of the Western Equatorial Pacific-Ocean: *Journal of Geophysical Research - Oceans*, v. 96, no. C7, p. 3343–3357, doi: 10.1029/91JC01256.
- Marshall, J., Donohoe, A., Ferreira, D., and McGee, D., 2013, The ocean's role in setting the mean position of the Inter-Tropical Convergence Zone: *Climate Dynamics*, v. 42, no. 7-8, p. 1967–1979, doi: 10.1007/s00382-013-1767-z.
- Maslin, M.A., and Burns, S.J., 2000, Reconstruction of the Amazon Basin Effective Moisture Availability over the Past 14,000 Years: *Science*, v. 290, no. 5, p. 2285–2287, doi: 10.1126/science.290.5500.2285.
- Maslin, M.A., Ettwein, V.J., Wilson, K.E., Guilderson, T.P., Burns, S.J., and Leng, M.J., 2011, Dynamic boundary-monsoon intensity hypothesis: evidence from the deglacial Amazon River discharge record: *Quaternary Science Reviews*, v. 30, no. 2, p. 3823–3833, doi: 10.1016/j.quascirev.2011.10.007.
- Mayorga, E., Aufdenkampe, A.K., Masiello, C.A., Krusche, A.V., Hedges, J.I., Quay, P.D., Richey, J.E., and Brown, T.A., 2005, Young organic matter as a source of carbon dioxide outgassing from Amazonian rivers: *Nature*, v. 436, no. 7050, p. 538–541, doi: 10.1038/nature03880.
- McGee, D., Donohoe, A., Marshall, J., and Ferreira, D., 2014, Changes in ITCZ location and cross-equatorial heat transport at the Last Glacial Maximum, Heinrich Stadial 1, and the mid-Holocene: *Earth and Planetary Science Letters*, v. 390, no. C, p. 69–79, doi: 10.1016/j.epsl.2013.12.043.
- McManus, J.F., François, R., Gherardi, J.M., Keigwin, L.D., and Brown-Leger, S., 2004, Collapse and rapid resumption of Atlantic meridional circulation linked to deglacial climate changes: *Nature*, v. 428, no. 6985, p. 834–837, doi: 10.1038/nature02494.
- Meade, R.H., Dunne, T., Richey, J.E., DE M Santos, U., and Salati, E., 1985, Storage and remobilization of suspended sediment in the lower Amazon river of Brazil.: *Science*, v. 228, no. 4698, p. 488–490, doi: 10.1126/science.228.4698.488.
- Mix, A.C., Morey, A.E., and Pisias, N.G., 1999, Foraminiferal faunal estimates of paleotemperature: Circumventing the no-analog problem yields cool ice age tropics: *Paleoceanography*, v. 14, p.350-359, doi: 10.1029/1999PA900012

- Mohtadi, M., Prange, M., Oppo, D.W., De Pol-Holz, R., Merkel, U., Zhang, X., Steinke, S., and Lückge, A., 2014, North Atlantic forcing of tropical Indian Ocean climate: *Nature*, v. 509, no. 7498, p. 76–80, doi: 10.1038/nature13196.
- Mosblech, N.A.S., Bush, M.B., Gosling, W.D., Hodell, D., Thomas, L., van Calsteren, P., Correa-Metrio, A., Valencia, B.G., Curtis, J., and van Woesik, R., 2012, North Atlantic forcing of Amazonian precipitation during the last ice age: *Nature Geoscience*, v. 5, no. 11, p. 817–820, doi: 10.1038/ngeo1588.
- Mounier, S., Braucher, R., and Benaim, J.Y., 1999, Differentiation of organic matter's properties of the Rio Negro basin by cross-flow ultra-filtration and UV-spectrofluorescence: *Water Research*, v. 33, no. 10, p. 2363–2373, doi: 10.1016/S0043-1354(98)00456-4.
- Mulitza, S., Boltovskoy, D., Donner, B., Meggers, H., PAUL, A., and Wefer, G., 2003, Temperature: $\delta^{18}\text{O}$ relationships of planktonic foraminifera collected from surface waters: *Palaeogeography, Palaeoclimatology, Palaeoecology*, v. 202, no. 1-2, p. 143–152, doi: 10.1016/s0031-0182(03)00633-3.
- Mulitza, S., Chiessi, C.M., Cruz, A.P.S., Frederichs, T.W., Gomes, J.G., Gurgel, M.H.C., Haberkern, J., Huang, E., Jovane, L., Kuhnert, H., Pittauerová, D., Reiners, S.J., Roud, S.C., Schefuß, E., et al., 2013, Response of Amazon sedimentation to deforestation, land use and climate variability. Cruise No. MSM20/3 (February 19–March 11, 2012), Recife (Brazil)–Bridgetown (Barbados). MARIA S. MERIAN-Berichte, MSM20/3: DFG Senatskommission für Ozeanographie.
- Mulitza, S., Chiessi, C.M., Schefuß, E., Lippold, J., Wichmann, D., Antz, B., Mackensen, A., PAUL, A., Prange, M., Rehfeld, K., Werner, M., Bickert, T., Frank, N., Kuhnert, H., et al., 2017, Synchronous and proportional deglacial changes in Atlantic meridional overturning and northeast Brazilian precipitation: *Paleoceanography*, v. 32, no. 6, p. 622–633, doi: 10.1002/2017PA003084.
- Muller-Karger, F.E., McClain, C.R., and Richardson, P.L., 1988, The dispersal of the Amazon's water: *Nature*, v. 333, no. 6168, p. 56–59, doi: 10.1038/333056a0.
- Nace, T.E., Baker, P.A., Dwyer, G.S., Silva, C.G., Rigsby, C.A., Burns, S.J., Giosan, L., Otto-Bliesner, B., Liu, Z., and Zhu, J., 2014, The role of North Brazil Current transport in the paleoclimate of the Brazilian Nordeste margin and paleoceanography of the western tropical Atlantic during the late Quaternary: *Palaeogeography, Palaeoclimatology, Palaeoecology*, v. 415, p. 3–13, doi: 10.1016/j.palaeo.2014.05.030.
- Niebler, H.S., Arz, H.W., Donner, B., Mulitza, S., Pätzold, J., and Wefer, G., 2003, Sea surface temperatures in the equatorial and South Atlantic Ocean during the Last Glacial Maximum (23-19 ka): *Paleoceanography*, v. 18, no. 3, 1069, doi: 10.1029/2003PA000902.
- Peterson, L.C., Haug, G.H., Hughen, K.A., and Röhl, U., 2000, Rapid changes in the hydrologic cycle of the tropical Atlantic during the last glacial.: *Science*, v. 290, no. 5498, p. 1947–1951, doi: 10.1126/science.290.5498.1947.
- Peterson, R.G., and Stramma, L., 1991, Upper-level circulation in the South Atlantic Ocean: Progress in oceanography, doi: 10.1016/0079-6611(91)90006-8.
- Quay, P.D., Wilbur, D.O., Richey, J.E., Hedges, J.I., Devol, A.H., and Victoria, R., 1992, Carbon Cycling in the Amazon River - Implications From the ^{13}C Compositions of Particles and Solutes: *Limnology and Oceanography*, v. 37, no. 4, p. 857–871, doi: 10.4319/lo.1992.37.4.0857
- Regenberg, M., Steph, S., Nürnberg, D., Tiedemann, R., and Garbe-Schönberg, D., 2009, Calibrating Mg/Ca ratios of multiple planktonic foraminiferal species with $\delta^{18}\text{O}$ -calcification temperatures: Paleothermometry for the upper water column: *Earth and Planetary Science Letters*, v. 278, no. 3-4, p. 324–336, doi: 10.1016/j.epsl.2008.12.019.
- Reimer, P.J., Bard, E., Bayliss, A., Beck, J.W., Blackwell, P.G., Bronk, R.C., Buck, C.E., Cheng, H., Edwards, R.L., Friedrich, M., Grootes, P.M., Guilderson, T.P., Hafllidason, H., Hajdas, I., et al., 2013, IntCal13 and Marine13 radiocarbon age calibration curves 0-50,000 years cal BP: *Radiocarbon*, v. 55, no. 4, p. 1869–1887, doi: 10.2458/azu_js_rc.55.16947.
- Rühlemann, C., Mulitza, S., Muller, P.J., Wefer, G., and Zahn, R., 1999, Warming of the tropical Atlantic Ocean and slowdown of thermohaline circulation during the last deglaciation: *Nature*, v. 402, no. 6761, p. 511–514, doi: 10.1038/990069
- Salisbury, J., Vandemark, D., Campbell, J., Hunt, C., Wissler, D., Reul, N., and Chapron, B., 2011, Spatial and temporal coherence between Amazon River discharge, salinity, and light absorption by colored organic

- carbon in western tropical Atlantic surface waters: *Journal of Geophysical Research - Oceans*, v. 116, p. C00H02–14, doi: 10.1029/2011JC006989.
- Schmidt, G.A., 1999, Forward modelling of carbonate proxy data from planktonic foraminifera using oxygen isotope tracers in a global ocean model: *Paleoceanography*, v. 14, p. 482–497, doi:10.1029/1999PA900025
- Schmuker, B., and Schiebel, R., 2002, Planktic foraminifers and hydrography of the eastern and northern Caribbean Sea: *Marine Micropaleontology*, v. 46, no. 3-4, p. 387–403, doi: 10.1016/S0377-8398(02)00082-8.
- Schneider, T., Bischoff, T., and Haug, G.H., 2014, Migrations and dynamics of the intertropical convergence zone: *Nature*, v. 513, no. 7516, p. 45–53, doi: 10.1038/nature13636.
- Schouten, S., Huguët, C., Hopmans, E.C., and Kienhuis, M., 2007, Improved analytical methodology and constraints on analysis of the TEX86 paleothermometer by high performance liquid chromatography/atmospheric pressure chemical ionization-mass spectrometry.: *Analytical Chemistry*, v. 79, p. 2940–2944, doi: 10.1029/2006GC001306/full.
- Schrag, D.P., Adkins, J.F., McIntyre, K., Alexander, J.L., Hodell, D.A., Charles, C.D., and McManus, J.F., 2002, The oxygen isotopic composition of seawater during the Last Glacial Maximum: *Quaternary Science Reviews*, v. 21, no. 1, p. 331–342, doi: 10.1016/S0277-3791(01)00110-X.
- Stainforth, R.M., Lamb, J.L., Luterbacher, H.P., Beard, J.H., and Jeffords, R., 1975, Cenozoic planktonic foraminiferal zonation and characteristics of index forms: *The University of Kansas Paleontological Contributions*, v. 62, p. 1–425.
- Stanford, J.D., Rohling, E.J., Bacon, S., Roberts, A.P., Grousset, F.E., Bolshaw, M., 2011, A new concept for the paleoceanographic evolution of Heinrich event 1 in the North Atlantic. *Quaternary Science Review*, v. 30, p. 1047–1066, doi:10.1016/j.quascirev.2011.02.003
- Steph, S., Regenberg, M., Tiedemann, R., Mulitza, S., and Nürnberg, D., 2009, Planktonic foraminiferal $\delta^{18}O$ values and apparent calcification depths of core-top samples along an east-west transect across the tropical Atlantic/Caribbean core-tops: Implications for reconstructing upper ocean stratification: *Marine Micropaleontology*, v. 71, p. 1–19, doi: 10.1594/pangaea.742421.
- Stramma, L., Rhein, M., Brandt, P., Dengler, M., Boning, C., and Walter, M., 2005, Upper ocean circulation in the western tropical Atlantic in boreal fall 2000: *Deep Sea Research Part I: Oceanographic Research Papers*, v. 52, no. 2, p. 221–240, doi: 10.1016/j.dsr.2004.07.021.
- Street-Perrott, F.A., Perrott, R.A., 1990, Abrupt climate fluctuations in the tropics: the influence of Atlantic Ocean circulation: *Nature*, v.343, p. 607–612, doi:10.1038/343607a0
- Stríkis, N.M., Chiessi, C.M., Cruz, F.W., Vuille, M., Cheng, H., Souza Barreto, E.A., Mollenhauer, G., Kasten, S., Karmann, I., Edwards, R.L., Bernal, J.P., and Sales, H.D.R., 2015, Timing and structure of Mega-SACZ events during Heinrich Stadial 1: *Geophysical Research Letters*, v. 42, no. 1, p. 5477–5484, doi: 10.1002/2015GL064048.
- Thompson, L.G., Mosleythompson, E., Davis, M.E., Lin, P.N., Henderson, K.A., Coledai, J., Bolzan, J.F., and Liu, K.B., 1995, Late-Glacial Stage and Holocene Tropical Ice Core Records From Huascarán, Peru: *Science*, v. 269, no. 5220, p. 46–50.
- Timm, O., and Timmermann, A., 2007, Simulation of the last 21000 years using accelerated transient boundary conditions: *Journal of Climate*, v. 20, no. 17, p. 4377–4401, doi: 10.1175/JCLI4237.1.
- Trend-Staid, M., and Prell, W.L., 2002, Sea surface temperature at the Last Glacial Maximum: A reconstruction using the modern analog technique: *Paleoceanography*, v. 17, no. 4, p. 1-18, doi: 10.1029/2000PA000506.
- Voigt, I., Cruz, A. P. S., Mulitza, S., Chiessi, C. M., Mackensen, A., Lippold, J., Antz, B., Zabel, M., Zhang, Y., Barbosa, C. F., Tisserand, A. A., 2017, Variability in mid-depth ventilation of the western Atlantic Ocean during the last deglaciation: *Paleoceanography*, doi: 10.1002/2017PA003095
- Volbers, A., and Henrich, R., 2004, Calcium carbonate corrosiveness in the South Atlantic during the Last Glacial Maximum as inferred from changes in the preservation of *Globigerina bulloides*: A proxy to determine deep-water circulation patterns?: *Marine Geology*, v. 204, no. 1-2, p. 43–57, doi: 10.1016/S0025-3227(03)00372-4.

- Wang, L.J., 2000, Isotopic signals in two morphotypes of *Globigerinoides ruber* (white) from the South China Sea: implications for monsoon climate change during the last glacial cycle: *Palaeogeography, Palaeoclimatology, Palaeoecology*, v. 161, no. 3-4, p. 381–394, doi: 10.1016/S0031-0182(00)00094-8.
- Wang, X., Auler, A.S., Edwards, R.L., Cheng, H., and Cristalli, P.S., 2004, Wet periods in northeastern Brazil over the past 210 kyr linked to distant climate anomalies: *Nature*, v. 432, no. 7018, p. 740–743, doi: 10.1038/nature03067.
- Wang, X., Edwards, R.L., Auler, A.S., Cheng, H., Kong, X., Wang, Y., Cruz, F.W., Dorale, J.A., Chiang, H.-W., 2017, Hydroclimate changes across the Amazon lowlands over the past 45,000 years: *Nature*, p. 541, v. 204–207, doi:10.1038/nature20787
- Weldeab, S., Schneider, R.R., and Kölling, M., 2006, Deglacial sea surface temperature and salinity increase in the western tropical Atlantic in synchrony with high latitude climate instabilities: *Earth and Planetary Science Letters*, v. 241, no. 3-4, p. 699–706, doi: 10.1016/j.epsl.2005.11.012.
- Wilson, K.E., Maslin, M.A., and Burns, S.J., 2011, Evidence for a prolonged retroflexion of the North Brazil Current during glacial stages: *Palaeogeography, Palaeoclimatology, Palaeoecology*, v. 301, no. 1-4, p. 86–96, doi: 10.1016/j.palaeo.2011.01.003.
- Wittmann, H., Blanckenburg, von, F., Maurice, L., Guyot, J.L., Filizola, N., and Kubik, P.W., 2011, Sediment production and delivery in the Amazon River basin quantified by in situ-produced cosmogenic nuclides and recent river loads: *Geological Society of America Bulletin*, v. 123, no. 5-6, p. 934–950, doi: 10.1130/B30317.1.
- Zell, C., Kim, J.-H., Abril, G., Sobrinho, R.L., Dorhout, D., Moreira-Turcq, P., and Damsté, J.S.S., 2013, Impact of seasonal hydrological variation on the distributions of tetraether lipids along the Amazon River in the central Amazon basin: implications for the MBT/CBT paleothermometer and the BIT index: *Frontiers in Microbiology*, v. 4, doi: 10.3389/fmicb.2013.00228.
- Zhang, Y., Chiessi, C.M., Mulitza, S., Zabel, M., Trindade, R.I.F., Hollanda, M.H.B.M., Dantas, E.L., Govin, A., Tiedemann, R., and Wefer, G., 2015, Origin of increased terrigenous supply to the NE South American continental margin during Heinrich Stadial 1 and the Younger Dryas: *Earth and Planetary Science Letters*, v. 432, p. 1–8, doi: 10.1016/j.epsl.2015.09.054.
- Zhang, Y., Zhang, X., Chiessi, C.M., Mulitza, S., Zhang, X., Lohmann, G., Prange, M., Behling, H., Zabel, M., Govin, A., Sawakuchi, A.O., Cruz, F.W., and Wefer, G., 2016, Equatorial Pacific forcing of western Amazonian precipitation during Heinrich Stadial 1: *Scientific Reports*, v. 6, doi: 10.1038/srep35866.
- Zhang, Y., Chiessi, C.M., Mulitza, S., Sawakuchi, A.O., Häggi, C., Zabel, M., Schefuß, E., Crivellari, S., Wefer, G., 2017, Different precipitation patterns across tropical South America during Heinrich and Dansgaard-Oeschger stadials: *Quaternary Science Reviews*, v. 177, p. 1-9, doi:10.1016/j.quascirev.2017.10.012

Chapter 3 . Different precipitation patterns across tropical South America during Heinrich and Dansgaard-Oeschger stadials

Yancheng Zhang^{1,*}, Cristiano M. Chiessi², Stefan Mulitza¹, André O. Sawakuchi³,
Christoph Häggi¹, Matthias Zabel¹, Rodrigo C. Portilho-Ramos³, Enno Schefuß¹,
Stefano Crivellari³, Gerold Wefer¹

¹ MARUM–Center for Marine Environmental Sciences, University of Bremen, Germany

² School of Arts, Sciences and Humanities, University of São Paulo, São Paulo, Brazil

³ Institute of Geosciences, University of São Paulo, São Paulo, Brazil

Published in *Quaternary Science Reviews* (2017) 177, 1-9

Disclaimer:

Although the work reported in this publication is portrayed as a chapter rather than an appendix, this choice was motivated by the pivotal role of this work in the development of the research of this thesis. This manuscript involved a substantial contribution by the candidate in the development of the interpretation and construction of the text.

Abstract:

Detailed knowledge about tropical South American precipitation patterns during Heinrich (H) and Dansgaard-Oeschger (DO) stadials provides relevant insights into the possible evolution of Amazonian hydroclimate under future climate change. Sediment core GeoB16224-1 (ca. 7° N), raised from a site in the continental slope off French Guiana in western equatorial Atlantic under the influence of the Amazon River discharge, documents the impacts of H and DO stadials on both inorganic (i.e., Fe/Ca record) and organic (i.e., alkenone C₃₇ concentration and C₃₇/ C₃₈ ratio) geochemistry between 41 and 13 ka BP. Our results show millennial-scale covariations of increased Fe/Ca values with decreased C₃₇ concentration and C₃₇/ C₃₈ ratios during H and DO stadials. Comparing our high temporal resolution data with previously published records from ca. 17° N to 4° S, we are able to differentiate the influence of H and DO stadials upon tropical South American precipitation. We find that records under the influence of the South American summer monsoon (e.g., western Amazon) and the northern edge of the Intertropical Convergence Zone (ITCZ) (e.g., northernmost South America) exhibit strong climate shifts during both H and DO stadials, but regions under the influence of the southern edge of the ITCZ (e.g., northeastern Brazil) experience a weaker reaction during DO stadials than during H stadials.

3.1 Introduction

Greenland ice cores document a succession of millennial-scale cold intervals during the last glacial period that were recognized as Heinrich (H) and Dansgaard-Oeschger (DO) stadials (Dansgaard et al., 1993). In general, H stadials are characterized by the presence of massive layers of ice-rafted debris (IRD) in the North Atlantic (Heinrich, 1988; Bond et al., 1992), while DO stadials are typically associated with cooling phases without the occurrence of IRD layers (e.g., Svensson et al., 2006; Sanchez Goni and Harrison, 2010). H and DO stadials, although probably triggered by different mechanisms (e.g., Alvarez-Solas et al., 2010; Zhang et al., 2014a), are both believed to involve decreases in the strength of the Atlantic meridional overturning circulation (AMOC) (e.g., Clark et al., 2002; Henry et al., 2016). Such decreases in AMOC strength, which were characterized by large amplitudes during H stadials but moderate amplitudes during DO stadials (e.g., EPICA Project Members, 2006; Böhm et al., 2015; Henry et al., 2016), had a fundamental role in regulating millennial-scale tropical climate change (e.g., Voelker 2002) like abrupt reorganizations of the monsoon systems over Asia (Wang et al., 2001; Burns et al., 2003) and North America (Asmerom et al., 2010; Wagner et al., 2010).

Millennial-scale AMOC slowdowns also influenced the Intertropical Convergence Zone (ITCZ) and the South American summer monsoon (SASM) (Fig.1a-b), and thus precipitation over tropical South America. For a greatly weakened AMOC during H stadials (McManus et al., 2004; Böhm et al., 2015), numerous studies demonstrated a precipitation decrease over northernmost South America (e.g., Peterson et al., 2000; Deplazes et al., 2013), and an increase over northeastern (NE) Brazil (e.g., Arz et al., 1998; Wang et al., 2004; Jaeschke et al., 2007) and south eastern (SE) Brazil (e.g., Cruz et al., 2005; Wang et al., 2006), in the tropical Andes (e.g., Baker and Fritz, 2015) as well as over the western (e.g., Kanner et al., 2012; Mosblech et al., 2012; Cheng et al., 2013a) and eastern Amazon Basin (e.g., Wang et al., 2017). By contrast, only a few records showed millennial-scale variations of the hydrological cycle during DO stadials, e.g., wet conditions at Lake Titicaca in the central Andes (Fritz et al., 2010). The sparse hydroclimate records of the DO stadials across tropical South America hinder a thorough understanding of their impacts. Importantly, the AMOC reduction under anthropogenic greenhouse-gas-derived climate scenarios, projected to be 20-40% until the end of this century (e.g., Cheng et al., 2013b; Rahmstorf et al., 2015), would be comparable with the reconstructed amplitude of AMOC slowdowns during DO

stadials (e.g., Zhang et al., 2014a, b). Further knowledge about the regional patterns of tropical South American precipitation during DO stadials is thus of utmost importance to estimate future changes in Amazon hydroclimate that strongly influences Amazonian ecosystems (e.g., Malhi et al., 2008, 2009).

In this paper, we disentangle the regional responses of tropical South American precipitation to H and DO stadials. First, we determine prominent covariations of inorganic (i.e., Fe/Ca) and organic (i.e., alkenone C₃₇ concentration and C₃₇/C₃₈ ratio) geochemical compositions throughout H and DO stadials from 41 to 13 ka BP (calibrated kilo annum before present) by analyzing sediment core GeoB16224-1 raised from a location under the influence of the Amazon River discharge (see section 3.2.1). Second, we compare our results with five high temporal resolution paleo-hydrological records along a meridional transect across Central and South America (between ca. 17°N and 4°S) to unravel the spatial characteristics of terrestrial precipitation changes during H and DO stadials. Our results show different amplitudes of precipitation increases over NE Brazil across H and DO stadials, which were probably attributed to the different magnitudes of the corresponding AMOC slowdowns.

3.2 Material and methods

3.2.1 Sediment core GeoB16224-1

The 760-cm long gravity core GeoB16224-1 (6°39.38' N, 52°04.99' W, 2510 m water depth) was retrieved from the continental slope off French Guiana during RV MS Merian cruise MSM20/3 (Fig. 1; Mulitza et al., 2013). At this site, prominent seasonal variations of sea surface salinity, e.g., between March (ca. 36 psu) and September (ca. 34.5 psu) (Zweng et al., 2013; Fig. 3-1a-b), indicate the influence of Amazon freshwater discharge (e.g., Müller-Karger et al., 1988; Lentz, 1995). Large amounts (ca. 250×10^6 t yr⁻¹) of fluvial sediments from the Amazon River mouth are also transported by the North Brazil Current (NBC) towards the continental margin off French Guiana and beyond (e.g., Allison et al., 2000). Overall, core site GeoB16224-1 is suitably located to document variations in Amazon discharge during millennial-scale cold climate intervals at northern high latitudes (Zhang et al., 2015).

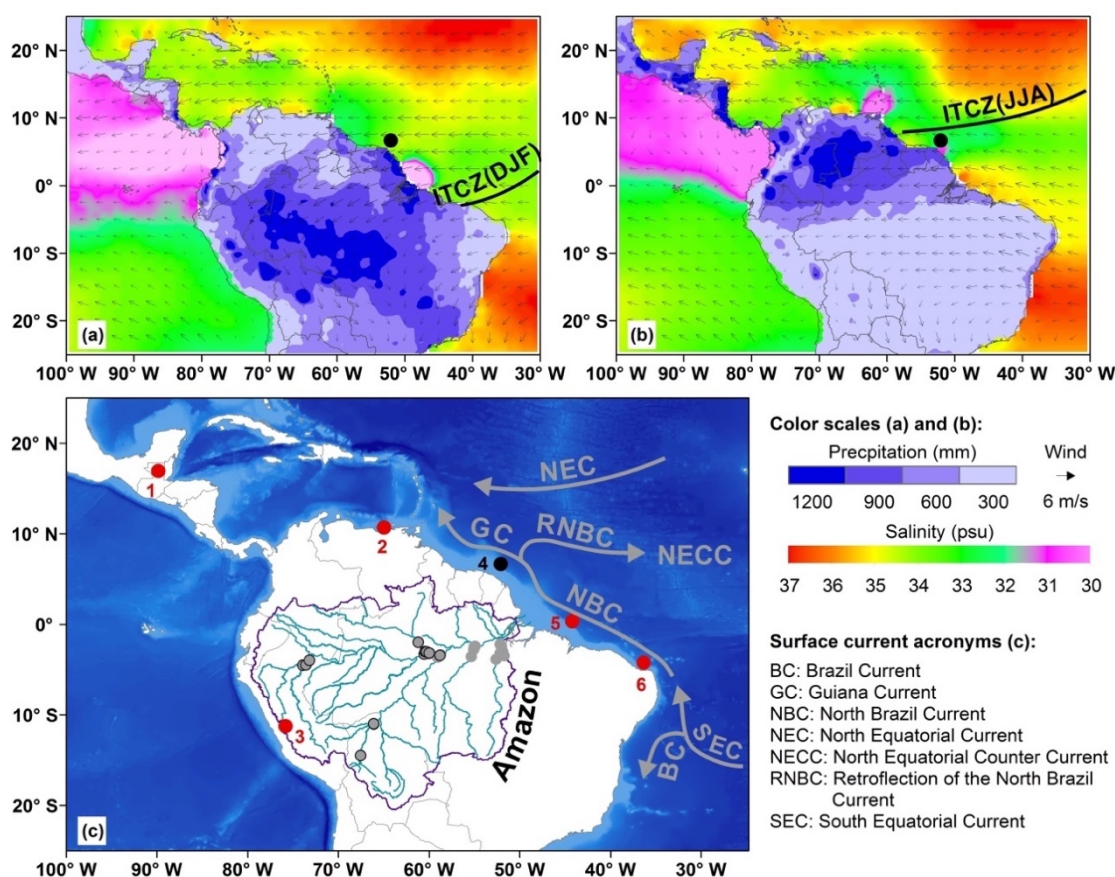


Figure 3-1. Location of paleorecords and environmental setting over tropical South America and the adjacent oceans. Monthly averaged terrestrial precipitation (1981e2010) from the University of Delaware (<http://climate.geog.udel.edu/~climate/>), wind field from the NOAA/OAR/ESRL PSD (<http://www.esrl.noaa.gov/psd/>) and mean sea surface salinity (SSS) from the World Ocean Atlas 2013 (Zweng et al., 2013) are given for (a) austral summer (December-January-February (DJF) for precipitation, March for SSS) and (b) austral winter (June- July-August (JJA) for precipitation, September for SSS). The schematic positions of the Intertropical Convergence Zone (ITCZ) over the Atlantic during DJF and JJA (black lines) are also shown. (c) Grey arrows mark surface currents over the western tropical Atlantic (Johns et al., 1998) that are relevant for this study, circles denote the location of sediment core GeoB16224-1 (black, the same as in (a) and (b)) and previously published paleoclimate records (red) discussed in the text (for detailed information about each site see Table 1) as well as the suspended sediment samples (grey circles with black outlines for published results, grey circles without outline for new data) used for the endmember unmixing analysis (see section 3.2.4). (For interpretation of the references to colour in this figure legend, the reader is referred to the web version of this article).

3.2.2 Age model

Fifteen radiocarbon (^{14}C) measurements performed on samples of mixed planktonic foraminifera (i.e., *Globigerinoides ruber* and *Globigerinoides sacculifer*; see Zhang et al., 2015) showed that the upper 600 cm of sediment core GeoB16224-1 cover the last ca. 41 ka. These ^{14}C ages were used to establish the age model of core GeoB16224-1 and also estimate the associated uncertainties (Fig. 3-2) by using the R script BACON version 2.2 (Blaauw and

Christen 2011) and the IntCal13 calibration curve (Reimer et al., 2013) with a reservoir age of 400 ± 100 (1σ error) years. Default parameter settings, except for mem.mean (set to 0.7) and acc.shape (set to 1.5), were applied. An ensemble of 10,000 age-depth realizations derived from BACON has been used to calculate median age and the 2σ age uncertainty at 5 mm resolution (Häggi et al., 2017). Here we only present the results of core GeoB16224-1 for the interval 41-13 ka BP.

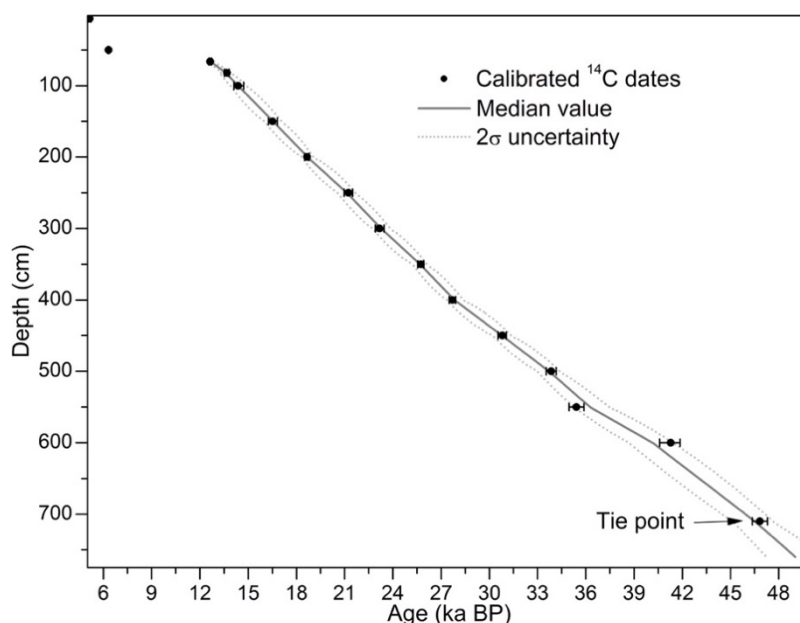


Figure 3-2. Age model of core GeoB16224-1 based on calibrated ^{14}C ages by the IntCal13 curve (black dots) and BACON software (solid lines). Grey lines represent the median age and $2s$ uncertainty (dashed grey) derived from the BACON software (section 3.2.2 of the main text). We assume an age control point at 710 cm as 46830 ± 470 years from a well-dated stalagmite from El Condor (Cheng et al., 2013a) to obtain the age model for whole core GeoB16224-1 using the BACON software, based on i) small changes in accumulation rate of sediment core GeoB16224-1, ii) the similarity between variations of both inorganic (Fe/Ca, $\delta^{13}\text{C}$ and $\delta^{18}\text{O}$ of benthic foraminifers (unpublished data)) and organic proxies in this core with stalagmite $\delta^{18}\text{O}$ records from the Andes. The inclusion of this age tie point at 710 cm would not modify the age model of the investigated period between 13 and 41 ka BP (please note that there might also be a hiatus prior to ca. 12 ka BP).

3.2.3 Major element composition

Major element intensities of core GeoB16224-1 were determined by scanning the surface of the archive half at 5 mm steps with an X-ray fluorescence (XRF) core-scanner (AVAATECH no.2) at the MARUM, University of Bremen. The XRF data were obtained with generator settings of 10 kV, a current of 0.40 mA, and a sampling time of 20 seconds. To calibrate the scanner intensities, we also analyzed elemental concentrations on bulk

sediment samples from the working half. In total, 50 discrete samples of about 10 ml wet sediment were freeze-dried, powdered and homogenized using an agate mortar. Measurements were performed with a PANalytical Epsilon3-XL XRF spectrometer equipped with a rhodium tube, several filters and a SSD5 detector. The raw data were processed against certified sediment standards. Standard deviations for the single elements were <1 %. The discrete measurements and scanner data were combined to derive high-resolution calibrated proportions of elements with a log-ratio regression approach (Weltje and Tjallingii, 2008), in which Ca was used as the denominator element (R^2 was 0.83, Fig. S7-1). We use down core Fe/Ca data to trace variations in terrigenous sediment input (Zabel et al., 1999; Govin et al., 2012), Fe/K data to reconstruct changes in the intensity of chemical weathering (e.g., Mulitza et al., 2008), and Al/Si data to assess variations in grain-size of fluvial sediments (e.g., Bouchez et al., 2011; Sun et al., 2017). However, we raise a note of caution for the interpretation of the Al/Si down core record as an indicator of grain-size since other processes like changes in opal flux may also impact the record (Govin et al., 2012).

Besides, a set of 28 suspended sediment samples from different tributaries of the Amazon River (Fig. 4-1c, Table S7-1) was measured for major element concentrations. First, we collected suspension samples by using a submersible pump at 60% water depth in the channel thalweg of each sampling site during the dry (November 2011) and wet (May 2012) seasons. At least 4 L of water were filtered by using cellulose filters (0.2 mm), which were immediately dried and packed in plastic bags for transportation. Then, the filters with suspended material were digested in Teflon liners with a microwave system (MLS, 1200 MEGA) by adding 7 ml HNO₃ (65%), 0.5 ml HF (40%), 0.5 ml HCl (30%) and 0.5 ml MilliQ. All acids were of suprapure quality. Finally, element concentrations, except Si which was lost during total digestion procedure, were measured by ICP- OES (Agilent 720; precision of 2%, standard deviation of 1e3%) (Table S7-1).

3.2.4 Endmember unmixing analysis

An endmember unmixing model (e.g., Mulitza et al., 2010; Collins et al., 2013) was applied for the suspended sediment samples and down core records to determine past changes in the relative input of different components. We included two terrigenous endmembers (i.e., Andes and lowland) as the source of fluvial material and one marine endmember, representing the marine biogenic fraction. The 28 new and 18 previously published

geochemical data of suspended sediment samples from different tributaries of the Amazon River (Fig. 3-1c; Sholkovitz et al., 1978; Bouchez et al., 2011, 2012; Govin et al., 2014; data are provided in Supplementary Table S7-1) were combined to define the two terrigenous endmembers. For the marine endmember we only considered Si and Ca concentrations (Table S7-2). Neither the Si nor Ca content were measured at site GeoB16224-1, we therefore assigned the Si and Ca proportions using biogenic opal and carbonate measurements from nearby sites respectively (Table S7-2) because the western tropical Atlantic experienced low accumulation of biogenic opal in sediments (Govin et al., 2014) and small changes in glacial-interglacial productivity (Rühlemann et al., 1996). Moreover, multiple iterations of the endmember unmixing analysis allowed the estimation of uncertainties in relation to different: (i) modern terrigenous endmember compositions (which were assumed as constant over time); (ii) different sets of lowland elemental proportions (e.g., Si concentrations, Table S7-1); and (iii) marine endmember compositions (Si and Ca proportions, Table S7-2). The endmember proportions are expressed as the median values of all iterations with a non-parametric 95% confidence interval (2.5th and 97.5th percentiles, not shown).

3.2.5 Alkenone analysis

To determine variations in primary productivity, we analyzed alkenone concentrations and variations in the ratio of the C_{37}/C_{38} alkenones. Alkenones are long-chain lipid biomarkers that are exclusively produced by haptophytes (Marlowe et al., 1984). Alkenones are usually used as a temperature proxy (e.g., Prahl and Wakeham, 1987) but their accumulation rates also serve as an indicator of primary productivity (e.g., Villanueva et al., 1998). Moreover, the C_{37}/C_{38} ratio can be used to disentangle the relative contributions of coastal and open marine haptophyte species, where low C_{37}/C_{38} ratios reflect the predominance of coastal haptophytes, and high ratios represent a larger fraction of open marine haptophytes (Conte et al., 1998). Following the methodology described in Häggi et al. (2015), we extracted lipid biomarkers from freeze-dried and ground samples from sediment core GeoB16224-1. Then, the compounds were measured by using a Thermo Fisher Scientific Focus gas chromatograph equipped with a 30 m Rxi™- 5 ms column (30 m, 0.25 mm, 0.25 mm) and a flame ionization detector. Compound quantification was achieved by comparing peak areas to external ketone standards and an internal 2-nonodecanone standard.

Deviations in reproducibility of lipid quantification is <5 % based on replicate standard analyses.

3.3 Results

The down core Fe/Ca record of sediment core GeoB16224-1 increases significantly during H stadials 1-4 and DO stadials (in particular during DO stadials 5-8; Fig. 3-3b). The Fe/K record shows distinct peaks during H stadials 1e4, while changes during DO stadials are rather small (Fig. 3-3e). The Al/Si values exhibit limited variations throughout the investigated interval (Fig. 3-3f). The 28 new suspended sediment samples collected from different tributaries of the Amazon River generally have high contents in Al, Fe, K and Si (Supplementary Table S7-1). The endmember unmixing analysis suggests that Andean-sourced terrigenous sediments account on average for ca. 70 % of the total sediment deposited at the core site (Fig. 3-3g), and experience minor increases during H stadials 1, 3 and 4, and DO stadials 5-8 (Fig. 3-4g). Additionally, the C₃₇ concentration and C₃₇/C₃₈ ratio show low values during both H and DO stadials (except H Stadial 1), and high values during DO interstadials (Fig. 3-3c-d).

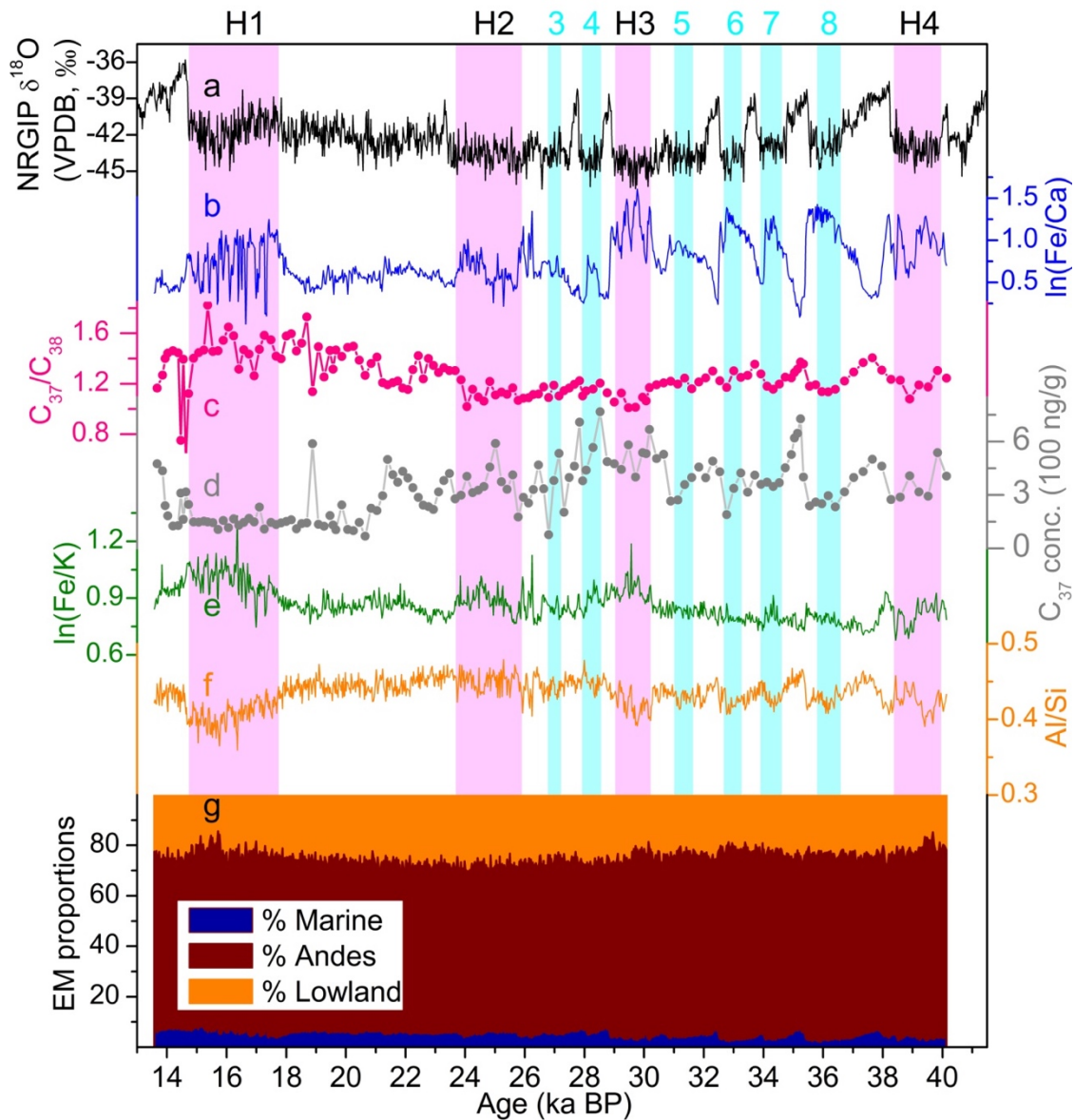


Figure 3-3. Downcore geochemistry of sediment core GeoB16224-1. (a) NGRIP ice core d18O record to highlight Heinrich (H) stadials (pink bars) and Dansgaard-Oeschger (DO) stadials (cyan bars) (Rasmussen et al., 2014), (b) $\ln(\text{Fe}/\text{Ca})$, (c) alkenone C_{37}/C_{38} and (d) C_{37} concentration, (e) $\ln(\text{Fe}/\text{K})$, (f) Al/Si as well as (g) the endmember (EM) modeled proportions based on major elements. (For interpretation of the references to colour in this figure legend, the reader is referred to the web version of this article).

3.4 Discussion

3.4.1 Increases in the Fe/Ca ratio during H and DO stadials

The neodymium (Nd) isotopic composition of sediments core GeoB16224-1 revealed very small variations (mean value of -11.65 ± 0.5), indicating that the terrigenous fraction

deposited at the site was uninterruptedly sourced in the Amazon Basin over the past 30 ka (Zhang et al., 2015). Down core variations in the Fe/K record in core GeoB16224-1 (Fig. 3-3e) may demonstrate recurrent intensifications of chemical weathering over the tropical Andes during H stadials relative to DO stadials. Because of the grain-size control on the geochemical composition of suspended sediments from the Amazon River (e.g., Bouchez et al., 2011; Sun et al., 2017), the small amplitude of changes in the Al/Si record (Fig. 3-3f) suggests no significant modifications of grain-size sorting over the investigated period. This may be related to the long-distance transport pathway of fine-grained sediments within the Amazon River drainage to the offshore location. Remarkably, variations in Fe/Ca values from core GeoB16224-1 (Figs. 3b and 4e) are in very good agreement with stalagmite $\delta^{18}O$ records from the tropical Andes (such as the Pacupahuain Cave, Kanner et al., 2012, Fig. 3-4d) and the $^{231}Pa/^{230}Th$ records from the Bermuda Rise (an indicator of the AMOC strength) (Böhm et al., 2015; Henry et al., 2016, Fig. 3-4f).

. Different precipitation patterns across tropical South America during Heinrich and Dansgaard-Oeschger stadials

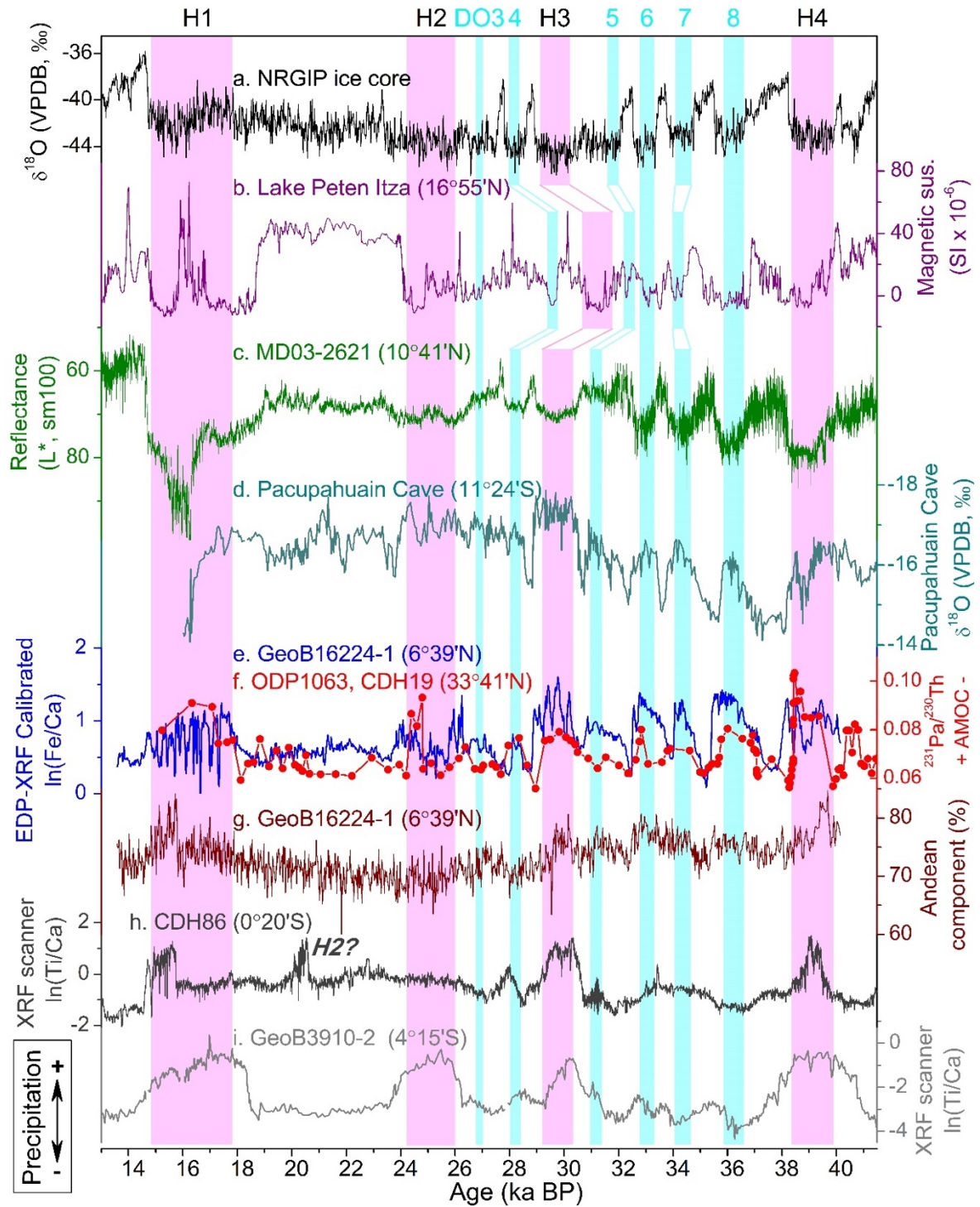


Figure 3-4. Paleoprecipitation records across Central and tropical South America. (a) NGRIP ice core $\delta^{18}\text{O}$ record and time windows of Heinrich (H) stadials (pink bars) and Dansgaard-Oeschger (DO) stadials (cyan bars) (Rasmussen et al., 2014), (b) magnetic susceptibility from Lake Petén Itzá (Escobar et al., 2012), (c) total reflectance of sediment core MD03-2621 (Deplazes et al., 2013), (d) Pacupahuain Cave $\delta^{18}\text{O}$ record (Kanner et al., 2012), (e) $\ln(\text{Fe}/\text{Ca})$ and (g) proportion of Andean material within the terrigenous fraction of core GeoB16224-1 (this study), (f) $^{231}\text{Pa}/^{230}\text{Th}$ from Bermuda Rise (combination of 15.2-24.8 ka BP from ODP 1063 (Böhm et al., 2015) and 24.8-41 ka BP from CDH19 (Henry et al., 2016)), (h) Ti/Ca record of sediment core CDH86 (Nace et al., 2014), (i) Ti/Ca record of sediment core GeoB3910-2 (Jaeschke et al., 2007). Note that H stadial 2 in core CDH86 (h) is misplaced (it thus requires direct radiocarbon measurement for last 20 ka of this core, Nace et al., 2014).

Based on the in-phase relationship between the Pacupahuain Cave $\delta^{18}\text{O}$ record and our Fe/Ca record throughout H stadials and DO cycles (Fig. 3-4d-e and 3-5c-d), we infer that both records were controlled by the same mechanism. It is likely that enhanced precipitation over the Andes, in response to slowdowns in the strength of the AMOC, mobilized more fine-grained sediments that were quickly transported throughout the basin and deposited in the western equatorial Atlantic. This is actually supported by previous studies (e.g., Meade et al., 1985) which demonstrated that fine-grained sediments from the Andean tributaries Solimões and Madeira Rivers (representing ca. 90% of the total inorganic sediment input from the Amazon River to the western Atlantic) are delivered downstream to the ocean within two months (March-April) after the austral summer rainfall peak. An increase of suspended sediment input at the core location would result in less favorable conditions for haptophyte productivity and would thereby explain the reduced C_{37} concentrations (Häggi et al., 2015, Fig. 3-3d).

Today, terrigenous sediments deposited at our core site mainly originate in the Amazon Basin (Govin et al., 2014; Zhang et al., 2015) and are transported from the Amazon River mouth by the NBC northwestward flow (Fig. 3-1a-b). During H and DO stadials, decrease in the AMOC strength (Böhm et al., 2015; Henry et al., 2016; Fig. 3-4e-f) led to a weakened NBC (Nace et al., 2014; Zhang et al., 2015), which could still transport the Andean-sourced sediments to the core site and thus cause decreased C_{37} concentrations (Fig. 3-3d) (and C_{37} alkenone flux as well, Fig. S7-2). Furthermore, southward shifts of the ITCZ along with AMOC slowdowns (Wang et al., 2004; Jaeschke et al., 2007) might have been accompanied by southward migrations of its oceanic counterpart, i.e., the shallow mixed layer below the ITCZ (e.g., Portilho-Ramos et al., 2017). This could have further reduced the abundance of open ocean haptophytes at our core site as supported by decreased C_{37} concentration and lower $\text{C}_{37}/\text{C}_{38}$ ratios (Fig. 3c-d), which indicates more coastal (or freshwater) haptophytes. In addition, changes in bottom water chemistry along with the weakened AMOC during H and DO stadials (e.g., enhanced remineralization of organic matter as described in Schmittner and Lund, 2015) may have also contributed to partial dissolution of marine carbonates, which then could have further increased the Fe/Ca values in core GeoB16224-1 during cold stadials. However, this assumption is refuted by the fragmentation index in core GeoB16224-1 (Fig. S7-3) which indicates enhanced carbonate dissolution during H and DO stadials. Overall, we suggest that the Fe/Ca record most probably reflects the combined effect of sediment discharge and oceanic conditions, although

we cannot disentangle the impact of limited changes in precipitation and sea level on sediment dynamics on the continental slope off French Guiana. Conversely, low Fe/Ca values together with increased C_{37} concentrations and C_{37}/C_{38} ratios in our core during DO interstadials (Fig. 3-3b-d, Fig. S7-2) can be attributed to: (i) decreased precipitation over the Andes and (ii) northward shift of the shallow mixed layer below the ITCZ. These processes would be associated to a strengthened AMOC.

Notably, the C_{37}/C_{38} record shows low values over ca. 23-21 ka BP. This may also indicate a higher contribution of coastal haptophytes during the Last Glacial Maximum (LGM, 23-19 ka BP), when the AMOC was stronger than during H stadial 1 (Böhm et al., 2015) and the deposition areas were closer to the coast. Nevertheless, a detailed understanding of these low C_{37}/C_{38} values requires more investigation because increased C_{37} concentration and alkenone flux during the LGM seem to be at odds with the conditions of H and DO stadials (Fig. 3-3c-d, Fig. S7-2).

3.4.2 Spatial changes in South American precipitation during H and DO stadials

Increased precipitation over the tropical Andes during H and DO stadials was attributed to a stronger SASM, despite some elusive intervals, e.g., H Stadial 3 (Mosblech et al., 2012) and DO Stadial 3 (Kanner et al., 2012). In fact, the SASM dominates rainfall across the Amazon Basin to the south of the equator, while the ITCZ is the main atmospheric feature that controls precipitation over northernmost South America and NE Brazil (Fig. 3-1a-b; Barros et al., 2002; Vera et al., 2006; Baker and Fritz, 2015). Comparing well-dated records along a north-south transect across Central and South America (Fig. 3-1c and Table 3-1) enables to differentiate the regional response of riverine suspended material to climate changes associated with H and DO stadials. During H stadials, the compiled records indicate decreased rainfall in two cores to the north of our site (i.e., PI-2/6 and MD03-2621; Fig. 3-4b-c) (Escobar et al., 2012; Deplazes et al., 2013) but increased rainfall in Pacupahuain Cave (Fig. 3-4d, Kanner et al., 2012;) and two cores offshore NE Brazil (i.e., CDH86 and GeoB3910-2; Fig. 3-4h-i) (Jaeschke et al., 2007; Nace et al., 2014). During DO stadials, and in particular for DO stadials 5-8, we observe the same anti-phased relationship of precipitation between Pacupahuain Cave and the two cores to the north of our core site (Figs. 3-4b-d and 3-5b-c; Kanner et al., 2012; Deplazes et al., 2013). However, the two cores off NE Brazil show weak increases of $\ln(\text{Ti}/\text{Ca})$ records (thus less significant input of terrigenous

sediment) across DO stadials (Figs. 3-4h-i and 3-5e) (Jaeschke et al., 2007; Nace et al., 2014). Notably, the temporal resolutions of these proxy records to the south of our core site, i.e., cores CDH86 (ca. 8 years per sample, Fig. 3-4h; Nace et al., 2014) and GeoB3910-2 (ca. 40 years per sample, Fig. 3-4i; Jaeschke et al., 2007) (Table 3-1), are sufficiently high to resolve potential climatic signals related to the DO stadials.

Site in Fig. 3-	Core ID	Latitude	Longitude	Altitude (m)	Dating	Proxy	Resolution (mm / year)*	Reference
1	PI-2/6	16.9° N	89.8° W	-71	¹⁴ C	Magnetic susceptibility	10 / ca. 10	Escobar et al., 2012
2	MD03-2621	10.7° N	65.0° W	-847	Match with ¹⁴ C-dated cores nearby	Total reflectance	0.07 / ca. 0.15	Deplazes et al., 2013
3	P09-PH12	11.2° S	75.8° W	3800	U-Th	δ ¹⁸ O	0.1-0.2 / ca. 32	Kanner et al., 2012
4	GeoB16224-1	6.7° N	52.1° W	-2510	¹⁴ C	ln(Fe/Ca), C ₃₇ , C ₃₇ /C ₃₈	5 / ca. 26.5	This study
5	CDH86	0.3° N	44.2° W	-3107	¹⁴ C	Ti/Ca	2 / ca. 7.5	Nace et al., 2014
6	GeoB3910-2	4.2° S	36.3° W	-2362	¹⁴ C	Ti/Ca	4 / ca. 40	Jaeschke et al., 2007

Table 3-1. Coordinates and other information for sediment core GeoB16224-1 and previously published paleorecords depicted in Figs.3-1, 3-4 and 3-5. * Represents the measurement step (in mm) and the related temporal resolution (in year).

During H stadials, freshwater perturbation in the high latitudes of the North Atlantic and the subsequent slowdown of the AMOC (e.g., Böhm et al., 2015) led to a steeper latitudinal sea surface temperature gradient over the North Atlantic. This induced a southward displacement of the ITCZ mean position, which increased precipitation over NE Brazil (Wang et al., 2004; Strikis et al., 2015; Mulitza et al., 2017). Accordingly, enhanced input of fluvial sediments to the continental margin was detected at core sites offshore NE Brazil (Arz et al., 1998; Jaeschke et al., 2007; Nace et al., 2014; Zhang et al., 2015). Together with its impact on the eastern tropical Pacific climatology, the AMOC slowdown during H stadials also produced anomalous wet conditions over the tropical Andes (Kanner et al., 2012; Zhang et al., 2016). By contrast, the DO stadials likely only involved a moderate decrease (less than ca. 50%) of the AMOC (Zhang et al., 2014a, b) in comparison to the significant slowdown (or even a virtual shutdown) associated with H stadials (e.g., McManus et al., 2004; Böhm et al., 2015). The weakened AMOC during DO stadials also caused an

intensification of the SASM, supported by enhanced precipitation over the tropical Andes (e.g., Kanner et al., 2012) and the eastern Amazon (Wang et al., 2017). However, the attenuated reduction of the AMOC was likely unable to shift the ITCZ mean position as far south as during H stadials, thus not significantly increasing the delivery of fluvial sediments to the core locations on continental margin off NE Brazil (e.g., Jaeschke et al., 2007; Nace et al., 2014) as observed in Fig. 3-4h-i. This interpretation is also consistent with climate model simulations that showed only slight changes in precipitation over NE Brazil between DO stadials and interstadials (e.g., Zhang et al., 2014a), which may be further substantiated by more investigations of other climate model simulations. However, it is also worth stressing that the deposition of fluvial sediments is strongly influenced by the local current regime and that the sensitivity of elemental ratios to document millennial-scale climate variability may decrease with increasing distance from the river mouth.

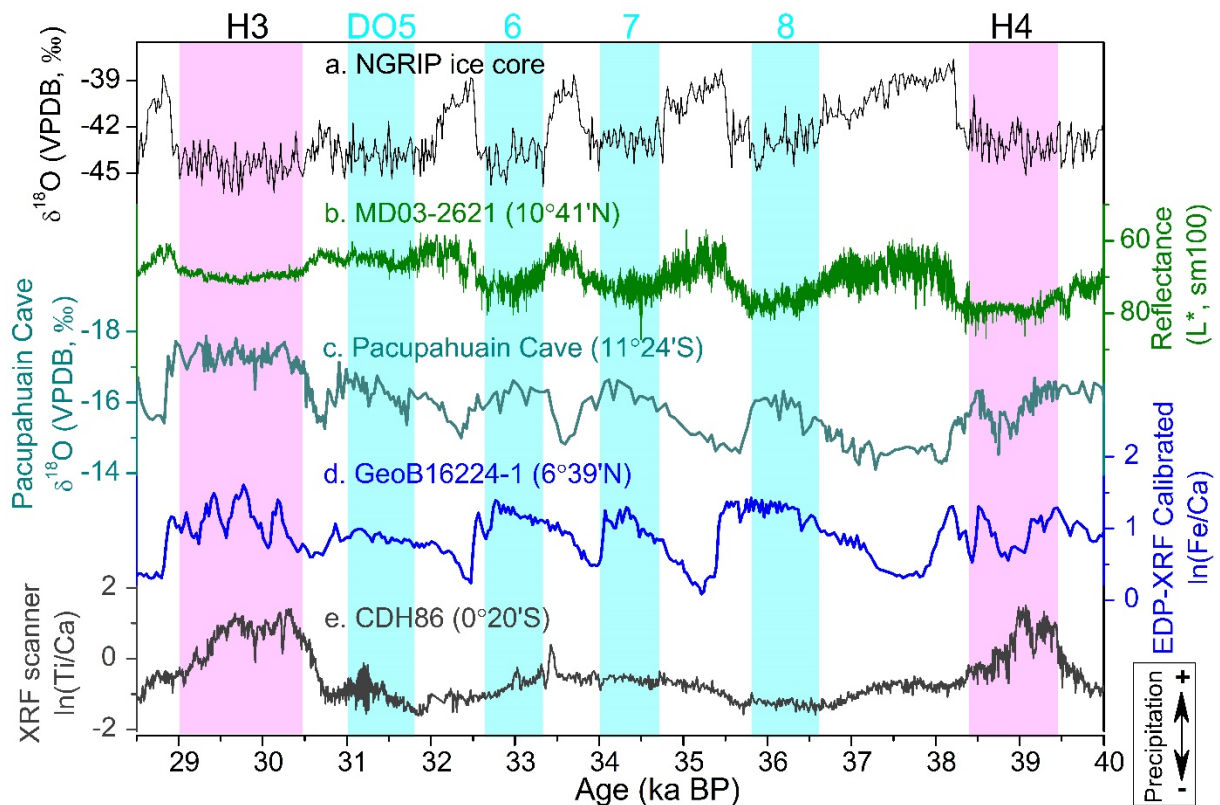


Figure 3-5. Detailed comparison of paleoprecipitation records for tropical South America between 40 and 28 ka BP. (a) time windows of Heinrich (H) stadials (pink bars) and Dansgaard-Oeschger (DO) stadials (cyan bars) as outlined from the NGRIP ice core $\delta^{18}\text{O}$ record (Rasmussen et al., 2014), (b) total reflectance of core MD03-2621 (Deplazes et al., 2013), (c) Pacupahuain Cave $\delta^{18}\text{O}$ record (Kanner et al., 2012), (d) $\ln(\text{Fe}/\text{Ca})$ record of core GeoB16224-1, (e) Ti/Ca record of core CDH86 (Nace et al., 2014).

Considering the different behavior of continental precipitation changes to the north (Figs. 3-4b-c and 3-5b) and south of our core site (Figs. 3-4h-i and 3-5e), it is also possible that the northern and southern boundaries of the ITCZ responded independently to DO stadials. Indeed, this hypothesis was proposed to explain the characteristics of ITCZ rainfall over tropical South America during H stadial 1 (Maslin et al., 2011). Moreover, we also notice that precipitation changes during DO stadials exhibit longitudinal differences: (i) significant positive anomaly over the Andes (Kanner et al., 2012); (ii) slight positive anomaly over eastern Amazonia (Wang et al., 2017) and NE Brazil. Previous studies reported an east-west antiphase of tropical South American precipitation during the early Holocene (Cruz et al., 2009; Cheng et al., 2013a) that was attributed to orbital forcing, but calling for a similar mechanism is not possible for DO stadials because of the qualitatively different boundary conditions. Unfortunately, our results are insufficient to decipher the physical mechanism that caused the zonal patterns of precipitation changes across tropical South America during DO stadials. Thus, further investigation on this issue would improve our understanding of the ITCZ shifts along with partial AMOC changes.

3.5 Conclusions

Geochemical analyses of sediment core GeoB16224-1 (ca. 7°N), raised from the continental slope off French Guiana in the western equatorial Atlantic, reveal millennial-scale positive anomalies in Fe/Ca ratios and negative anomalies in alkenone C₃₇ concentrations and C₃₇/C₃₈ ratios across H and DO stadials between 41 and 13 ka BP. Such coupled variations may be attributed to: (i) enhanced input of terrigenous sediment from the tropical Andes and (ii) reduced oceanic primary productivity due to enhanced suspended sediment input. The two mechanisms can be related to a weakened AMOC. Comparing five high temporal resolution paleo precipitation records across Central and South America between ca. 17°N and 4°S, we further characterized changes in the pattern of tropical South American precipitation during H and DO stadials. Both H and DO stadials triggered a strengthening of the SASM and a southward migration of the ITCZ. However, NE Brazilian precipitation, which is today under the control of the ITCZ, experienced significant increases during H stadials and less intense increases during DO stadials. We suggest that the moderate reduction of the AMOC during DO stadials, compared to the nearly shutdown during H

. Different precipitation patterns across tropical South America during Heinrich and Dansgaard-Oeschger stadials

stadials, was likely unable to shift the ITCZ mean position as far to the south as during H stadials.

3.6 References

- Allison, M.A., Lee, M.T., Ogston, A.S., Aller, R.C. 2000. Origin of Amazon mudbanks along the northeastern coast of South America. *Mar. Geol.* 163(1-4), 241-256.
- Alvarez-Solas, J., Charbit, S., Ritz, C., Paillard, D., Ramstein, G., Dumas, C. 2010. Links between ocean temperature and iceberg discharge during Heinrich events. *Nat. Geosci.* 3, 122-126.
- Arz, H.W., Pätzold, J., Wefer, G. 1998. Correlated millennial-scale changes in surface hydrography and terrigenous sediment yield inferred from last-glacial marine deposits off northeastern Brazil. *Quaternary Res.* 50(2), 157-166.
- Asmerom, Y., Polyak, V.J., Burns, S.J. 2010. Variable winter moisture in the southwestern United States linked to rapid glacial climate shifts. *Nat. Geosci.* 3, 114-117.
- Baker, P. A. & Fritz, S. C. 2015. Nature and causes of Quaternary climate variation of tropical South America. *Quat. Sci. Rev.* 124, 31-47.
- Barros, V., Doyle, M., González, M., Camilloni, I., Bejarán, R., Caffera, R.M. 2002. Climate variability over subtropical South America and the South American monsoon: a review. *Meteorological.* 27, 33-58.
- Blaauw, M., Christen, J.A. 2011. Flexible paleoclimate age-depth models using an autoregressive Gamma Process. *Bayesian Anal.* 6, 457-474.
- Böhm, E., Lippold, J., Gutjahr, M., Frank, M., Blaser, P., Antz, B., Fohlmeister, J., Frank, N., Andersen, M.B., Deininger, M. 2015. Strong and deep Atlantic meridional overturning circulation during the last glacial cycle. *Nature* 517, 73-76.
- Bond, G., Heinrich, H., Broecker, W., Labeyrie, L., Mcmanus, J., Andrews, J., Huon, S., Jantschik, R., Clasen, S., Simet, C. 1992. Evidence for massive discharges of icebergs into the North Atlantic ocean during the last glacial period. *Nature* 360, 245-249.
- Bouchez, J., Gaillardet, J., France-Lanord, C., Maurice, L., Dutra-Maia, P. 2011. Grain size control of river suspended sediment geochemistry: Clues from Amazon River depth profiles. *Geochem. Geophys. Geosyst.* 12, Q03008, doi: 10.1029/2010gc003380.
- Bouchez, J., Gaillardet, J., Lupker, M., Louvat, P., France-Lanord, C., Maurice, L., Armijos, E., Moquet, J.-S., 2012. Floodplains of large rivers: Weathering reactors or simple silos? *Chem. Geol.* 332-333, 166-184.
- Burns, S.J., Fleitmann, D., Matter, A., Kramers, J., Al-Subbary, A.A. 2003. Indian Ocean Climate and an Absolute Chronology over Dansgaard/Oeschger Events 9 to 13. *Science* 301, 1365-1367.
- Cheng, H., Sinha, A., Cruz, F.W., Wang, X., Edwards, R.L., d'Horta, F.M., Ribas, C.C., Vuille, M., Stott, L.D., Auler, A.S. 2013a. Climate change patterns in Amazonia and biodiversity. *Nat. Commun.* 4(1411), doi:10.1038/ncomms2415.
- Cheng, W., Chiang, J. C. H., Zhang, D. 2013b. Atlantic Meridional Overturning Circulation (AMOC) in CMIP5 models: RCP and historical simulations. *J. Climate* 26, 7187-7197.
- Clark, P.U., Pisias, N.G., Stocker, T.F., Weaver, A.J. 2002. The role of the thermohaline circulation in abrupt climate change. *Nature* 415, 863-869.
- Collins, J.A., Govin, A., Mulitza, S., Heslop, D., Zabel, M., Hartmann, J., Röhl, U., and Wefer, G. 2013. Abrupt shifts of the Sahara-Sahel boundary during Heinrich stadials. *Clim. Past* 9, 1181-1191.
- Conte, M.H., Thompson, A., Lesley, D., Harris, R.P. 1998. Genetic and physiological influences on the alkenone/alkenoate versus growth temperature relationship in *Emiliania huxleyi* and *Gephyrocapsa oceanica*. *Geochim. Cosmochim. Acta* 62, 51-68.

- Cruz, F.W.J., Burns, S.J., Karmann, I., Sharp, W.D., Vuille, M., Cardoso, A.O., Ferrari, J.A., Silva Dias, P.L., Viana, O.J. 2005. Insolation-driven changes in atmospheric circulation over the past 116,000 years in subtropical Brazil. *Nature*. 434, 63-66.
- Cruz, F.W., Vuille, M., Burns, S.J., Wang, X., Cheng, H., Werner, M., Edwards, R.L., Karmann, I., Auler, A.S., Nguyen, H. 2009. Orbitally driven east-west antiphasing of South American precipitation. *Nat. Geosci.* 2, 210-214.
- Dansgaard, W., Johnsen, S.J., Clausen, H.B., Dahl-Jensen, D., Gundestrup, N.S., Hammer, C.U., Hvidberg, C.S., Steffensen, J.P., Sveinbjörnsdóttir, A.E., Jouzel, J., Bond, G. 1993. Evidence for general instability of past climate from a 250-kyr ice-core record. *Nature* 364, 218-220.
- Deplazes, G., Lückge, A., Peterson, L.C., Timmermann, A., Hamann, Y., Hughen, K.A., Röhl, U., Laj, C.E., Cane, M.A., Sigman, D.M., Haug, G.H. 2013. Links between tropical rainfall and North Atlantic climate during the last glacial period. *Nat. Geosci.* 6, 213-217.
- EPICA Community Members. 2006. One-to-one coupling of glacial climate variability in Greenland and Antarctica. *Nature* 444, 195-198.
- Escobar, J., Hodell, D.A., Brenner, M., Curtis, J.H., Gilli, A., Mueller, A.D., Anselmetti, F.S., Ariztegui, D., Grzesik, D.A., Pérez, L., Schwab, A., Guilderson, T.P. 2012. A 43 ka record of paleoenvironmental change in the Central American lowlands inferred from stable isotopes of lacustrine ostracods. *Quat. Sci. Rev.* 37, 92-104.
- Fritz, S.C., Baker, P.A., Ekdahl, E., Seltzer, G.O., Stevens, L.R. 2010. Millennial-scale climate variability during the last glacial period in the tropical Andes. *Quat. Sci. Rev.* 29, 1017-1024.
- Govin, A., Holzwarth, U., Heslop, D., Ford Keeling, L., Zabel, M., Mulitza, S., Collins, J.A., Chiessi, C.M. 2012. Distribution of major element ratios in Atlantic surface sediments (36°N–49°S): imprint of terrigenous input and continental weathering. *Geochem. Geophys. Geosyst.* 13, Q01013. <http://dx.doi.org/10.1029/2011gc003785>.
- Govin, A., Chiessi, C. M., Zabel, M., Sawakuchi, A. O., Heslop, D., Hörner, T., Zhang, Y., and Mulitza, S. 2014. Terrigenous input off northern South America driven by changes in Amazonian climate and the North Brazil Current retroflexion during the last 250 ka. *Clim. Past* 10, 843-862.
- Häggi, C., Chiessi, C.M., and Schefuß, E. 2015. Testing the D/H ratio of alkenones and palmitic acid as salinity proxies in the Amazon Plume. *Biogeosciences* 12, 7239-7249.
- Häggi, C., Chiessi, C.M., Merkel, U., Mulitza, S., Prange, M., Schulz, M., Schefuß, E. 2017. Response of the Amazon rainforest to late Pleistocene climate variability. *Earth Planet. Sci. Lett.* 479(1), 50-59.
- Heinrich, H. 1988. Origin and consequences of cyclic ice rafting in the northeast Atlantic ocean during the past 130,000 years. *Quaternary Res.* 29, 142-152.
- Henry, L.G., McManus, J.F., Curry, W.B., Roberts, N.L., Piotrowski, A.M., Keigwin, L.D. 2016. North Atlantic ocean circulation and abrupt climate change during the last glaciation. *Science* 353(6298), 470-474.
- Jaeschke, A., Rühlemann, C., Arz, H., Heil, G., Lohmann, G. 2007. Coupling of millennial-scale changes in sea surface temperature and precipitation off northeastern Brazil with high-latitude climate shifts during the last glacial period. *Paleoceanography* 22(4), doi:10.1029/2006PA001391.
- Johns, W.E., Lee, T.N., Beardsley, R.C., Candela, J., Limeburner, R., Castro, B. 1998. Annual cycle and variability of the North Brazil Current. *J. Phys. Oceanogr.* 28, 103-128.
- Kanner, L.C., Burns, S.J., Cheng, H., Edwards, R.L. 2012. High latitude forcing of the South American Summer Monsoon during the Last Glacial. *Science* 335, 570-573.
- Lentz, S.J. 1995. Seasonal variations in the horizontal structure of the Amazon Plume inferred from historical hydrographic data. *J. Geophys. Res.-Oceans*, 100, 2391-2400.
- Malhi, Y., Aragão, L. E.O.C., Galbraith, D., Huntingford, C., Fisher, R., Zelazowski, P., Sitch, S., McSweeney, C., and Meir, P. 2009. Exploring the likelihood and mechanism of a climate-change-induced dieback of the Amazon rainforest. *Proc. Natl. Acad. Sci. USA.* 106(49), 20610-20615.
- Malhi, Y., Roberts, J.T., Betts, R.A., Killeen, T.J., Li, W., Nobre, C.A. 2008. Climate Change, Deforestation, and the Fate of the Amazon. *Science* 390, 169-172.

- Marlowe, I.T., Green, J.C., Neal, A.C., Brassell, S.C., Eglinton, G. and Course, P.A. 1984. Long-Chain (n-C37-C39) Alkenones in the Prymnesiophyceae: Distribution of Alkenones and other Lipids and their Taxonomic Significance. *British Phycological Journal* 19, 203-216.
- Maslin, M.A., Ettwein, V.J., Wilson, K.E., Guilderson, T.P., Burns, S.J., Leng, M.J. 2011. Dynamic boundary-monsoon intensity hypothesis: evidence from the deglacial Amazon River discharge record. *Quat. Sci. Rev.* 30, 3823-3833.
- McManus, J.F., R. Francois, J.M. Gherardi, L.D. Keigwin, and S. Brown-Leger. 2004. Collapse and rapid resumption of Atlantic meridional circulation linked to deglacial climate changes. *Nature* 428, 834-837.
- Meade, R.H., Dunne, T., Richey, J.E., De M. Santos, U., Salati, E. 1985. Storage and Remobilization of Suspended Sediment in the Lower Amazon River of Brazil, *Science* 228, 488-490.
- Mosblech, N.A.S., Bush, M.B., Gosling, W.D., Hodell, D., Thomas, L., van Calsteren, P., Correa-Metrio, A., Valencia, B.G., Curtis, J., van Woesik, R. 2012. North Atlantic forcing of Amazonian precipitation during the last ice age. *Nat. Geosci.* 5, 817-820.
- Mulitza, S., Chiessi, C.M., Cruz, A.P.S., Frederichs, T.W., Gomes, J.G., Gurgel, M.H.C., Haberkern, J., Huang, E., Jovane, L., Kuhnert, H., Pittauerová, D., Reiners, S.J., Roud, S.C., Schefuß, E., Schewe, F., Schwenk, T.A., Sicoli-Seoane, J.C., Sousa, S.H.M., Wangner, D.J., Wiers S., 2013. Response of Amazon sedimentation to deforestation, land use and climate variability. Cruise No. MSM20/3 (February 19 - March 11, 2012), Recife (Brazil) - Bridgetown (Barbados). MARIA S. MERIAN-Berichte, MSM20/3, 86 pp., DFG Senatskommission für Ozeanographie, doi:10.2312/cr_msm20_3.
- Mulitza S., Chiessi C. M., Schefuß E., Lippold J., Wichmann D., Antz B., Mackensen A., Paul A., Prange M., Rehfeld K., Werner M., Bickert T., Frank N., Lynch-Stieglitz J., Ramos R., Sawakuchi A., Schulz M., Schwenk T., Tiedemann R., Vahlenkamp M., Zhang Y. 2017. Synchronous and proportional deglacial changes in Atlantic Meridional Overturning and northeast Brazilian precipitation. *Paleoceanography*, 32, doi: 10.1002/2017PA003084.
- Mulitza, S., Heslop, D., Pittauerova, D., Fischer, H.W., Meyer, I., Stuut, J.-B.W., Zabel, M., Mollenhauer, G., Collins, J.A., Kuhnert, H., Schulz, M. 2010. Increase in African dust flux at the onset of commercial agriculture in the Sahel region. *Nature* 466, 226-228.
- Mulitza, S., Prange, M., Stuut, J.-B., Zabel, M., Dobeneck, T.-von, Itambi, A.C., Nizou, J., Schulz, M., Wefer, G. 2008. Sahel megadroughts triggered by glacial slowdowns of Atlantic meridional overturning. *Paleoceanography* 23, doi: 10.1029/2008PA001637
- Müller-Karger, F.E., McClain, C.R., Richardson, P.L. 1988. The dispersal of the Amazon's water. *Nature* 333, 56-59.
- Nace, T.E., Baker, P.A., Dwyer, G.S., Silva, C.G., Rigsby, C.A., Burns, S.J., Giosan, L., Otto-Bliesner, B., Liu, Z., Zhu, J. 2014. The role of North Brazil Current transport in the paleoclimate of the Brazilian Nordeste margin and paleoceanography of the western tropical Atlantic during the late Quaternary. *Palaeogeogr. Palaeoclimatol. Palaeoecol.* 415, 3-13.
- Peterson, L.C., Haug, G.H., Hughen, K.A., Röhl, U. 2000. Rapid changes in the hydrologic cycle of the tropical Atlantic during the Last Glacial. *Science* 290, 1947-1951.
- Portilho-Ramos R.C., Chiessi C. M., Zhang Y., Mulitza S., Kucera M., Siccha M., Prange M., Paul A. 2017. Meridional shifts of Atlantic equatorial divergence zone in response to millennial forcing. *Scientific Reports* 7, doi:10.1038/s41598-017-01629-z.
- Prahl, F., and Wakeham, S.G. 1987. Calibration of unsaturation patterns in long-chain ketone compositions or paleotemperature assessment. *Nature* 330, 367-369.
- Rahmstorf, S., Box, J.E., Feulner, G., Mann, M.E., Robinson, A., Rutherford, S., Schaffernicht, E.J. 2015. Exceptional twentieth-century slowdown in Atlantic Ocean overturning circulation. *Nature Climate Change* 5, 475-480.
- Rasmussen, S.O., Bigler, M., Blockley, S.P., Blunier, T., Buchardt, S.L., Clausen, H.B., Cvijanovic, I., Dahl-Jensen, D., Johnsen, S.J., Fischer, H., Gkinis, V., Guillevic, M., Hoek, W.Z., Lowe, J.J., Pedro, J.B., Popp, T., Seierstad, I.K., Steffensen, J.P., Svensson, A.M., Vallelonga, P., Vinther, B.M., Walker, M.J.C., Wheatley, J.J., Winstrup, M. 2014. A stratigraphic framework for abrupt climatic changes during the Last Glacial period based on three synchronized Greenland ice-core records: refining and extending the INTIMATE event stratigraphy. *Quat. Sci. Rev.* 106, 14-28.

- Reimer, P.J., Bard, E., Bayliss, A., Beck, J.W., Blackwell, P.G., Bronk Ramsey, C., Buck, C.E., Cheng, H., Edwards, R.L., Friedrich, M., Grootes, P.M., Guilderson, T.P., Haflidason, H., Hajdas, I., Hatté, C., Heaton, T.J., Hoffmann, D.L., Hogg, A.G., Hughen, K.A., Kaiser, K.F., Kromer, B., Manning, S.W., Niu, M., Reimer, R.W., Richards, D.A., Scott, E.M., Southon, J.R., Staff, R.A., Turney, C.S.M., van der Plicht, J., 2013. IntCal13 and Marine13 radiocarbon age calibration curves 0-50,000 years cal BP. *Radiocarbon* 55(4), 1869-1887.
- Rühlemann, C., Frank, M., Hale, W., Mangini, A., Mulitza, S., Muller, P.J., Wefer, G. 1996. Late Quaternary productivity changes in the western equatorial Atlantic: evidence from Th-230-normalized carbonate and organic carbon accumulation rates. *Mar. Geol.* 135(1-4), 127-152.
- Sanchez Goñi M.F., Harrison S.P. 2010. Millennial-scale climate variability and vegetation changes during the Last Glacial: Concepts and terminology. *Quat. Sci. Rev.* 29, 2823-2827.
- Schmittner, A. and Lund, D.C. 2015. Early deglacial Atlantic overturning decline and its role in atmospheric CO₂ rise inferred from carbon isotopes ($\delta^{13}\text{C}$). *Clim. Past* 11, 135-152,
- Sholkovitz, E.R., van Grieken, R., Eisma, D., 1978. The major-element composition of suspended matter in the Zaire river and estuary. *Netherlands Journal of Sea Research*, 12, 407-413.
- Strikis, N.M., Chiessi, C.M., Cruz, F.W., Vuille, M., Cheng, H., Barreto, E.A.S., Mollenhauer, G., Kasten, S., Karmann, I., Edwards, R.L., Bernal, J.P., Sales, H.R. 2015. Timing and structure of Mega-SACZ events during Heinrich Stadial 1. *Geophys. Res. Lett.* 42, 5477-5484.
- Sun, S., Schefuß, E., Mulitza, S., Chiessi, C.M., Sawakuchi, A.O., Zabel, M., Baker, P.A., Hefter, J., Mollenhauer, G. 2017. Origin and processing of terrestrial organic carbon in the Amazon system: lignin phenols in river, shelf and fan sediments. *Biogeosciences* 14, 2495-2512.
- Svensson, A., Andersen, K.K., Bigler, B., Clausen, H.B., Dahl-Jensen, D., Davies, S.M., Johnsen, S.J., Muscheler, R., Rasmussen, S.O., Röthlisberger, R., Steffensen, J.P., Vinther, B.M. 2006. The Greenland Ice Core Chronology 2005, 15-42 ka. Part 2: comparison to other records. *Quat. Sci. Rev.* 25, 3258-3267.
- Vera, C., Higgins, W., Amador, J., Ambrizzi, T., Garreaud, R., Gochis, D., Gutzler, D., Lettenmaier, D., Marengo, J., Mechoso, C.R., Nogues-Paegle, J., Silva-Dias, P.L., Zhang, C. 2006. Towards a Unified View of the American Monsoon Systems. *J. Clim.* 19, 4977-5000.
- Villanueva, J., Grimalt, J.O., Labeyrie, L.D., Cortijo, E., Vidal, L., Louis-Turon, J. 1998. Precessional forcing of productivity in the North Atlantic Ocean. *Paleoceanography* 13, 561-571.
- Voelker, A.H.L. 2002. Global distribution of centennial-scale records for Marine Isotope Stage (MIS) 3: a database. *Quat. Sci. Rev.* 21, 1185-1212.
- Wagner, J.D.M., Cole, J.E., Beck, J.W., Patchett, P.J., Henderson, G.M. & Barnett, H.R. 2010. Moisture variability in the southwestern United States linked to abrupt glacial climate change. *Nat. Geosci.* 3, 110-113.
- Wang, X., Auler, A.S., Edwards, R.L., Cheng, H., Cristalli, P.S., Smart, P.L., Richards, D.A., Shen, C. 2004. Northeastern Brazil wet periods linked to distant climate anomalies and rainforest boundary changes. *Nature* 432, 740-743.
- Wang, X., Auler, A.S., Edwards, R.L., Cheng, H., Ito, E., Solheid, M. 2006. Interhemispheric anti-phasing of rainfall during the last glacial period. *Quat. Sci. Rev.* 25(23-24), 3391-3403.
- Wang, Y.J., Cheng, H., Edwards, R.L., An, Z.S., Wu, J.Y., Shen, C.-C., Dorale, J.A. 2001. A High-Resolution Absolute-Dated Late Pleistocene Monsoon Record from Hulu Cave, China. *Science* 294, 2345-2348.
- Wang, X., Edwards, R.L., Auler, A.S., Cheng, H., Kong, X., Wang, Y., Cruz, F.W., Dorale, J.A., Chiang H-W. 2017. Hydroclimate changes across the Amazon lowlands over the past 45,000 years. *Nature* 541, 204-207.
- Weltje, G.J., Tjallingii, R. 2008. Calibration of XRF core scanners for quantitative geochemical logging of sediment cores: Theory and application. *Earth Planet. Sci. Lett.* 274, 423-438.
- Zabel, M., Bickert, T., Dittert, L., Haese, R. 1999. Significance of the sedimentary Al/Ti ratio as an indicator for variations in the circulation patterns of the equatorial North Atlantic. *Paleoceanography* 14(6), 789-799.

. Different precipitation patterns across tropical South America during Heinrich and Dansgaard-Oeschger stadials

- Zhang, X., Lohmann, G., Knorr, G., Purcell, C. 2014a. Abrupt glacial climate shifts controlled by ice sheet changes. *Nature* 512, 290-294.
- Zhang, X., Prange, M., Merkel, U., Schulz, M. 2014b. Instability of the Atlantic overturning circulation during Marine Isotope Stage 3. *Geophys. Res. Lett.* 41, doi:10.1002/2014GL060321.
- Zhang, Y., Chiessi, C.M., Mulitza, S., Zabel, M., Trindade, R.I., Hollanda, M.H.B., Dantas, E.L., Govin, A., Tiedemann, R., Wefer, G. 2015b. Origin of increased terrigenous supply to the NE South American continental margin during Heinrich Stadial 1 and the Younger Dryas. *Earth Planet. Sci. Lett.* 432, 493-500.
- Zhang, Y., Zhang, X., Chiessi, C.M., Mulitza, S., Zhang, X., Lohmann, G., Prange, M., Behling, H., Zabel, M., Govin, A., Sawakuchi, A.O., Cruz, F.W., Wefer, G. 2016. Equatorial Pacific forcing of western Amazonian precipitation during Heinrich Stadial 1. *Sci. Rep.* 6, doi: 10.1038/srep35866.
- Zweng, M.M, Reagan, J.R., Antonov, J.I., Locarnini, R.A., Mishonov, A.V., Boyer, T.P., Garcia, H.E., Baranova, O.K., Johnson, D.R., Seidov, D., Biddle, M.M. 2013. *World Ocean Atlas 2013. 2, Salinity*. S. Levitus, Ed., A. Mishonov Technical Ed.; NOAA Atlas NESDIS 74, 39 pp.

Chapter 4. The thermal response of the western tropical Atlantic to slowdown events of the Atlantic Meridional Overturning Circulation

Stefano Crivellari^{1,*}, Cristiano Mazur Chiessi², Henning Kuhnert³, Christoph Häggi³, Gesine Mollenhauer⁴, Rodrigo da Costa Portilho-Ramos¹, Enno Schefuß³, Stefan Mulitza³

¹Institute of Geosciences – University of São Paulo – São Paulo – Brazil.

²School of Arts, Sciences and Humanities – University of São Paulo – São Paulo – Brazil.

³MARUM – Centre for Marine Environmental Sciences – University of Bremen – Bremen – Germany.

⁴Alfred Wegener Institute for Polar and Marine Research – Bremerhaven – Germany.

Abstract

During millennial-scale changes in the strength of the Atlantic Meridional Overturning Circulation (AMOC) the western tropical Atlantic plays an important role in the redistribution of heat between hemispheres. The proper evaluation of the climatic implications of this mechanism depends on an accurate geographic characterization of sea surface temperature (SST) variations during such events. Published SST reconstructions from the western tropical Atlantic show systematic inconsistencies that are apparently related to the employed temperature proxy (i.e., U^k_{37} versus Mg/Ca). In general, while alkenone values indicate cooling during Heinrich Stadials, Mg/Ca values show warming. In order to better constrain this inconsistency, we sampled core GeoB16224-1 retrieved off French Guiana and reconstructed water temperatures at high resolution using Mg/Ca on the foraminifera species *Globigerinoides ruber*, TEX₈₆, alkenones and modern analogue technique (MAT) transfer functions using planktonic foraminifera assemblages calibrated for 50 m water depth. Our alkenone and Mg/Ca results confirm the previously reported inconsistency. Moreover, MAT-derived temperatures show covariance with alkenone based temperatures. We hypothesize that during severe slowdown events of the AMOC, a steeper meridional temperature gradient together with a southward shift of the Intertropical Convergent Zone (ITCZ) produced not only an increase in SST but also a stronger upper water column stratification and a shoaling of the thermocline, decreasing subsurface temperatures. Mg/Ca and TEX₈₆ results recorded the increase in SST related to AMOC slowdown. On the other hand, alkenone and MAT values registered the decrease in subsurface temperatures triggered by the southward migration of the ITCZ. Our new high-resolution temperature records allow a better

characterization of the thermal response of the upper water column in the tropical western Atlantic to slowdown events of the AMOC, reconciling discrepant records.

4.1 Introduction

When abrupt temperature oscillations observed in Greenland (e.g., Andersen et al., 2004) are compared to Antarctic temperature records (e.g., Barbante et al., 2006), a peculiar antiphasing characterizes millennial-scale events in which Antarctic warming is contemporaneous with North Atlantic cooling. Intervals of heat retention in the southern hemisphere at the expense of heat export to the northern hemisphere were likely caused by slowdown of the Atlantic Meridional Overturning Circulation (AMOC) (Barker et al., 2009; Broecker, 1998; Stocker, 2003). This thermal *bipolar seesaw* (Mix et al., 1986) is the fundamental pattern of sea surface temperatures (SST) in the Atlantic Ocean during millennial-scale climate change events. It is also coherently represented in most water hosing experiments with climate models (Kageyama et al., 2009; Knutti et al., 2004; Liu et al., 2009; Lohmann, 2003).

SST reconstructions from the western tropical Atlantic however, show controversial results. Positive SST anomalies derived from foraminiferal Mg/Ca from the NE Brazilian continental margin have been associated with AMOC slowdown (Nace et al., 2014; Weldeab et al., 2006) during northern hemisphere millennial cold events. Similarly, positive SST_{Mg/Ca} anomalies have also been observed in the Guiana Basin (Crivellari et al., 2018), the western Caribbean Sea (Schmidt et al., 2004) and the Gulf of Mexico (Flower et al., 2004). Positive SST anomalies in the Tobago Basin were derived from planktonic foraminifera-based modern analogue technique (MAT) (Hüls and Zahn, 2000) and alkenones (Rühlemann et al., 1999). Conversely, Jaeschke's et al. (2007) alkenone temperature reconstruction for the NE Brazilian continental margin show consistently colder temperatures during Heinrich Stadials (HS) 4 3 and 2. Similarly, Rama-Corredor's et al. (2015) alkenone paleotemperature record from Guiana Basin also show negative anomalies during these periods.

It emerges that while Mg/Ca-derived SST records show positive anomalies (Weldeab et al., 2006; Nace et al., 2014) during slowdown events of the AMOC, most nearby alkenone-derived SST records show negative anomalies at the same time (Jaeschke et al., 2007; Rama-Corredor et al., 2015). One problem of the Mg/Ca-derived SST reconstructions from the western tropical Atlantic is that they either are low resolution (e.g., Nace et al., 2014) or

encompass only HS1 (e.g., Weldeab et al., 2006). Thus, the sea surface thermal response of the western tropical Atlantic to AMOC slowdown events remains uncertain.

Here we present high resolution temperature records based on *Globigerinoides ruber* Mg/Ca, the alkenone unsaturation index U^k_{37} , TEX₈₆, and planktonic foraminifera-based MAT for the western tropical Atlantic covering the period between 48 – 13 cal ka BP. Our Mg/Ca and TEX₈₆ records show positive temperature anomalies during the HS4 – HS1 slowdown events of the AMOC HS4 - HS1. Nevertheless, our alkenone and MAT temperature reconstructions indicate negative anomalies during HS3 and HS1. Our multiproxy high-resolution temperature reconstruction provides critical information on (i) the thermal behaviour and stratification of the upper water column during HS events, (ii) the transmission of fast climate variability from high latitudes to the tropics, (iii) the usability of the U^k_{37} temperature proxy under the influence of estuarine environments. These topics are of fundamental importance given the essential role of the tropical Atlantic in regulating heat transport across hemispheres (Macdonald and Wunsch, 1996).

4.2 Core location and regional setting

The 760 cm-long gravity core GeoB16224-1 (6°39.38' N, 52°04.99' W, 2510 m water depth) (Fig. 4-1) was retrieved from the continental slope off French Guiana in the western tropical Atlantic during RV MS Merian cruise MSM20/3 (Mulitza et al., 2013). The upper water column at the core site is influenced by the North Brazil Current (NBC) which originates from the northern branch of the South Equatorial Current and flows north-westward into the Caribbean Sea (Stramma et al., 2005). The NBC transports the Amazon River freshwater plume toward the core site delivering a large amount of sediments to the continental margin off French Guiana and to the Caribbean Sea (Allison et al., 2000). The core site is located within the latitudinal range of migration of the Intertropical Convergence Zone (ITCZ) which moves between 12° N (austral winter) and 5° S (austral summer) (Philander et al., 1996; Schneider et al., 2014).

Modern SST is on average 27.7 °C and varies between about 27 °C in January - March and 28 °C in July - September (Locarnini et al., 2013). Modern sea surface salinity (SSS) at the core location is directly influenced by the Amazon River freshwater discharge (Lentz, 1995; Müller-Karger et al., 1988). The annual cycle of SSS ranges from ca. 32 in November – January to ca. 25 in May – July (Salisbury et al., 2011) coinciding with minimum Amazon

. The thermal response of the western tropical Atlantic to slowdown events of the Atlantic Meridional Overturning Circulation

River discharge in November (ca. $0.8 \times 10^5 \text{ m}^3 \text{ sec}^{-1}$) and maximum discharge in May (ca. $2.4 \times 10^5 \text{ m}^3 \text{ sec}^{-1}$), respectively (Lentz, 1995).

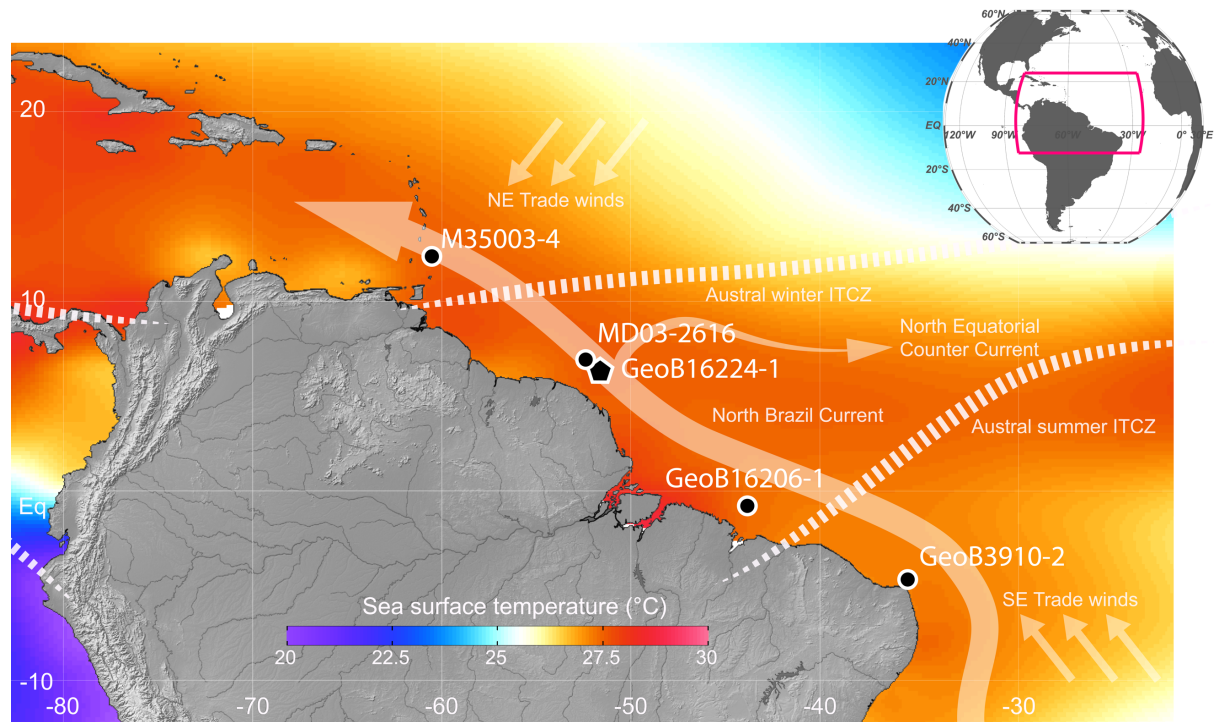


Figure 4-1. Location of marine sediment core GeoB16224-1 investigated in this study (black pentagon), as well as the following other sediment cores mentioned in the text (black circles): M35003-4 (Portilho-Ramos et al., 2017), MD03-2616 (Rama-Corredor et al., 2015), GeoB16206-1 (Portilho-Ramos et al., 2017), GeoB3910-2 (Jaeschke et al., 2007). The northwestward-flowing North Brazil Current and the eastward-flowing North Equatorial Counter Current are represented by the white arrows (Peterson and Stramma, 1991). Schematized provenience of prevalent trade winds is illustrated with group of three white arrows. The dotted lines display the approximate locations of the Intertropical Convergence Zone (ITCZ) during austral winter (June-August) and austral summer (December-February). Annual sea surface temperature is displayed in the color shading (Locarnini et al., 2013).

4.3 Material and methods

4.3.1 Chronology

The age model of sediment core GeoB16224-1 covers the period 48–13 cal ka BP (Fig. 4-2). It is based on fifteen calibrated radiocarbon (^{14}C) ages (Zhang et al., 2015) as well as one tie point beyond the radiocarbon range to the well dated stalagmite stable oxygen isotope ($\delta^{18}\text{O}$) record from El Condor Cave (Cheng et al., 2013) as previously published by

Häggi et al. (2017) (Table 1). For the radiocarbon ages, at least 7 mg of well-preserved specimens of *G. ruber* were analysed via AMS. The age model and associated uncertainties were calculated by using the R script BACON version 2.2 (Blaauw and Christeny, 2011) and the IntCal13 calibration curve (Reimer et al., 2013) with a reservoir correction age of 400 ± 100 yr. (1σ error). This method is the same as in Häggi et al. (2017) and Zhang et al. (2017) for the same core. A total of 10,000 age-depth realizations have been used to calculate the median age and the 1σ analytical uncertainty at 5 mm resolution (Fig. 4-2).

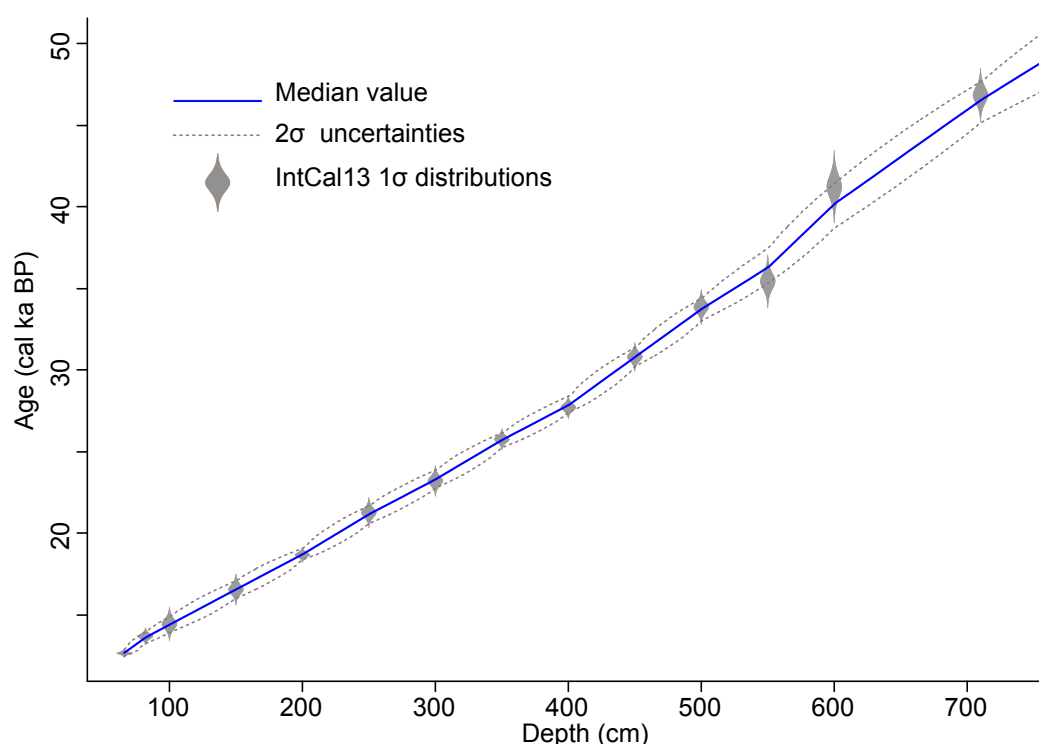


Figure 4-2. Age model of core GeoB16224-1, based on radiocarbon (^{14}C) measurements (grey symbols) by Zhang et al. (2015), also used in the present study. An additional age control point (46830±470 years) at 710 cm core depth was assumed by fitting the Heinrich Stadial 5 Fe/Ca peak from GeoB16224-1 to the well-dated stalagmite from El Condor (Cheng et al., 2013). The age model and associated uncertainties were calculated with the R script BACON version 2.2 (Blaauw and Christeny, 2011) and the IntCal13 calibration curve (Reimer et al., 2013) with a reservoir correction age of 400 ± 100 yr. (1σ error). The construction of the age model follows the methods applied by Zhang et al. (2017) and Häggi et al. (2017) on the same core. Grey dotted lines indicate the analytical uncertainty of the median age (blue line) and the 2σ uncertainty at 5 mm resolution calculated by combining down core Monte Carlo proxy time series realizations. Note that prior to ca 12 cal ka BP there might be a sedimentary hiatus in core GeoB16224-1.

Sediment core	Depth (cm)	Species	Lab. No.	¹⁴ C AMS ages ±1σ error (yr BP)	Calibrated ages ±2σ error (yr BP)
GeoB16224-1	6	<i>G. sacculifer</i> , <i>G. ruber</i>	Poz - 49098	4910 ± 35	5126 ± 80
GeoB16224-1	50	<i>G. sacculifer</i> , <i>G. ruber</i>	Beta - 356373	5920 ± 30	6318 ± 38
GeoB16224-1	66	Mixed planktonic foraminifera	Beta - 377698	11110 ± 30	12635 ± 77
GeoB16224-1	82	Mixed planktonic foraminifera	Beta - 377699	12220 ± 40	13667 ± 152
GeoB16224-1	100	<i>G. sacculifer</i> , <i>G. ruber</i>	Beta - 356374	12760 ± 50	14420 ± 300
GeoB16224-1	150	Mixed planktonic foraminifera	Poz - 49099	14090 ± 70	16537 ± 277
GeoB16224-1	200	<i>G. sacculifer</i> , <i>G. ruber</i>	Beta - 356375	15790 ± 60	18660 ± 137
GeoB16224-1	250	<i>G. sacculifer</i> , <i>G. ruber</i>	Beta - 356376	17980 ± 70	21245 ± 267
GeoB16224-1	300	<i>G. sacculifer</i> , <i>G. ruber</i>	Beta - 356377	19640 ± 80	23193 ± 272
GeoB16224-1	350	<i>G. sacculifer</i> , <i>G. ruber</i>	Beta - 356378	21820 ± 90	25740 ± 189
GeoB16224-1	400	<i>G. sacculifer</i> , <i>G. ruber</i>	Beta - 356379	23980 ± 120	27700 ± 204
GeoB16224-1	450	Mixed planktonic foraminifera	Beta - 356380	26930 ± 140	30792 ± 254
GeoB16224-1	500	Mixed planktonic foraminifera	Beta - 377700	30110 ± 180	33854 ± 310
GeoB16224-1	550	Mixed planktonic foraminifera	Beta - 377701	31950 ± 180	35428 ± 463
GeoB16224-1	600	Mixed planktonic foraminifera	Beta - 377702	37070 ± 180	41222 ± 634
Tie point	710	Stalagmite calcite (Cheng et al., 2013)			46830 ± 470

Table 4-1. Radiocarbon ages employed in the construction of the age model of gravity core GeoB16224-1. AMS radiocarbon ages are from (Zhang et al., 2015). The age at 710 cm has been calculated by matching of the XRF record of core GeoB16224-1 (Zhang et al., 2015) to the El Condor speleothem chronology (Cheng et al., 2013). The radiocarbon ages at 6 cm and at 50 cm were excluded from the age model.

4.3.2 Mg/Ca-based temperatures

Core GeoB16224-1 was sampled every 2 cm for Mg/Ca analyses. Samples for Mg/Ca were wet-sieved, oven-dried at 50 °C overnight, and the residue from the 150 μm mesh sieve stored in glass vials. Hand picking of foraminiferal tests was performed under a binocular microscope. Foraminiferal tests were selected to fit sizes between 250 and 350 μm, free of adherent particles or chamber fillings. Each sample was picked for *G. ruber* (white) sensu stricto (Wang, 2000) for a total of 311 samples. Between 20 and 30 specimens of *G. ruber* were crushed and cleaned following the protocol described by Barker et al. (2003). The analytical procedure is identical to that described by Kuhnert and Mulitza (2011). Measurements were carried out on a ThermoQuest Element2 sector field inductively coupled plasma–mass spectrometer at the University of Bremen. Elemental concentrations were inferred from analysing the isotopes ²⁵Mg and ⁴³Ca in low instrument resolution and ²⁷Al and ⁵⁵Mn in medium resolution. For Mg and Ca concentrations, the analytical error (±1 standard

error of the mean, based on 10 runs) was always better than 0.2 %. The reproducibility of replicates from the same solutions measured on different days was 0.9 % on average.

The effectiveness of the cleaning procedure was monitored based on the Mn/Ca and Al/Ca ratios. Al/Ca (indicative of clay minerals) was usually below 0.1 mmol/mol, and samples with > 0.3 mmol/mol were discarded. Mn/Ca was 260 μ mol/mol on average. Mn/Ca and Mg/Ca showed inverse trends during the deglacial and were otherwise uncorrelated, indicating that Mn-bearing phases did not influence Mg/Ca through the addition of Mg.

We used the calibration equation from Regenberg et al. (2009) to calculate SST: $Mg/Ca = 0.4 \exp(0.094 * SST)$.

The core site lies well above the modern and glacial lysocline (Volbers and Henrich, 2004), and core GeoB16224-1 shows low shell fragmentation index (Zhang et al., 2017). Therefore, we assume planktonic foraminiferal faunal composition and Mg/Ca paleotemperature to be unaffected by dissolution.

4.3.3 $U^{k'}_{37}$ and TEX₈₆-based temperatures

In this study we use two independent biomarker-based proxies. On the one hand, we use the $U^{k'}_{37}$ index based on the temperature dependent under saturation of long-chain alkenones produced by haptophyte algae (Prah and Wakeham 1987). On the other hand, we use the TEX₈₆ index based on the distribution of isoprenoid Glycerol Dialkyl Glycerol Tetraether produced by crenarchaeota (Schouten et al. 2002).

The $U^{k'}_{37}$ index has been successfully applied in many areas and is thought to reflect temperatures in the mixed zone, where autotroph productivity is highest (e.g., Müller 1998). Under strong riverine influence there is however a potential underestimation of $U^{k'}_{37}$ based temperature values likely caused by adverse conditions for haptophyte algae due to light limitation and low salinity in sediment rich river plumes (Häggi et al. 2015). For $U^{k'}_{37}$ temperature reconstructions we used the calibration by Müller et al. 1998.

$$U^{k'}_{37} = \frac{C_{37:2}}{C_{37:2} + C_{37:3}}$$

with $SST = U^{k'}_{37} / 0.033 - 0.069$

The TEX_{86} index has been reported to reflect subsurface temperatures (Huguet et al. 2007). Recent studies however suggest that TEX_{86} temperatures can represent a great depth range (Hurley et al., 2017). Riverine input has also been reported to impact TEX_{86} temperatures and is potentially important when the BIT index value describing the relative abundance of terrigenous branched GDGTs and crenarchaeol is above 0.3 (Weijers 2006). At our core site, BIT is consistently >0.3 (data not shown). One way to circumvent potential interference of riverine produced crenarchaeol is to use the updated TEX_{86L} index, which does not include crenarchaeol (Kim et al. 2010). Hence, we used the TEX_{86L} index for our reconstructions.

$$TEX_{86L} = \log \frac{GDGT\ II}{GDGT\ I + GDGT\ II + GDGT\ III}$$

with $SST = 67.5 * TEX_{86L} + 46.9$.

For comparison we also used the TEX_{86H} index, specifically calibrated for areas with $SST > 15\ ^\circ C$ (Kim et al. 2015).

$$TEX_{86H} = \log \frac{GDGT\ II + GDGT\ III + Cren'}{GDGT\ I + GDGT\ II + GDGT\ III + Cren'}$$

with $SST = 68.4 * TEX_{86H} + 38.6$.

Biomarker based temperature reconstructions were performed on the same sample set as described in Haggi et al. (2017). Lipid extraction and separation procedures followed the same protocol as described in Haggi et al. (2016). In short, this included ASE extraction with dichloromethane : methanol 9:1 on freeze-dried and homogenized sediment samples, subsequent saponification and separation over silica gel columns into apolar hydrocarbon, ketone and polar fractions using hexane, dichloromethane and dichloromethane: methanol 1:1 as subsequent eluents. U^k_{37} measurements were conducted on the ketone fraction using a Thermo Fisher Scientific Focus gas chromatograph equipped with a 30m Rxi™-5ms column (30 m, 0.25 mm, 0.25 μm) and a flame ionization detector. Alkenones were quantified by comparing the integrated peak areas of the compounds to external standard solutions.

GDGT measurements were conducted on the polar fraction and are described in detail in Crivellari et al. (2018).

4.3.4 Planktonic foraminiferal assemblage and MAT-based temperatures

Subsurface temperatures were estimated from a planktonic foraminifera transfer function determined by the modern analogue technique (MAT) using the software C2 (Juggins, 2003). Planktonic foraminifera assemblage from core GeoB16224-1 were dry picked from the >150 μm size fraction and quantified in relative abundances from splits containing more than 300 specimens per sample. The taxonomy was based on Stainforth et al. (1975) and Hemleben et al. (1989). The planktonic foraminifera calibration dataset used here comprised 407 surface samples from the Atlantic Ocean between 30° N and 30° S from the MARGO database (Kucera et al., 2005a, 2005b). Since (i) ca. 70% of the planktonic foraminifera species present in our core (*i.e.*, *G. ruber*, *Globigerinoides sacculifer*, *Globigerina glutinata* and *Globigerinella siphonifera*) inhabit the upper 60 m of the water column (Ravelo et al., 1990; Schmuker and Schiebel, 2002; Steph et al., 2009) and (ii) reconstructions derived from transfer functions based on planktonic foraminifera in the tropical Atlantic are more sensitive to subsurface than surface temperatures (Telford et al., 2013), we extracted and calibrated the modern annual temperature values for 50m water depth from WOA 2013 (Locarnini et al., 2013), following Portilho-Ramos et al. (2017). For our MAT transfer function we employed the squared chord distance as a similarity measure and used the weighted mean of the best 10 modern analogues as reconstruction result (Kucera et al., 2005a). Using the leave-one-out cross-validation method, the root mean square error of prediction (RMSEP) of the transfer function was calculated as 1.02 °C ($R^2=0.90$).

4.4 Results

4.4.1 Mg/Ca temperatures

Mg/Ca (temperature) values range between 3.02 and 5.05 mol/mol (21.5 – 27 °C; Fig. 4-3b). Background glacial temperatures cluster around 23.5 °C. On top of a long-term cooling from 48 until ca. 19 cal ka BP, five distinct positive temperature anomalies correspond to HS5 to HS1 (Fig. 4-3b). Temperature increases amounted to 1.5 – 2 °C for HS5, HS4, HS1,

and 1 – 1.5 °C during HS3 and HS2. Prior to 30 cal ka BP, Mg/Ca-based temperatures show higher variability relative to the interval 30 – 13 cal ka BP.

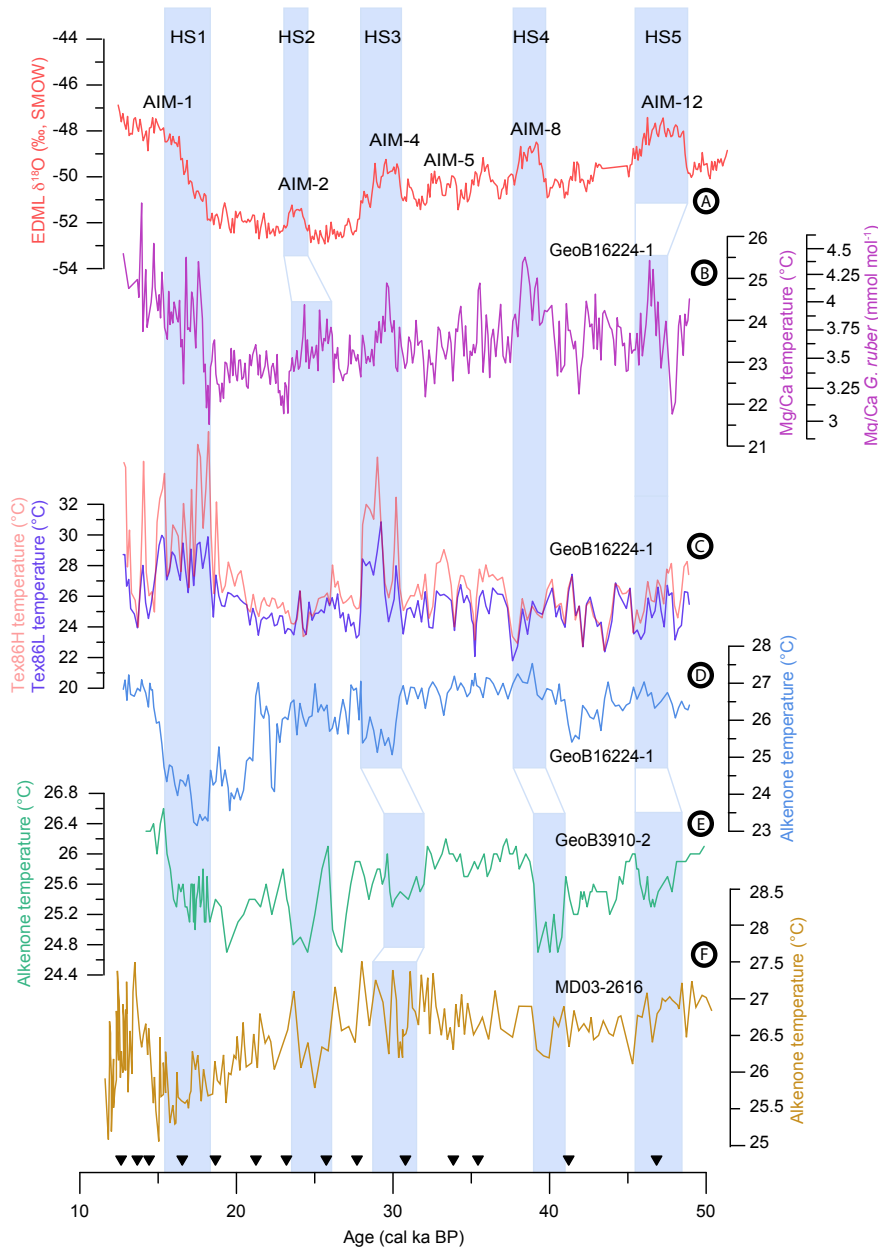


Figure 4-3. Temperature proxy records from gravity core GeoB16224-1 together with $U^{k'37}$ temperatures from the Guiana Basin and off NE Brazil, as well as an Antarctic stable oxygen isotope ($\delta^{18}O$) record. (a) $\delta^{18}O$ record from the EPICA Dronning Maud Land (EDML) ice core. Antarctica Isotope Maxima (AIM) are labeled above each event (Barbante et al., 2006). (b) *Globigerinoides ruber* Mg/Ca-based temperatures from core GeoB16224-1 (this study). (c) TEX₈₆H and TEX₈₆L-based temperatures from core GeoB16224-1 (this study). (d) $U^{k'37}$ temperatures from core GeoB16224-1 (this study). (e) $U^{k'37}$ temperatures from core GeoB3910-2 retrieved off NE Brazil (Jaeschke et al., 2007). (f) $U^{k'37}$ temperatures from core MD03-2616 retrieved from the Guiana Basin (Rama-Corredor et al., 2015). Black triangles over the horizontal axis show the calibrated radiocarbon ages of core GeoB16224-1 as well as the tie-point used to produce its age model. The Heinrich Stadial (HS) events 5 to 1 are indicated by the blue bars.

4.4.2 TEX₈₆L temperatures and crenarchaeol concentrations

TEX₈₆L-based temperatures display a similar variability as Mg/Ca-SST (Fig. 4-3b,c). Background glacial temperatures of ca. 24 °C are comparable with the Mg/Ca temperatures. Prior to ca. 30 cal ka BP, the variability is higher relative to the interval 30 - 13 cal ka BP. Two outstanding positive temperature anomalies are detected during HS3 and HS1. Both events show warming by ca. 2 °C. A minor warming event of ca. 1.5 °C is also detected during HS2. Although the TEX₈₆L record registered clear warming during HS3 - 1, no positive temperature anomaly is present during HS 5 and 4.

We further compared ln(Fe/Ca) and crenarchaeol concentration in the sediment in order to identify unusual crenarchaeol sources. We notice a long-term decrease in concentration in crenarchaeol over the investigated period (Fig. 4-4c). However, if sedimentation rates are taken into account, no appreciable long-term change in crenarchaeol flux is observed. A high degree of variability characterizes the period between 48 and 40 cal ka BP. From 40 cal ka BP onward, background values of ca. 300 ng/g are interposed by 100 – 150 ng/g increases during HS4 - 2 and late HS1.

4.4.3 U^k₃₇ temperatures

Our U^k₃₇ temperature record has a different geometry with respect to Mg/Ca and TEX₈₆L temperature reconstructions (Fig. 4-3b-d). Long term U^k₃₇temperatures remain mostly unchanged from 48 cal ka BP until ca. 30 cal ka BP. Subsequently, a cooling trend culminates between the Last Glacial Maximum (LGM) and HS1. At HS1 the record shows a negative anomaly of up to 3 °C even though the timing is poorly constrained. A sudden warming characterizes the transition from HS1 to the Bølling-Allerød. During HS2, no significant variation is observed. HS3 shows again a clear (ca. 1 °C) decrease in U^k₃₇temperatures as well as between 44 and 41 cal ka BP. The long-term variability and background temperatures in our U^k₃₇ record match those from nearby core MD03-2616 (Rama-Corredor et al., 2015) (Fig. 4-3d, f) which is located ca. 130 km north-westward from our site (Fig. 4-1). The MD03-2616 U^k₃₇ temperatures show negative anomalies during HS4, HS2 and HS1 but to a smaller extent (up to 1.5 °C). Glacial background temperatures of the two records are comparable, as are the timings of the onset of pre-LGM cooling trends. Some differences occur; generally, the magnitude of long-term temperature changes in

GeoB16224-1 is greater than that in MD03-2616. Moreover, negative temperature anomalies for HS4 and HS2 in core MD03-2616 are not reproduced by our core. In contrast, the cooling event coinciding with HS3 in our core is not clearly detectable in core MD03-2616. During HS1, glacial cooling continues in both MD03-2616 and GeoB16224-1. In both records, the termination of HS1 is characterized by an abrupt warming trend starting at ca. 15 cal ka BP. Both records do not register increasing temperatures during HS. Negative temperature anomalies are also found in core GeoB3910-2 for HS5 - 2 (Jaeschke et al., 2007). $U^{k'}_{37}$ derived temperature from our core and from core MD03-2616 cool from ca 30 cal ka BP onward; this trend is not present in neither $TEX_{86}L$ nor Mg/Ca temperatures.

4.4.4 Planktonic foraminiferal assemblage and MAT-based temperatures

The subsurface temperature at 50m-water depth derived from MAT was reconstructed for the period between 33–13 cal ka BP (Fig. 4-5e). It ranged from 22 °C to 26.6 °C with occasional sharp negative excursions of 2.8 °C – 3.6 °C corresponding to HS3 -1 (Fig. 4-5e). Despite differences in sampling resolution, negative excursions in subsurface temperatures show opposite trends in comparison to warm surface temperature derived by Mg/Ca. They are, however, in-phase with $U^{k'}_{37}$ temperatures during these millennial-scale paleoclimatic events (Fig. 4-5e). The trend common to the MAT-derived and the $U^{k'}_{37}$ temperatures suggests that both proxies represent the same environment, i.e., the subsurface rather than surface.

4.5 Discussion

4.5.1 Mg/Ca temperature record from GeoB16224-1 compared to other reconstructions

Mg/Ca-based temperatures from core GeoB16224-1 unequivocally show warming events concomitantly to all HS since ca. 48 cal ka BP (Fig. 4-3a). Additionally, we find a remarkably good agreement between our Mg/Ca-based temperature record and $\delta^{18}O$ from Antarctica ice core EDML (Barbante et al., 2006) (Fig. 4-3b). Barbante et al. (2006) defined the increases in the EDML $\delta^{18}O$ record as Antarctic Isotope Maxima (AIM) which are connected to warming events in the Atlantic sector of the Southern Ocean. AIM 12, 8, 2, 4

and 1 are well represented in our Mg/Ca temperature record and correspond to reduced northward heat flux in the Atlantic due to a weak AMOC (Barker et al., 2009; Broecker, 1998; Stocker, 2003).

Our Mg/Ca-based temperature reconstruction agrees well with other temperature reconstructions from the tropical western Atlantic. Upper ocean temperature records from off NE Brazil (Weldeab et al., 2006; Nace et al., 2014), the Orca Basin (Williams et al., 2010), Colombia Basin (Schmidt et al., 2004), Cariaco Basin (Schmidt et al., 2012) and Tobago Basin (Rühlemann et al., 1999), show warm HS. Nevertheless, our Mg/Ca results do not agree with $U^{k'}_{37}$ temperature reconstructions from GeoB16224-1 (this study) and nearby sites (i.e., ca. 130 km to the northeast, core MD03-2616; Rama-Corredor et al., 2015) or further southeast off NE Brazil (i.e., ca. 2130 km to the southeast, core GeoB3910-2; Jaeschke et al. 2007), where evidence for negative upper ocean temperature anomalies during HS have been reported (Figs. 4-1, 4-3e,f). Apparently, the reconstructed upper ocean temperature response to changes in AMOC strength seems to be related to the analytical method itself, namely if Mg/Ca or $U^{k'}_{37}$. While Mg/Ca-based reconstructions show warming during HS (Schmidt et al., 2004, 2012; Weldeab et al., 2006; Williams et al., 2010; Nace et al., 2014), $U^{k'}_{37}$ temperatures tend to show cooling instead (Jaeschke et al. 2007; Rama-Corredor et al., 2015).

Jaeschke et al. (2007) recognized the disagreement of their $U^{k'}_{37}$ temperature record with the Mg/Ca-based temperature record from Weldeab et al. (2006) and argued that re-suspension and advection of alkenone molecules were responsible for colder temperatures during HS1. Although other HS have not been directly addressed in their study, Jaeschke et al. (2007) further suggest that temperatures in the western tropical Atlantic might be affected by glacial boundary conditions. Ice sheet coverage and colder global temperatures could determine a northern hemisphere teleconnection, with negative temperature anomalies during HS (Jaeschke et al., 2007). Rama-Corredor et al. (2015) suggested that cool $U^{k'}_{37}$ temperatures during HS in the western tropical Atlantic are a response to the sudden freshening and cooling of the North Atlantic by the propagation of Kelvin and Rossby waves. These waves would be responsible for the transmission of colder temperatures towards low Atlantic latitudes. Yet, most of the paleotemperature records and model outputs indicate an increase in western tropical Atlantic SST during events of AMOC slowdown resulting from the decrease in the northward heat transport (Kageyama et al., 2009; Knutti et al., 2004; Liu et al., 2009; Lohmann, 2003).

4.5.2 $U^{k'_{37}}$ and TEX_{86L} temperature records from GeoB16224-1 compared to other reconstructions

Similarly to the Mg/Ca-based temperature record, the TEX_{86L} -based temperature reconstruction indicates positive temperature anomalies during HS3 - 1 (Fig. 4-3b,c). Warming events in both records are comparable in duration, timing and amplitude, suggesting that both proxies reflect the same thermal conditions. However, the expected HS5 and HS4 positive temperature anomalies are not represented in our TEX_{86L} record. The higher variance present in this portion of the TEX_{86L} record may mask a positive temperature anomaly during HS5 and HS4.

Our $U^{k'_{37}}$ temperature reconstruction shows important differences relative to our Mg/Ca and TEX_{86L} temperature records and has a clear antiphase behaviour during HS1 and HS3 (Fig. 4-3c,d). On the other hand, our $U^{k'_{37}}$ temperature reconstruction shares similarities with other $U^{k'_{37}}$ temperature records from Guiana Basin and NE Brazil (Fig. 4-3d-f) (Jaeschke et al., 2007; Rama-Corredor et al., 2015). For instance, we find negative temperature anomalies during HS3 - 1 similar to the negative temperature anomalies on HS5 and HS4 of the $U^{k'_{37}}$ record from Jaeschke et al. (2007).

Other examples of upper ocean temperature divergence between Mg/Ca- and $U^{k'_{37}}$ records have been reported from the eastern tropical Atlantic (Leduc et al., 2010; Weldeab et al., 2007). The work from Leduc et al. (2010) features a comprehensive compilation of Mg/Ca and $U^{k'_{37}}$ temperature reconstructions and identifies contrasting or divergent SST evolution in low latitudes. Weldeab et al. (2007) described Holocene warming and cooling trends for Mg/Ca- and $U^{k'_{37}}$ reconstructions, respectively. A strong seasonal influence in the local hydrography and nutrient input from the Niger River in the Gulf of Guinea were suggested as the cause of the $U^{k'_{37}}$ temperature divergence from Mg/Ca (Weldeab et al., 2007). These hydrological conditions are analogous to those at our core site where strong terrestrial discharge from the Amazon River is taking place during HSs.

4.5.3 Considerations on the use of Mg/Ca, TEX_{86L} and $U^{k'_{37}}$ as temperature proxies

The preference of *G. ruber* for oligotrophic waters (e.g., Hemleben et al., 1989) makes this species particularly suited as a signal carrier of upper water column conditions in the western tropical Atlantic (e.g., Hu et al., 2004). Core top investigations on *G. ruber* ecology show a strict preference for a surface habitat (Chiessi et al., 2007; Farmer et al., 2007; Steph

et al., 2009), even in the presence of low salinity surface water lenses (Crivellari et al., 2018). Our core site is located in well ventilated non-abyssal depths (Volbers and Henrich, 2004) and core GeoB16224-1 shows a low foraminiferal shell fragmentation index during HS4 - 1 (Zhang et al., 2017). Therefore, we can safely assume that *G. ruber* Mg/Ca strictly reflects surface temperatures unaffected by dissolution.

TEX₈₆ is apparently not affected by water salinity and nutrient concentration (Wuchter et al., 2004), nor by grazing and digestion of zooplankton (Huguet et al., 2006). However there are potential uncertainties in the use of TEX₈₆ which is affected by a high input of terrestrial organic matter (Weijers et al., 2006) and seasonality (Herfort et al., 2006; Schouten et al., 2002; Sluijs et al., 2006). GDGT export to the sedimentary record may take place at various depths depending on the structure of the water column and the ecology of ammonia-oxidizing Thaumarchaeota (Tierney, 2013). Regions with steep nutri-thermocline such as upwelling zones may force a subsurface temperature signal on the TEX₈₆ (Chen et al., 2014; Kim et al., 2012; Lopes et al., 2010). In the western Atlantic it has been observed that GDGT export occurs from a layer nominally associated with a peak in ammonia concentration which coincides with sub-thermocline depths (Hurley et al., 2017). Nevertheless, if the GDGT export is compared to in-situ temperature measurements in the western Atlantic, TEX₈₆ derived temperatures are apparently unrelated to the export depth window but are rather well correlated with surface water temperatures instead (Hurley et al., 2017). Our TEX_{86L} temperature record from GeoB16224-1 has a comparable or slightly higher background temperature relative to Mg/Ca suggesting that reconstructed TEX_{86L} temperature is likely tracking surface thermal conditions.

Even though the background temperatures registered by the TEX_{86H} record are in alignment with other SST reconstructions (Jaeschke et al., 2007; Weldeab et al., 2006), the positive SST anomalies observed during HS3 and HS1 yield unrealistically high values (i.e., 34 – 36 °C during HS3 and HS1, Fig. 4-3c). When the fractional abundances of the individual isoprenoid GDGT are considered, we notice that crenarchaeol tends to resemble the ln(Fe/Ca) on HS3 - 1 in spite of crenarchaeol being predominantly supplied from the marine domain (Fig. 4-4b,c). Increase in ln(Fe/Ca) is consistent with an increase in terrigenous discharge due to increased precipitation during HS (Zhang et al., 2015, 2017). This suggests that crenarchaeol seems to be supplied, at least in part, also from land, which might have affected the TEX_{86H} temperature reconstruction during stadials. In fact, if we adopt the TEX_{86L}

calibration, which excludes the crenarchaeol isomer from the calculation (Kim et al., 2010), colder peak values of ca. 29 °C characterize the warmings at HS3 and HS1 (Fig. 4-3c).

It is possible that non-thermal physiological effects are also partially responsible for the departure between Mg/Ca- and $U^{k'}_{37}$ temperature reconstructions. *Emiliana huxleyi* culture experiments from Prahl et al. (2006) showed that the $U^{k'}_{37}$ signature in marine sediments tends to represent the history of stressed populations whereby the presence of nutrient stress conditions produces a temperature bias towards lower values. Excess of terrigenous input can cause bloom events that, although associated with high nutrient abundance, are ultimately terminated with nutrient deficiency at the sea surface by the intense grazing activity and enhanced biological pump (Miller, 2004). Culture experiments from several authors show that temperature underestimation may arise under distressed conditions of nutrient deprivation (Epstein et al., 1998; Prahl, 2003; Versteegh et al., 2001). Zhang et al. (2017) found that high $\ln(\text{Fe}/\text{Ca})$ in core GeoB16224-1 occurs synchronously with low alkenone C_{37} concentrations during both H and DO stadials. This has been interpreted as decreased primary productivity during periods of high terrigenous input, due to an increase in the suspended sediment load causing less favourable conditions for haptophyte proliferation (Häggi et al., 2015). $U^{k'}_{37}$ negative temperature anomalies in GeoB16224-1 during HS3 and HS1 are indeed associated with an increase in terrigenous input (Fig. 4-5d). This could indicate that the cooler temperatures recorded by the $U^{k'}_{37}$ may stem from low salinity conditions and general distressed conditions in the upper mixed layer (Häggi et al. 2015).

A similar high terrigenous input regime at site MD03-2616 (Rama-Corredor et al., 2015) may have equally biased the $U^{k'}_{37}$ negative temperature anomalies registered during slowdown events of the AMOC at that site (Fig. 4-3f). Since no indicator for terrigenous flux is available for core MD03-2616, we rely on the dataset from core GeoB16224-1, which is located ca. 130 km to the south-east (Fig. 4-1) to substantiate this assumption.

Importantly, the $U^{k'}_{37}$ temperature reconstruction from the open waters of the Tobago Basin, deviate from the other $U^{k'}_{37}$ temperature reconstructions from the tropical western Atlantic (i.e., Jaeschke et al., 2007; Rama-Corredor et al., 2015; this study) by showing positive temperature anomalies during HS2 and HS1 (Fig. 4-5b) (Rühlemann et al., 1999), in agreement with nearby Mg/Ca-based temperature reconstructions (i.e., Schmidt et al., 2004; Williams et al., 2010) and lower latitude Mg/Ca records as well (Weldeab et al., 2006; this study). At the Tobago Basin, terrigenous influence from the Orinoco river would be at its

minimum because of the typically arid northern South American hydroclimate during HS associated with a southward shift of the ITCZ (Deplazes et al., 2013; Escobar et al., 2012; Peterson, 2000; Zhang et al., 2017).

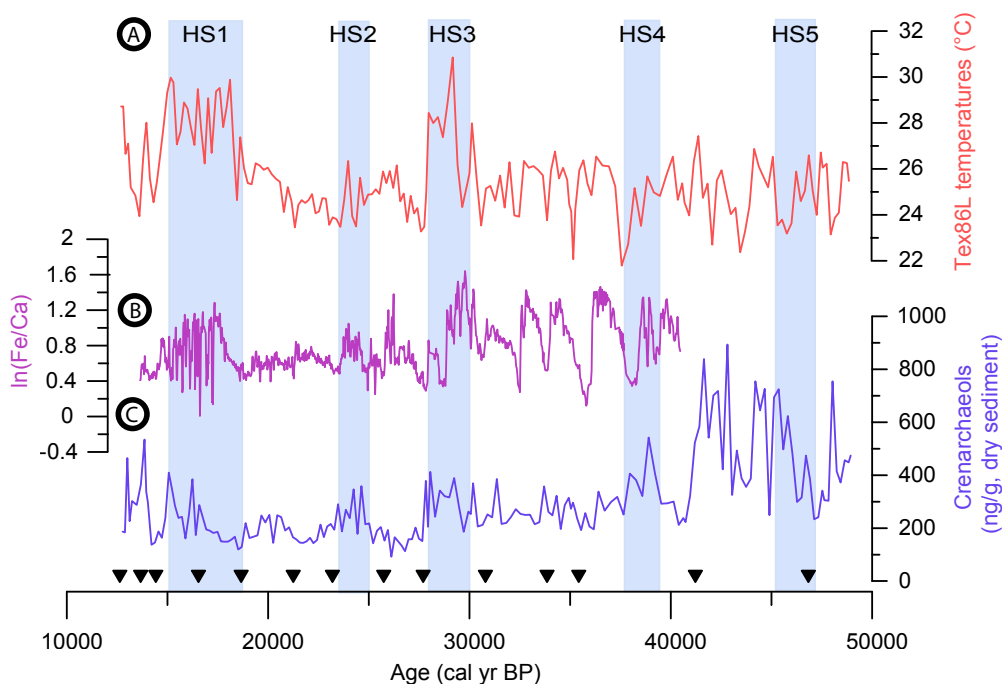


Figure 4-4. Comparison between TEX₈₆L-based temperatures, ln (Fe/Ca) (indicating terrigenous input), and concentration of crenarchaeol (marine GDGTs) indicating from core GeoB16224-1. (a) TEX₈₆L-based temperatures from core GeoB16224-1 (this study). (b) ln(Fe/Ca) from core GeoB16224-1 (Zhang et al., 2017). (c) Crenarchaeol concentration normalized for sample weight from core GeoB16224-1 (this study). Black triangles as in Fig. 4-3. The Heinrich Stadial (HS) events 5 to 1 are indicated by the blue bars.

4.5.4 Possible effects of seasonality on U^k₃₇ temperature reconstructions

Seasonal variability in the production of alkenones can exert a strong influence on U^k₃₇ temperatures (Turich et al., 2013). During austral winter the ITCZ is at its northernmost position and the zonal winds are dominated by the SE trade winds that blow along-shore. This, in turn, could add the effect of Ekman upwelling and shoaling of the nutrient-thermocline, further reducing subsurface temperatures. These conditions have been linked to increased accumulation of coccolithophorids in the western tropical Atlantic (Gibbs, 1980;

López-Otálvaro et al., 2008). However, this scenario is not compatible with the HS boundary conditions in which the low level tropical Atlantic wind field would be dominated by NE trade winds instead of the SE trade winds (Baker et al., 2001; Broccoli, 2000; Zhang et al., 2016). Moreover, we could not find any indication of increased upwelling throughout GeoB16224-1 record, as evidenced by the lack of upwelling indicators in the planktic foraminifera assemblage and oxygen stable isotopes (not shown).

During the season of peak discharge by the Amazon River (May-July) (Salisbury et al., 2011), the increase in the nutrient supply could favour silicate-producing nannoplankton (i.e., diatoms) outcompeting alkenone producing haptophyte algae (i.e., Haake et al., 1993; Sancetta, 1995; Weldeab et al., 2007). This could shift the main coccolithophorids export to a season of about 1 °C colder SSTs and low river discharge. Nevertheless, the modern seasonal SST amplitude is incapable to fully explain the observed negative temperature anomalies in the U^{k}_{37} record on GeoB16224-1 during HS.

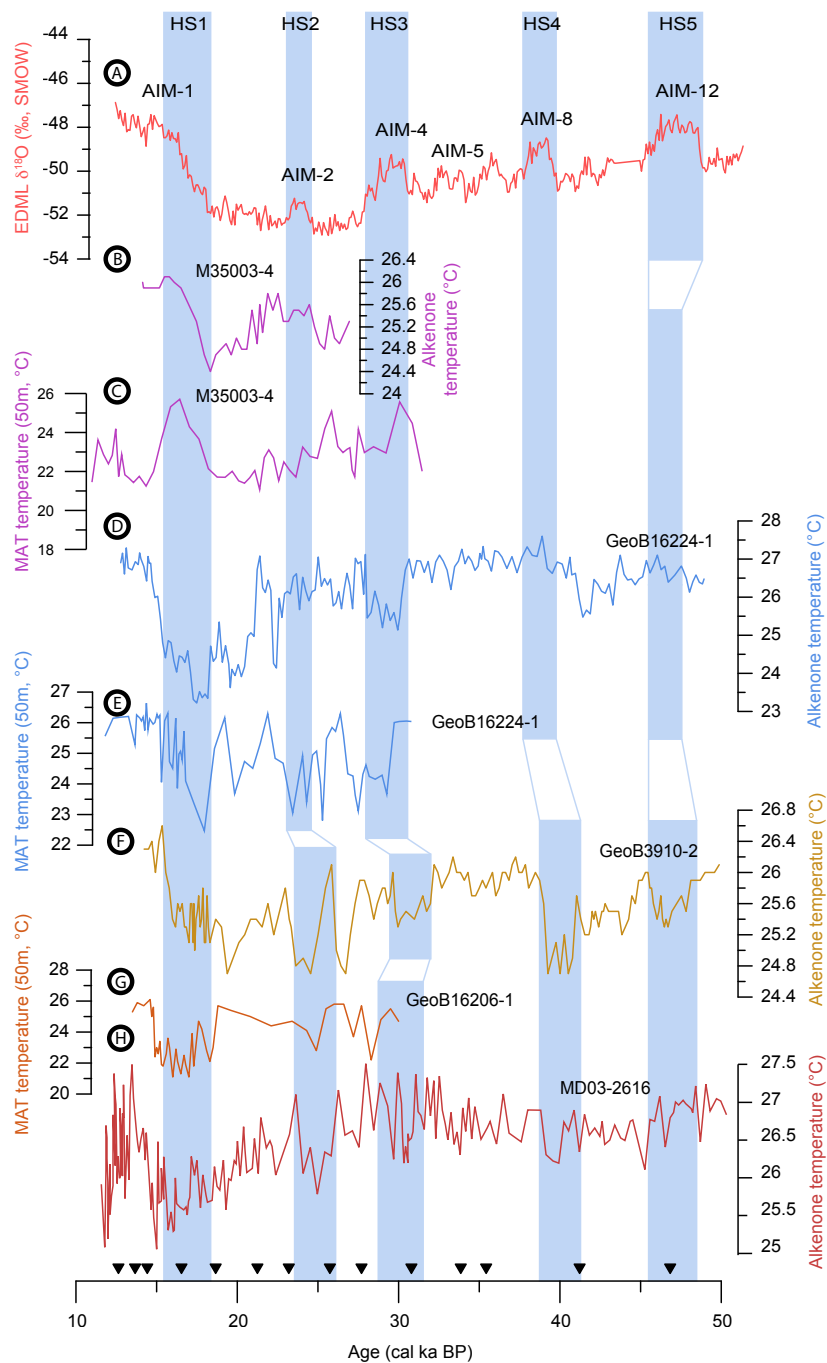


Figure 4-5. Comparison between the U^{k}_{37} and modern analog technique (MAT)-based temperature records from gravity core GeoB16224-1 with U^{k}_{37} and MAT-based temperature reconstructions from other locations in the western tropical Atlantic. (a) Stable oxygen isotope ($\delta^{18}O$) record from the EPICA Dronning Maud Land (EDML) ice core. Antarctic Isotope Maxima (AIM) are labeled above each event (Barbante et al., 2006). (b) U^{k}_{37} temperatures from core M35003-4 from the Tobago Basin (Rühlemann et al., 1999). (c) MAT temperatures from core M35003-4 (Portilho-Ramos et al., 2017; Hüls and Zahn, 2000). (d) U^{k}_{37} temperatures from core GeoB16224-1 (this study). (e) MAT temperatures from core GeoB16224-1 (this study). (f) U^{k}_{37} temperatures from core GeoB3910-2 retrieved off NE Brazil (Jaeschke et al., 2007). (g) MAT temperatures from core GeoB16206-1 (Portilho-Ramos et al., 2017). (h) U^{k}_{37} temperatures from core MD03-2616 from the Guiana Basin (Rama-Corredor et al., 2015). Black triangles as in Fig. 4-3. The Heinrich Stadial (HS) events 5 to 1 are indicated by the blue bars.

4.5.5 Subsurface sensitivity of $U^{k'}_{37}$ temperatures and MAT-based temperatures from GeoB16224-1

Our reconstructed MAT subsurface temperatures (50 m) and $U^{k'}_{37}$ temperatures show negative anomalies during HS3 - 1 (Fig. 4-5e). This is consistent with a subsurface cooling associated with the meridional shift of the ITCZ and the consequent freshening and increased stratification of the upper water column (Portilho-Ramos et al., 2017). In GeoB16224-1 increases in $\ln(\text{Fe}/\text{Ca})$ are associated with reduced alkenone concentrations and lower C_{37}/C_{38} ratios (Zhang et al., 2017). This has been interpreted as reduced abundance of open ocean haptophytes, which indicates more coastal (or freshwater) haptophytes resulting from a shallow mixed layer when the ITCZ passes over the region.

Similarly, off NE Brazil (core GeoB16206-1, Fig. 4-1), the southward migration of the ITCZ causes the development of a rainfall-induced shallow mixed layer. The prolonged ITCZ residency and the related increase in rainfall determine an increase in water stratification and a shoaling of the nutri-thermocline (de Boyer Montégut et al., 2007; Mignot et al., 2007). In fact MAT (50 m) temperatures from core GeoB16206-1 show subsurface cooling during HS2, HS1 and the Younger Dryas (Portilho-Ramos et al., 2017, Fig. 4-5g).

Analogously, reconstructed temperatures using $U^{k'}_{37}$ and MAT (50 m) from the Tobago Basin (core M35003-4, Fig. 4-1) indicate warmer temperatures and a deepening of the thermocline (Portilho-Ramos et al., 2017; Rühlemann et al., 1999) during HS3 - 1 (Fig. 4-5c). During Heinrich-like events, the southward migration of the ITCZ causes dryer conditions over northern South America decreasing the Orinoco River output. Less stratified waters lead to a deeper nutri-thermocline (Peterson et al., 2000; Vink et al., 2000, 2001, 2002).

Meridional movements of the ITCZ change upper water column stratification which is related to the strength of the barrier layer. A low salinity surface layer reduces the downward flux of heat and promotes colder temperatures at the subsurface. Based on our MAT (50 m) results we argue that the colder temperatures registered by the $U^{k'}_{37}$ during HS, despite the abundance of Mg/Ca records showing warmer SST, could be explained by sensitivity of $U^{k'}_{37}$ to subsurface rather than to sea surface temperatures.

The suggestion of a subsurface temperature signal recorded by $U^{k'}_{37}$ has also been put forward by other authors. The influence of temperatures reflecting the chlorophyll maximum in $U^{k'}_{37}$ records has been suggested for the Cariaco Basin (Goñi et al., 2003; Turich et al., 2013). Similar results were obtained in the Mediterranean Sea that indicate alkenones are

primarily synthesized at depths of highest primary production (Bentaleb et al., 1999). A sediment trap study in the Arabian Sea has also shown that $U^{k'}_{37}$ temperatures fit best with subsurface temperatures during boreal fall and spring intermonsoon periods (Prahl et al., 2000).

A subsurface signal recorded in $U^{k'}_{37}$ temperature records from the western tropical Atlantic could also explain why the $U^{k'}_{37}$ reconstruction off NE Brazil (Jaeschke et al., 2007) shows negative anomalies during HS5 and HS4 (Fig. 4-3e), whereas our record and the one from Rama-Corredor et al. (2014) show no significant temperature changes throughout these events (Fig. 4-3d, f). The southernmost position reached by the ITCZ is ca. 1 °S (Portilho-Ramos et al., 2017 and references therein) causing a much stronger water stratification at locations proximal to core site GeoB3910-2 (Jaeschke et al., 2007), relative to latitudes of ca. 6° N close to the location of GeoB16224-1 and MD03-2616 (Rama-Corredor et al., 2014) (Fig. 4-1).

We consider likely that the divergence between Mg/Ca or TEX₈₆L and $U^{k'}_{37}$ temperatures from GeoB16224-1 result from the ecological preferences of alkenone producing algae to subsurface depths in the water column. The thermal signal recorded by $U^{k'}_{37}$ in the western tropical Atlantic likely reflects vertical movements of the thermocline which respond to increase (decrease) in the stratification of the upper water column during periods of increased (decreased) direct ITCZ-related precipitation and Amazonian river discharge (de Boyer Montégut et al., 2007; Mignot et al., 2007). Additionally, at our core site, a likely contribution to the increased stratification of the upper water column is deriving from the stronger fresh water outflow of the Amazon River during HSs (Crivellari et al., 2018). Consequent increase in terrigenous discharge during the same intervals, could impart a colder non-thermal effect to $U^{k'}_{37}$ temperatures that would sum to the effect of a lower subsurface temperature (Häggi et al., 2015; Zhang et al., 2015).

4.6 Conclusions

The examination of four independent temperature proxies from sediment core GeoB16224-1 shows the thermal response of the upper water column of the western tropical Atlantic to slowdown events of the AMOC. Different proxies analysed in our core and in neighbouring cores from the western tropical Atlantic systematically recorded different signals. Generally, Mg/Ca and TEX₈₆L show positive temperature anomalies during HS

while U^k_{37} and MAT (50m) show negative anomalies instead. Distressed conditions and low salinities stemming from enhanced Amazon River output during HSs might partially explain the negative temperature deviations of the U^k_{37} records. However, similar negative temperature anomalies in our MAT (50 m) record during AMOC slowdowns indicate the presence of a real temperature signature rather than shifts in the seasonality of alkenone fluxes or other non-thermal effects. As the ITCZ migrated southward during HS, regional precipitation increased the stratification of the upper water column and stimulated shoaling of the thermocline causing colder subsurface temperatures. In fact, the regions that experienced the clearing of the ITCZ (i.e., Tobago Basin), showed opposite trends (i.e., deepening of the thermocline and positive subsurface temperature anomalies during HS). Our high-resolution temperature records allowed to better characterize the actual thermal behaviour of the upper water column in the western tropical Atlantic. Furthermore, this work represents the attempt to reconcile the apparent discrepancy between already published temperature records in the region.

4.7 References

- Allison, M.A., Lee, M.T., Ogston, A.S., Aller, R.C., 2000. Origin of Amazon mudbanks along the northeastern coast of South America. *Mar. Geol.* 163, 241–256. doi:10.1016/S0025-3227(99)00120-6
- Andersen, K.K., Azuma, N., Barnola, J.-M., Bigler, M., Biscaye, P., Caillon, N., Chappellaz, J., Clausen, H.B., Dahl-Jensen, D., Fischer, H., Flückiger, J., Fritzsche, D., Fujii, Y., Goto-Azuma, K., Grønbold, K., Gundestrup, N.S., Hansson, M., Huber, C., Hvidberg, C.S., Johnsen, S.J., Jonsell, U., Jouzel, J., Kipfstuhl, S., Landais, A., Leuenberger, M., Lorrain, R., Masson-Delmotte, V., Miller, H., Motoyama, H., Narita, H., Popp, T., Rasmussen, S.O., Raynaud, D., Rothlisberger, R., Ruth, U., Samyn, D., Schwander, J., Shoji, H., Siggard-Andersen, M.-L., Steffensen, J.P., Stocker, T., Sveinbjörnsdóttir, A.E., Svensson, A., Takata, M., Tison, J.-L., Thorsteinsson, T., Watanabe, O., Wilhelms, F., White, J.W.C., 2004. High-resolution record of Northern Hemisphere climate extending into the last interglacial period. *Nature* 431, 147–151. doi:10.1038/nature02805
- Arz, H.W., Pätzold, J., Wefer, G., 1999. The deglacial history of the western tropical Atlantic as inferred from high resolution stable isotope records off northeastern Brazil. *Earth Planet. Sci. Lett.* 167, 105–117. doi:10.1016/S0012-821X(99)00025-4
- Baker, P.A., Rigsby, C.A., Seltzer, G.O., Fritz, S.C., Lowenstein, T.K., Bacher, N.P., Veliz, C., 2001. Tropical climate changes at millennial and orbital timescales on the Bolivian Altiplano. *Nature* 409, 698–701. doi:10.1038/35055524
- Barbante, C., Barnola, J.-M., Becagli, S., Beer, J., Bigler, M., Boutron, C., Blunier, T., Castellano, E., Cattani, O., Chappellaz, J., Dahl-Jensen, D., Debret, M., Delmonte, B., Dick, D., Falourd, S., Faria, S., Federer, U., Fischer, H., Freitag, J., Frenzel, A., Fritzsche, D., Fundel, F., Gabrielli, P., Gaspari, V., Gersonde, R., Graf, W., Grigoriev, D., Hamann, I., Hansson, M., Hoffmann, G., Hutterli, M.A., Huybrechts, P., Isaksson, E., Johnsen, S., Jouzel, J., Kaczmarek, M., Karlin, T., Kaufmann, P., Kipfstuhl, S., Kohno, M., Lambert, F., Lambrecht, A., Lambrecht, A., Landais, A., Lawer, G., Leuenberger, M., Littot, G., Loulergue, L., Lüthi, D., Maggi, V., Marino, F., Masson-Delmotte, V., Meyer, H., Miller, H., Mulvaney, R., Narcisi, B., Oerlemans, J., Oerter, H., Parrenin, F., Petit, J.-R., Raisbeck, G., Raynaud, D., Röthlisberger, R., Ruth, U., Rybak, O., Severi, M., Schmitt, J., Schwander, J., Siegenthaler, U., Siggard-Andersen, M.-L., Spahni, R., Steffensen, J.P., Stenni, B., Stocker, T.F., Tison, J.-L., Traversi, R., Udisti,

- R., Valero-Delgado, F., van den Broeke, M.R., van de Wal, R.S.W., Wagenbach, D., Wegner, A., Weiler, K., Wilhelms, F., Winther, J.-G., Wolff, E., 2006. One-to-one coupling of glacial climate variability in Greenland and Antarctica. *Nature* 444, 195–198. doi:10.1038/nature05301
- Barker, S., Diz, P., Vautravers, M.J., Pike, J., Knorr, G., Hall, I.R., Broecker, W.S., 2009. Interhemispheric Atlantic seesaw response during the last deglaciation. *Nature* 457, 1097–1102. doi:10.1038/nature07770
- Barker, S., Greaves, M., Elderfield, H., 2003. A study of cleaning procedures used for foraminiferal Mg/Ca paleothermometry. *Geochemistry, Geophys. Geosystems* 4, 1–20. doi:10.1029/2003GC000559
- Bentaleb, I., Grimalt, J.O., Vidussi, F., Marty, J.C., Martin, V., Denis, M., Hatté, C., Fontugne, M., 1999. The C37 alkenone record of seawater temperature during seasonal thermocline stratification. *Mar. Chem.* 64, 301–313. doi:10.1016/S0304-4203(98)00079-6
- Blaauw, M., Christeny, J.A., 2011. Flexible paleoclimate age-depth models using an autoregressive gamma process. *Bayesian Anal.* 6, 457–474. doi:10.1214/11-BA618
- Broccoli, A.J., 2000. Tropical cooling at the last glacial maximum: An atmosphere-mixed layer ocean model simulation. *J. Clim.* 13, 951–976. doi:10.1175/1520-0442(2000)013<0951:TCATLG>2.0.CO;2
- Broecker, W.S., 1998. Paleoocean circulation during the 1st deglaciation: A bipolar seesaw? *Paleoceanography* 13, 119–121.
- Chen, W., Mohtadi, M., Schefuß, E., Mollenhauer, G., 2014. Organic-geochemical proxies of sea surface temperature in surface sediments of the tropical eastern Indian Ocean. *Deep Sea Res. Part I Oceanogr. Res. Pap.* 88, 17–29. doi:10.1016/j.dsr.2014.03.005
- Cheng, H., Sinha, A., Cruz, F.W., Wang, X., Edwards, R.L., d’Horta, F.M., Ribas, C.C., Vuille, M., Stott, L.D., Auler, A.S., 2013. Climate change patterns in Amazonia and biodiversity. *Nat. Commun.* 4, 1411. doi:10.1038/ncomms2415
- Cheng, J., Liu, Z., He, F., Otto-Bliesner, B.L., Brady, E.C., Wehrenberg, M., 2013. Simulated Two-Stage Recovery of Atlantic Meridional Overturning Circulation During the Last Deglaciation. *Abrupt Clim. Chang. Mech. Patterns, Impacts* 75–92. doi:10.1029/2010GM001014
- Chiessi, C.M., Ulrich, S., Mulitza, S., Pätzold, J., Wefer, G., 2007. Signature of the Brazil-Malvinas Confluence (Argentine Basin) in the isotopic composition of planktonic foraminifera from surface sediments. *Mar. Micropaleontol.* 64, 52–66. doi:10.1016/j.marmicro.2007.02.002
- Crivellari, S., Chiessi, C.M., Kuhnert, H., Häggi, C., da Costa Portilho-Ramos, R., Zeng, J.-Y., Zhang, Y., Schefuß, E., Mollenhauer, G., Hefter, J., Alexandre, F., Sampaio, G., Mulitza, S., 2018. Increased Amazon freshwater discharge during late Heinrich Stadial 1. *Quat. Sci. Rev.* 181, 144–155. doi:10.1016/j.quascirev.2017.12.005
- de Boyer Montégut, C., Mignot, J., Lazar, A., Cravatte, S., 2007. Control of salinity on the mixed layer depth in the world ocean: 1. General description. *J. Geophys. Res. Ocean.* 112. doi:10.1029/2006JC003953
- Deplazes, G., Lückge, A., Peterson, L.C., Timmermann, A., Hamann, Y., Hughen, K.A., Röhl, U., Laj, C., Cane, M.A., Sigman, D.M., Haug, G.H., 2013. Links between tropical rainfall and North Atlantic climate during the last glacial period. *Nat. Geosci.* 6, 213–217. doi:10.1038/ngeo1712
- Epstein, B.L., D’Hondt, S., Quinn, J.G., Zhang, J., Hargraves, P.E., 1998. An effect of dissolved nutrient concentrations on alkenone-based temperature estimates. *Paleoceanography* 13, 122–126. doi:10.1029/97PA03358
- Escobar, J., Hodell, D.A., Brenner, M., Curtis, J.H., Gilli, A., Mueller, A.D., Anselmetti, F.S., Ariztegui, D., Grzesik, D.A., Pérez, L., Schwab, A., Guilderson, T.P., 2012. A ~43-ka record of paleoenvironmental change in the Central American lowlands inferred from stable isotopes of lacustrine ostracods. *Quat. Sci. Rev.* 37, 92–104. doi:10.1016/j.quascirev.2012.01.020
- Farmer, E.C., Kaplan, A., de Menocal, P.B., Lynch-Stieglitz, J., 2007. Corroborating ecological depth preferences of planktonic foraminifera in the tropical Atlantic with the stable oxygen isotope ratios of core top specimens. *Paleoceanography* 22, 1–14. doi:10.1029/2006PA001361
- Flower, B.P., Hastings, D.W., Hill, H.W., Quinn, T.M., 2004. Phasing of deglacial warming and Laurentide Ice Sheet meltwater in the Gulf of Mexico. *Geology* 32, 597–600. doi:10.1130/G20604.1

- Gibbs, R.J., 1980. Wind-controlled coastal upwelling in the western equatorial Atlantic. *Deep Sea Res. Part A. Oceanogr. Res. Pap.* 27, 857–866. doi:10.1016/0198-0149(80)90049-7
- Goñi, M.A., Aceves, H.L., Thunell, R.C., Tappa, E., Black, D., Astor, Y., Varela, R., Muller-Karger, F., 2003. Biogenic fluxes in the Cariaco Basin: A combined study of sinking particulates and underlying sediments. *Deep. Res. Part I Oceanogr. Res. Pap.* 50, 781–807. doi:10.1016/S0967-0637(03)00060-8
- Haake, B., Ittekkot, V., Rixen, T., Ramaswamy, V., Nair, R.R., Curry, W.B., 1993. Seasonality and interannual variability of particle fluxes to the deep Arabian sea. *Deep. Res. Part I* 40, 1323–1344. doi:10.1016/0967-0637(93)90114-I
- Häggi, C., Chiessi, C.M., Merkel, U., Mulitza, S., Prange, M., Schulz, M., Schefuß, E., 2017. Response of the Amazon rainforest to late Pleistocene climate variability. *Earth Planet. Sci. Lett.* 479, 50–59. doi:10.1016/j.epsl.2017.09.013
- Häggi, C., Chiessi, C.M., Schefuß, E., 2015. Testing the D/H ratio of alkenones and palmitic acid as salinity proxies in the Amazon Plume. *Biogeosciences* 12, 7239–7249. doi:10.5194/bg-12-7239-2015
- Hemleben, C., Spindler, M., Anderson, O.R., 1989. Modern Planktonic Foraminifera. doi:10.1007/978-1-4612-3544-6
- Herfort, L., Schouten, S., Boon, J.P., Sinninghe Damsté, J.S., 2006. Application of the TEX86 temperature proxy to the southern North Sea. *Org. Geochem.* 37, 1715–1726. doi:10.1016/j.orggeochem.2006.07.021
- Hu, C., Montgomery, E.T., Schmitt, R.W., Muller-Karger, F.E., 2004. The dispersal of the Amazon and Orinoco River water in the tropical Atlantic and Caribbean Sea: Observation from space and S-PALACE floats. *Deep. Res. Part II Top. Stud. Oceanogr.* 51, 1151–1171. doi:10.1016/j.dsr2.2004.04.001
- Huguet, C., Cartes, J.E., Sinninghe Damsté, J.S., Schouten, S., 2006. Marine crenarchaeotal membrane lipids in decapods: Implications for the TEX86 paleothermometer. *Geochemistry, Geophys. Geosystems* 7. doi:10.1029/2006GC001305
- Hüls, M., Zahn, R., 2000. Millennial-scale sea surface temperature variability in the western tropical North Atlantic from planktonic foraminiferal census counts. *Paleoceanography* 15, 659–678. doi:10.1029/1999PA000462
- Hurley, S.J., Lipp, J.S., Close, H.G., Hinrichs, K.-U., Pearson, A., 2017. Distribution and export of isoprenoid tetraether lipids in suspended particulate matter from the water column of the Western Atlantic Ocean. *Org. Geochem.* doi:10.1016/j.orggeochem.2017.11.010
- Jaeschke, A., Rühlemann, C., Arz, H., Heil, G., Lohmann, G., 2007. Coupling of millennial-scale changes in sea surface temperature and precipitation off northeastern Brazil with high-latitude climate shifts during the last glacial period. *Paleoceanography* 22, 1–10. doi:10.1029/2006PA001391
- Juggins, S., 2003. C2 user guide: Software for ecological and palaeoecological data analysis and visualization.
- Kageyama, M., Mignot, J., Swingedouw, D., Marzin, C., Alkama, R., Marti, O., 2009. Glacial climate sensitivity to different states of the Atlantic Meridional Overturning Circulation: results from the IPSL model. *Clim. Past* 5, 551–570. doi:10.5194/cp-5-551-2009
- Kim, J.H., Crosta, X., Willmott, V., Renssen, H., Bonnin, J., Helmke, P., Schouten, S., Sinninghe Damsté, J.S., 2012. Holocene subsurface temperature variability in the eastern Antarctic continental margin. *Geophys. Res. Lett.* 39, 3–8. doi:10.1029/2012GL051157
- Kim, J.H., van der Meer, J., Schouten, S., Helmke, P., Willmott, V., Sangiorgi, F., Koç, N., Hopmans, E.C., Damsté, J.S.S., 2010. New indices and calibrations derived from the distribution of crenarchaeal isoprenoid tetraether lipids: Implications for past sea surface temperature reconstructions. *Geochim. Cosmochim. Acta* 74, 4639–4654. doi:10.1016/j.gca.2010.05.027
- Knutti, R., Flückiger, J., Stocker, T.F., Timmermann, A., 2004. Strong hemispheric coupling of glacial climate through freshwater discharge and ocean circulation. *Nature* 430, 851–856. doi:10.1038/nature02786
- Kucera, M., Rosell-Melé, A., Schneider, R., Waelbroeck, C., Weinelt, M., 2005a. Multiproxy approach for the reconstruction of the glacial ocean surface (MARGO). *Quat. Sci. Rev.* 24, 813–819. doi:10.1016/j.quascirev.2004.07.017
- Kucera, M., Weinelt, M., Kiefer, T., Pflaumann, U., Hayes, A., Weinelt, M., Chen, M.-T., Mix, A.C., Barrows, T.T., Cortijo, E., Duprat, J., Juggins, S., Waelbroeck, C., 2005b. Reconstruction of sea-surface

- temperatures from assemblages of planktonic foraminifera: multi-technique approach based on geographically constrained calibration data sets and its application to glacial Atlantic and Pacific Oceans. *Quat. Sci. Rev.* 24, 951–998. doi:10.1016/j.quascirev.2004.07.014
- Kuhnert, H., Mulitza, S., 2011. Multidecadal variability and late medieval cooling of near-coastal sea surface temperatures in the eastern tropical North Atlantic. *Paleoceanography* 26. doi:10.1029/2011PA002130
- Leduc, G., Schneider, R., Kim, J.H., Lohmann, G., 2010. Holocene and Eemian sea surface temperature trends as revealed by alkenone and Mg/Ca paleothermometry. *Quat. Sci. Rev.* 29, 989–1004. doi:10.1016/j.quascirev.2010.01.004
- Lentz, S.J., 1995. Seasonal variations in the horizontal structure of the Amazon Plume inferred from historical hydrographic data. *J. Geophys. Res.* 100, 2391. doi:10.1029/94JC01847
- Liu, Z., Otto-Bliesner, B.L., He, F., Brady, E.C., Tomas, R., Clark, P.U., Carlson, A.E., Lynch-Stieglitz, J., Curry, W., Brook, E., Erickson, D., Jacob, R., Kutzbach, J., Cheng, J., 2009. Transient Simulation of Last Deglaciation with a New Mechanism for Bolling-Allerod Warming. *Science* (80-). 325, 310–314. doi:10.1126/science.1171041
- Locarnini, R.A., Mishonov, A. V., Antonov, J.I., Boyer, T.P., Garcia, H.E., Baranova, O.K., Zweng, M.M., Paver, C.R., Reagan, J.R., Johnson, D.R., Hamilton, M., Seidov, D., 2013. *World Ocean Atlas 2013. Vol. 1: Temperature.*, S. Levitus, Ed.; A. Mishonov, Technical Ed.; NOAA Atlas NESDIS. doi:10.1182/blood-2011-06-357442
- Lohmann, G., 2003. Atmospheric and oceanic freshwater transport during weak Atlantic overturning circulation. *Tellus, Ser. A Dyn. Meteorol. Oceanogr.* 55, 438–449. doi:10.1034/j.1600-0870.2003.00028.x
- Lopes, R.A., Prange, M., Castañeda, I.S., Schefuß, E., Mulitza, S., Schulz, M., Niedermeyer, E.M., Sinninghe, J.S., Schouten, S., 2010. Glacial – interglacial variability in Atlantic meridional overturning circulation and thermocline adjustments in the tropical North Atlantic. *Earth Planet. Sci. Lett.* 300, 407–414. doi:10.1016/j.epsl.2010.10.030
- López-Otálvaro, G.-E., Flores, J.A., Sierro, F.J., Cacho, I., Grimalt, J.-O., Michel, E., Cortijo, E., Labeyrie, L., 2008. Late Pleistocene paleoproductivity patterns during the last climatic cycle in the Guyana Basin as revealed by calcareous nannoplankton. *eEarth Discuss.* 3, 11–40. doi:10.5194/eed-3-11-2008
- Macdonald, A.M., Wunsch, C., 1996. An estimate of global ocean circulation and heat fluxes. *Nature* 382, 436–439. doi:10.1038/382436a0
- Mignot, J., de Boyer Montégut, C., Lazar, A., Cravatte, S., 2007. Control of salinity on the mixed layer depth in the world ocean: 2. Tropical areas. *J. Geophys. Res. Ocean.* 112, 1–12. doi:10.1029/2006JC003954
- Miller, C.B., 2004. *Biological Oceanography*. Blackwell Science, Oxford.
- Mix, A.C., Ruddiman, W.F., McIntyre, A., 1986. Late Quaternary paleoceanography of the Tropical Atlantic, 1: Spatial variability of annual mean sea-surface temperatures, 0-20,000 years B.P. *Paleoceanography* 1, 43–66. doi:10.1029/PA001i001p00043
- Muller-Karger, F.E., McClain, C.R., Richardson, P.L., 1988. The dispersal of the Amazon’s water. *Nature* 333, 56–59. doi:10.1038/333056a0
- Nace, T.E., Baker, P.A., Dwyer, G.S., Silva, C.G., Rigsby, C.A., Burns, S.J., Giosan, L., Otto-Bliesner, B., Liu, Z., Zhu, J., 2014. The role of North Brazil Current transport in the paleoclimate of the Brazilian Nordeste margin and paleoceanography of the western tropical Atlantic during the late Quaternary. *Palaeogeogr. Palaeoclimatol. Palaeoecol.* 415, 3–13. doi:10.1016/j.palaeo.2014.05.030
- Peterson, L.C., 2000. Rapid Changes in the Hydrologic Cycle of the Tropical Atlantic During the Last Glacial. *Science* (80-). 290, 1947–1951. doi:10.1126/science.290.5498.1947
- Philander, S.G.H., Gu, D., Halpern, D., Lambert, G., Lau, N.C., Li, T., Pacanowski, R.C., 1996. Why the ITCZ is mostly north of the equator. *J. Clim.* 9, 2958–2972. doi:10.1175/1520-0442(1996)009<2958:WTIIMN>2.0.CO;2
- Portilho-Ramos, R.C., Chiessi, C.M., Zhang, Y., Mulitza, S., Kucera, M., Siccha, M., Prange, M., Paul, A., 2017. Coupling of equatorial Atlantic surface stratification to glacial shifts in the tropical rainbelt. *Sci. Rep.* 7, 1561. doi:10.1038/s41598-017-01629-z

- Prahl, F.G., 2003. Physiological impacts on alkenone paleothermometry. *Paleoceanography* 18, 1–7. doi:10.1029/2002PA000803
- Prahl, F.G., Dymond, J., Sparrow, M.A., 2000. Annual biomarker record for export production in the central Arabian Sea. *Deep. Res. Part II Top. Stud. Oceanogr.* 47, 1581–1604. doi:10.1016/S0967-0645(99)00155-1
- Rama-Corredor, O., Martrat, B., Grimalt, J.O., López-Otalvaro, G.E., Flores, J.A., Sierro, F., 2015. Parallelisms between sea surface temperature changes in the western tropical Atlantic (Guiana Basin) and high latitude climate signals over the last 140 000 years. *Clim. Past* 11, 1297–1311. doi:10.5194/cp-11-1297-2015
- Ravelo, A.C., Fairbanks, R.G., Philander, S.G.H., 1990. Reconstructing tropical Atlantic hydrography using planktonic foraminifera and an ocean model. *Paleoceanography* 5, 409–431. doi:10.1029/PA005i003p00409
- Regenberg, M., Steph, S., Nürnberg, D., Tiedemann, R., Garbe-Schönberg, D., 2009. Calibrating Mg/Ca ratios of multiple planktonic foraminiferal species with $\delta^{18}\text{O}$ -calcification temperatures: Paleothermometry for the upper water column. *Earth Planet. Sci. Lett.* 278, 324–336. doi:10.1016/j.epsl.2008.12.019
- Reimer, P.J., Bard, E., Bayliss, A., Beck, J.W., Blackwell, P.G., Ramsey, C.B., Buck, C.E., Cheng, H., Edwards, R.L., Friedrich, M., Grootes, P.M., Guilderson, T.P., Haflidason, H., Hajdas, I., Hatté, C., Heaton, T.J., Hoffmann, D.L., Hogg, A.G., Hughen, K.A., Kaiser, K.F., Kromer, B., Manning, S.W., Niu, M., Reimer, R.W., Richards, D.A., Scott, E.M., Southon, J.R., Staff, R.A., Turney, C.S.M., van der Plicht, J., 2013. IntCal13 and Marine13 Radiocarbon Age Calibration Curves 0–50,000 Years cal BP. *Radiocarbon* 55, 1869–1887. doi:10.2458/azu_js_rc.55.16947
- Rühlemann, C., Mulitza, S., Muller, P.J., Wefer, G., Zahn, R., 1999. Warming of the tropical Atlantic Ocean and slowdown of thermohaline circulation during the last deglaciation. *Nature* 402, 511–514. doi:10.1038/990069
- Salisbury, J., Vandemark, D., Campbell, J., Hunt, C., Wisser, D., Reul, N., Chapron, B., 2011. Spatial and temporal coherence between Amazon River discharge, salinity, and light absorption by colored organic carbon in western tropical Atlantic surface waters. *J. Geophys. Res. Ocean.* 116, 1–14. doi:10.1029/2011JC006989
- Sancetta, C., 1995. Diatoms in the Gulf of California: Seasonal flux patterns and the sediment record for the last 15,000 years. *Paleoceanography* 10, 67–84. doi:10.1029/94PA02796
- Schmidt, M.W., Chang, P., Hertzberg, J.E., Them, T.R., Ji, L., Otto-Bliesner, B.L., 2012. Impact of abrupt deglacial climate change on tropical Atlantic subsurface temperatures. *Proc. Natl. Acad. Sci.* 109, 14348–14352. doi:10.1073/pnas.1207806109
- Schmidt, M.W., Spero, H.J., Lea, D.W., 2004. Links between salinity variation in the Caribbean and North Atlantic thermohaline circulation. *Nature* 428, 160–163. doi:10.1038/nature02346
- Schmuker, B., Schiebel, R., 2002. Planktic foraminifers and hydrography of the eastern and northern Caribbean Sea. *Mar. Micropaleontol.* 46, 387–403. doi:10.1016/S0377-8398(02)00082-8
- Schneider, T., Bischoff, T., Haug, G.H., 2014. Migrations and dynamics of the intertropical convergence zone. *Nature* 513, 45–53. doi:10.1038/nature13636
- Schouten, S., Hopmans, E.C., Schefuß, E., Sinninghe Damsté, J.S., 2002. Distributional variations in marine crenarchaeotal membrane lipids: A new tool for reconstructing ancient sea water temperatures? *Earth Planet. Sci. Lett.* 204, 265–274. doi:10.1016/S0012-821X(02)00979-2
- Sluijs, A., Schouten, S., Pagani, M., Woltering, M., Brinkhuis, H., Damsté, J.S.S., Dickens, G.R., Huber, M., Reichert, G.-J., Stein, R., Matthiessen, J., Lourens, L.J., Pedentchouk, N., Backman, J., Moran, K., the Expedition 302 Scientists, 2006. Subtropical Arctic Ocean temperatures during the Palaeocene/Eocene thermal maximum. *Nature* 441, 610–613. doi:10.1038/nature04668
- Stainforth, R.M., Lamb, J.L., Luterbacher, H., Beard, J.H., Jeffords, R.M., 1975. *Cenozoic Planktonic Foraminiferal Zonation and Characteristics of Index Forms*, University of Kansas Paleontological Contributions. Article 62. The Paleontological Institute, The University of Kansas, Kansas.
- Steph, S., Regenberg, M., Tiedemann, R., Mulitza, S., Nürnberg, D., 2009. Stable isotopes of planktonic foraminifera from tropical Atlantic/Caribbean core-tops: Implications for reconstructing upper ocean stratification. *Mar. Micropaleontol.* 71, 1–19. doi:10.1016/j.marmicro.2008.12.004

- Stocker, T.F., 2003. Global change: south dials north. *Nature* 424, 496–499. doi:10.1038/424496a
- Stramma, L., Rhein, M., Brandt, P., Dengler, M., Böning, C., Walter, M., 2005. Upper ocean circulation in the western tropical Atlantic in boreal fall 2000. *Deep. Res. Part I Oceanogr. Res. Pap.* 52, 221–240. doi:10.1016/j.dsr.2004.07.021
- Telford, R.J., Li, C., Kucera, M., 2013. Mismatch between the depth habitat of planktonic foraminifera and the calibration depth of SST transfer functions may bias reconstructions. *Clim. Past* 9, 859–870. doi:10.5194/cp-9-859-2013
- Tierney, J.E., 2013. Biomarker-Based Inferences of Past Climate: The TEX86 Paleotemperature Proxy, 2nd ed, *Treatise on Geochemistry: Second Edition*. Elsevier Ltd. doi:10.1016/B978-0-08-095975-7.01032-9
- Turich, C., Schouten, S., Thunell, R.C., Varela, R., Astor, Y., Wakeham, S.G., 2013. Comparison of TEX86 and U37K' temperature proxies in sinking particles in the Cariaco Basin. *Deep. Res. Part I Oceanogr. Res. Pap.* 78, 115–133. doi:10.1016/j.dsr.2013.02.008
- Versteegh, G.J.M., Riegman, R., De Leeuw, J.W., Jansen, J.H.F., 2001. U37K' values for *Isochrysis galbana* as a function of culture temperature, light intensity and nutrient concentrations. *Org. Geochem.* 32, 785–794. doi:10.1016/S0146-6380(01)00041-9
- Volbers, A.N.A., Henrich, R., 2004. Calcium carbonate corrosiveness in the South Atlantic during the Last Glacial Maximum as inferred from changes in the preservation of *Globigerina bulloides*: A proxy to determine deep-water circulation patterns? *Mar. Geol.* 204, 43–57. doi:10.1016/S0025-3227(03)00372-4
- Wang, L., 2000. Isotopic signals in two morphotypes of *Globigerinoides ruber* (white) from the South China Sea: Implications for monsoon climate change during the last glacial cycle. *Palaeogeogr. Palaeoclimatol. Palaeoecol.* 161, 381–394. doi:10.1016/S0031-0182(00)00094-8
- Weijers, J.W.H., Schouten, S., Spaargaren, O.C., Sinninghe Damsté, J.S., 2006. Occurrence and distribution of tetraether membrane lipids in soils: Implications for the use of the TEX86 proxy and the BIT index. *Org. Geochem.* 37, 1680–1693. doi:10.1016/j.orggeochem.2006.07.018
- Weldeab, S., Schneider, R.R., Kölling, M., 2006. Deglacial sea surface temperature and salinity increase in the western tropical Atlantic in synchrony with high latitude climate instabilities. *Earth Planet. Sci. Lett.* 241, 699–706. doi:10.1016/j.epsl.2005.11.012
- Weldeab, S., Schneider, R.R., Müller, P., 2007. Comparison of Mg/Ca- and alkenone-based sea surface temperature estimates in the fresh water-influenced Gulf of Guinea, eastern equatorial Atlantic. *Geochemistry, Geophys. Geosystems* 8, 1–10. doi:10.1029/2006GC001360
- Williams, C., Flower, B.P., Hastings, D.W., Guilderson, T.P., Quinn, K.A., Goddard, E.A., 2010. Deglacial abrupt climate change in the Atlantic Warm Pool: A Gulf of Mexico perspective. *Paleoceanography* 25, 1–12. doi:10.1029/2010PA001928
- Wuchter, C., Schouten, S., Coolen, M.J.L., Sinninghe Damsté, J.S., 2004. Temperature-dependent variation in the distribution of tetraether membrane lipids of marine Crenarchaeota: Implications for TEX86 paleothermometry. *Paleoceanography* 19, 1–10. doi:10.1029/2004PA001041
- Zhang, Y., Chiessi, C.M., Mulitza, S., Sawakuchi, A.O., Häggi, C., Zabel, M., Portilho-Ramos, R.C., Schefuß, E., Crivellari, S., Wefer, G., 2017. Different precipitation patterns across tropical South America during Heinrich and Dansgaard-Oeschger stadials. *Quat. Sci. Rev.* 177, 1–9. doi:10.1016/j.quascirev.2017.10.012
- Zhang, Y., Chiessi, C.M., Mulitza, S., Zabel, M., Trindade, R.I.F., Hollanda, M.H.B.M., Dantas, E.L., Govin, A., Tiedemann, R., Wefer, G., 2015. Origin of increased terrigenous supply to the NE South American continental margin during Heinrich Stadial 1 and the Younger Dryas. *Earth Planet. Sci. Lett.* 432, 493–500. doi:10.1016/j.epsl.2015.09.054
- Zhang, Y., Zhang, X., Chiessi, C.M., Mulitza, S., Zhang, X., Lohmann, G., Prange, M., Behling, H., Zabel, M., Govin, A., Sawakuchi, A.O., Cruz, F.W., Wefer, G., 2016. Equatorial Pacific forcing of western Amazonian precipitation during Heinrich Stadial 1. *Nat. Publ. Gr.* 1–7. doi:10.1038/srep35866

Chapter 5 . Concluding remarks

5.1 Summary of the research

In summary, the research conducted in this thesis firstly focused on a detailed characterization of HS1 in the Amazon hydrology. HS1 is associated with an extreme AMOC slowdown event. The hydrological response of the Amazon Basin to this event shows a degree of complexity, with a succession of two distinct phases that we were able to better characterize using the high-resolution record offered by marine sediment core GeoB16224-1. We then investigated to what degree the climatic response to HS is different from DOS in the tropical Americas. Relative to HS, DOS are associated to only moderate AMOC slowdowns. By confronting high resolution XRF data from marine sediment core GeoB16224-1 with five previously published continental records distributed across a latitudinal range within Central and South America, we find that DOS causes intensification of SASM but with a muted increase in precipitation over NE Brazil. Finally, given the importance of an accurate SST mapping in the western tropical Atlantic to understand the evolution of the cross-hemisphere temperature gradient, we analysed core GeoB16224-1 with a multitude of temperature proxies. We find a systematic discrepancy between $U^{k'}_{37}$ -MAT and Mg/Ca-TEX_{86L} which is probably linked to different depth sensitivity of the two proxy groups. During periods of reduced AMOC we observe warming of surface temperatures (as indicated by Mg/Ca and TEX_{86L}) due to heat accumulation and cooling of subsurface waters (as indicated by $U^{k'}_{37}$ and MAT (50 m) due to ITCZ related precipitation, increase in water stratification and shallowing of the thermocline.

5.2 General overview

Heinrich Stadial 1 is probably the most prominent millennial-scale climate change event of the last glacial. To some extent, it may represent a past analogue for a possible decrease in strength of the AMOC. Yet, the response of Amazonian hydroclimate to this major event is poorly known. To date, no record combines the necessary high temporal resolution, areal coverage, and diversity of proxies for an appropriate characterization of the HS1's chain of events in the Amazon Basin and the western equatorial Atlantic. Based in a high resolution marine sediment core retrieved off French Guiana (under the influence of the Amazon fresh water and terrigenous discharge) we present records of sea surface temperature

(Mg/Ca of planktonic foraminifera), sea surface salinity ($\delta^{18}\text{O}$ and Mg/Ca of planktonic foraminifera, as well as δD of palmitic acid), and terrigenous input (BIT index and abundance of *G. ruber*). Together with existing data of plant wax $\delta^{13}\text{C}$ *n*-alkanes, bulk sediment $\ln(\text{Fe}/\text{Ca})$ and benthic foraminifera $\delta^{13}\text{C}$ from the same core, an integrated picture of changes in Amazonian hydroclimate emerges where a succession of two phases characterizes the evolution of precipitation and erosion. During the first phase of HS1 from 18 to 16.9 cal ka BP, our records show an abrupt increase in SST concurrent with a prompt increase in the delivery of terrigenous sediments and organic matter to the western equatorial Atlantic. From 16.9 to 14 ka, the second phase of HS1, our records show a decrease in the discharge of sediments associated with decreased SSS in the western equatorial Atlantic. We suggest that a migration and strengthening of the main locus of precipitation from the western Amazon/tropical Andes to the central Amazonian plains/cratonic Brazilian shield was responsible for the markedly reduced clastic sediment yield by the Amazon River. The transition from the first to the second phase of HS1 was also characterized by: (i) a southward shift of the tropical rain belt and marked decrease of precipitation over northernmost South America; and (ii) a strong reduction in SSS on the western equatorial Atlantic despite the inefficiency of a sluggish AMOC to export salty waters to the northern hemisphere.

By analyzing high resolution $\ln(\text{Fe}/\text{Ca})$, alkenone C_{37} concentrations and $\text{C}_{37}/\text{C}_{38}$ ratios across HS and DOS between 41 and 13 cal ka BP, we notice that the effect of a sluggish AMOC impart positive anomalies on $\ln(\text{Fe}/\text{Ca})$ and negative anomalies on C_{37} concentrations. Such paired variation could be attributed to: (i) increase in terrigenous sediment sourcing from the tropical Andes; and (ii) a decrease in primary productivity related to abundant suspended sediment load and consequent light limitation. In order to better characterize the different impact of HS and DOS to tropical American hydrology, we compared five high temporal resolution precipitation records across Central and South America distributed between 17°N and 4°S . We find that both HS and DOS caused southward migration of the ITCZ and stronger SASM. However, hydrological regimes that are affected primarily by ITCZ related precipitation (i.e., NE Brazil) experienced more intense precipitation during HS and less intense precipitation during DOS. We therefore propose that, unlike HS, moderate reduction of the AMOC during DOS caused a southern shift of the ITCZ mean position which was unable to shift as far to the south.

An accurate characterization of the thermal response of the upper water column of the western tropical Atlantic to slowdown events of the AMOC was accomplished by analysing

four independent temperature proxies from sediment core GeoB16224-1. We identify systematic differences among these records and also among temperature records from neighbouring cores from the western tropical Atlantic. On GeoB16224-1, Mg/Ca and TEX₈₆L show positive temperature anomalies during HS while U^K₃₇ and MAT (50 m) show negative anomalies instead. We therefore hypothesized that distressed conditions and low salinities stemming from enhanced Amazon River output during HS might partially explain the negative temperature deviations of the U^K₃₇ records. Nevertheless, the similar negative temperature anomalies in our MAT (50 m) record during AMOC slowdowns indicate the presence of a real temperature signature which superimposes on the effect of seasonality of alkenone fluxes or other non-thermal effects. During HS, regional precipitation resulting from a southern shift of the ITCZ increased the stratification of the upper water column and shoaled the thermocline causing colder subsurface temperatures. In fact, regions from which the ITCZ is moving away (i.e., Tobago Basin), showed opposite trends (i.e., deepening of the thermocline and positive subsurface temperature anomalies during HS). We infer that whereas TEX₈₆ and Mg/Ca respond to surface temperatures, U^K₃₇ and MAT (50 m) are affected by subsurface temperature variations which respond to vertical movement of the thermocline. The presence of ITCZ related precipitation is the most likely responsible for the increased stratification and consequent shoaling of the thermocline. Nevertheless important non-thermal physiological effects on the alkenone export has also to be taken into account. The presence of low SST and large amount of suspended particulate might imprint a negative temperature bias on the U^K₃₇. However, this alone is unlikely to explain the entire variability in the U^K₃₇ temperature signal. Furthermore, this work represents an attempt to reconcile the apparent discrepancy between already published temperature records in the region.

Chapter 6 . Appendix 1 – Supplementary material to chapter 2

For the construction of the age model the BACON routine for R software package has been utilized (Blaauw and Christen, 2011), the age model being utilized has been produced and published by Zhang et al. (2017) and Häggi et al. (2017) on the same core. Along the BACON default parameters, the following settings were applied: mem.mean = 0.7, acc.shape = 1.5. Where mem.mean defines how much the accumulation rate of a particular depth in a core depends on the depth above it, and acc.shape describe the shape of the accumulation rate Gaussian distribution. Ages were modelled from a t-distribution with 3 degrees of freedom (t.a = 3, t.b = 4). These parameters describe the student-t type of age estimates that aims to encompass the unknown true error.

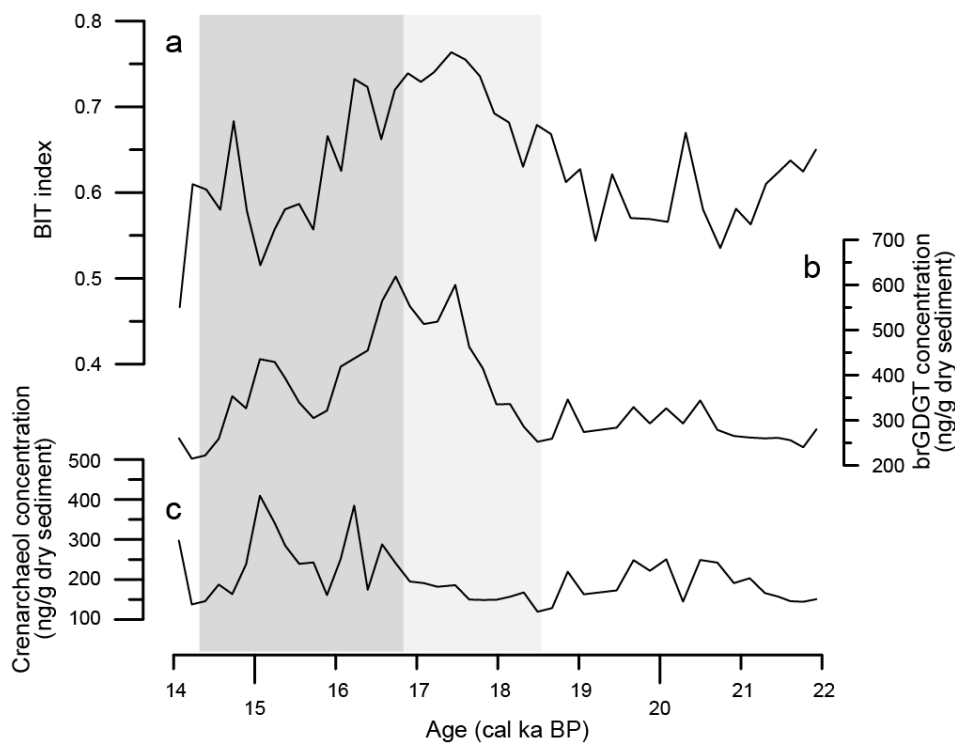


Figure S6-1. Comparison between (a) the branched and isoprenoid tetraether (BIT) index and its components namely the concentration of (b) brGDGT and (c) crenarchaeols from core GeoB16224-1 investigated in this study. Notice that the BIT index record closely resembles the brGDGT concentration record, suggesting that changes in the terrestrial component of the BIT index largely dominate the BIT index signal.

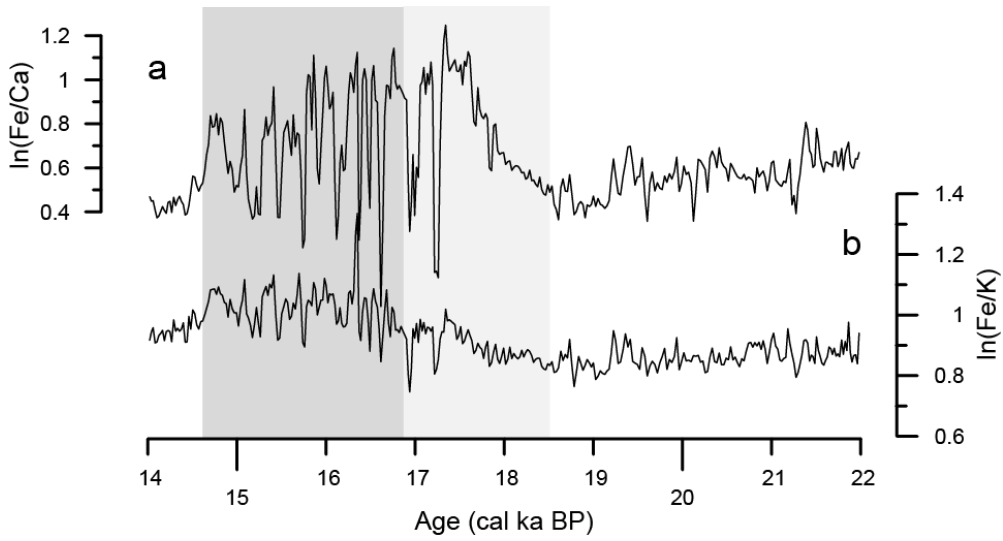


Figure S6-2. Comparison between (a) $\ln(\text{Fe}/\text{Ca})$ and (b) $\ln(\text{Fe}/\text{K})$ from core GeoB16224-1 (Zhang et al., 2017) investigated in this study.

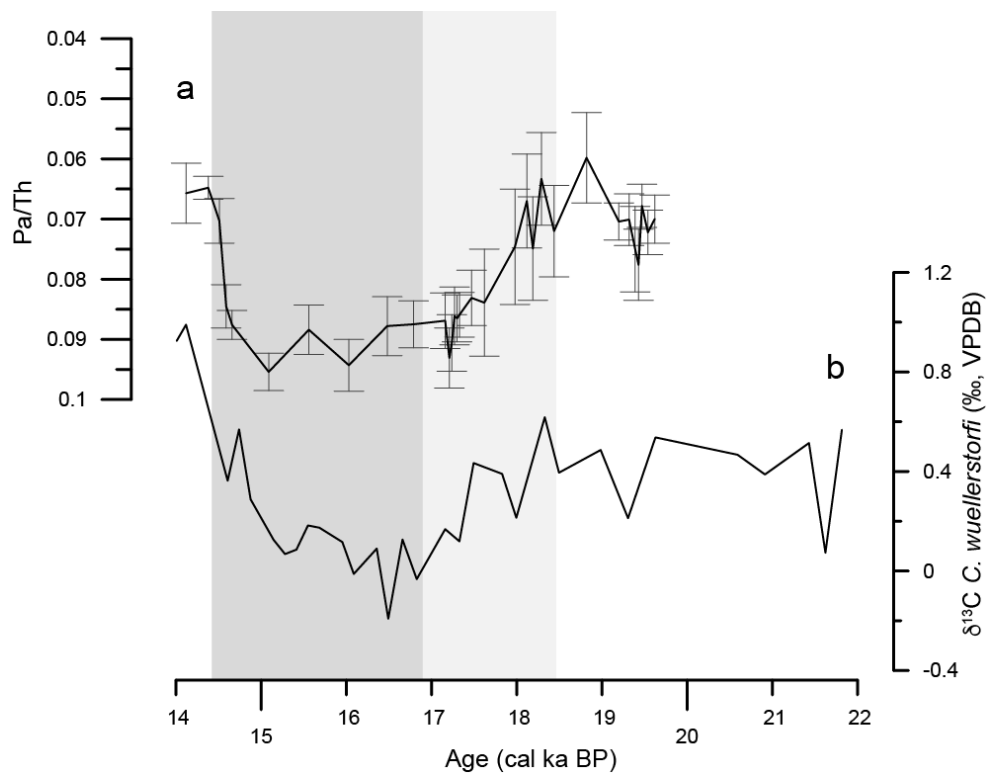


Figure S6-3. Comparison between (a) Pa/Th record of core OCE326-GGC5 from the Bermuda Rise (McManus et al., 2004) and (b) $\delta^{13}\text{C}$ of the benthic species *Cibicoides wuellerstorfi* from core GeoB16224-1 (Voigt et al., 2017) investigated in this study.

6.1 References

- Blaauw, M., and Christen, J., 2011, Flexible Paleoclimate Age-Depth Models Using an Autoregressive Gamma Process: Bayesian Analysis, v. 6, no. 3, p. 457–474, doi: 10.1214/11-BA618.
- Häggi C., Chiessi, C. M., Merkel, U., Mulitza, S., Prange, M., Schulz, M., Schefuß, E., 2017, Response of the Amazon rainforest to late Pleistocene climate variability: Earth and Planetary Science Letter, v. 479, p. 50-59, doi: 10.1016/j.epsl.2017.09.013
- McManus, J.F., François, R., Gherardi, J.M., Keigwin, L.D., and Brown-Leger, S., 2004, Collapse and rapid resumption of Atlantic meridional circulation linked to deglacial climate changes: Nature, v. 428, no. 6985, p. 834–837, doi: 10.1038/nature02494.
- Voigt, I., Cruz, A. P. S., Mulitza, S., Chiessi, C. M., Mackensen, A., Lippold, J., Antz, B., Zabel, M., Zhang, Y., Barbosa, C. F., Tisserand, A. A., 2017, Variability in mid-depth ventilation of the western Atlantic Ocean during the last deglaciation: Paleoceanography, doi: 10.1002/2017PA003095
- Zhang, Y., Chiessi, C.M., Mulitza, S., Sawakuchi, A.O., Häggi, C., Zabel, M., Schefuß, E., Crivellari, S., Wefer, G., 2017, Different precipitation patterns across tropical South America during Heinrich and Dansgaard-Oeschger stadials: Quaternary Science Reviews, v. 177, p. 1-9, doi:10.1016/j.quascirev.2017.10.012

Chapter 7. Appendix 2 – Supplementary material to chapter 3

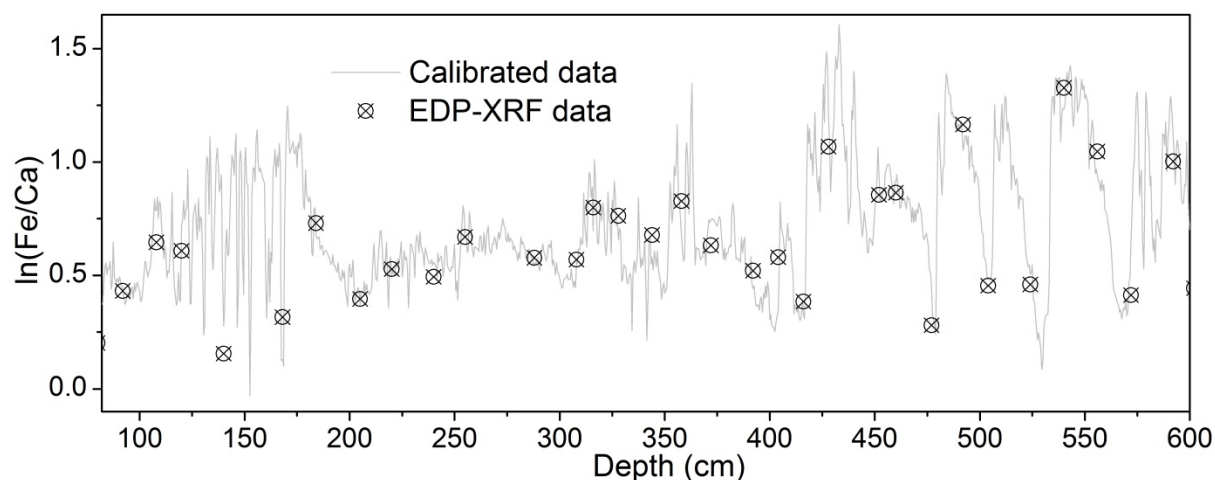


Figure S7-1. Comparison of elemental ratios in core GeoB16224-1 obtained by energy dispersive polarization X-ray fluorescence (EDP-XRF) spectroscopy and XRF-calibrated data. Down core $\ln(\text{Fe}/\text{Ca})$ values are presented versus depth for both the XRF-calibrated data (grey line) and the EDP-XRF measurements (crossed dots). The R^2 ($R^2=0.83$) value is the mean R^2 of all element/Ca log-ratio regressions (Weltje and Tjallingii, 2008).

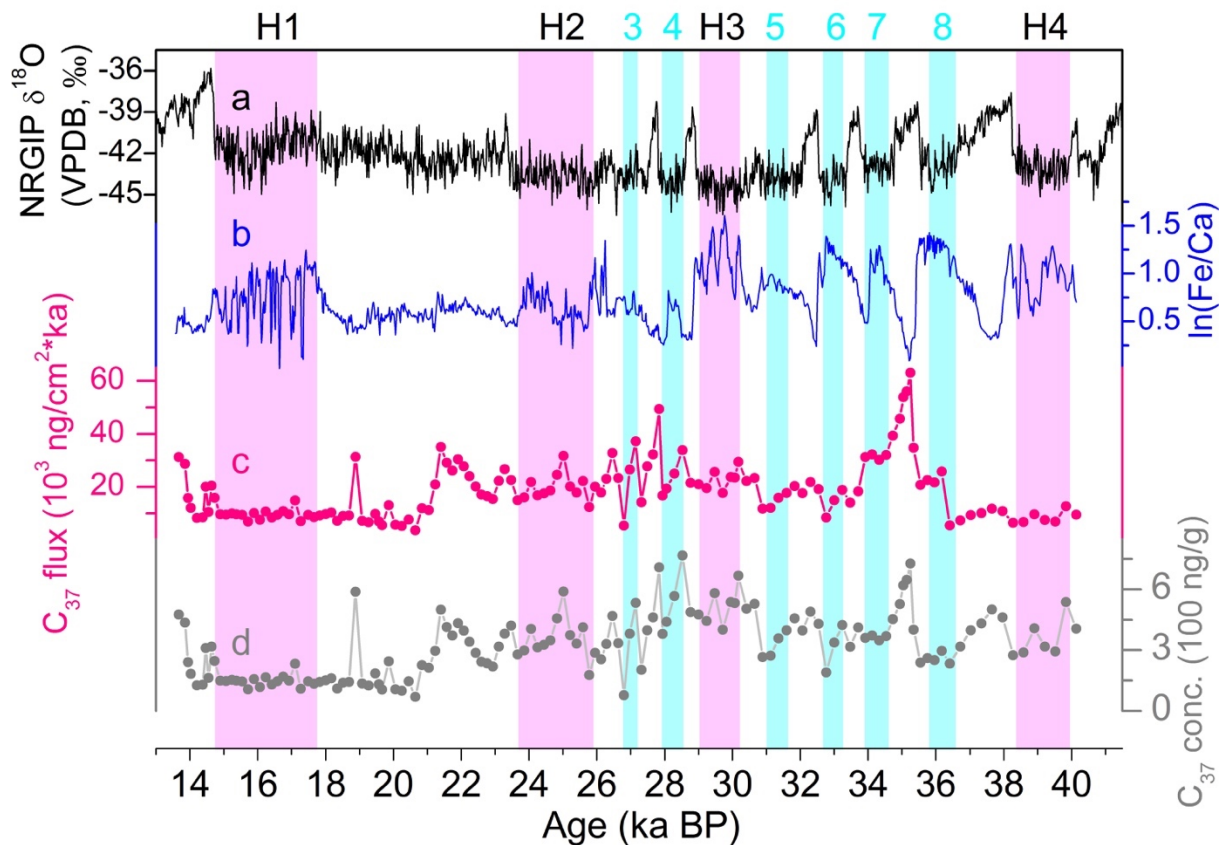


Figure S7-2. The C_{37} alkenone flux calculated based on i) C_{37} alkenone concentration and ii) accumulation rate and iii) dry bulk density of sediment in core GeoB16224-1. In general, the C_{37} alkenone flux showed similar pattern as the C_{37} alkenone concentration. For DO stadials 8-7, we note a relatively high C_{37} alkenone flux. Because there are no significant changes in dry bulk density of sediment core GeoB16224-1, the higher C_{37} flux is closely related to the sedimentation rate. We suggest that more radiocarbon dates, in particular for the DO cycles, may allow a clear understanding of sediment deposition and thus the C_{37} alkenone flux calculation.

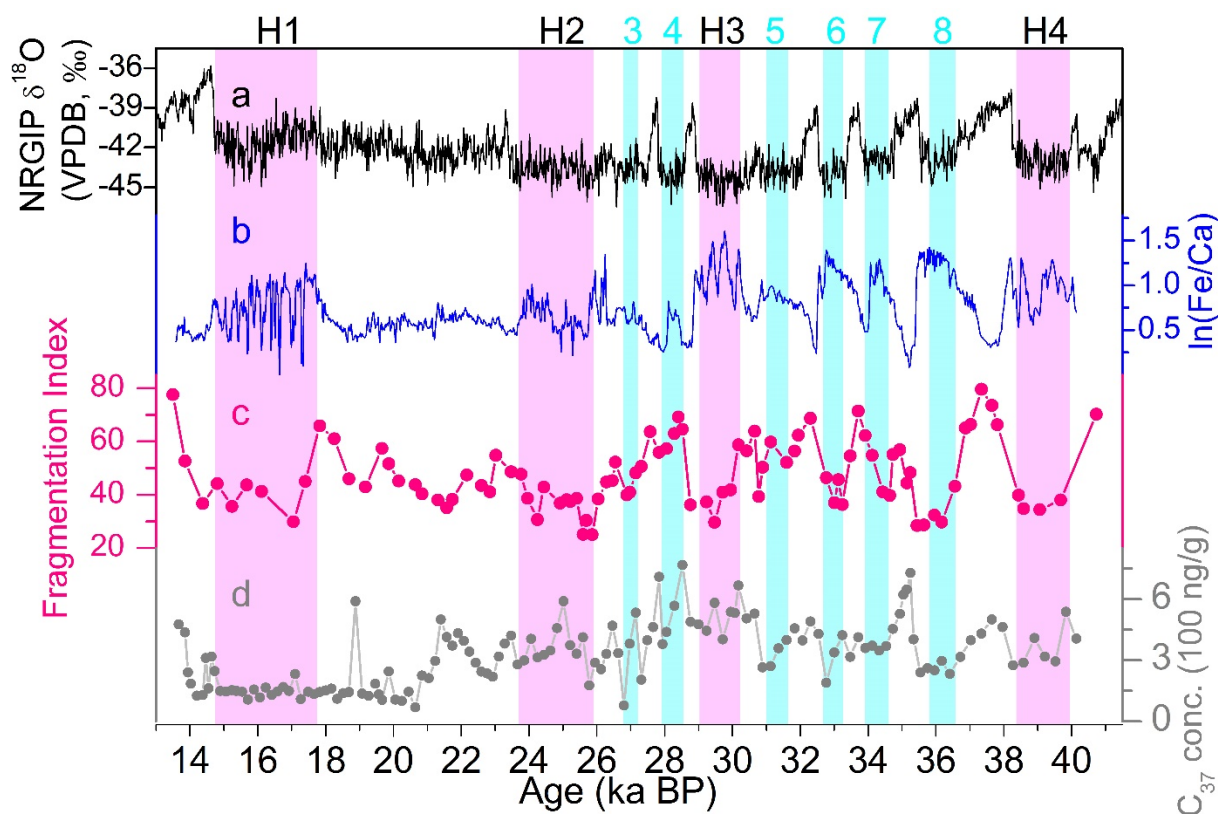


Figure S7-3. The fragmentation index by using abundance of planktonic and benthic foraminifera from totally 102 samples in core Geob16224-1, which indicated the variations of carbonate dissolution over the past 40 ka BP. If compared to the $\ln(\text{Fe}/\text{Ca})$ ratios, we clearly observed reduced dissolution of marine carbonate (as highlighted by decreased values of fragmentation index) during both the H and DO stadials. Thus, this result exclude our assumption that the carbonate dissolution contribute somehow to the changes of $\ln(\text{Fe}/\text{Ca})$ ratios.

No.	River	Lat (°N)	Long (°E)	Al (%)	Si (%)*	K (%)	Ca (%)	Fe (%)	Ti (%)	Reference
1	Madeira MAO 22b	-3.64	-59.02	22.09	60.00	5.12	0.77	11.22	0.81	This study
2	Madeira MAO 25c	-3.53	-58.91	22.04	60.00	5.17	0.75	11.20	0.83	This study
3	Madeira MAO 28c	-3.44	-58.80	21.99	60.00	5.22	0.78	11.21	0.80	This study
4	Madeira MAO 38	-3.66	-59.07	20.95	60.00	5.61	0.79	11.55	1.11	This study
5	Madeira MAO 42	-3.52	-58.90	21.39	60.00	5.27	0.69	11.72	0.92	This study
6	Madeira MAO 45	-3.42	-58.79	21.10	60.00	5.24	0.67	12.12	0.87	This study
7	Madeira AM-06-35	-3.41	-58.79	22.75	57.66	5.94	0.66	11.79	1.19	Bouchez et al., 2011
8	Madeira AM-06-38	-3.41	-58.79	19.36	63.45	5.18	0.65	10.20	1.16	Bouchez et al., 2011
9	Madeira AM-06-43	-3.41	-58.78	21.47	60.13	5.63	0.65	10.95	1.17	Bouchez et al., 2011
10	Madeira AM-05-15	-3.45	-58.81	22.41	58.66	5.86	0.69	11.22	1.17	Bouchez et al., 2011
11	Beni	-11.00	-66.09	18.11	65.71	5.29	0.48	9.34	1.07	Bouchez et al., 2012

	AM-07-09									
	Madre de									
12	Dios	-10.96	-66.10	20.76	60.45	4.81	1.20	11.46	1.32	Bouchez et al., 2012
	AM-07-14									
13	Beni	-14.47	-67.53	20.43	62.01	5.81	0.57	10.13	1.05	Bouchez et al., 2012
	AM-07-04									
14	Solimões	-3.29	-60.02	28.5	60.00	1.21	0.26	8.82	1.21	This study
	MAO 05d									
15	Solimões	-3.27	-60.29	22.2	60.00	4.15	1.86	10.69	1.10	This study
	MAO 10d									
16	Solimões	-3.20	-59.89	22.32	60.00	4.05	1.78	10.81	1.04	This study
	MAO 13d									
17	Solimões	-3.29	-60.40	19.77	60.00	3.29	1.94	14.05	0.96	This study
	MAO 72									
18	Solimões	-3.31	-60.04	19.46	60.00	3.35	1.85	14.37	0.98	This study
	MAO 77									
19	Solimões	-3.22	-59.88	19.92	60.00	3.27	1.91	13.89	1.02	This study
	MAO 80									
20	Solimões	-3.31	-60.55	21.98	59.20	4.61	1.94	11.14	1.13	Bouchez et al., 2011
	AM-06-09									
21	Marañón	-4.52	-73.91	19.99	61.24	4.37	3.44	9.91	1.07	Bouchez et al., 2012
	AM-08-24									
22	Marañón	-4.48	-73.55	19.92	56.52	4.40	8.78	9.31	1.06	Bouchez et al., 2012
	AM-08-33									
23	Amazonas	-4.00	-73.16	19.14	62.34	4.74	2.77	9.89	1.13	Bouchez et al., 2012
	AM-08-05									
24	Negro	-2.00	-61.20	34.60	45.00	1.80	0.90	17.00	0.80	Sholkovitz et al., 1978
25	Negro	-3.06	-60.30	38.20	45.00	1.30	0.50	13.50	1.50	Govin et al., 2014
	MAO 01									
26	Negro	-3.05	-60.35	30.60	45.00	5.70	2.50	14.80	1.40	Govin et al., 2014
	MAO 02f									
27	Negro	-3.08	-60.21	38.30	45.00	1.70	0.50	13.20	1.40	Govin et al., 2014
	MAO 03c									
28	Negro	-3.02	-60.44	32.40	45.00	2.50	1.30	17.30	1.50	Govin et al., 2014
	MAO 81									
29	Negro	-3.06	-60.29	33.40	45.00	0.70	1.00	18.40	1.40	Govin et al., 2014
	MAO 83									
30	Negro	-3.18	-60.00	33.50	45.00	0.00	0.80	19.20	1.40	Govin et al., 2014
	MAO 93									
31	Tapajós	-2.81	-55.07	37.42	45.00	1.56	2.98	12.05	0.99	This study
	STM 24									
32	Tapajós	-3.59	-55.33	40.44	45.00	1.30	1.10	11.18	0.98	This study
	STM 33									
33	Tapajós	-2.47	-54.99	36.95	45.00	0.84	2.10	14.06	1.05	This study
	STM 37									
34	Tapajós	-2.43	-54.94	35.25	45.00	1.37	3.42	14.03	0.92	This study
	STM 39									
35	Tapajós	-2.43	-54.92	33.93	45.00	0.34	1.34	18.48	0.91	This study
	STM 11									
36	Tapajós	-2.80	-55.08	34.27	45.00	0.37	0.75	18.73	0.88	This study
	STM 13									
37	Tapajós	-2.47	-55.00	31.28	45.00	1.00	1.71	20.28	0.73	This study
	STM 19									
38	Xingu	-3.22	-52.15	34.02	45.00	4.12	2.22	13.59	1.04	This study
	XA 01									
39	Xingu	-3.88	-52.59	35.37	45.00	3.00	2.07	13.44	1.12	This study
	XA 19									
40	Xingu	-3.49	-51.69	36.74	45.00	2.95	1.66	12.56	1.08	This study
	XA 23									

41	Xingu XA 26	-2.65	-51.98	34.97	45.00	3.82	1.68	13.40	1.13	This study
42	Xingu XA 28	-3.01	-51.85	35.20	45.00	3.05	1.83	13.84	1.08	This study
43	Xingu XA 39	-3.22	-52.14	33.05	45.00	1.29	1.76	17.76	1.13	This study
44	Xingu XA 49	-3.40	-51.97	33.87	45.00	0.97	1.35	17.80	1.01	This study
45	Xingu XA 53	-2.63	-51.97	30.67	45.00	0.92	2.08	20.52	0.81	This study
46	Xingu XA 73	-2.22	-52.16	29.38	45.00	0.82	1.44	22.60	0.76	This study

Table S7-1. Major element composition of river suspended material used for the endmember unmixing analysis (elemental proportions are given in weight percent and were calculated such as the sum of the six elements considered in this study is 100%). * Because of Si loss during total digestion (section 3.2.3 of the main text), the Si proportion of the 28 new river samples is assigned, i.e., 60% for samples from Andean tributaries Solimões and Madeira Rivers based on previously published data (Bouchez et al., 2011, 2012), and 45% for samples in lowland tributaries Negro (Govin et al., 2014), Tapajós and Xingu Rivers (Sholkovitz et al., 1978). An error of Si proportion (e.g., $\pm 2.5\%$) is also included in the endmember unmixing analysis. We run three sets of 1000 Monte-Carlo iterations with different Si proportions of river suspended samples.

Since the 45% Si hypothesis for lowland tributaries was based only on samples from the Negro River (see No. 24-30 in Table S7-1), we also applied the different Si proportions (i.e., 30% and 60% Si hypotheses) to perform the endmember unmixing analysis (Fig. S7-3, which only shows results of Si hypothesis within the range of 40%-50% for lowland tributaries). For the 30% Si hypothesis, we obtained high Andean proportion (ca. 84%) within terrigenous components, if compared to ca. 46% for the 60% Si hypothesis and ca. 73% for the 45% Si hypothesis. Previous studies (e.g., Milliman and Meade, 1983; Rimington, 1999) indicated that Andean materials are likely to account for about 70-80% of Amazon sediment discharge. Thus, the Si hypothesis for lowland tributaries within the range of 30%-45% is appropriate. Besides, we also note that very small changes in grain-size could cause large difference in down core evolution of end member models. For example, our results showed ca. 4-8% difference in Andean proportion, although grain-size of Andes-sourced sediments exhibited very small change and Si content was 40% for lowland samples. By contrast, if Si content occupied 50% for lowland samples, the same variations in grain-size of Andes-sourced sediments led to ca. 15-35% difference in Andean component.

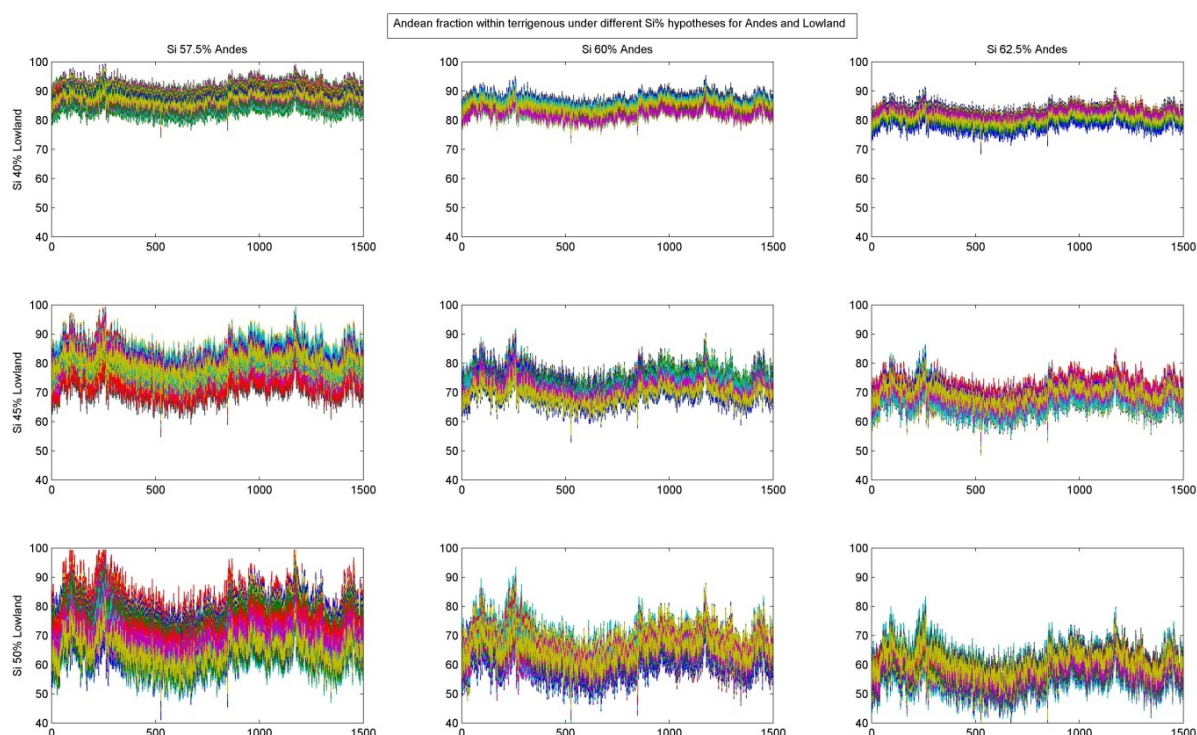


Figure S7-4. Results of the endmember unmixing analyses based on different Si hypotheses for lowland and Andes endmembers. We use a range of the Si proportions from 57.5% to 62.5% for the Andes (see panels in horizontal direction); while for the lowland, we use the range between 40% and 50% (see panels in vertical direction) (note the x-axis is the number of XRF scanning data with a step of 5mm, thus double as core length 750cm). Table S2. Summary of the terrigenous and marine biogenic endmembers (EM) used in the unmixing analysis (section 3.2.4 of the main text) for sediment core GeoB16224-1. Numbers in terrigenous EM columns refer to Table S7-1.

Core site	1 st terrigenous EM	2 nd terrigenous EM	Marine EM ^a
GeoB16224-1	Andean tributaries (1-23)	Lowland tributaries (24-46)	95 (\pm 1) % Ca 5 (\pm 1) % Si ^b

Table S7-2. Summary of the terrigenous and marine biogenic endmembers (EM) used in the unmixing analysis (section 3.2.4 of the main text) for sediment core GeoB16224-1. Numbers in terrigenous EM columns refer to Table S7-1. a The marine biogenic endmember includes only Ca and Si, which are derived from the carbonate and biogenic opal content of surface sediments in nearby sites (Lochte et al., 2000; <http://doi.pangaea.de/10.1594/PANGAEA.53229>). Values in parentheses are the errors on the composition included in the 95% confidence intervals of endmember unmixing analysis. b Nutrient-rich freshwater from the Amazon River stimulates siliceous productivity in surface waters off the Amazon mouth, as substantiated by high diatom abundance and high biogenic silica (up to 40 %) (DeMaster et al., 1983). However, the low carbonate content (ca. 7.5 %) measured in our study area indicates low biological activity, which was not sufficiently large to raise the carbonate content to 10% (Gibbs, 1973). Thus, the low biogenic silica content (< 1 %) of surface sediments still generates the high Si proportion in the endmember's composition. In addition, the error on respective Ca and Si proportions that we used during the Monte-Carlo analysis accounts for small variations in biogenic opal content.

7.1 References

- Bouchez, J., et al. 2011. Grain size control of river suspended sediment geochemistry: Clues from Amazon River depth profiles, *Geochem. Geophys. Geosyst.*, 12, Q03008, 10.1029/2010gc003380.
- Bouchez, J., et al. 2012. Floodplains of large rivers: Weathering reactors or simple silos? *Chem. Geol.* 332–333, 166–184.
- Cheng, H., et al. 2013. Climate change patterns in Amazonia and biodiversity. *Nat. Commun.* 4, doi: 10.1038/ncomms2415.
- DeMaster, D.J., et al. 1983. Biological uptake and accumulation of silica on the Amazon continental shelf. *Geochimica et Cosmochimica Acta*, 47, 1713–1723.
- Gibbs, R.J., 1973. The bottom sediments of the Amazon shelf and tropical Atlantic Ocean. *Marine Geology* 14, 39–45.
- Govin, A., et al. 2014. Terrigenous input off northern South America driven by changes in Amazonian climate and the North Brazil Current retroflexion during the last 250 ka, *Clim. Past* 10, 843–862.
- Lochte, K., et al. 2000. Atlantic data base for exchange processes at the deep sea floor (ADEPD). Data collected and published through EU-project ADEPD (MAS3-CT97-0126-ADEPD) 1998/99, Institute for Baltic Sea Research, Warnemünde, Germany, hdl:10013/epic.32910.d001.
- Milliman, J.D., Meade, R.H. 1983. World-wide delivery of river sediments to the oceans. *Journal of Geology*, 91, 1-21.
- Rimington, N. 1999. Depositional history of sands on the Amazon Fan. Ph.D. thesis, University of Cardiff.
- Sholkovitz, E.R., et al. 1978. The major-element composition of suspended matter in the Zaire river and estuary, *Netherlands Journal of Sea Research*, 12, 407–413.
- Weltje, G.J., Tjallingii, R., 2008. Calibration of XRF core scanners for quantitative geochemical logging of sediment cores: Theory and application. *Earth Planet. Sci. Lett.* 274, 423–438.